

Analysis of Human Behavior for Robot Design and Control

Lead Guest Editor: Francesca Cordella

Guest Editors: Loredana Zollo and Michelle Johnson





Analysis of Human Behavior for Robot Design and Control

Applied Bionics and Biomechanics

Analysis of Human Behavior for Robot Design and Control

Lead Guest Editor: Francesca Cordella

Guest Editors: Loredana Zollo and Michelle Johnson



Copyright © 2020 Hindawi Limited. All rights reserved.

This is a special issue published in "Applied Bionics and Biomechanics." All articles are open access articles distributed under the Creative Commons Attribution License, which permits unrestricted use, distribution, and reproduction in any medium, provided the original work is properly cited.

Editorial Board

Alberto Borboni, Italy
Andrea Cereatti, Italy
Laurence Cheze, France
Christian Cipriani, Italy
Jose L. Contreras-Vidal, USA
Agnès Drochon, France
Fabio Esposito, Italy
Ángel Gil-Agudo, Spain
Eugenio Guglielmelli, Italy
Hiroaki Hobara, Japan
Zhongmin Jin, China
Kiros Karamanidis, Germany
Justin Keogh, Australia
Thibault Lemaire, France
Andrea Marinozzi, Italy
Jose Merodio, Spain
Juan C. Moreno, Spain
Estefanía Peña, Spain
Raimondo Penta, United Kingdom
Mohammad Rahimi-Gorji, Belgium
Simo Saarakkala, Finland
Vittorio Sansalone, France
Fong-Chin Su, Taiwan
Wei Tan, USA
Amir A. Zadpoor, The Netherlands
Stefano Zaffagnini, Italy
Li-Qun Zhang, USA
Nigel Zheng, USA

Contents

Analysis of Human Behavior for Robot Design and Control

Francesca Cordella , Loredana Zollo , and Michelle J. Johnson
Editorial (2 pages), Article ID 1726347, Volume 2020 (2020)

Hierarchical Task-Parameterized Learning from Demonstration for Collaborative Object Movement

Siyao Hu  and Katherine J. Kuchenbecker 
Research Article (25 pages), Article ID 9765383, Volume 2019 (2019)

Design Analysis and Experimental Study of Robotic Chair for Proton Heavy Ion Radiotherapy

Yongde Zhang , Zhikang Yang, Jingang Jiang , Xuesong Dai, Peiwang Qin, Shijie Guo , and Sihao Zuo
Research Article (15 pages), Article ID 6410941, Volume 2019 (2019)

Human Gait Analysis Metric for Gait Retraining

Tyagi Ramakrishnan, Seok Hun Kim, and Kyle B. Reed 
Research Article (8 pages), Article ID 1286864, Volume 2019 (2019)

Kinematic Parameters for Tracking Patient Progress during Upper Limb Robot-Assisted Rehabilitation: An Observational Study on Subacute Stroke Subjects

Michela Goffredo , Stefano Mazzoleni , Annalisa Gison, Francesco Infarinato , Sanaz Pournajaf, Daniele Galafate, Maurizio Agosti, Federico Posteraro , and Marco Franceschini
Research Article (12 pages), Article ID 4251089, Volume 2019 (2019)

Measurement and Analysis of Gait Pattern during Stair Walk for Improvement of Robotic Locomotion Rehabilitation System

Sang-Eun Park, Ye-Ji Ho, Min Ho Chun, Jaesoon Choi , and Youngjin Moon 
Research Article (12 pages), Article ID 1495289, Volume 2019 (2019)

Effect of Common Pavements on Interjoint Coordination of Walking with and without Robotic Exoskeleton

Jinlei Wang, Jing Qiu , Lei Hou, Xiaojuan Zheng, and Suihuai Yu
Research Article (8 pages), Article ID 5823908, Volume 2019 (2019)

Bioinspired Implementation and Assessment of a Remote-Controlled Robot

Yves Rybarczyk  and Diogo Gil Carvalho
Research Article (10 pages), Article ID 8575607, Volume 2019 (2019)

Prediction Algorithm of Parameters of Toe Clearance in the Swing Phase

Tamon Miyake , Masakatsu G. Fujie, and Shigeki Sugano
Research Article (10 pages), Article ID 4502719, Volume 2019 (2019)

Anthropomorphism Index of Mobility for Artificial Hands

Immaculada Llop-Harillo , Antonio Pérez-González , and Verónica Gracia-Ibáñez 
Research Article (11 pages), Article ID 7169034, Volume 2019 (2019)

Editorial

Analysis of Human Behavior for Robot Design and Control

Francesca Cordella ¹, Loredana Zollo ¹, and Michelle J. Johnson²

¹Unit of Advanced Robotics and Human-Centred Technologies, Campus Bio-Medico University of Rome, Rome, Italy

²Department of Physical Medicine and Rehabilitation, University of Pennsylvania, Philadelphia, USA

Correspondence should be addressed to Francesca Cordella; f.cordella@unicampus.it

Received 21 January 2020; Accepted 22 January 2020; Published 4 February 2020

Copyright © 2020 Francesca Cordella et al. This is an open access article distributed under the Creative Commons Attribution License, which permits unrestricted use, distribution, and reproduction in any medium, provided the original work is properly cited.

Advances in biologically inspired robotic systems that is aimed at reproducing mechanics, control, sensory and actuation systems of human beings are rapidly growing, especially in the fields of human-robot interaction and cooperation. Indeed, studying and replicating the human behavior can provide new insights into the development of robotic and mechatronic systems operating in the medical domain (rehabilitation, assistance, and surgery) and, more in general, in all the application domains where collaborative robotics is being applied.

In this special issue, we present several challenging aspects of analysis and modeling of human behavior in robotics with special attention to a key aspect, i.e., how modeling and analysis can be translated into concrete guidelines for robot design and control. The focus is on novel systems and methods for the observation and analysis of human behavior and advanced approaches to replicate this behavior in robotic systems conceived for human-robot interaction. In particular, this special issue will provide an evidence of the paramount role of human behavior analysis and, in general, human inspiration in the following domains: robot teleoperation, design and control of robotic hands for prostheses, development of patient-tailored rehabilitation protocols, and design and control of assistive and rehabilitation devices (e.g., lower-limb rehabilitation devices, exoskeletons, and head and neck positioning devices).

The paper by Rybarczyk et al. shows the intuitiveness of human control of a bioinspired motion pattern with respect to nonbioinspired control. The quality of the user control of a mobile robot was assessed by comparing teleoperated control of the bioinspired motion pattern where the robot

speed is set according to the two-third power law—a law that underlies human-like motion behavior—with the manual steering mode where speed and direction is under the users' control and the nonbioinspired steering mode where speed is set linearly with direction. The results demonstrated that the performance in terms of time required to complete the path, number of collisions with obstacles, and trajectory smoothness are significantly better in the biological condition than in the two other conditions. Therefore, implementing a human-like behavior on a robot could significantly simplify the ability of a human operator to control it.

Llop-Harillo et al. present an index that evaluates the anthropomorphism of artificial robotic hands for amputees by comparing the dexterity of artificial hands with the human hand. The index was derived by studying human grasping actions, functionality of human hands, and the components of robotic hands. Thirteen prosthetic robot hands are evaluated. Results obtained by the comparison of the proposed index with other metric indexes showed that the index is quick, appropriate, and efficient in evaluating the anthropomorphism of artificial robotic hands. Therefore, it could represent a useful tool in the hand design stage to maximize hand functionality.

The paper by Hu et al. proposes to explore a new method to enable faster robot learning from humans. The study uses a hierarchical learning from demonstration structure of task-parameterized models for everyday object movement tasks. The approach uses the task-parameterized Gaussian mixture model (TP-GMM) algorithm to encode sets of demonstrations in separate models each corresponding to a different task. It is shown that the approach produces better results

as compared with learning a single TP-GMM model and allows the robot to generalize movements to undemonstrated ones. The results have been validated both in simulations and on real hardware.

Goffredo et al. analyzed kinematic data registered on 68 poststroke patients during 20 daily sessions of robot-aided upper-limb rehabilitation. A planar end-effector robot was used, and motor performance was evaluated during point-to-point trajectories executed with different direction changes. The obtained results, in terms of movement accuracy, movement speed, number of peak speed, and task completion time, demonstrated an improvement in motor performance dependent on movement direction and the level of motor impairment. Their work suggests that rapid changes in kinematic data can be seen over the first 5 sessions and may be maximum for movements involving the shoulder and elbow flexion and extension. This outlines the importance of designing patient-tailored rehabilitative protocols.

In Ramakrishnan et al., traditional approaches to gait parameter analysis are examined to give a more comprehensive and broader perspective of gait. In particular, a new combined gait asymmetry metric (CGAM) was developed using 13 spatial, temporal, and kinetic gait parameters. The new index was used to evaluate how rehabilitation therapies change gait asymmetries on six poststroke patients. The experimental results showed that the proposed CGAM metric has the potential to be used as a quantitative metric for impairments causing gait asymmetries, where a decrease in the CGAM score after therapy means that subject gait improved.

The work by Wang et al. explores how human gait during overground walking on different grounds (i.e., different kind of pavements) affect interjoint coordination (knee-ankle and hip-knee) with and without exoskeleton. Experimental tests were performed on 8 healthy subjects and the continuous relative phase (CRP) has been analyzed to examine changes in kinematics across one gait cycle. The obtained results revealed that CRP is independent of whether or not the exoskeleton is used but varies depending on the compressive capacity and unevenness of pavements. CRP is a promising parameter for use in optimizing the design of exoskeletons for motor recovery and ambulation in real-world environments.

In Park et al.'s study, human gait during stair walking is explored to improve the design of gait training robots. The study highlights the importance of stair walk training. By analyzing stair gait patterns of 6 healthy subjects and using the obtained results, in terms of angular trajectories, joint range of motion, and joint relative displacement, they extract standard patterns of stair ascent and descent to be applied on a lower-limb robotic rehabilitation system for vertical motion of footplates. The resulting trajectories enabling natural stair-climbing motions.

In the paper by Miyake et al., human gait is again studied to improve exoskeleton design and the control of overground walking in exoskeletons. The study proposes a new method based on a radial basis function network to predict toe clearance during walking, with the aim of decreasing the risk of tripping. The authors measured several parameters of the

hip, knee, and ankle joints of 11 subjects (data from 6 subjects were used for training the network and data from 5 subjects were used for testing the approach) at the beginning of the swing phase. The obtained results demonstrated that the proposed approach can be used to predict both the maximum toe clearance in the earlier swing phase and the minimum toe clearance in the later swing phase at the same time.

Finally, the paper by Zhang et al. explores human head and neck kinematics for the critical cancer treatment. They present a novel design for a proton heavy ion radiotherapy chair with a head and neck positioning device. The design is based on kinematic analysis of posture and on ergonomic evaluations. The proposed design was tested on 12 healthy subjects and the obtained results demonstrated that the proposed device meets the head and neck positioning requirements of users proving that a human-centred design is useful.

Conflicts of Interest

The editors declare that they have no conflicts of interest regarding the publication of this Special Issue.

Acknowledgments

We would like to express our gratitude to all authors who made this special issue possible.

*Francesca Cordella
Loredana Zollo
Michelle J. Johnson*

Research Article

Hierarchical Task-Parameterized Learning from Demonstration for Collaborative Object Movement

Siyao Hu ¹ and Katherine J. Kuchenbecker ^{1,2}

¹Department of Mechanical Engineering and Applied Mechanics and GRASP Laboratory, University of Pennsylvania, Philadelphia 19104, USA

²Haptic Intelligence Department, Max Planck Institute for Intelligent Systems, 70569 Stuttgart, Germany

Correspondence should be addressed to Siyao Hu; siyaohu@seas.upenn.edu

Received 18 April 2019; Accepted 28 August 2019; Published 2 December 2019

Guest Editor: Francesca Cordella

Copyright © 2019 Siyao Hu and Katherine J. Kuchenbecker. This is an open access article distributed under the Creative Commons Attribution License, which permits unrestricted use, distribution, and reproduction in any medium, provided the original work is properly cited. The publication of this article was funded by Max Planck.

Learning from demonstration (LfD) enables a robot to emulate natural human movement instead of merely executing preprogrammed behaviors. This article presents a hierarchical LfD structure of task-parameterized models for object movement tasks, which are ubiquitous in everyday life and could benefit from robotic support. Our approach uses the task-parameterized Gaussian mixture model (TP-GMM) algorithm to encode sets of demonstrations in separate models that each correspond to a different task situation. The robot then maximizes its expected performance in a new situation by either selecting a good existing model or requesting new demonstrations. Compared to a standard implementation that encodes all demonstrations together for all test situations, the proposed approach offers four advantages. First, a simply defined distance function can be used to estimate test performance by calculating the similarity between a test situation and the existing models. Second, the proposed approach can improve generalization, e.g., better satisfying the demonstrated task constraints and speeding up task execution. Third, because the hierarchical structure encodes each demonstrated situation individually, a wider range of task situations can be modeled in the same framework without deteriorating performance. Last, adding or removing demonstrations incurs low computational load, and thus, the robot's skill library can be built incrementally. We first instantiate the proposed approach in a simulated task to validate these advantages. We then show that the advantages transfer to real hardware for a task where naive participants collaborated with a Willow Garage PR2 robot to move a handheld object. For most tested scenarios, our hierarchical method achieved significantly better task performance and subjective ratings than both a passive model with only gravity compensation and a single TP-GMM encoding all demonstrations.

1. Introduction

Many modern humanoid robots are designed to operate in human environments, like homes and hospitals. If designed well, such robots could help humans accomplish tasks and lower their physical and/or mental workload. One particularly interesting task type is jointly manipulating an object with a partner [1], as it requires human collaboration, shared physical control, and adapting to new situations. The way in which one creates new robot behaviors or updates known behaviors should be intuitive and natural so that users who are not familiar with robotics can easily customize the robot to their specific environment and needs. This research is

aimed at designing an intelligent robot controller that achieves these desired characteristics.

As opposed to having an operator devise control policies and reprogram the robot for every new situation it encounters, learning from demonstration (LfD, also known as programming by demonstration (PbD)) provides a direct method for robots to learn and replicate human behaviors [2, 3]. LfD control policies are learned from demonstrations in which a human teacher controls the robot to accomplish the task. Various learning algorithms are suitable for encoding interactions recorded during demonstrations, such as hidden Markov models (HMMs) [4] and hidden semi-Markov models (HSMMs) [5]. By extending the HSMM

framework, Rozo et al. enabled the robot to be proactive if the partner does not follow the demonstrations, which were encoded by the observed temporal patterns and sequential information [6]. Dynamic motion primitives (DMPs) [7] provide another framework for interaction encoding, for example, learning an adaptive, sensor-driven interaction between two coupled agents [8]. Instead of learning or placing basis functions for the forcing term, Pervez et al. presented a DMP-based method that accommodates spatial and temporal variations in demonstrations, different initial and final conditions, and partial executions by directly encoding the phase variable and forcing term value in a Gaussian mixture model (GMM) and synthesizing the forcing term at test time using Gaussian mixture regression (GMR) [9].

Another promising learning framework is using a GMM and GMR directly on the demonstrated trajectories, where multiple channels of information (e.g., position and velocity of the robot gripper) are encoded jointly by a GMM. The conditional probability density function of the outputs on the inputs can be calculated and used in GMR for a wide range of applications such as trajectory retrieval [10]. The task-parameterized GMM (TP-GMM) framework utilizes task parameters to annotate demonstrations, and it allows generalization to undemonstrated situations by manipulating the demonstrated data with respect to the undemonstrated task parameters [11]. Rozo et al. used the TP-GMM framework for human-robot collaborative tasks, additionally modeling the robot dynamics with an impedance model that has unit mass and constant damping [12]. In a similar spirit, Pervez and Lee developed task-parameterized DMP (TP-DMP) to include such task parameters in a mixture of GMMs [13], extending the GMM that previously encoded only the phase variable and the forcing term value in [9].

In addition to utilizing various learning frameworks, LfD approaches create the opportunity for the robot to determine when new demonstrations are needed, thus avoiding poor or even dangerous actions. Uncertainty in generalized trajectories or cost functions has been used as a trigger for requesting demonstrations, where uncertainty can be calculated from, e.g., Query by Bagging [14] or a Gaussian Process (GP) [15]. Chernova and Veloso used confidence in execution to detect unfamiliar or ambiguous states that require new demonstrations [16]. In another approach, a GMM gating model that is based on observed human motions determines whether the test task is likely to be contained in the Interaction ProMPs that the robot has already learned or whether new demonstrations are necessary [17]. In these approaches, the new test is compared to what the robot has experienced, and new demonstrations are requested when the robot deems it necessary. On the other hand, Abi-Farraj et al. considered generalized trajectories for refining the learned distribution via an information gain threshold so that the robot does not need to request additional demonstrations [18].

Many approaches are aimed at building skill libraries from demonstrations. For example, Muelling et al. learn a library of DMPs from demonstrations for table tennis, and at test time, the output control policy is a weighted average of the DMP skills generated from a kernel function on input

stimuli (hitting position and velocity) and weight parameters that prioritize certain skills obtained using reinforcement learning [19]. Since a weighted average was used as a means for generalization, predicting task performance for tests was difficult, i.e., the combination of a set of good demonstrations may not necessarily result in good behavior, and thus, reinforcement learning was necessary to prune or prioritize certain skills in the DMP library [19]. As a result, when a new motion primitive is added or an existing one is deleted, the library may need to be retrained for it to converge again. In contrast, online learning is achieved in [17] by incrementally building the GMM gating model and the Interaction ProMPs, while the gating model selects only one most likely model for generalization. Other examples that incrementally build skill libraries from new demonstrations include [20–22]. Existing methods that incrementally train GMMs have also been adapted for TP-GMMs [23].

In this paper, we propose a hierarchical framework that considers the three aspects of LfD mentioned above. First, we utilize the TP-GMM algorithm [11] as the basis for demonstration encoding and generalization because of its validated merits in many tasks. Second, our utility functions operate on task parameters and allow the robot to determine when to request new demonstrations. Third, we incrementally build a library of TP-GMMs to continuously improve test performance as new demonstrations become available.

Our approach is most similar in spirit to [13, 17]. Akin to [13], we build a single skill (GMM) from one or more demonstrations corresponding to the same task parameters. We also aim to learn from a small number of available demonstrations and overcome the sparsity of task parameters in training data, although our approach uses a gating function (as does [17]) to choose the most applicable skill for generalization with TP-GMM instead of mixing skills together [13]. Consequently, it is possible to determine when new demonstrations are required in both our approach and [17] but not in [13], and our approach can incrementally build the skill library as new demonstrations become available, while [13] learns from batch data. Another important difference between our approach and [13] is that because task parameters are encoded in GMMs and their numerical differences determine the relative contributions of the mixture [13], it is not straightforward to include orientation of relevant objects/frames in the task parameters: for example, a Euler angle of 0.9π rad is numerically closer to 0.5π rad than to -0.9π rad, but one could expect the skill from -0.9π rad to be more relevant when extrapolating to 0.9π rad.

As for [17], demonstrations are represented by linear combinations of basis functions, and the weights are encoded in the GMM. As a result, each demonstration contributes only one data point to the GMM training procedure, and the dimensionality of the weight space depends on the number of basis functions, which may need to be high to have enough expressiveness in constructing the trajectories; these two factors combined may make it necessary to acquire a large number of demonstrations to avoid overfitting. In addition, task parameters are not considered in [17], and thus, this approach is more suitable when distinguishing and performing multiple types of tasks, e.g., if the robot needs to



FIGURE 1: Training and testing scenarios for collaborative manipulation with a Willow Garage PR2. (a) The teacher teleoperates the robot to manipulate an object with the partner. (b) The robot collaborates with the partner during evaluation.

hand over objects and help humans stand up. In contrast, our approach and [13] consider different instances of the same task type and are aimed at improving generalization performance when, e.g., the position of the human receiving the object changes. Finally, our approach utilizes TP-GMM directly on trajectories, so it is possible to include the position, velocity, time, and/or force dimensions in the model depending on the task, making our approach more versatile than the trajectory retrieval functions in [13, 17].

The main contributions of this work are a hierarchical LfD structure of task-parameterized models for object movement tasks, as well as analysis of the generalization performance of TP-GMM and the proposed hierarchical framework both in simulation and on real hardware. The simulated movement task shows that our hierarchical structure can predict test performance via a utility function that measures task situation similarity, improve generalization performance, and reduce computational load during training. The real movement task shows that a robot controlled by the proposed hierarchical structure collaborates with human subjects more effectively than TP-GMM or a passive robot. We focus on an object movement task, such as the scenario shown in Figure 1, because it is ubiquitous in everyday life and could benefit from robot assistance.

2. Materials and Methods

In this section, we first briefly introduce the TP-GMM algorithm [11] and use a simplistic task to illustrate potential issues with its typical implementation. Then, we introduce the proposed hierarchical structure that utilizes TP-GMM, which we instantiate and compare against typical TP-GMM in a simulated movement task. Finally, we detail the human-subject study where naive users collaboratively manipulated an object with a Willow Garage PR2 and evaluated its performance with the typical TP-GMM algorithm, the proposed hierarchical structure, and passive gravity compensation.

2.1. Overview of the Task-Parameterized Gaussian Mixture Model Algorithm. We use TP-GMM [11] to encode demonstrations and generate controller commands during test time. TP-GMM has been used to enable a robot to learn collaborative beam lifting [24] as well as object transportation and chair assembly [12]; its typical implementation, which we call vanilla TP-GMM (VT), has shown good generalization capabilities in these applications.

In the following sections, we use task situations to denote particular instances of a task: for example, in the object-moving task, moving from point A to point B and moving from point A to point C are two different task situations. In the context of TP-GMM, the task parameters fully define a task situation.

2.1.1. The TP-GMM Algorithm. The n th demonstration ($n = 1, 2, \dots, N$) contains L_n data points ($\{\xi_{n,l}\}_{l=1}^{L_n}$), and each data point may have dimensions of time, position, velocity, etc., at a given time step. The task parameters (\mathbf{p}) are defined as P affine transformations ($\{\mathbf{A}_p, \mathbf{b}_p\}_{p=1}^P$) that include information about the task situation (e.g., poses of the start and goal frames). In addition, task parameters need to be compatible with the data; for example, if each data point contains the instantaneous 3D Cartesian position and velocity of the robot gripper, i.e., $\xi = [\mathbf{x}^\top \mathbf{v}^\top]^\top$, one can define

$$\mathbf{A}_p = \begin{bmatrix} \mathbf{R}_p & \mathbf{0} \\ \mathbf{0} & \mathbf{R}_p \end{bmatrix} \quad (1)$$

and $\mathbf{b}_p = [\mathbf{r}_p^\top \ \mathbf{0}^\top]^\top$, where \mathbf{R}_p and \mathbf{r}_p represent the orientation and position of the p th relevant reference frame so that matrix operations such as $\mathbf{A}_p^{-1}(\xi - \mathbf{b}_p)$ are valid and physically meaningful.

Algorithm 1 includes a brief overview of the TP-GMM algorithm. The training step contains only the ENCODE function, which transforms data points into each task frame

```

procedure VT-TRAIN( $\{\{\xi_{n,l}\}_{l=1}^{L_n}\}_{n=1}^N, \{\mathbf{p}_{\text{train},n}\}_{n=1}^N$ )
   $\Pi = \text{ENCODE}(\{\{\xi_{n,l}\}_{l=1}^{L_n}\}_{n=1}^N, \{\mathbf{p}_{\text{train},n}\}_{n=1}^N)$ 
  return  $\Pi$ 
procedure VT-TEST( $\Pi, \mathbf{p}_{\text{test}}$ )
   $\pi = \text{DECODE}(\Pi, \mathbf{p}_{\text{test}})$ 
   $\xi^e = \text{GMR}(\pi, \xi^e)$ 
  return  $\xi^e$ 
procedure ENCODE( $\{\{\xi_{n,l}\}_{l=1}^{L_n}\}_{n=1}^N, \{\mathbf{p}_{\text{train},n}\}_{n=1}^N$ )
  for  $n = 1$  to  $N$  do
    for  $l = 1$  to  $L_n$  do
      for  $p = 1$  to  $P$  do
         $\mathbf{X}_{n,l}^{(p)} = \mathbf{A}_{\text{train},n,p}^{-1}(\xi_{n,l} - \mathbf{b}_{\text{train},n,p})$ 
         $\mathbf{X}_{n,l} = [\mathbf{X}_{n,l}^{(1)\top} \ \mathbf{X}_{n,l}^{(2)\top} \ \dots \ \mathbf{X}_{n,l}^{(P)\top}]^\top$ 
   $\Pi = \{\pi_m, \{\mu_m^{(p)}, \Sigma_m^{(p)}\}_{p=1}^P\}_{m=1}^M$ 
   $= \text{FITGMM}(\{\{\mathbf{X}_{n,l}\}_{l=1}^{L_n}\}_{n=1}^N)$ 
  return  $\Pi$ 
procedure DECODE( $\Pi, \mathbf{p}_{\text{test}}$ )
  for  $m = 1$  to  $M$  do
    for  $p = 1$  to  $P$  do
       $\hat{\mu}_m^{(p)} = \mathbf{A}_{\text{test},p} \mu_m^{(p)} + \mathbf{b}_{\text{test},p}$ 
       $\hat{\Sigma}_m^{(p)} = \mathbf{A}_{\text{test},p} \Sigma_m^{(p)} \mathbf{A}_{\text{test},p}^\top$ 
       $\Sigma_m = \left( \sum_{p=1}^P \hat{\Sigma}_m^{(p-1)} \right)^{-1}$ 
       $\mu_m = \Sigma_m \sum_{p=1}^P \hat{\Sigma}_m^{(p-1)} \hat{\mu}_m^{(p)}$ 
   $\pi = \{\pi_m, \mu_m, \Sigma_m\}_{m=1}^M$ 
  return  $\pi$ 
procedure GMR( $\pi, \xi^e$ )
  for  $m = 1$  to  $M$  do
     $\mu_m = [\mu_m^e \ \mu_m^e]^\top$ 
     $\Sigma_m = \begin{bmatrix} \Sigma_m^e & \Sigma_m^e \\ \Sigma_m^e & \Sigma_m^e \end{bmatrix}$ 
     $\hat{\mu}_m = \mu_m + \Sigma_m^e \Sigma_m^e^{-1} (\xi^e - \mu_m^e)$ 
     $h_m = \pi_m \mathcal{N}(\xi^e | \mu_m^e, \Sigma_m^e) / \sum_{m'=1}^M \pi_{m'} \mathcal{N}(\xi^e | \mu_{m'}^e, \Sigma_{m'}^e)$ 
     $\xi^e = \sum_{m=1}^M h_m \hat{\mu}_m$ 
  return  $\xi^e$ 

```

ALGORITHM 1: Given demonstrations $\{\{\xi_{n,l}\}_{l=1}^{L_n}\}_{n=1}^N$ for N situations $\{\mathbf{p}_{\text{train},n}\}_{n=1}^N$ and test situation \mathbf{p}_{test} , find a trajectory ξ^e for the test situation using vanilla TP-GMM.

and then fits a TP-GMM $\Pi = \{\pi_m, \{\mu_m^{(p)}, \Sigma_m^{(p)}\}_{p=1}^P\}_{m=1}^M$, where M is the number of Gaussian clusters, π_m is the mixture coefficient, and $\{\mu_m^{(p)}, \Sigma_m^{(p)}\}$ are the Gaussian mean and covariance matrices of the m th cluster in the p th task frame. The FITGMM function is close to the standard procedure in fitting a GMM with expectation maximization. The testing step includes two functions: DECODE transforms each Gaussian cluster in Π according to the test task parameters and generates a regular GMM π in the global frame, and GMR computes a trajectory for the test situation, which can be used as controller commands. For example, the output ξ^e could

be the velocity and the input ξ^e the position of a robot gripper, i.e., during automatic execution, the robot could derive the desired velocity given its current position.

TP-GMM exploits locally consistent features among demonstrations in each task frame (ENCODE) and transforms them according to new situations (DECODE), generally yielding reliable performance for both interpolation and extrapolation in many applications [12, 24].

However, TP-GMM does not have an explicit estimate of how well the local information would perform with respect to the new task situation in GMR; therefore, it cannot determine when new demonstrations are necessary. For example, it may have poor generalization when the new task situation is too different from what has been demonstrated. In addition, GMR may have trouble even when the test situation is exactly the same as a demonstrated one, depending on the quality and consistency of the demonstrated data. These potential issues are illustrated in the next section.

2.1.2. TP-GMM with a Simplistic Task. Suppose the task of interest is moving from a known start position to a known goal position on a one-dimensional line, and the strategy that generates demonstrations uniformly connects the start and goal points in 100 time steps, as shown in Figure 2. In this example, data points contain $\xi = [t \ x]^\top$, where $t = 1, 2, \dots, 100$ is the time step and x is the coordinate. Consequently, we include the start and the goal task frames for task parameters when training a TP-GMM, and for each, we have $\mathbf{A} = \mathbf{I}_2$ and $\mathbf{b} = [0 \ r]^\top$, where r represents the location of the frame. Without loss of generality, the start positions of all task situations are at $x = 0$.

Using vanilla TP-GMM with $M = 3$ in Algorithm 1, we can generalize trajectories for different test situations ($\xi^e = t$ and $\xi^e = x$), as shown in Figure 3. We use three clusters in this simulation because they generally cover the trajectories well and require little time to train, but other numbers work as well.

It can be seen that the generalized trajectories cover the distance between the start and goal positions well (Figure 3(a)), but they no longer contain uniform step lengths (Figure 3(b)). If the start and goal are close to each other (e.g., demonstration 1 in Figure 3), the generalized trajectory may even reverse the direction of motion at time values around 30 and 70, where the dominant Gaussian cluster changes. On the other hand, if the start and goal are far from each other (e.g., test 3 in Figure 3), the generalized trajectory may cause very large velocities near the same time points. Inconsistencies such as reversed motion direction and high magnitude velocity may cause instabilities on real hardware and might seem like faulty behaviors to a naive user. Another inconsistency is that the generalized first and last trajectory points do not always align with the prescribed start and goal positions, as shown in Figure 3(b), which may cause jumps at the beginning and end of autonomous execution. Importantly, although the types and locations of the inconsistencies can vary in different implementations, their existence is not specific to the task or the number of clusters used in simulation.

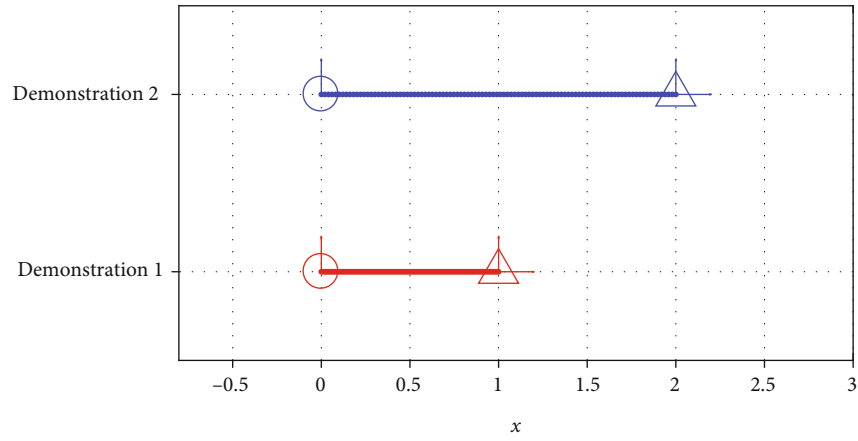
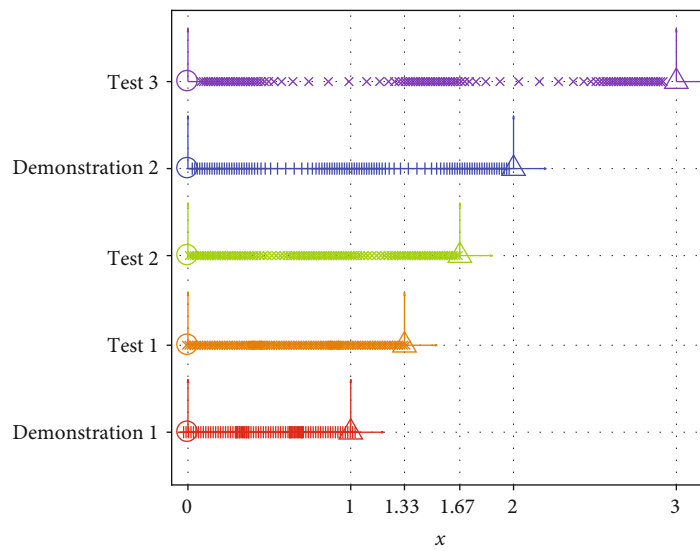
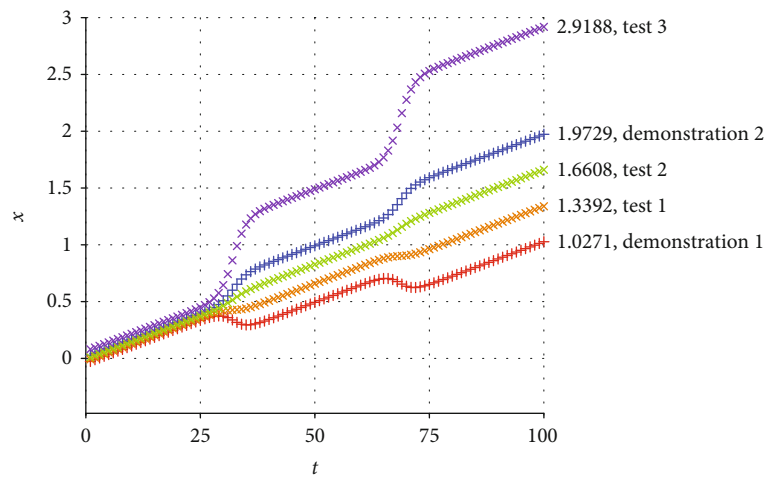


FIGURE 2: Demonstrated trajectories for a simplistic movement task. Circles represent the start positions, and triangles represent the goal positions of the task situations.



(a)



(b)

FIGURE 3: Generalized trajectories for the two demonstrated situations and three new test situations using vanilla TP-GMM. (a) Generalized trajectories. (b) Generalized trajectories over time.

What causes this difficulty with generalization? TP-GMM can be viewed as being similar to a regression algorithm: task parameters are the independent variables, and trajectories are generalized from local information in each task frame. Consequently, the exact information from each individual training point may be lost (e.g., demonstration 1 in Figure 3). In addition, because the function that maps task parameters to trajectories is highly nonlinear, the regression model does not have enough information to accurately generalize for a test point outside of the trained region (e.g., test 3 in Figure 3). Vanilla TP-GMM can have good generalization properties (test 2 in Figure 3), but it does not offer an estimate of generalized performance and thus cannot differentiate between tests 1, 2, and 3. Instead, it has to rely on the robot controller to handle the potential peculiarities of the generated trajectory. Additionally, because information from demonstrations is stored locally with respect to each task frame, the original global strategy (in this case, connecting start and goal positions with uniform step lengths) is largely lost after modeling in TP-GMM.

2.2. Hierarchical Task-Parameterized Learning from Demonstration. To preserve the powerful generalization capability of TP-GMM and overcome the previously discussed shortcomings, we propose a hierarchical structure (HS) that explicitly reasons about task parameters using three utility functions in the following steps.

First, we define a distance function that operates on a pair of task situations and outputs a scalar value, representing how similar the two situations are to each other. We argue that this scalar value can serve to estimate test performance, which can then be a trigger for requesting demonstrations. Second, sets of demonstrations associated with the same task parameters are each encoded as their own TP-GMM. Third, given a test situation, we use the distance function to select the TP-GMM from only the most similar situation. In addition, with only one situation per TP-GMM, we can manipulate the Gaussian clusters to enhance generalization with two morphing functions, because the exact information and strategy from that individual training data set are preserved. Finally, the hierarchical structure makes it straightforward to encode a large variety of task situations in the same framework.

This section empirically validates the distance function as a test performance estimator, the steps in the proposed hierarchical structure, and the improvements of our approach compared to vanilla TP-GMM for a simulated movement task.

2.2.1. Simulated Task Definition. We use a movement task with three task frames, representing the start ($\mathbf{R}_1, \mathbf{r}_1$), goal ($\mathbf{R}_2, \mathbf{r}_2$), and via ($\mathbf{R}_3, \mathbf{r}_3$) points on a two-dimensional plane. Task parameters for these frames include rotation matrices with x -axes parallel to a vector pointing from the start to the goal, z -axes pointing out of the page, and y -axes following the right-hand rule. The demonstration strategy uniformly connects the start and via points using a straight line with 100 time steps and then uniformly connects the via and goal points using a straight line with another 100 time steps

($\xi = [t \ x \ y]^T$, where $t = 1, 2, \dots, 200$), as shown in Figure 4. We call a unique specification of the frame ranges a *task configuration*.

We use this example task to instantiate the utility functions and the evaluation procedure in the following subsections. Nevertheless, the hierarchical structure can also be used in other tasks and/or with different data dimensions (such as in Section 2.3).

2.2.2. Distance Function. For the example task, we define the distance function in Algorithm 2 for two task situations (\mathbf{p}_A and \mathbf{p}_B): the task frames of the compared situations are transformed into their start frames, and the distance function value is calculated as the sum of squares of the distances between the corresponding goal and via points. Note that there may be many possible definitions for the distance function; for example, one could also choose to include a norm on the rotation matrices. Our particular definition builds on the understanding that TP-GMM aligns clusters in each task frame, and thus, the task frames' positions with respect to each other are more important than their absolute positions in the world frame.

To understand the distance function, consider the two-frame task in Section 2.1.2, where Algorithm 2 would simply calculate the square of the distances between the goals of each situation. In particular, $\text{DISTANCE}(\mathbf{p}_{\text{test},3}, \mathbf{p}_{\text{demo},1}) = (3 - 1)^2 = 4$, while $\text{DISTANCE}(\mathbf{p}_{\text{test},3}, \mathbf{p}_{\text{demo},2}) = (3 - 2)^2 = 1$. Therefore, test 3 would be considered more similar to demonstration 2 than it is to demonstration 1.

2.2.3. Situation and GMM Morphing. Similar to using DMP on generalized trajectories from a GP to ensure that the prescribed goals are reached [15], we introduce a generalization-enhancing strategy that is specific to the movement task: if the start and goal points become farther or closer to each other, then the trajectory can be proportionately stretched or compressed in the start-goal direction to accommodate the change:

$$\mathbf{T} = \frac{(\mathbf{r}_2 - \mathbf{r}_1)(\mathbf{r}_2 - \mathbf{r}_1)^T}{(\mathbf{r}_2 - \mathbf{r}_1)^T(\mathbf{r}_2 - \mathbf{r}_1)}, \quad (2)$$

$$\mathbf{r} = [x \ y]^T, \quad (3)$$

$$\begin{aligned} \mathbf{r}' &= \mathbf{r}_1 + \alpha \mathbf{T}(\mathbf{r} - \mathbf{r}_1) + (\mathbf{I} - \mathbf{T})(\mathbf{r} - \mathbf{r}_1) \\ &= (\mathbf{I} + \alpha \mathbf{T} - \mathbf{T})\mathbf{r} - (\alpha - 1)\mathbf{Tr}_1, \end{aligned} \quad (4)$$

where \mathbf{T} is the projection operator along a unit vector from start (\mathbf{r}_1) to goal (\mathbf{r}_2), \mathbf{r} is an arbitrary point of the original trajectory, α is the scalar value representing the extent of stretching or compression, and \mathbf{r}' is the proportionately changed new trajectory point, as shown in Figure 5.

Consequently, we can generate task parameters and Gaussian clusters for the new situation in the same manner. Algorithm 3 details how this process can be carried out in accordance with the current definition of $\xi = [t \ x \ y]^T$ (see definitions of \mathbf{T}' and \mathbf{T}''), where \mathbf{T} is defined in Equation

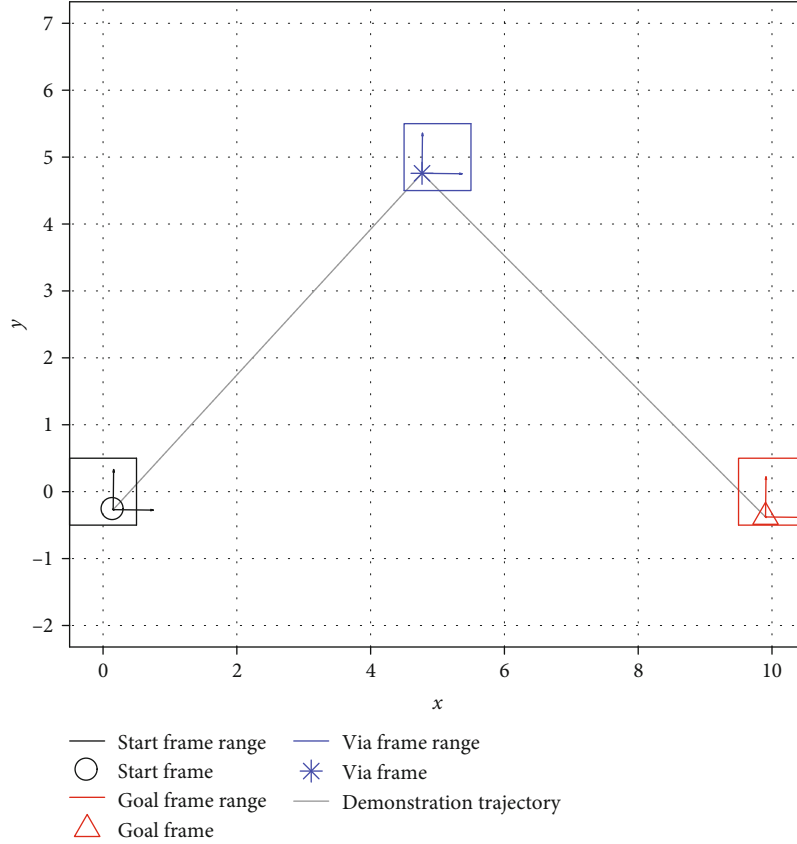


FIGURE 4: An example task situation and its trajectory. The frame ranges show the regions from which each task frame is randomly sampled.

```

procedure DISTANCE( $\mathbf{p}_A, \mathbf{p}_B$ )
   $d = 0$ 
  for  $j = 2$  to  $3$  do
     $d = d + \|\mathbf{R}_{1,A}^T(\mathbf{r}_{j,A} - \mathbf{r}_{1,A}) - \mathbf{R}_{1,B}^T(\mathbf{r}_{j,B} - \mathbf{r}_{1,B})\|$ 
  return  $d$ 

```

ALGORITHM 2: Distance function.

(3). The morphed task situation and GMM clusters are plotted in Figure 5.

2.2.4. Hierarchical Structure. With the utility functions defined in Algorithms 2 and 3, we propose a hierarchical structure for TP-GMM, shown in Algorithm 4. Demonstrations from each situation are encoded in separate TP-GMMs (Π_n) in the training step. In the test step, the new situation is maximally matched with each demonstrated situation (the $\arg \min$ step in the **for** loop), and we select the overall best match n^* for generalization in the DECODE function if the matched result d_{n^*} is below a prescribed threshold. If the threshold is exceeded, new demonstrations should be requested. This process serves as a gating function, similar to the one in [17]. Finally, the Gaussian clusters in the generated world-frame GMM π^* are inversely morphed with $\alpha_{n^*}^{-1}$ to ensure that the final GMM π is compatible with and applicable to the actual,

desired test situation \mathbf{p}_{test} . Note that the $\arg \min$ step in the **for** loop in Algorithm 4 can be solved analytically, because of the linear operations on the task parameters and the L2-norms.

2.2.5. Validation of HS in Simulation. We conducted simulations to empirically validate the hierarchical structure and compare its performance with vanilla TP-GMM (VT). The simulation procedure is detailed in Algorithm 5. We used $N_{\text{train}} = 2, 3, \dots, 10$ and $M_{\text{test}} = 100$ to explore how test performance changes with an increasing number of demonstrated situations. We repeated SIM 20 times for each value of N_{train} so that we could extensively sample both training and test situations. We used $d_{\text{threshold}} = \infty$ with HS to disable new demonstration requests because VT cannot preemptively stop execution. Finally, we used three different task configurations of start, goal, and via frame sampling ranges to verify the hierarchical framework's performance.

Figure 6 shows sample generalized trajectories for a test with three demonstrated task situations. We used EVAL in Algorithm 5 to calculate *generalization errors* as the squares of the distances between the first generalized trajectory point and the start frame, the last trajectory point and the goal frame, and the 100th trajectory point and the via frame. These three pairs of points should coincide for a trajectory that was perfectly generated according to the original demonstration strategy, yielding zero error.

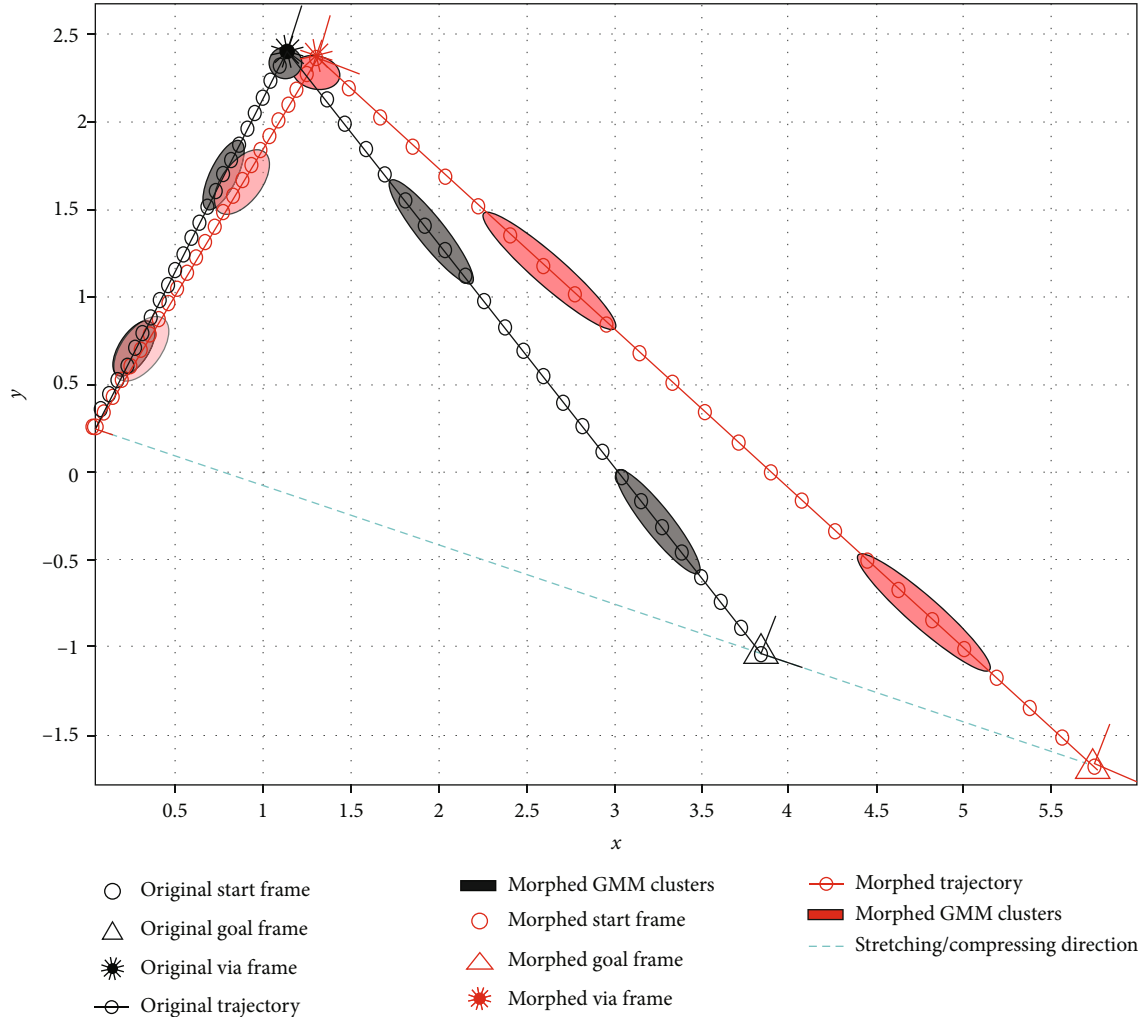


FIGURE 5: Illustration of Equations (2), (3) and (4) and the morphing functions in Algorithm 3. The original task frames are randomly sampled, and the original trajectory and GMM clusters are generated from the demonstration strategy and trained accordingly. The morphed frames, trajectory, and GMM clusters are calculated from the original ones with $\alpha = 1.5$. Note that the original and morphed start frames coincide.

(1) *Distance Function as a Performance Estimator.* For the task configuration shown in Figure 4, Figure 7 shows the accumulated generalization errors against the corresponding distance function values. For brevity, we show results only when two, five, or eight situations were demonstrated. The general trend that the upper bounds of the generalization errors are roughly linearly proportional to the distance function value is true for all numbers of demonstrations. In other words, the distance value can serve as a cautious estimator of generalization errors so that if the user needs to maintain a minimum level of performance (maximum allowed generalization error), he or she can prevent task execution if the distance value is above a certain threshold and can instead provide more demonstrations to the robot.

(2) *Generalization Performance.* Figure 7 shows that HS achieved better performance (lower generalization errors) than VT. The accumulated generalization errors are shown for a few different task configurations in Figure 8 to fully verify that observation. It can be seen that as the number

of demonstrated situations increases from two to nine (we explain the results with ten situations in the next point), generalization errors become lower for both VT and HS. Nevertheless, HS almost always has significantly better performance than VT.

To showcase the difference in performance during interpolation/extrapolation, we performed an additional test where the training demonstrations were generated from the task configuration shown in Figure 4, while the goal frame ranges of test task configurations may be closer to or farther away from the start frame range, as shown in Figure 9. Because TP-GMM utilizes affine transformations as task parameters as opposed to scalar values or position vectors, we chose these test task configurations to indicate that the test task parameters could be drawn from the same distribution as the training task parameters (interpolation, test goal frame range 3) or from different distributions (extrapolation, test goal frame ranges 1, 2, 4, and 5). The simulation procedure was the same as Algorithm 5, and we used $N_{\text{train}} = 5$

```

procedure MORPH_TASK( $\mathbf{p}, \alpha$ )
  for  $i = 1$  to 3 do
     $\mathbf{R}'_i = \mathbf{R}_i$ 
     $\mathbf{r}'_i = (\mathbf{I} + \alpha\mathbf{T} - \mathbf{T})\mathbf{r}_i - (\alpha - 1)\mathbf{T}\mathbf{r}_1$ 
     $\mathbf{A}'_i = \begin{bmatrix} 1 & \mathbf{0} \\ \mathbf{0} & \mathbf{R}'_i \end{bmatrix}$ 
     $\mathbf{b}'_i = \begin{bmatrix} 0 & \mathbf{r}'_i \end{bmatrix}^\top$ 
  return  $\Pi$ 
procedure MORPH_GMM( $\pi, \alpha, \mathbf{p}$ )
   $\mathbf{T}' = \begin{bmatrix} 1 & \mathbf{0} \\ \mathbf{0} & \mathbf{I} + \alpha\mathbf{T} - \mathbf{T} \end{bmatrix}$ 
   $\mathbf{T}'' = \begin{bmatrix} 1 & \mathbf{0} \\ \mathbf{0} & (\alpha - 1)\mathbf{T} \end{bmatrix}$ 
  for  $m = 1$  to  $M$  do
     $\boldsymbol{\mu}'_m = \mathbf{T}'\boldsymbol{\mu}_m - \mathbf{T}''\mathbf{b}_1$ 
     $\boldsymbol{\Sigma}'_m = \mathbf{T}'\boldsymbol{\Sigma}_m\mathbf{T}'^\top$ 
   $\pi' = \{\pi_m, \boldsymbol{\mu}'_m, \boldsymbol{\Sigma}'_m\}_{m=1}^M$ 
  return  $\pi'$ 

```

ALGORITHM 3: Utility functions that morph task situations and Gaussian clusters in GMMs.

and $M_{\text{test}} = 100$. The accumulated generalization errors are shown in Figure 10. It can be seen that performance was the best for both VT and HS during interpolation, and performance decreased more severely for heavier extrapolation (test goal frame ranges 1 and 5). Nevertheless, HS consistently achieved better results than VT in all configurations.

(3) *Effect of an Outlier Situation.* We mentioned that TP-GMM can be seen as a regression algorithm, with the task parameters as independent variables and the trajectories as dependent variables. Therefore, we explored the effect of having outlier training data in TP-GMM when there were ten demonstrated situations in the simulation procedure: the tenth situation had a different sampling range for the via frame, as shown in the top panels of Figure 8. It can be seen that VT suffered from this single outlier: compared to results with nine and sometimes even two demonstrated situations (see e_1 in Figure 8(a) and e_2 in Figure 8(c)), average generalization errors increased when demonstrations from ten situations were available, even though more training data is often assumed to improve test performance. On the other hand, HS was not affected by the outlier and maintained the same level of performance, because task parameters were used to first filter the training data, and only the most similar situation was used in generalization.

Note that although the outlier situations differ from the majority of the training data from the model's point of view, they may still be of interest to users and hence should be learned by the robot. Therefore, it may be more sensible for vanilla TP-GMM to encode the different situations in a separate model so that the robot can handle the outlier situations

without affecting performance for the regular situations. However, to the best of our knowledge, allowing a robot to automatically determine when to create a new model is still an open problem regarding TP-GMM, precisely because the strengths of TP-GMM include handling data from varied task situations.

(4) *Training Time.* Another advantage that HS offers is reducing computational load when demonstrations from new situations become available gradually. The VT-TRAIN function always encodes all demonstrations together, which means previously encoded demonstrations have to be stored for reuse later. On the other hand, because HS-TRAIN encodes each situation in a separate TP-GMM, only new data needs processing when it becomes available. Figure 11 shows the time spent only in training TP-GMMs as the number of available situations increases in the simulation procedure: HS consistently took little time to encode new data, while VT had to spend more time encoding everything.

Note that here we stored all demonstrations and computed a new TP-GMM every time for VT, instead of using one of the incremental TP-GMM methods in [23] because of the following reasons. First, the generative technique in [23] does not save computation time compared to VT because it samples trajectories using the existing model to represent previously encoded trajectories, which are then encoded with new trajectories to form a completely new model. Furthermore, performance may suffer because sampled trajectories are used in the new model instead of actual demonstrations. Second, the model addition technique in [23] will also take strictly more time than HS because it encodes new demonstrations in a new model like HS and then has to concatenate and optimize the previous and the new models together. Third, the direct update technique [23] assumes that the old demonstrations and the new ones are drawn from the same distribution, which is problematic because we sample from a relatively large number of task situations or even an outlier situation.

The advantage of reduced computational load is also true when removing demonstrations. In this example, HS can identify the outlier in the 10 demonstrated situations, because it was never selected for generalization, and thus, the corresponding TP-GMM could be deleted from the robot's database without affecting performance. In contrary, there is no inherent method in VT to identify the outlier, and even if a human operator identifies the outlier situation to be deleted, a new TP-GMM has to be trained from scratch to recover the performance of the nine remaining inlier demonstrations. Incremental methods such as [15, 23] do not seem to consider removing demonstrations.

2.2.6. *Comparison Summary between HS and VT.* Compared to vanilla TP-GMM, the proposed hierarchical structure has higher complexity because it encodes a separate TP-GMM for each demonstrated task situation and has several utility functions to compare and morph test situations against demonstrated ones. However, this structured approach enables a robot to differentiate between the demonstrated situations

```

procedure HS-TRAIN( $\{\{\xi_{n,l}\}_{l=1}^{L_n}\}_{n=1}^N, \{\mathbf{P}_{\text{train},n}\}_{n=1}^N$ )
  for  $n = 1$  to  $N$  do
     $\Pi_n = \text{ENCODE}(\{\xi_{n,l}\}_{l=1}^{L_n}, \mathbf{P}_{\text{train},n})$ 
  return  $\{\Pi_n\}_{n=1}^N$ 
procedure HS-TEST( $\{\Pi_n\}_{n=1}^N, \{\mathbf{P}_{\text{train},n}\}_{n=1}^N, \mathbf{P}_{\text{test}}, d_{\text{threshold}}$ )
  for  $n = 1$  to  $N$  do
     $\alpha_n = \arg \min_{\alpha} \text{DISTANCE}(\text{MORPH\_TASK}(\mathbf{p}_{\text{test}}, \alpha), \mathbf{P}_{\text{train},n})$ 
     $\mathbf{p}_n = \text{MORPH\_TASK}(\mathbf{p}_{\text{test}}, \alpha_n)$ 
     $d_n = \text{DISTANCE}(\mathbf{p}_n, \mathbf{P}_{\text{train},n})$ 
   $n^* = \arg \min_n d_n$ 
  if  $d_{n^*} < d_{\text{threshold}}$ 
     $\pi^* = \text{DECODE}(\Pi_{n^*}, \mathbf{P}_{n^*})$ 
     $\pi = \text{MORPH\_GMM}(\pi^*, \alpha_{n^*}^{-1}, \mathbf{P}_{\text{test}})$ 
     $\xi^e = \text{GMR}(\pi, \xi^v)$ 
    return  $\xi^e$ 
  else
    Request new demonstrations.
  return

```

ALGORITHM 4: Given demonstrations $\{\{\xi_{n,l}\}_{l=1}^{L_n}\}_{n=1}^N$ for N situations $\{\mathbf{P}_{\text{train},n}\}_{n=1}^N$ and test situation \mathbf{p}_{test} , find a trajectory ξ^e for the test situation using hierarchical TP-GMM.

and select the most similar experience for trajectory generalization. As a result, the robot can halt autonomous execution if its expected performance is lower than a predefined threshold. In contrast, VT does not offer these abilities. Because HS selectively uses demonstrations during generalization, test performance can also be improved via situation-specific manipulation of trajectories using the morphing functions. Moreover, it is possible to include a wide variety of task situations in the same HS framework without decreasing performance, while VT may lose situation-specific information because it effectively averages all demonstrations. Lastly, new demonstrations can easily be added to the skill library by creating a new TP-GMM, and poor or no-longer-wanted demonstrations that are already encoded can easily be removed with the hierarchical structure.

Special care needs to be considered when defining the utility functions in HS. For tasks such as object movement, Cartesian distances between corresponding task frames can readily be used in the distance function because they utilize the same information that TP-GMM considers. As for the morphing functions, our example validates the effectiveness of the hierarchical structure even with their simple and intuitive definitions. Other approaches, such as using reinforcement learning to optimize task parameters [25], may be used as well at the expense of additional design effort and computational load.

2.3. Experiment Validation on Real Hardware. We tested our proposed learning structure using a Willow Garage PR2 in the real collaborative object-manipulating task shown in Figure 1. The PR2 has two mirrored arms, each with four revolute arm joints and three revolute wrist joints. We collected demonstrations for three different task situations and con-

ducted a human-subject study to validate the generalization performance of the proposed hierarchical structure in this task. Fifteen adults participated in the study, each completing the collaborative object-manipulation task under various task situations, experiencing the demonstration process, and filling out questionnaires to evaluate their interactions with the robot. The Penn IRB approved all experimental procedures under protocol 829536. Subjects gave informed consent and received no compensation for participating.

2.3.1. Task Definition. The left arm of the PR2 robot holds an object (a rigid rectangular plate) together with the human partner; the robot and the participant collaborate to move the object from a start position to a goal position while avoiding an obstacle. The plate has a mass of 0.77 kg and a size of 0.30 m by 0.20 m by 0.01 m, and the obstacle is a slightly tapered plastic cylinder with a top radius of 0.23 m, as shown in Figure 1. The minimum and maximum distances between the robot end-effector at robot-shoulder height and the shoulder joint are about 0.4 m and 0.82 m, so the size of the obstacle is significant when compared to the robot's workspace. Thus, the robot's trajectories during collaborative movement need to make sense for the human partner for the task to be successful.

2.3.2. Demonstrating Procedure. When collecting demonstrations, we used the PR2's right arm as the master and its left arm as the slave in bilateral teleoperation [26]. The teacher guided the master to help the human partner accomplish the desired task with the slave arm, therefore directly feeling the motions and limits of the robot arm, similar to how demonstrations are done in kinesthetic teaching. Demonstration recordings included the Cartesian

```

procedure SIM( $N_{\text{train}}, M_{\text{test}}, \text{start\_range}, \text{goal\_range}, \text{via\_range}$ )
  for  $n = 1$  to  $N_{\text{train}}$  do
    Sample  $\mathbf{p}_{\text{train},n}$  from sampling ranges
    Generate a demonstration trajectory  $\{\xi_{n,l}\}_{l=1}^{200}$ 
     $\Pi_{\text{VT}} = \text{VT-TRAIN}(\{\{\xi_{n,l}\}_{l=1}^{200}\}_{n=1}^{N_{\text{train}}}, \{\mathbf{p}_{\text{train},n}\}_{n=1}^{N_{\text{train}}})$ 
     $\{\Pi_n\}_{n=1}^N = \text{HS-TRAIN}(\{\{\xi_{n,l}\}_{l=1}^{200}\}_{n=1}^{N_{\text{train}}}, \{\mathbf{p}_{\text{train},n}\}_{n=1}^{N_{\text{train}}})$ 
  for  $m = 1$  to  $M_{\text{test}}$  do
    Sample  $\mathbf{p}_{\text{test},m}$  from sampling ranges
    for  $n = 1$  to  $N_{\text{train}}$  do
       $d_{m,n} = \text{DISTANCE}(\mathbf{p}_{\text{test},m}, \mathbf{p}_{\text{train},n})$ 
       $d_m = \min d_{m,n}$ 
       $\xi_{\text{VT}}^e = \text{VT-TEST}(\Pi_{\text{VT}}, \mathbf{p}_{\text{test}})$ 
       $\xi_{\text{HS}}^e = \text{HS-TEST}(\{\Pi_n\}_{n=1}^{N_{\text{train}}}, \{\mathbf{p}_{\text{train},n}\}_{n=1}^{N_{\text{train}}}, \mathbf{p}_{\text{test}}, \infty)$ 
       $e_{\text{VT},m} = \text{EVAL}(\mathbf{p}_{\text{test},m}, \xi_{\text{VT}}^e)$ 
       $e_{\text{HS},m} = \text{EVAL}(\mathbf{p}_{\text{test},m}, \xi_{\text{HS}}^e)$ 
  return  $\{d_m\}_{m=1}^{M_{\text{test}}}, \{e_{\text{VT},m}\}_{m=1}^{M_{\text{test}}}, \{e_{\text{HS},m}\}_{m=1}^{M_{\text{test}}}$ 
procedure EVAL( $\mathbf{p}, \xi$ )
   $e_1 = \|\xi_1 - \mathbf{r}_1\|$ 
   $e_2 = \|\xi_2 - \mathbf{r}_2\|$ 
   $e_3 = \|\xi_3 - \mathbf{r}_3\|$ 
  return  $\{e_1, e_2, e_3\}$ 

```

ALGORITHM 5: Simulation procedure.

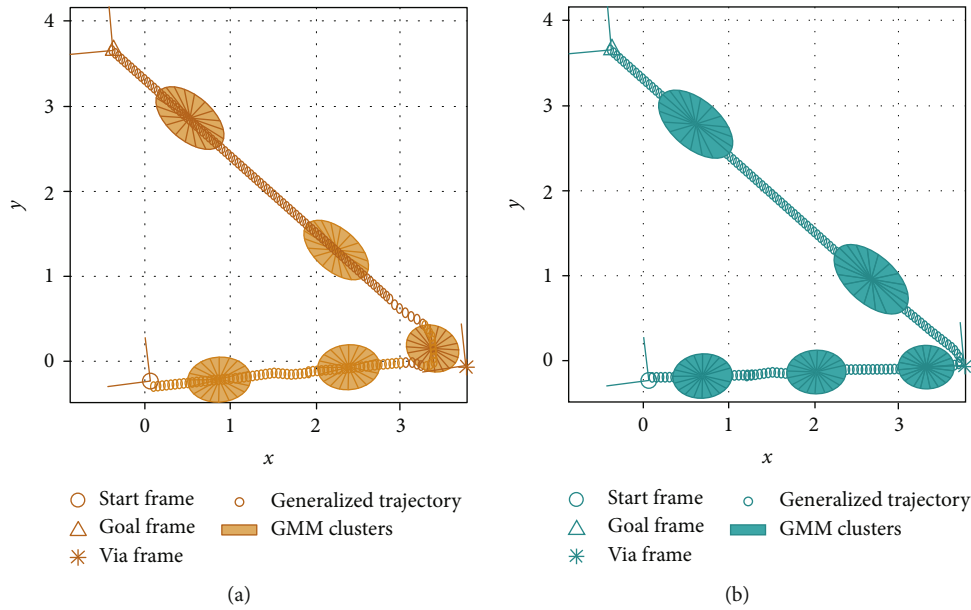


FIGURE 6: Generalized trajectories for a test when three demonstrated task situations are available: (a) vanilla TP-GMM (VT); (b) hierarchical structure (HS).

position of the slave's wrist center calculated from forward kinematics. Force feedback between the master and the slave was achieved through a joint-level proportional-derivative (PD) torque controller, and therefore, no force or torque sensor was required.

For the master-side wrist joints, an additional virtual fixture [27] was applied to help the teacher control the robot's

hand orientation. The virtual fixture torques were calculated using a PD controller with zero desired velocity:

$$\tau_{i,\text{vf}} = K_p(q_{i,\text{vf}} - q_{i,m}) - K_d \dot{q}_{i,m}, \quad (5)$$

where $q_{i,m}$ are the desired wrist joint angles for the virtual fixture. In the current work, we used the virtual fixture to

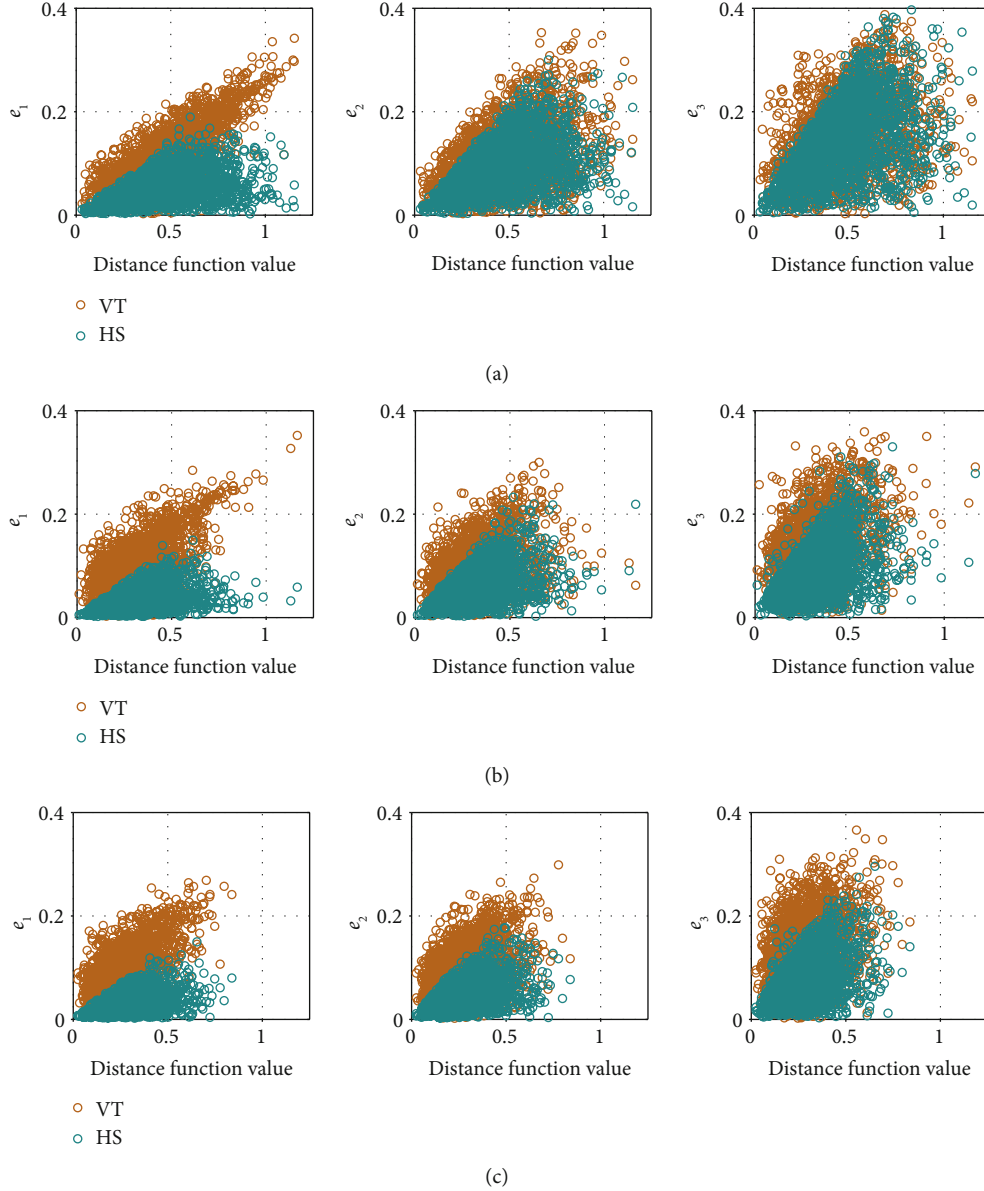


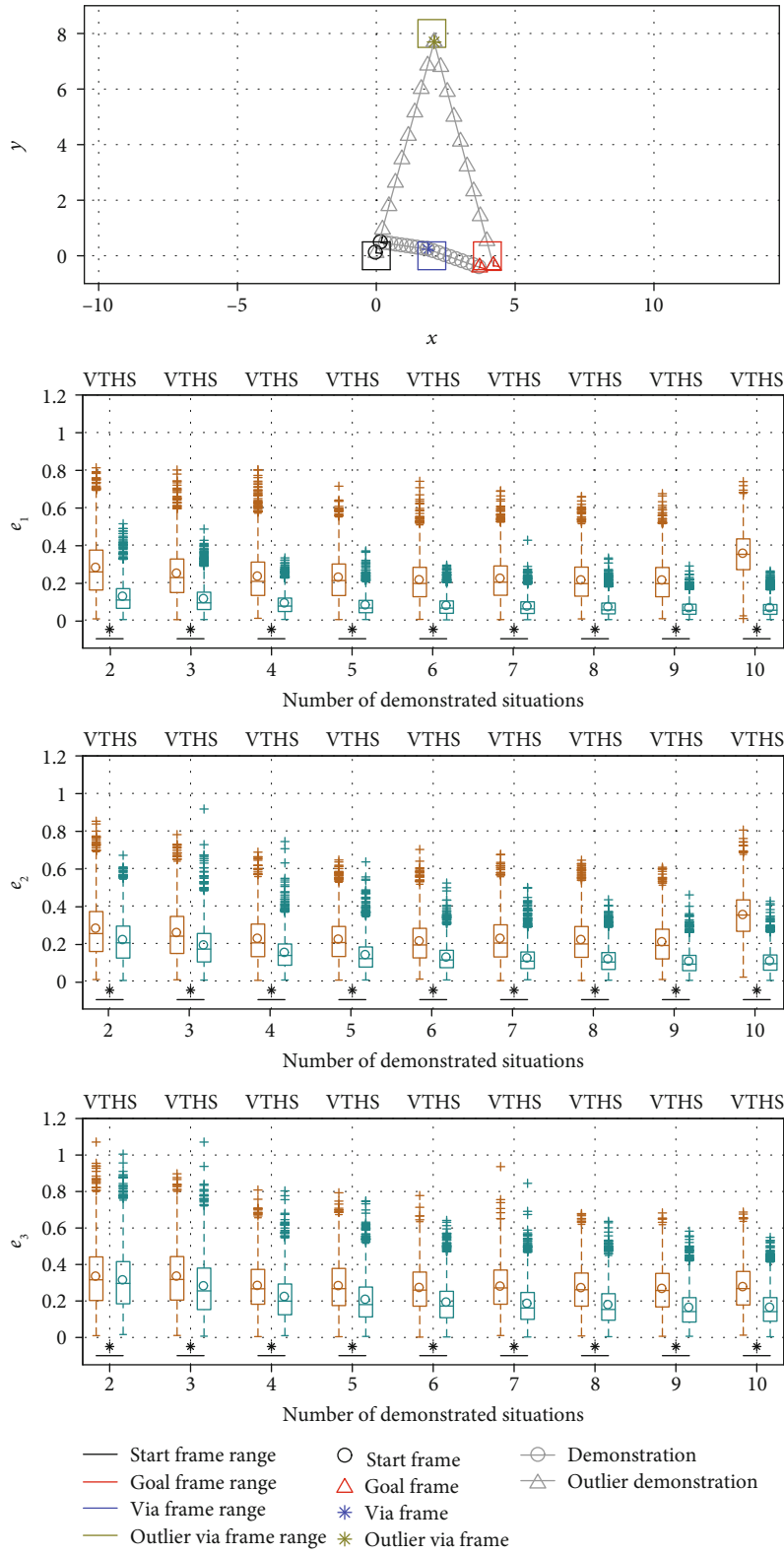
FIGURE 7: Generalization errors against distance metric when different numbers of situations were demonstrated during training: (a) with two situations; (b) with five situations; (c) with eight situations.

constrain one degree of freedom of the gripper orientation: the desired center axis of the gripper frame was constrained to be horizontal in the world frame, and $q_{i,vf}$ were found using inverse kinematics. The virtual fixture could also be used to satisfy task-specific requirements by choosing a different desired gripper orientation, e.g., when the carried object needs to be tilted to go through a doorway.

2.3.3. Training Procedure and Robot Controller. The task frames were defined to include positions \mathbf{r}_p and orientations \mathbf{R}_p of the start ($p = 1$), the goal ($p = 2$), and the obstacle ($p = 3$). When collecting demonstrations, we used forward kinematics to determine the start and the goal poses, and we calculated the obstacle's pose by making the robot's end-effector touch the edge of the cylindrical obstacle along its radial direction

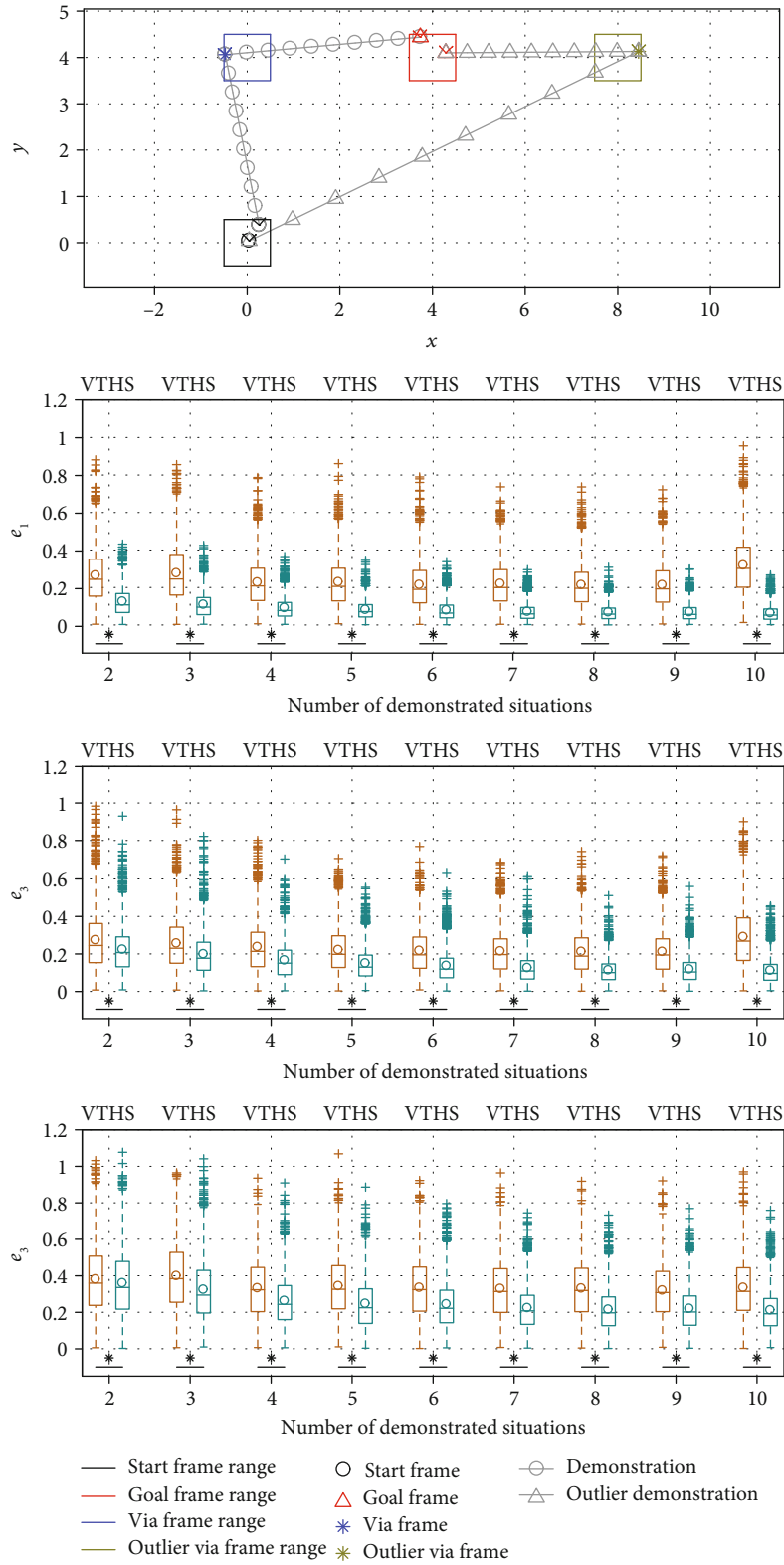
and adding an offset of the cylinder's radius. Because the start, goal, and obstacle frames may have different orientations in each task situation, we expanded the previously listed distance function (Algorithm 2) to iteratively align all task frames, as shown in Algorithm 6.

We assumed the existence of a desired trajectory corresponding to each task situation. Given the robot's wrist trajectories (\mathbf{x}) for a situation of interest, we resampled all trajectories to L data points based on trajectory length and used standard GMM/GMR to generate an *average trajectory* (\mathbf{x}_{avg}) in the world frame for that task situation. We then derived a *desired trajectory* for the task situation: $\mathbf{x}_{des} = \left[\left\{ \mathbf{x}_{avg,l} \right\}_{l=l_d+1}^L \quad \mathbf{x}_{interp} \right]$, where l_d serves as a look-ahead variable to make the robot appear more active during execution



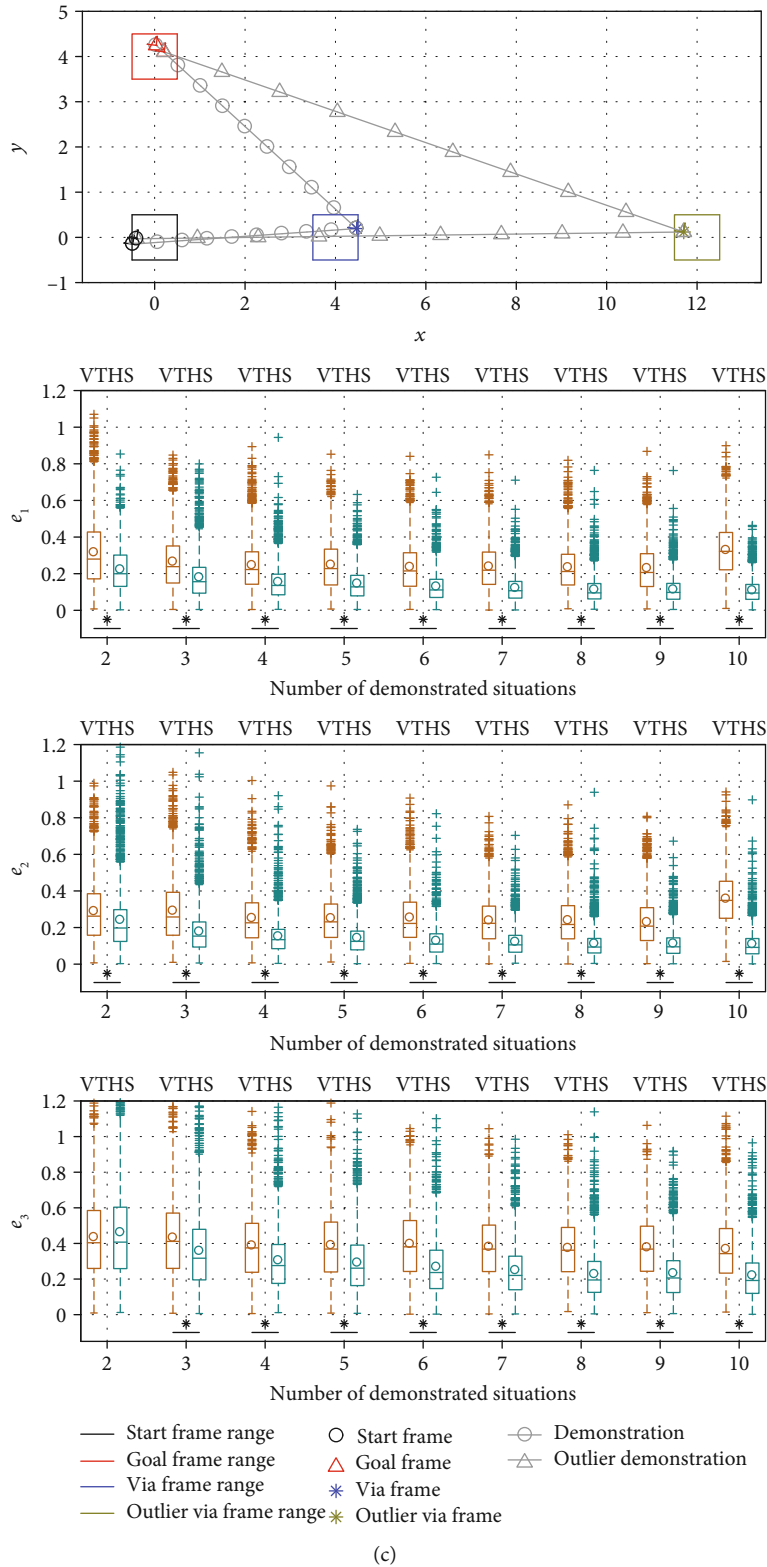
(a)

FIGURE 8: Continued.



(b)

FIGURE 8: Continued.



(c)

FIGURE 8: Comparison of generalization errors when different numbers of situations were demonstrated. The robot behavior abbreviations shown at the top stand for vanilla TP-GMM (VT) and hierarchical structure with TP-GMM (HS). Top panels show task configurations and samples of task situations, where each task frame was sampled from the specified range. When ten situations were demonstrated, the via frame of the tenth situation was drawn from an outlier range. Panels in the bottom three rows show boxplots of error metrics with different numbers of demonstrated situations in the corresponding task configurations. The center box lines represent the medians, and the box edges are the 25th and 75th percentiles. Circles show mean values. An asterisk and a horizontal line below boxplots show that the mean error from HS is significantly lower than the mean error from VT with $p < 0.001$.

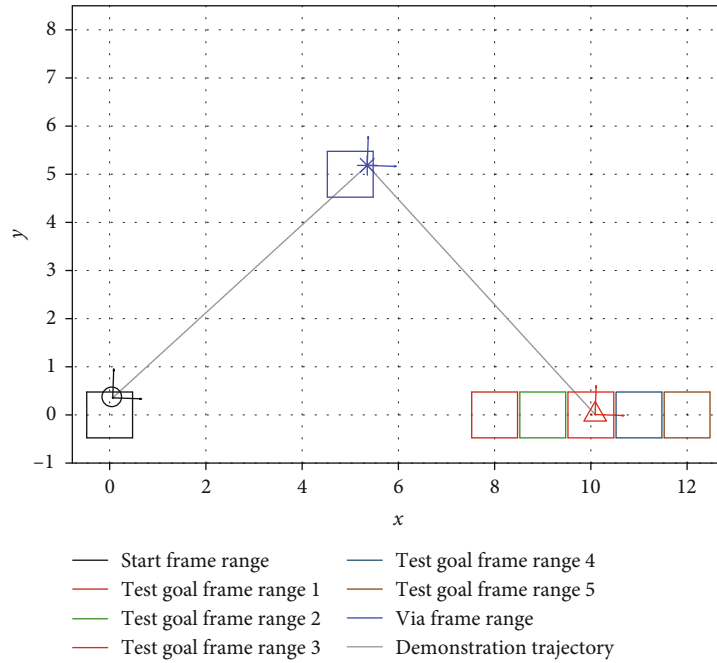


FIGURE 9: The test task configurations to evaluate interpolation/extrapolation performance. Note that the test goal frame range 3 is the same as the training goal frame range, so it evaluates interpolation performance.

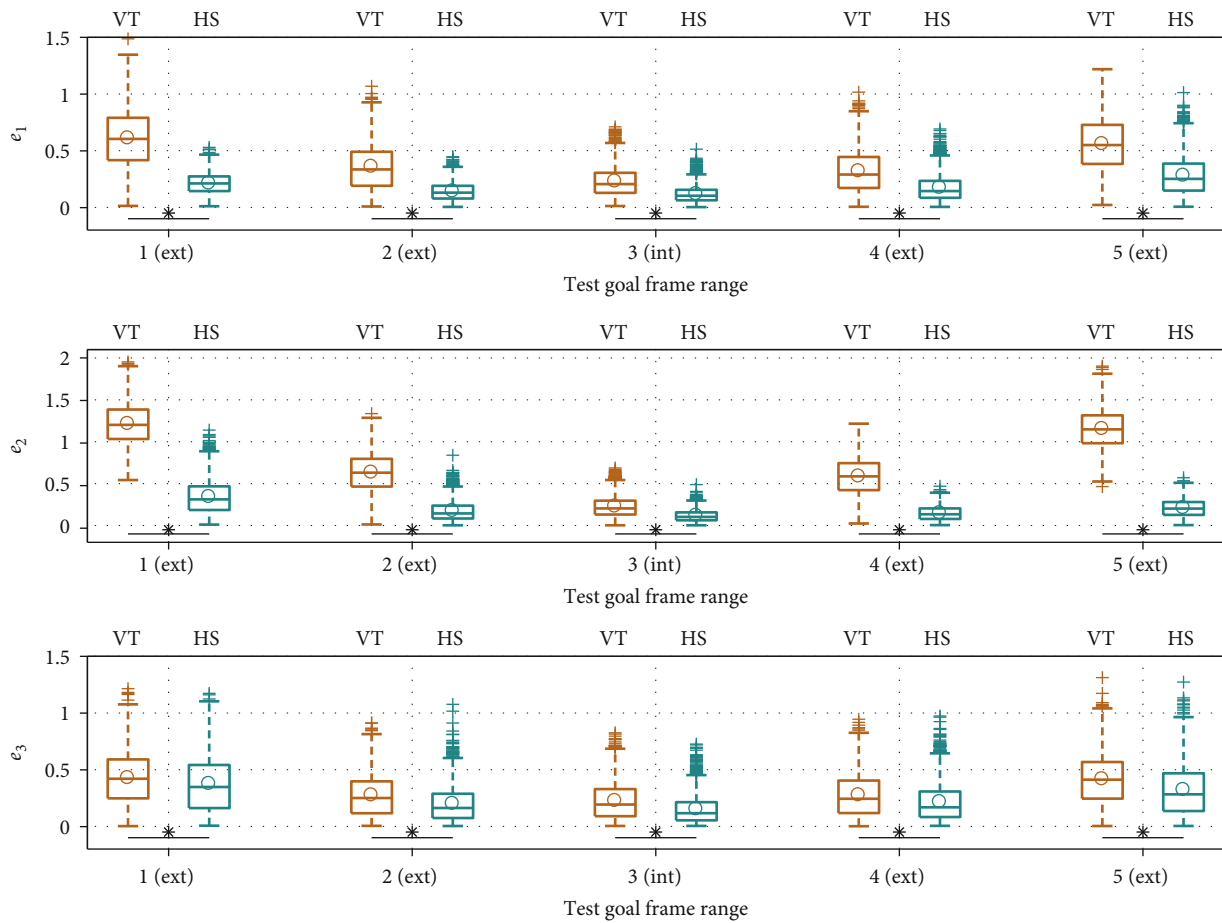


FIGURE 10: Performance comparison during interpolation (int) and extrapolation (ext). An asterisk and a horizontal line below boxplots show cases where the mean error from HS is significantly lower than VT with $p < 0.001$.

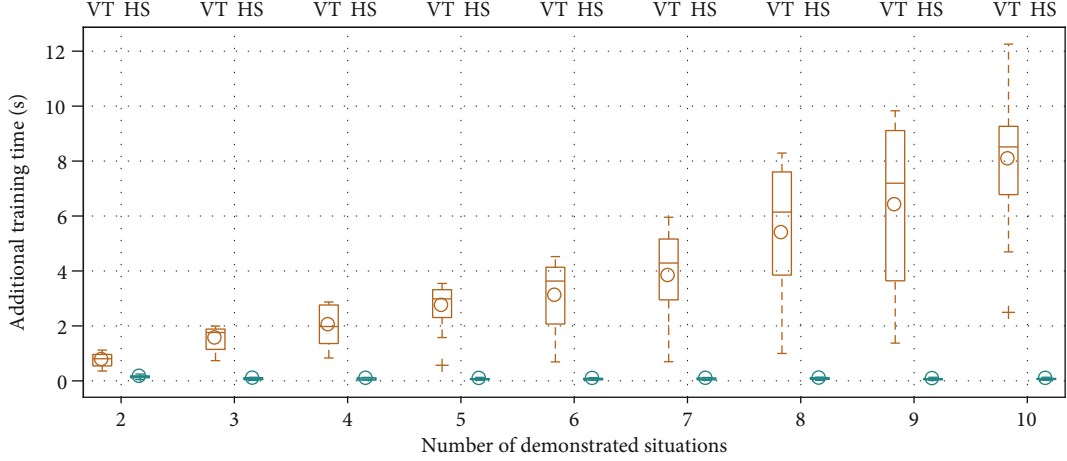


FIGURE 11: Additional time spent to train TP-GMMs increased as more demonstrated situations became available for VT but remained low for HS.

```

Procedure DISTANCE( $\mathbf{p}_A, \mathbf{p}_B$ )
 $d = 0$ 
for  $i = 1$  to 3 do
  for  $j = 1$  to 3 do
     $d = d + \|\mathbf{R}_{i,A}^\top(\mathbf{r}_{j,A} - \mathbf{r}_{i,A}) - \mathbf{R}_{i,B}^\top(\mathbf{r}_{j,B} - \mathbf{r}_{i,B})\|$ 
  return  $d$ 

```

ALGORITHM 6: Distance function used in the user study.

and $\mathbf{x}_{\text{interp}}$ is a linearly interpolated trajectory between the last average trajectory point ($\mathbf{x}_{\text{avg},L}$) and the goal of the task situation (\mathbf{r}_2) in l_d steps. In the current work, $L = 500$ and $l_d = 50$. In the experiment, $\mathbf{x}_{\text{avg},L}$ was typically close the goal point, and thus, $\mathbf{x}_{\text{interp}}$ generally was a short line segment connecting $\mathbf{x}_{\text{avg},L}$ to the exact goal location.

We chose to learn TP-GMMs that use the robot's 3D wrist center position as the input and the desired 3D trajectory point calculated from above as the output: $\xi^i = \mathbf{x}$ and $\xi^e = \mathbf{x}_{\text{des}}$. Consequently, the task parameters were defined as

$$\mathbf{A}_p = \begin{bmatrix} \mathbf{R}_p & \mathbf{0} \\ \mathbf{0} & \mathbf{R}_p \end{bmatrix} \quad (6)$$

and $\mathbf{b}_p = [\mathbf{r}_p^\top \quad \mathbf{r}_p^\top]^\top$, $p = 1, 2, 3$. We chose to use position rather than time for parameterization to increase robustness [28] and eliminate the need for phase estimation (e.g., [29]) or dynamic time warping. In addition, we updated definitions of \mathbf{T}' and \mathbf{T}'' in Algorithm 3 to accommodate 3D trajectories and the dimensions of our TP-GMM:

$$\mathbf{T}' = \begin{bmatrix} \mathbf{I} + \alpha\mathbf{T} - \mathbf{T} & \mathbf{0} \\ \mathbf{0} & \mathbf{I} + \alpha\mathbf{T} - \mathbf{T} \end{bmatrix}, \quad (7)$$

$$\mathbf{T}'' = \begin{bmatrix} (\alpha - 1)\mathbf{T} & \mathbf{0} \\ \mathbf{0} & (\alpha - 1)\mathbf{T} \end{bmatrix}.$$

We selected three different task situations to collect demonstrations. We collected five demonstrations for each situation to ensure that the variability of trajectories was captured. The collected demonstrations and their task parameters were encoded in VT-TRAIN and HS-TRAIN, and the TP-GMMs ($\Pi_{\text{VT}}, \{\Pi_n\}_{n=1}^3$) were tested and evaluated in the user study. We used the Bayesian Information Criterion (BIC) [30] to determine the number of Gaussian clusters M for each TP-GMM (15 clusters for Π_{VT} and 4 or 5 clusters for each Π_n).

At test time, the PR2 robot could calculate a desired wrist position (\mathbf{x}_{des}) from its current wrist position at each time step using VT-TEST or HS-TEST, and a generic PD controller was used to generate the motor commands:

$$\boldsymbol{\tau} = \mathbf{J}^\top (\mathbf{K}(\mathbf{x}_{\text{des}} - \mathbf{x}) - \mathbf{B}\dot{\mathbf{x}}), \quad (8)$$

where \mathbf{J} is the Jacobian matrix of the position dimensions, and we chose \mathbf{K} and \mathbf{B} as diagonal matrices with 120 N m^{-1} and 10 N s m^{-1} . We also included a passive mode where the robot provided only gravity compensation for the half of the object's weight, with

$$\boldsymbol{\tau} = -\frac{1}{2} \mathbf{J}^\top m \mathbf{g}, \quad (9)$$

where m is the mass of the held object and \mathbf{g} is the gravity vector, assuming that the robot and the human share the object's weight equally. This control mode was included so we could directly test whether the complexity of TP-GMM confers any benefits.

2.3.4. User Study. We conducted a human-subject study to evaluate how the three described control algorithms affect task performance and how users perceive the robot behaviors in the collaborative movement task. Since the task situations were defined in the robot frame, we used a projector mounted on the ceiling to help participants identify and find the desired start, goal, and obstacle positions, as shown in Figure 12.

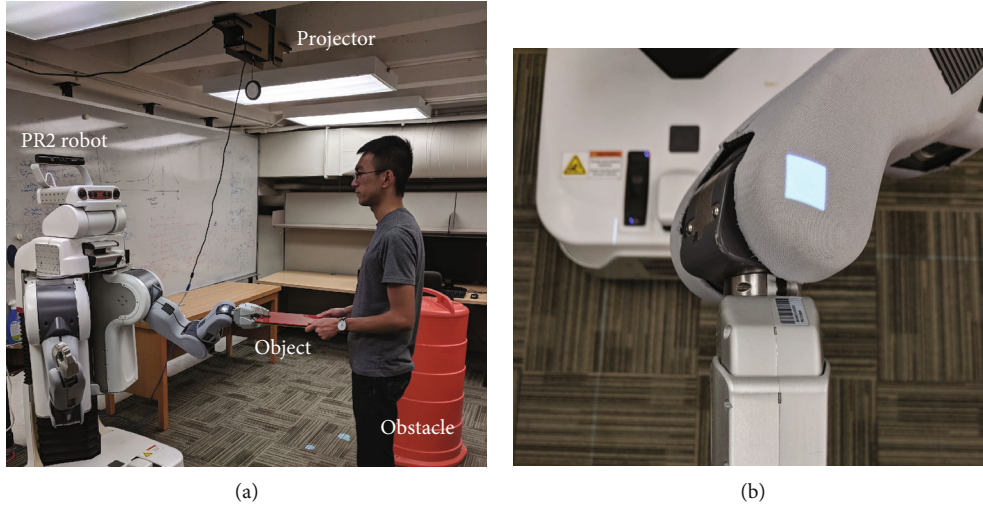


FIGURE 12: The experimental setup for the human-subject study. A projector helps the subject find the start, goal, and obstacle positions, and a square is projected on the PR2's wrist when the start position is reached.

(1) *Participants.* Our participant pool consisted of 15 University of Pennsylvania affiliates, including undergraduate and graduate students, postdoctoral associates, and visiting researchers. Of the 15 participants, three were female and 12 were male, with ages ranging from 22 to 35 years ($\mu = 26.3$, $\sigma = 3.42$).

(2) *Dependent Measures.* We recorded robot motions during each trial, and we used two quantitative measures to evaluate task performance: average trajectory length and average task completion time.

In addition, we used three questionnaires to evaluate the quality of the human-robot interactions during the task. First, the subject completed a Unified Theory of Acceptance and Use of Technology (UTAUT) survey [31] at the beginning and the end of the study. Results from the two surveys were compared to determine how interacting with the robot affected the general perception of subjects toward using the robot in everyday tasks.

Second, we adapted the questionnaire used in [32] and asked participants to answer the following questions on a 100-point scale from strongly disagree to strongly agree after each collaboration trial:

- (Q1) The robot moved too fast
- (Q2) The robot moved too slowly
- (Q3) The robot had problems doing the task
- (Q4) I felt safe when working with the robot
- (Q5) I trusted the robot to do the right thing at the right time
- (Q6) The robot and I worked well together

These questions sought to evaluate how subjects perceived the robot's behaviors and performance.

Third, a NASA-TLX survey [33] was administered after the participants experienced the process of providing demonstrations via teleoperation to gauge the workload of this interaction.

(3) *Procedure.* The human-subject study consists of two main components: collaborating with the robot and providing demonstrations. We chose to put the collaborating component first because it allows participants to become more familiar with the robot before demonstrating new movements.

The first component, collaborating with the robot, took place after the opening UTAUT survey. Participants were asked to collaborate with the robot to move the object from the start to the goal in five different situations. Four common situations, shown in Figure 13, were predetermined by the research team and were the same for all subjects, with situation 1 having the lowest and situation 4 having the highest d_{n^*} value. These common situations were chosen to be somewhat close to the training situations so that both VT and HS should intuitively work well. They span a relatively large portion of the robot's workspace (Figure 13(a)) and have varied configurations (Figure 13(b)). Recall that we use TP-GMMs to encode data with $\xi^i = \mathbf{x}$ and $\xi^e = \mathbf{x}_{des}$. Figure 14 shows the ξ^e dimensions of generalized VT and HS GMM clusters for two example test situations. Situation 5 was chosen by each subject so that a large number of situations were sampled in the study.

Participants compared three different robot behavior modes: (P) passive with gravity compensation for the object, (VT) active with vanilla TP-GMM, and (HS) active with hierarchical structure and TP-GMM. Therefore, each participant evaluated the collaboration in 15 different combinations of task situation and robot behavior. For each situation, we asked participants to experience all three robot behaviors sequentially (completing two collaborations under each robot behavior), and then reexperience and rate each robot behavior. After the subject evaluated all three robot behaviors, a new situation was presented. This process repeated until all five situations had been shown. For each subject, the five situations were presented

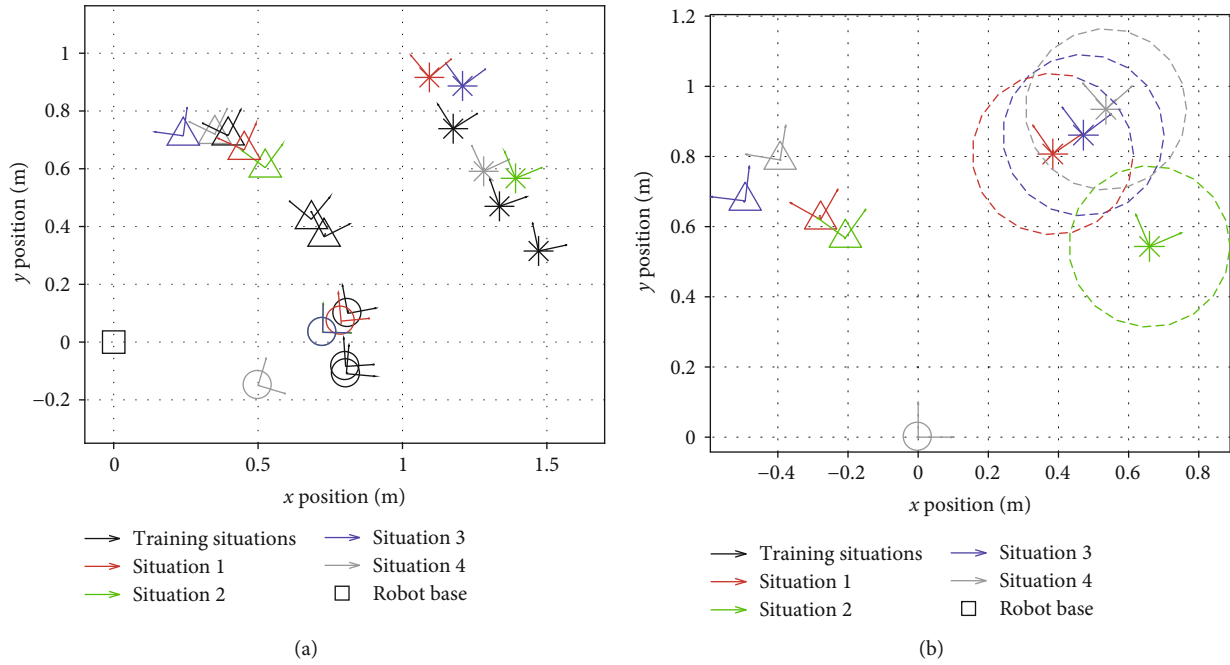


FIGURE 13: Task situations involved in the experiment. Circles represent the start frames, triangles the goal frames, and asterisks the obstacle frames. Dashed circles represent the boundary of the obstacle. Note that the start frames of situations 2 and 3 coincide. With respect to the three demonstrated situations, the d_{gr} values for these four common situations in Algorithm 4 with the definition in Algorithm 6 are 0.071 m^2 , 0.151 m^2 , 0.295 m^2 , and 0.398 m^2 : (a) training and the four common situations in world frame; (b) the four common situations aligned by their start frames.

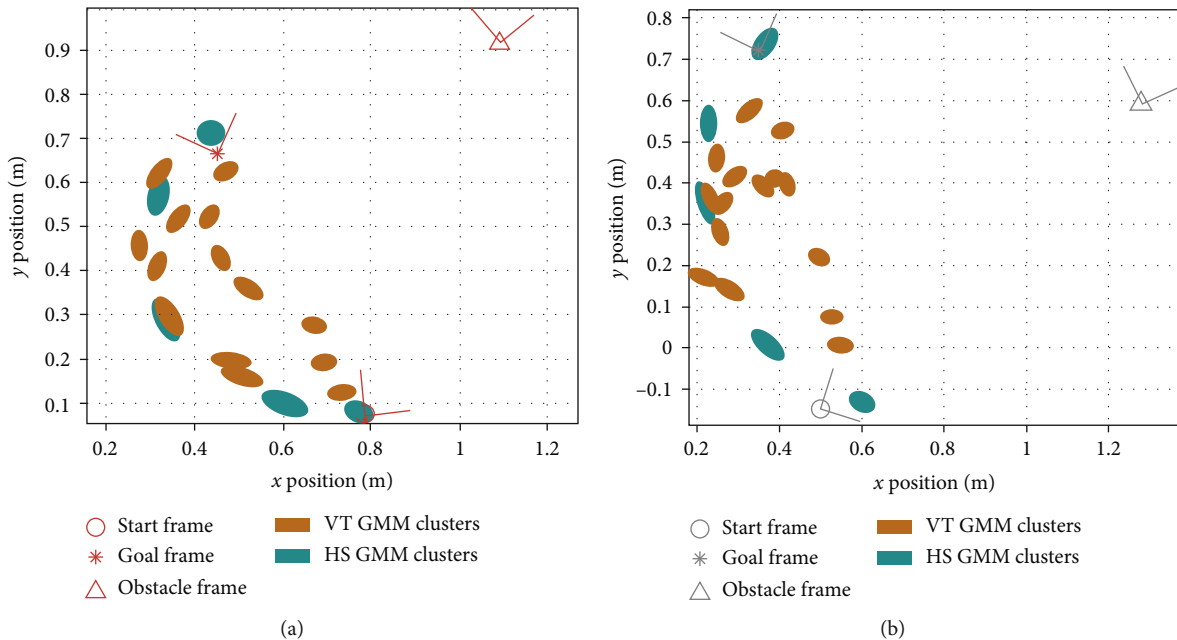


FIGURE 14: Generalized GMM clusters (ξ^e dimensions) for two test situations from Figure 10: (a) situation 1; (b) situation 4.

in a randomized order, and within each situation, the presentation order of the three robot behaviors was also randomized. Examples of human-robot interactions during the user study are shown in the supplementary video attachment.

Then, participants were presented with the second component of the study: providing demonstrations. The experimenter acted as the partner and moved the object with the robot, and the participant manipulated the

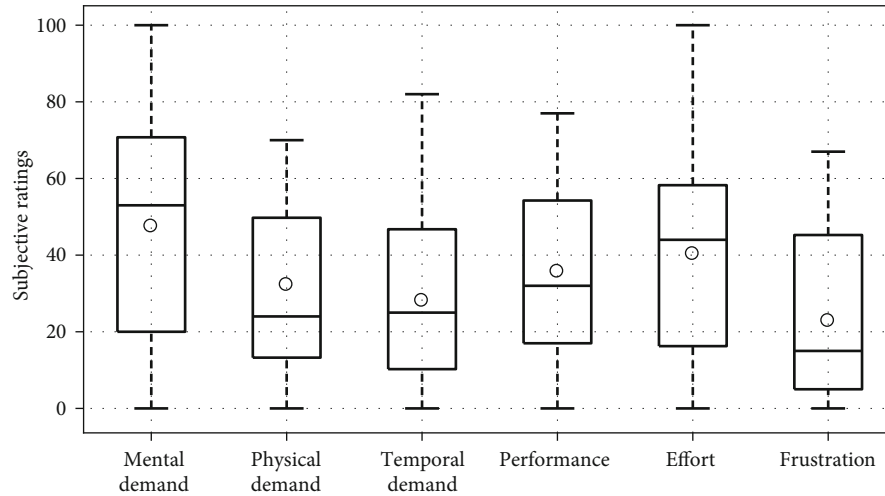


FIGURE 15: NASA-TLX ratings of the teaching procedure (lower is better). For the performance question, 0 indicates perfect and 100 indicates failure.

robot's right arm to teleoperate the slave arm. Each participant experienced the demonstrating process for three to five minutes and then filled out the NASA-TLX survey. Finally, the participant filled out the closing UTAUT survey.

(4) *Hypotheses*. Based on the dependent measures, our main hypotheses for this experiment were as follows:

- (i) The hierarchical structure (HS) will lead to better task performances, including shorter trajectory lengths and lower task completion times, compared to using vanilla TP-GMM (VT) and passive gravity compensation (P)
- (ii) Participants will be more satisfied with the robot when it uses the hierarchical structure (HS) to generate motion controls, compared to VT and P
- (iii) Given feedback after task execution in a wide variety of situations, the robot will be able to learn a decision boundary for when to ask for new demonstrations

3. Results

Figure 15 shows results from the NASA-TLX survey that subjects completed after providing demonstrations. The median value for "How mentally demanding was the task?" was 53 out of 100, and the median values for the other five questions were all below 50, indicating that the subjects perceived teaching by teleoperation as a low-to-moderate-effort task.

Objective performance at the collaborative movement task was determined by calculating the two quantitative measures of average trajectory length and average task completion time for the four common task situations. Results are shown in Figure 16. One-way repeated measures analysis of variance (ANOVA) was used to determine whether the differences in these measures between the three behavior modes under the same task situation were significant. If

there was, a Tukey-Kramer post hoc multiple comparison test was conducted to determine which robot behaviors produced significantly different ratings. It can be seen that with the hierarchical structure, traversed trajectories were significantly shorter and took significantly less time for almost all situations, while VT reduced average completion time compared to passive gravity compensation only in test situation 1, which is the most similar to the demonstrated situations.

Results from the subjective ratings under the four common task situations are shown in Figure 17. Plotted ratings of Q1, Q2, and Q3 were subtracted from 100 so that a higher rating is better for all questions. The same procedure used for the quantitative measures was used to determine significant differences. It can be seen that with passive gravity compensation, the robot almost always appeared significantly slower (Q1, Q2) and safer (Q4). No significant differences in perceived pace and safety were found between the two active modes. Compared to vanilla TP-GMM, the hierarchical structure appeared to have significantly fewer problems doing the task (Q3) in all situations. In situations 2 and 3, participants had more trust in the robot doing the right thing at the right time (Q5) with the hierarchical structure than vanilla TP-GMM. Finally, participants felt they worked better with the robot (Q6) with the hierarchical structure than the other two modes in situation 1. Figure 18 shows the sums of these ratings. Vanilla TP-GMM generally had the lowest rating sums. Significant differences were found between the hierarchical structure and vanilla TP-GMM in situations 2 and 4 as well as between passive gravity compensation and vanilla TP-GMM in situation 3.

Results from the subjective ratings under the participant-selected situations were used to validate the distance function as a performance estimator in the collaborative task. To acquire labels of successful/failed execution, we defined the following criterion: an HS success has a subjective rating sum that is greater than 80% of the largest sum of ratings for any control mode under any task situation from the corresponding subject. Figure 19(a) shows the classification

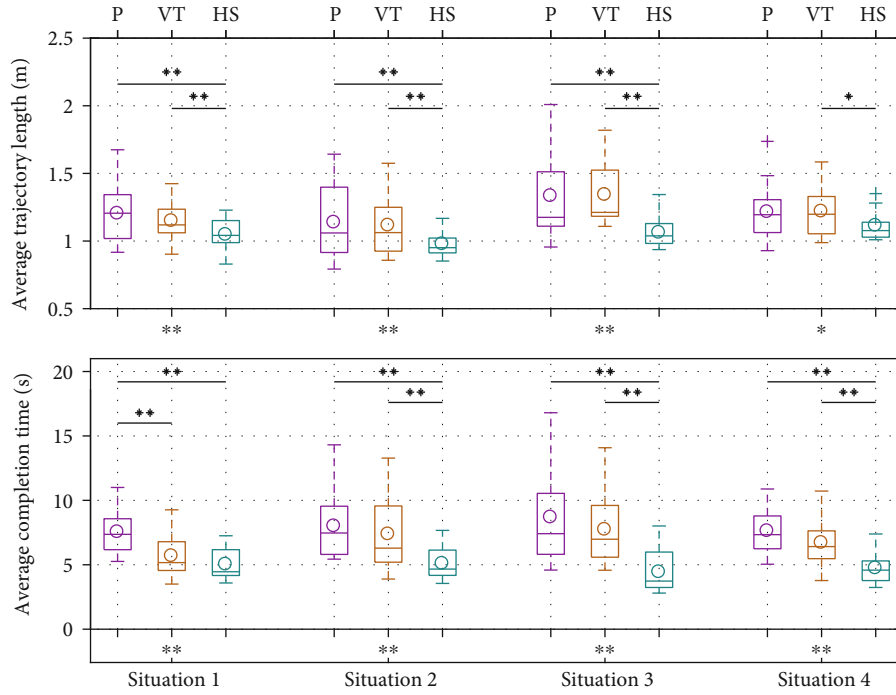


FIGURE 16: Comparison of quantitative measures for the four common task situations (lower is better). Asterisks under the x -axes show significant differences in each group, and asterisks and horizontal lines above boxplots show pairwise significant differences. $*p < 0.1$; $**p < 0.05$.

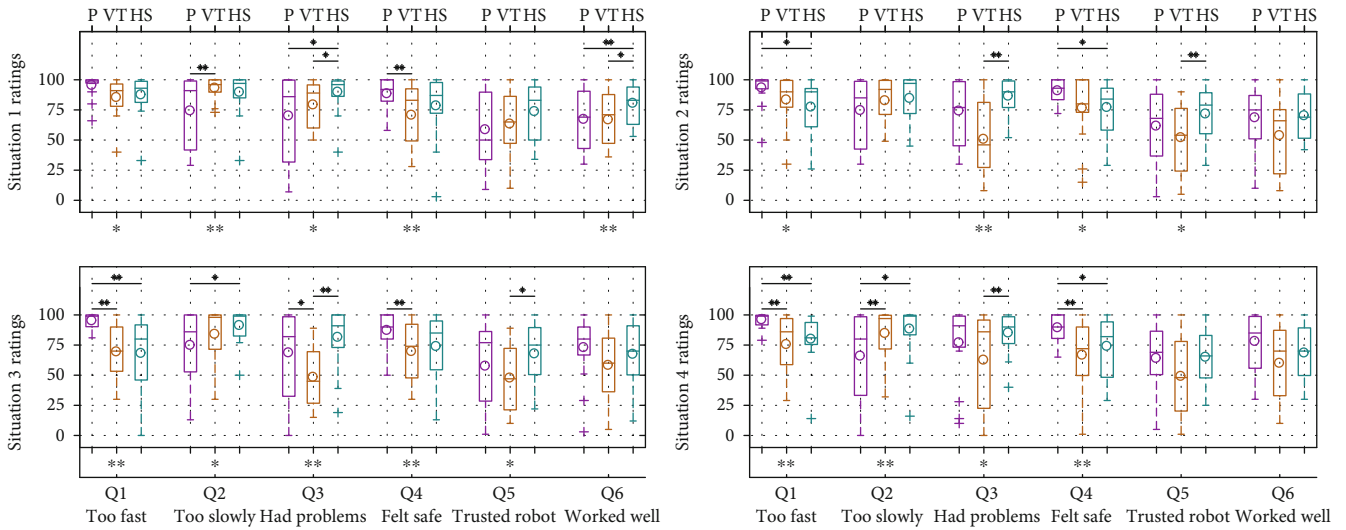


FIGURE 17: Comparison of subjective ratings (higher is better). Questions Q1–Q6 are detailed in Section 2.3.4. $*p < 0.1$; $**p < 0.05$.

results using the above criterion, where we additionally include a second feature dimension ($\max(\alpha_{n^*}, 1/\alpha_{n^*})$), which is calculated from the distance function in HS-TEST and represents the degree of stretching or compression in the morphing functions. We also plot the common situations in Figure 19(a) for completeness; these are manually labeled as successes with the hierarchical structure, because there were significant advantages in the quantitative measures

and some significant advantages in the subjective ratings. Three of the custom situations for which the hierarchical structure was rated as a failure are manually marked as being out of workspace, because the obstacle was placed so close to the robot that some GMM clusters of the hierarchical structure policy were outside of the robot’s workspace. As a result, the robot arm would become stuck when it first reached the workspace boundary following the control policy, and the

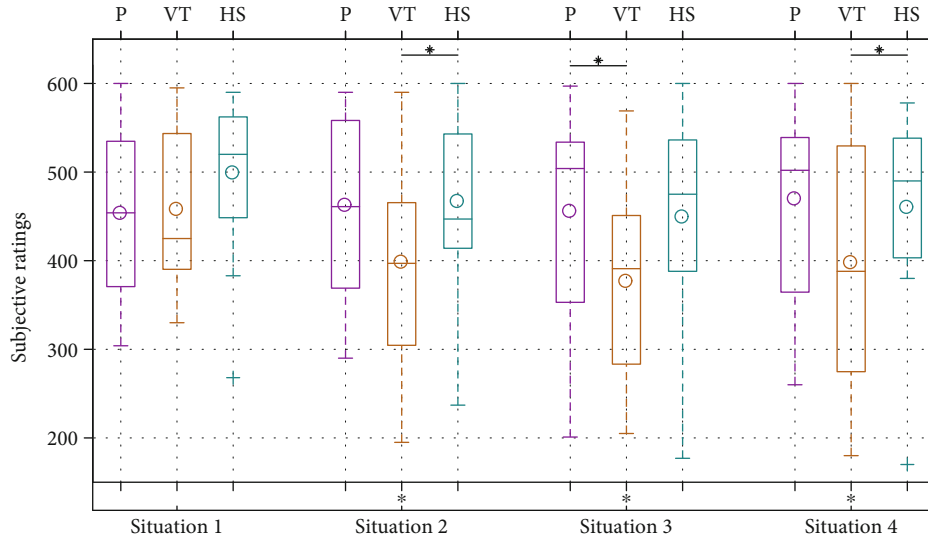


FIGURE 18: Comparison of sums of subjective ratings (higher is better). * $p < 0.1$.

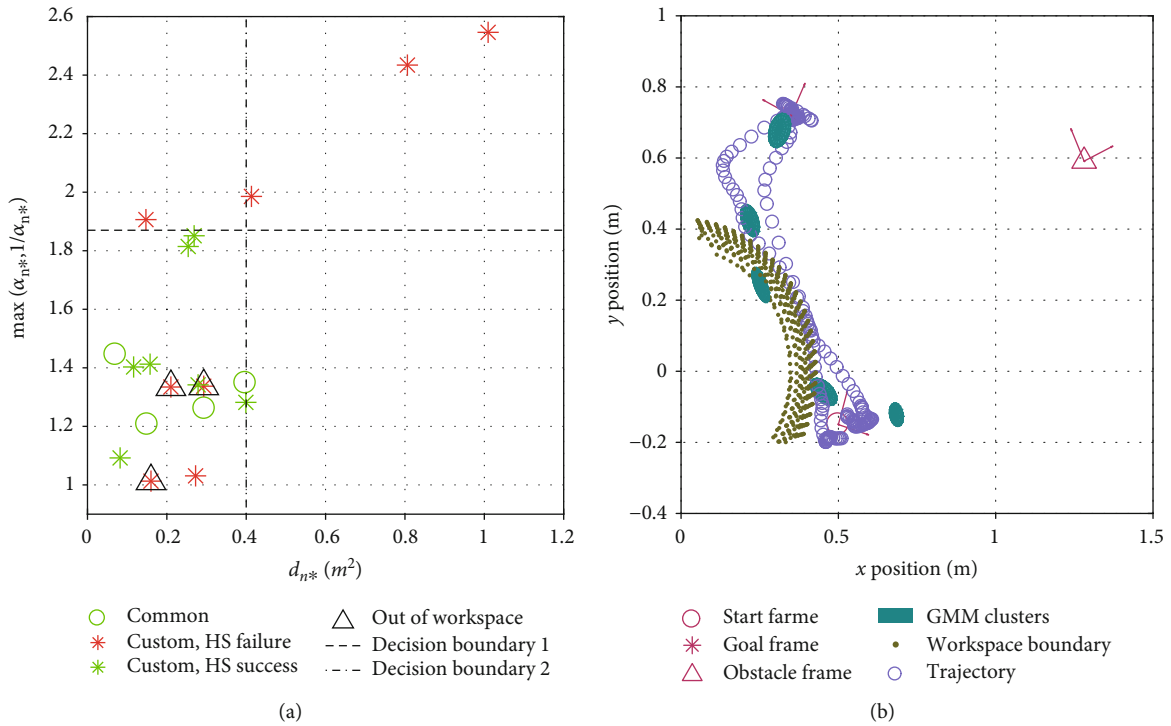


FIGURE 19: Learning when to request new demonstrations. (a) Rated success with the hierarchical structure. Two example decision boundaries are given. (b) An example with some GMM clusters outside of the workspace.

robot arm would then slide along the workspace boundary and appear less smooth to participants. This behavior at least partially caused these three poor ratings; an example is shown in Figure 19(b).

Note that each participant tested only one custom situation and hence contributed one data point to Figure 19(a). The distribution might look different if a single participant did all of the tested situations, and it might change for different participants. Nevertheless, not counting the out-of-

workspace situations, one could simply place a decision boundary for when to ask for new demonstrations at $\max(\alpha_{n^*}, 1/\alpha_{n^*}) = 1.87$ with one misclassified task situation or at $d_{n^*} = 0.4 \text{ m}^2$ with two misclassified data points.

Figure 20 shows the ratings from the UTAUT questions. Paired sample t -tests were used to determine whether the differences between the means of these ratings were significant. A significant difference was found for the question “I am afraid of breaking something while using the robot,”

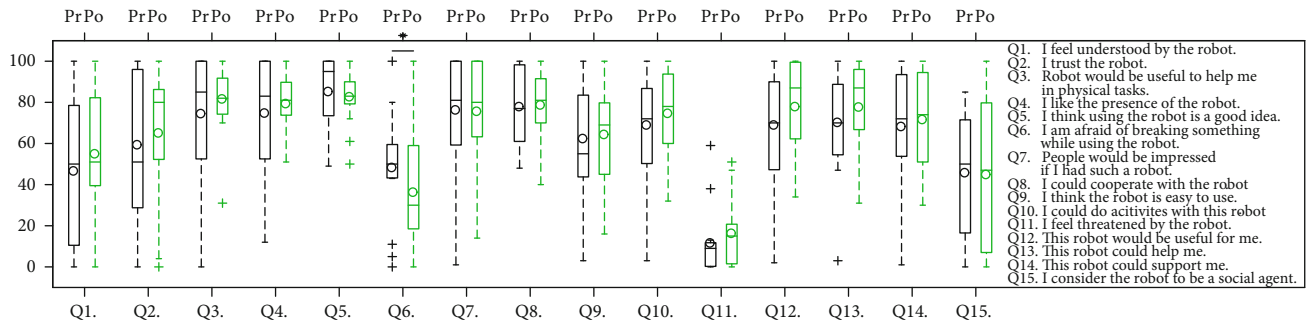


FIGURE 20: UTAUT ratings from prestudy (Pr) and poststudy (Po) surveys. * $p < 0.1$.

indicating subjects were less afraid of breaking something after the study. No significant differences were found for other questions.

4. Discussion

The results from the user study provide strong support for our first hypothesis: the significant differences in the quantitative measures in favor of HS indicate that explicitly reasoning about task situations and generalizing over selected demonstrations could lead to significantly better trajectories and hence better task performance. In comparison, although VT also uses task parameters to annotate and process the demonstrations in ENCODE and DECODE, it does not differentiate between demonstrated situations and thus cannot apply situation-specific trajectory and model morphing to better accommodate the test situation. As a result, VT falls short of HS in task performance. Passive gravity compensation offers little help to users and leads to the longest trajectory lengths and task completion times.

Hypothesis 2 centers on user perception of the three tested robot control modes. In the subjective ratings, HS was rated to be significantly less problematic (Q3) than VT in all situations, indicating that users were able to differentiate the two modes and preferred HS. Furthermore, HS achieved significantly higher ratings than VT for trust (Q5) and working well together (Q6) in particular situations. The sum of the subjective ratings generally favored the hierarchical structure and passive gravity compensation, with the former being perceived as fast and effective and the latter as slow and safe. Thus, we conclude that the subjective ratings support our second hypothesis.

Results from the custom situations provide some support for our third hypothesis, which stated that the robot would be able to learn a decision boundary for when to ask for new demonstrations in the object movement task. In the particular instance of Figure 19(a), only one situation would have been misclassified by the robot with decision boundary 1. We think that predicting the performance of generalized behaviors is a critical component of LfD, since demonstrations are typically available only for a small subset of task situations and robot designers often cannot test every possible one. In addition to uncertainty- or confidence-based methods, TP-GMM offers unique opportunities in this effort because it utilizes the task parameters that contain

additional information about the demonstrations and also enhance generalization capabilities. As for the custom situations with GMM clusters out of the robot's workspace, approaches to the Procrustes problem [34] could have been used to select an initial pose for the robot base before autonomous execution.

The NASA-TLX survey and the pre- and poststudy UTAUT surveys were not used to evaluate our hypotheses, but they provide some insights on the proposed approach. When subjects provided new demonstrations using our kinesthetic teleoperation method, they indicated that the heaviest workload was mental, most likely because the robot's motion was a mirror image of the demonstrated motion. In the pre- and poststudy UTAUT surveys, subjects became less afraid of breaking things when using the robot, suggesting that the human-robot interactions during the study had a slight positive effect on their opinions about the robot. Importantly, the participants experienced multiple robot behavior modes and multiple task situations where the robot might have worked well or poorly, which may explain the lack of significant changes in other questions.

5. Conclusions

The hierarchical structure proposed in this paper enables robots to additionally reason about task situations when utilizing TP-GMM. We showed that task performance can be improved in both interpolation and extrapolation scenarios and that computational load can be reduced with the hierarchical structure in simulation. We then showed that a robot can use the hierarchical structure to collaborate better with people in a real object movement task, also learning a decision boundary for when to ask for new demonstrations.

Data Availability

The data used to support the findings of this study are available from the corresponding author upon request.

Conflicts of Interest

The authors declare that there is no conflict of interest regarding the publication of this paper.

Acknowledgments

The authors would like to thank Haoran Shao for assisting with data collection and the subjects for taking part in the experimental study. This material is based upon work supported by the U.S. National Science Foundation under Grant 1328805 as part of the National Robotics Initiative.

Supplementary Materials

We show three example trials with typical interactions encountered in the human-subject study, where the start and goal positions were the same. The robot said “start” at the beginning of each trial, and it said “reached goal” when the object was successfully moved to the prescribed goal position. In example trial 1, the robot successfully and quickly finished the task with the subject. In example trial 2, the robot’s trajectory did not end at the goal location, and the human partner had to correct it by overpowering the robot. In example trial 3, the robot additionally did not make enough room for the partner to walk by the obstacle easily, so the subject slightly rotated his body when walking towards the goal. (*Supplementary Materials*)

References

- [1] H. Admoni, A. Dragan, S. S. Srinivasa, and B. Scassellati, “Deliberate delays during robot-to-human handovers improve compliance with gaze communication,” in *HRI '14 Proceedings of the 2014 ACM/IEEE International Conference on Human-Robot Interaction*, pp. 49–56, Bielefeld, Germany, March 2014.
- [2] A. Billard, S. Calinon, R. Dillmann, and S. Schaal, “Robot programming by demonstration,” in *Springer Handbook of Robotics*, pp. 1371–1394, Springer, 2008.
- [3] B. D. Argall, S. Chernova, M. Veloso, and B. Browning, “A survey of robot learning from demonstration,” *Robotics and Autonomous Systems*, vol. 57, no. 5, pp. 469–483, 2009.
- [4] S. Calinon, P. Evrard, E. Gribovskaya, A. Billard, and A. Kheddar, “Learning collaborative manipulation tasks by demonstration using a haptic interface,” in *2009 International Conference on Advanced Robotics*, pp. 1–6, Munich, Germany, June 2009.
- [5] S.-Z. Yu, “Hidden semi-Markov models,” *Artificial Intelligence*, vol. 174, no. 2, pp. 215–243, 2010.
- [6] L. Rozo, J. Silvério, S. Calinon, and D. G. Caldwell, “Learning controllers for reactive and proactive behaviors in human-robot collaboration,” *Frontiers in Robotics and AI*, vol. 3, p. 30, 2016.
- [7] A. J. Ijspeert, J. Nakanishi, and S. Schaal, “Trajectory formation for imitation with nonlinear dynamical systems,” in *Proceedings 2001 IEEE/RSJ International Conference on Intelligent Robots and Systems. Expanding the Societal Role of Robotics in the the Next Millennium (Cat. No.01CH37180)*, vol. 2, pp. 752–757, Maui, HI, USA, October–November 2001.
- [8] T. Kulvicius, M. Biehl, M. J. Aein, M. Tamosiunaite, and F. Wörgötter, “Interaction learning for dynamic movement primitives used in cooperative robotic tasks,” *Robotics and Autonomous Systems*, vol. 61, no. 12, pp. 1450–1459, 2013.
- [9] A. Pervez, A. Ali, J.-H. Ryu, and D. Lee, “Novel learning from demonstration approach for repetitive teleoperation tasks,” in *2017 IEEE World Haptics Conference (WHC)*, pp. 60–65, Munich, Germany, June 2017.
- [10] B. Akgun, M. Cakmak, J. W. Yoo, and A. L. Thomaz, “Trajectories and keyframes for kinesthetic teaching: a human-robot interaction perspective,” in *HRI '12 Proceedings of the Seventh Annual ACM/IEEE International Conference on Human-Robot Interaction*, pp. 391–398, Boston, Massachusetts, USA, March 2012.
- [11] S. Calinon, “A tutorial on task-parameterized movement learning and retrieval,” *Intelligent Service Robotics*, vol. 9, no. 1, pp. 1–29, 2016.
- [12] L. Rozo, S. Calinon, D. G. Caldwell, P. Jimenez, and C. Torras, “Learning physical collaborative robot behaviors from human demonstrations,” *IEEE Transactions on Robotics*, vol. 32, no. 3, pp. 513–527, 2016.
- [13] A. Pervez and D. Lee, “Learning task-parameterized dynamic movement primitives using mixture of GMMs,” *Intelligent Service Robotics*, vol. 11, no. 1, pp. 61–78, 2018.
- [14] D. Silver, J. A. Bagnell, and A. Stentz, “Active learning from demonstration for robust autonomous navigation,” in *2012 IEEE International Conference on Robotics and Automation*, pp. 200–207, Saint Paul, MN, USA, May 2012.
- [15] G. Maeda, M. Ewerton, T. Osa, B. Busch, and J. Peters, “Active incremental learning of robot movement primitives,” in *CoRL 2017 - 1st Annual Conference on Robot Learning*, pp. 37–46, Mountain View, US, November 2017.
- [16] S. Chernova and M. Veloso, “Interactive policy learning through confidence-based autonomy,” *Journal of Artificial Intelligence Research*, vol. 34, pp. 1–25, 2009.
- [17] D. Koert, S. Trick, M. Ewerton, M. Lutter, and J. Peters, “Online learning of an open-ended skill library for collaborative tasks,” in *2018 IEEE-RAS 18th International Conference on Humanoid Robots (Humanoids)*, pp. 1–9, Beijing, China, November 2018.
- [18] F. Abi-Farraj, T. Osa, N. P. J. Peters, G. Neumann, and P. R. Giordano, “A learning-based shared control architecture for interactive task execution,” in *2017 IEEE International Conference on Robotics and Automation (ICRA)*, pp. 329–335, Singapore, Singapore, May–June 2017.
- [19] K. Muelling, J. Kober, and J. Peters, “Learning table tennis with a mixture of motor primitives,” in *2010 10th IEEE-RAS International Conference on Humanoid Robots*, pp. 411–416, Nashville, TN, USA, December 2010.
- [20] D. Kulic, W. Takano, and Y. Nakamura, “Combining automated on-line segmentation and incremental clustering for whole body motions,” in *2008 IEEE International Conference on Robotics and Automation*, pp. 2591–2598, Pasadena, CA, USA, May 2008.
- [21] D. Lee and C. Ott, “Incremental kinesthetic teaching of motion primitives using the motion refinement tube,” *Autonomous Robots*, vol. 31, no. 2-3, pp. 115–131, 2011.
- [22] S. Calinon and A. Billard, “Incremental learning of gestures by imitation in a humanoid robot,” in *HRI '07 Proceedings of the ACM/IEEE International Conference on Human-robot Interaction*, pp. 255–262, Arlington, Virginia, USA, March 2007.
- [23] J. Hoyos, F. Prieto, G. Alenyà, and C. Torras, “Incremental learning of skills in a task-parameterized Gaussian mixture model,” *Journal of Intelligent & Robotic Systems*, vol. 82, no. 1, pp. 81–99, 2016.

- [24] P. Evrard, E. Gribovskaia, S. Calinon, A. Billard, and A. Kheddar, "Teaching physical collaborative tasks: object-lifting case study with a humanoid," in *2009 9th IEEE-RAS International Conference on Humanoid Robots*, pp. 399–404, Paris, France, December 2009.
- [25] Y. Huang, J. Silvério, L. Rozo, and D. G. Caldwell, "Generalized task-parameterized skill learning," in *2018 IEEE International Conference on Robotics and Automation (ICRA)*, pp. 1–5, Brisbane, QLD, Australia, May 2018.
- [26] G. Niemeyer, C. Preusche, S. Stramigioli, and D. Lee, "Telero-botics," in *Springer Handbook of Robotics*, pp. 1085–1108, Springer, 2016.
- [27] J. J. Abbott and A. M. Okamura, "Virtual fixture architectures for telemanipulation," in *2003 IEEE International Conference on Robotics and Automation (Cat. No.03CH37422)*, vol. 2, pp. 2798–2805, Taipei, Taiwan, Taiwan, September 2003.
- [28] J. Rey, K. Kronander, F. Farshidian, J. Buchli, and A. Billard, "Learning motions from demonstrations and rewards with time-invariant dynamical systems based policies," *Autonomous Robots*, vol. 42, no. 1, pp. 45–64, 2018.
- [29] G. Maeda, M. Ewerton, G. Neumann, R. Lioutikov, and J. Peters, "Phase estimation for fast action recognition and trajectory generation in human–robot collaboration," *The International Journal of Robotics Research*, vol. 36, no. 13-14, pp. 1579–1594, 2017.
- [30] G. Schwarz, "Estimating the dimension of a model," *The Annals of Statistics*, vol. 6, no. 2, pp. 461–464, 1978.
- [31] V. Venkatesh, M. G. Morris, G. B. Davis, and F. D. Davis, "User acceptance of information technology: toward a unified view," *MIS Quarterly*, vol. 27, no. 3, pp. 425–478, 2003.
- [32] P. A. Lasota and J. A. Shah, "Analyzing the effects of human-aware motion planning on close-proximity human–robot collaboration," *Human Factors: The Journal of the Human Factors and Ergonomics Society*, vol. 57, no. 1, pp. 21–33, 2015.
- [33] S. G. Hart and L. E. Staveland, "Development of NASA-TLX (task load index): results of empirical and theoretical research," *Advances in Psychology*, vol. 52, pp. 139–183, 1988.
- [34] P. H. Schönemann, "A generalized solution of the orthogonal Procrustes problem," *Psychometrika*, vol. 31, no. 1, pp. 1–10, 1966.

Research Article

Design Analysis and Experimental Study of Robotic Chair for Proton Heavy Ion Radiotherapy

Yongde Zhang ¹, Zhikang Yang,¹ Jingang Jiang ¹, Xuesong Dai,¹ Peiwang Qin,¹
Shijie Guo ², and Sihao Zuo³

¹Intelligent Machine Institute, Harbin University of Science and Technology, Harbin 150080, China

²Hebei University of Technology, Xiping Road Beichen District, 300401 Tianjin, China

³Foshan Baikang Robot Technology Co., Ltd., Shishan Town, Nanhai District, 528237 Foshan, China

Correspondence should be addressed to Yongde Zhang; zhangyd@hrbust.edu.cn

Received 4 March 2019; Revised 24 July 2019; Accepted 11 October 2019; Published 1 December 2019

Guest Editor: Michelle Johnson

Copyright © 2019 Yongde Zhang et al. This is an open access article distributed under the Creative Commons Attribution License, which permits unrestricted use, distribution, and reproduction in any medium, provided the original work is properly cited.

Proton heavy ion radiotherapy is widely used and currently represents the most advanced radiotherapy technology. However, at present, proton heavy ion radiotherapy chairs in fixed beam radiotherapy rooms do not have a head and neck positioning function. This paper presents a novel design for a proton heavy ion radiotherapy chair with a head and neck positioning device. The design of the posture adjustment mechanism and the head and neck positioning device of the treatment chair is based on U-TRIZ theory and ergonomics, respectively. A positive kinematic analysis of the posture adjusting mechanism was carried out, as well as a workspace analysis of the head and neck positioning device. Finally, positioning error experiment and ergonomic evaluation were performed on a prototype of the head and neck positioning device. The proposed design of the treatment chair satisfies the requirements for posture adjustment and achieves the head and neck positioning function. The experimental results also provide a basis for further optimization of the design.

1. Introduction

Proton heavy ion radiotherapy is a new type of radiotherapy that has stoked international interest in recent years and represents the most advanced radiotherapy technique and is the future trend for radiotherapy treatments for cancers [1]. The characteristics of the proton heavy ion beam include an inverse dose distribution and the formation of a sharp Bragg peak when entering the human body. The ion beam is highly lethal to tumors and accurately attacks tumor cells, which reduces damage to surrounding tissue. In addition, it induces double-strand DNA breaks, thereby reducing the chances of tumor recurrence and metastasis [2–5].

During proton heavy ion radiotherapy treatments, the sitting posture of the patients with head and neck cancer, lung cancer, orthopnea [6], dyspnea, and dysphagia is necessary. To meet the needs of the sitting posture for radiother-

apy, a number of scientific research institutes and medical device companies around the world have introduced special treatment chairs.

Schardt and Heeg designed a posture adjustment chair for patients with head and neck cancer in the heavy ion beam treatment room [7]. In 2006, Sommer et al. proposed a series of positioning chairs for radiotherapy patients [8]. The Orsay Proton Therapy Center in France developed a robotic chair for the treatment of head, neck, and eye tumors. Similarly, Chengdu Dr. Technology Co., Ltd. invented an automatic positioning chair for proton and heavy ion treatment of head and neck cancer [9]. In 2017, Guangdong Hengju Medical Technology Co., Ltd. designed a sitting posture fixation device for particle radiotherapy [10].

Nonetheless, existing radiotherapy chairs are still unsuitable for proton heavy ion fixed beam radiotherapy rooms and do not completely meet the requirement for six-degree-of-freedom (6-DOF) posture adjustment. Moreover, current

TABLE 1: The proton heavy ion radiotherapy work process.

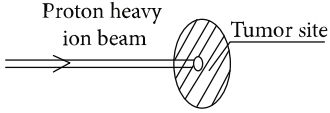
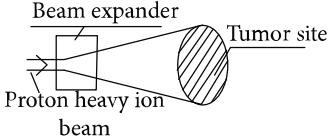
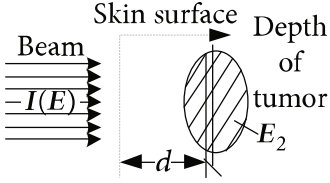
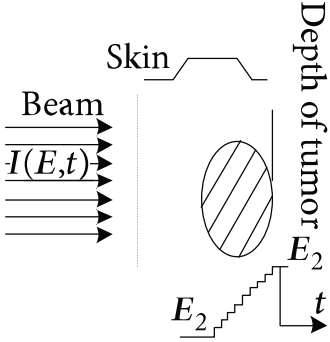
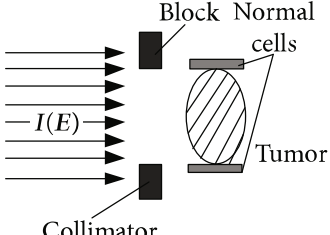
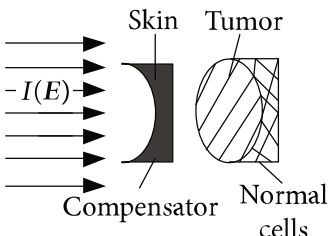
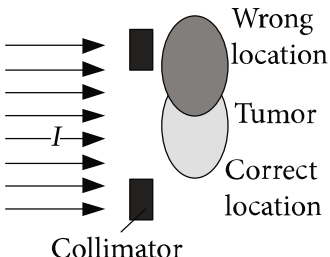
Order number	Working principle decomposition diagram	Principle description
a		<p>The proton heavy ion beam is accelerated by the accelerator and becomes a high-energy proton heavy ion beam.</p>
b		<p>High-energy proton heavy ion beams need to be expanded to cover the entire tumor site.</p>
c		<p>Select proton heavy ion beams of different energies for tumors of different depths.</p>
d		<p>The energy modulator is used to modulate the energy of the proton heavy ion beam, gradually increasing its energy and achieving fine treatment.</p>
e		<p>The beam collimator blocks the proton heavy ion beam directed to normal cells and avoids damage to normal cells.</p>
f		<p>The proton heavy ion beam needs to pass through a special compensator at the front of the skin to prevent damage to normal cells at the posterior edge of the tumor.</p>
g		<p>Introduce a precision positioning system to align the patient to the beam and avoid error irradiation.</p>

TABLE 1: Continued.

Order number	Working principle decomposition diagram	Principle description
h		In order to synchronize the proton heavy ion beam irradiation with the breathing and avoid the influence of breathing on the tumor size, it is necessary to equip a respiratory door control system.
i		A measurement and calibration system is required to ensure uniformity of the proton dose in the longitudinal and transverse directions.
j		A set of beam monitoring system is introduced to monitor whether the beam center, strength, and section distribution meet the requirements in real time.
k		The end of the proton heavy ion beam output needs to have a posture adjustment mechanism, and the treatment head is irradiated from different angles in order to obtain a good efficacy.

thermoplastic film head and neck fixation technologies are time-consuming, uncomfortable for the patient, and not universally applicable.

This paper presents the design of a proton heavy ion radiotherapy chair with a head and neck positioning function. The design was applied to the posture adjustment and head and neck positioning of patients in a fixed beam radiotherapy room. The device facilitates the application of the fixed beam of proton heavy ion irradiation of tumors from different directions and angles, enhances the effects of radiotherapy, and improves the efficiency, versatility, and comfort of head and neck positioning.

2. Methods

2.1. Mechanical Structure Design of Treatment Chair

2.1.1. Functional Requirement Analysis of Treatment Chair.

For proton heavy ion radiation therapy, a more complex and larger treatment system is needed than the system required for conventional X-ray and electron linear accelerators. The working principle of the proposed system is illustrated in Table 1 [11]. The treatment chair for sitting position radiotherapy with a proton heavy ion fixed beam

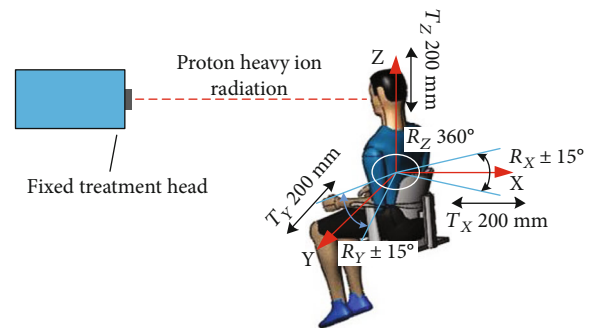


FIGURE 1: The function demand analysis of the posture adjustment.

must provide two functions: posture adjustment and head and neck positioning. The posture adjustment function enables the irradiation of tumors from different directions and angles using the fixed beam. Specific adjustment parameters include 200 mm movements in the X, Y, and Z directions, $\pm 15^\circ$ rotations about the x -axis and y -axis, and 360° rotations about the z -axis, as shown in Figure 1. The head and neck positioning function must quickly and comfortably restrict the degrees of freedom of the head and neck depending on the somatotype of the patient.

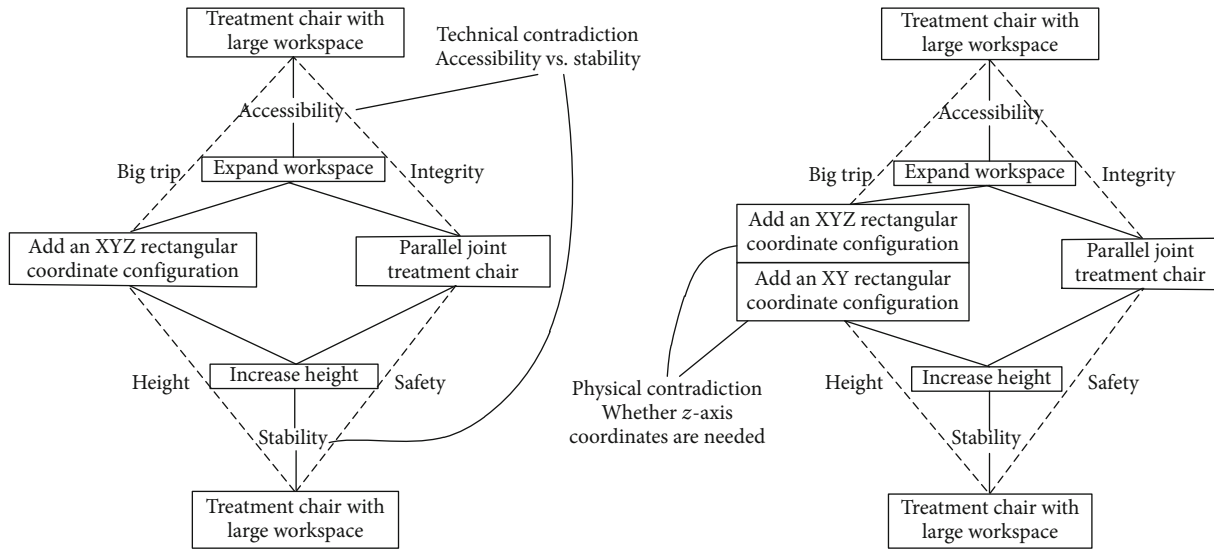


FIGURE 2: Technical contradiction and physical contradiction of treatment chair represented by the SAFC model.

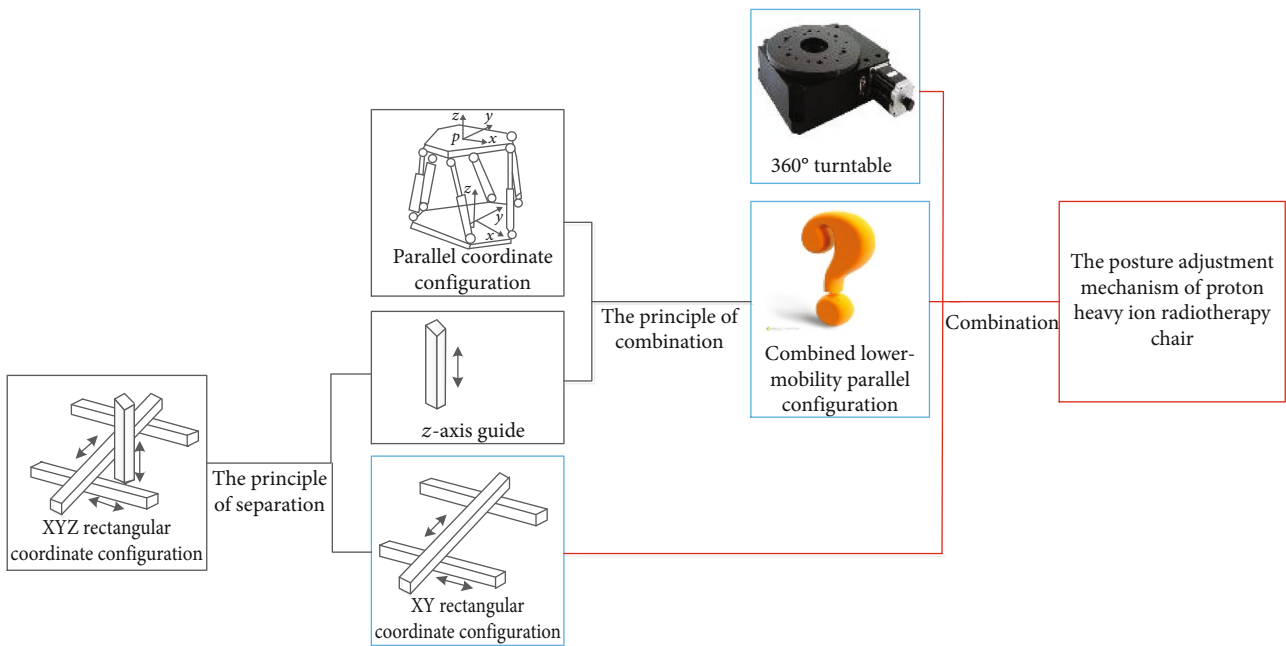


FIGURE 3: The analysis of posture adjustment mechanism based on U-TRIZ theory.

2.1.2. Design of Posture Adjustment Mechanism Based on U-TRIZ Theory. U-TRIZ theory is a function-oriented and attribute-centered TRIZ theory of inventive problem solving, which unifies several tools and methods, and is an effective tool for innovative design [12, 13]. The 6-DOF parallel platform has a small workspace and cannot meet the needs of patients that must move 200 mm in the X, Y, and Z directions. Thus, it is necessary to add an XYZ rectangular coordinate slipway to the parallel platform. However, this increases the height in the Z direction, reduces stability, and creates redundant degrees of freedom. Therefore, the SAFC model of U-TRIZ theory was used for the present analysis, as shown in Figure 2.

The technical contradiction and corresponding physical contradiction of the treatment chair design are shown in Figure 2. For the physical contradiction, the z-axis is separated from the XYZ rectangular coordinate configuration, then the z-axis is incorporated into the parallel configuration using the 40 inventive principles to produce a combined lower-mobility parallel coordinate configuration, which can only be adjusted by modifying the X and Y angles. Finally, the XY plane coordinate configuration, lower-mobility parallel configuration, and 360° turntable are combined to create the posture adjustment mechanism of the proton heavy ion radiotherapy chair, as shown in Figure 3.

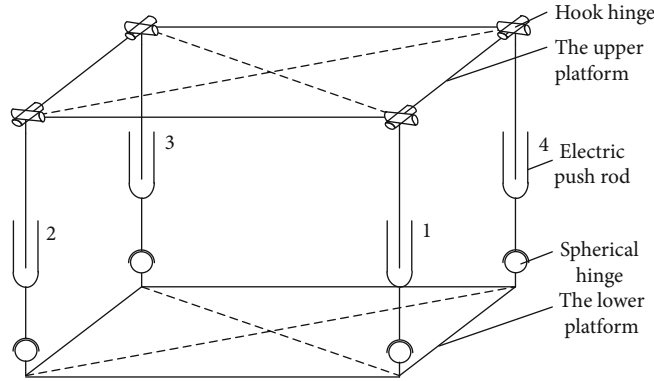


FIGURE 4: The common parallel mechanism.

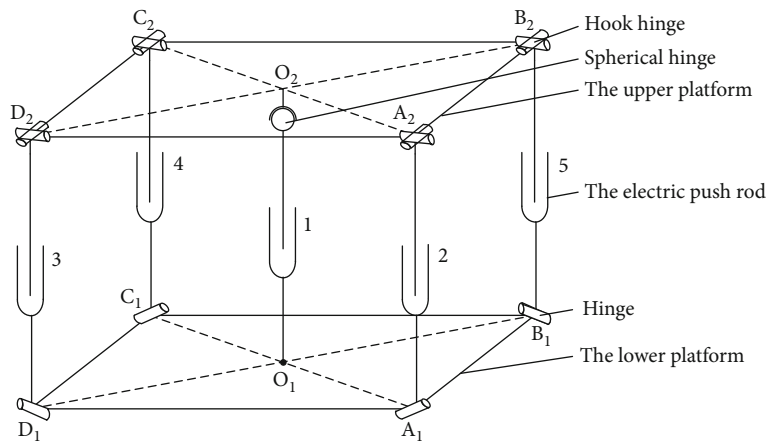


FIGURE 5: The schematic diagram of combined lower-mobility parallel mechanism.

The above scheme adds a bottom-fixed vertical lift electric push rod along the Z direction of the ordinary parallel mechanism, as shown in Figure 4, and replaces the spherical hinges at the lower end of the four branches with a single hinge by grouping them into a lower-mobility parallel mechanism, as shown in Figure 5. Electric push rod 1 is represented by O_1O_2 along the vertical direction of the z-axis. The bottom of the rod is fixed to the lower platform and the top is connected to the upper platform by spherical hinges, which allow vertical movements. Two active adjustment branches, A_1A_2 and B_1B_2 , are connected to the lower platform via two hinges at A_1 and B_1 that rotate around the pin. Electric push rods 2 and 3 are located in the middle and connected to the upper platform via hook hinges at A_2 and B_2 . Two passive adjustment branches, C_1C_2 and D_1D_2 , are connected in the same way as A_1A_2 and B_1B_2 and follow the stretching motion of the A_1A_2 and B_1B_2 branches while playing a supporting role. The degrees of freedom of the combined lower-mobility parallel mechanism can be determined as follows:

$$M_1 = 6(n - g - 1) + \sum_{i=1}^n f_i = 6 \times (12 - 14 - 1) + 20 = 2. \quad (1)$$

The DX3535A XY mobile unit (THK, Japan) and GT-135C single-stage high-precision hollow rotary platform reducer (Liming, Taiwan) were selected for generating translational motion in the X and Y directions and rotary motion in the Z direction, respectively.

For the analysis, a three-dimensional (3D) model of the proton heavy ion radiotherapy chair posture adjustment mechanism was established and is presented in Figure 6. The working principles of the mechanism can be described as follows: the XY moving unit and electric push rod 1 are adjusted to place the patient in a predetermined position, then the length of the electric push rods 3 and 5 is adjusted to rotate the patient a certain angle about the x-axis, the length of electric push rods 2 and 4 is adjusted to rotate the patient a certain angle about the y-axis, and finally, the 360° turntable is adjusted to rotate the patient a certain angle about the z-axis. Table 2 lists the performance parameters of the posture adjustment mechanism.

2.1.3. Design of Universal Head and Neck Positioning Device Based on Ergonomics. During the medical device design process, ergonomic standards typically include the size, appearance, convenient operation, and safety of the product [14, 15]. This paper adopts the ergonomic standards to

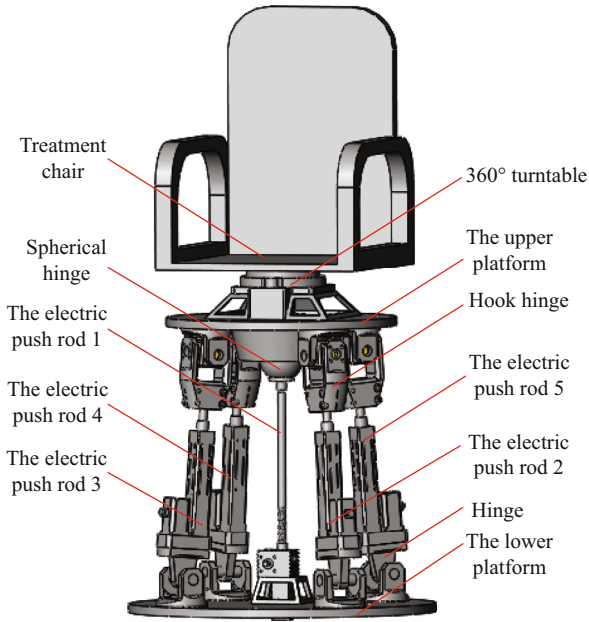


FIGURE 6: The 3D model of the proton heavy ion radiotherapy chair posture adjustment mechanism.

TABLE 2: The performance parameters of treatment chair posture adjustment mechanism.

The effective travel in the x -axis (mm)	350
The effective travel in the y -axis (mm)	350
The effective travel in the z -axis (mm)	200
x -axis angle adjustment ($^{\circ}$)	± 20
y -axis angle adjustment ($^{\circ}$)	± 20
z -axis angle adjustment ($^{\circ}$)	360
The maximum load (N)	2000
The number of DOF	6

modularize the universal head and neck positioning device. The three main submodules are the head circumference positioning, chin positioning, and backboard.

(1) *Head Circumference Positioning Module.* The function of the head circumference positioning module is to position the head from the plane of the head circumference and the top of the head, by setting three positioning points at equal angles on the head circumference of approximately elliptical shape and an anchor point on the top of the head. To realize the final position, the DOF of the head is restrained.

A 3D model of the head circumference positioning module was established, as shown in Figure 7. The working principle can be described as follows: a hand-operated handle screw passes through the special bearing end cover to match the inner diameter of the bearing; the outer diameter of the bearing is fixed to match the circular hole on the curved bracket of the positioning block and can be rotated; to fix the bearing, a special bearing end cover is inserted into the

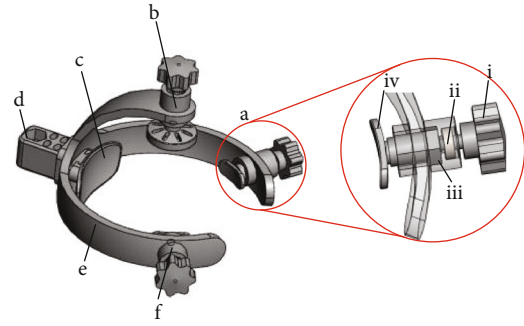


FIGURE 7: The 3D structure of the head circumference positioning module. (a) The adjustable head circumference positioning block 1 with (i) the hand-operated handle screw, (ii) bearing, (iii) screw nut, and (iv) the positioning block. (b) The adjustable head top positioning block. (c) The fixed head circumference positioning block. (d) The height adjustment mechanism. (e) Head circumference positioning bracket frame. (f) The adjustable head circumference positioning block 2.

circular hole on the curved bracket of the positioning block; and the screw nut matches the hand-operated handle screw and can move back and forth along the hexagonal prism hole in the head positioning block to realize front and rear adjustments of the positioning block. The same adjustment method was adopted for the adjustable head circumference positioning blocks 1 and 2 as well as the adjustable head circumference positioning block.

The size of the human body determines the geometric space and range of motion required for the design and is the basic information used in the man-machine system or product designs. In the present design, the size parameter range of the head and neck of the human body must be considered so that the final product meets the needs of different body types and improves patient comfort.

Head- and neck-related parameters were obtained from the Chinese standard GB10000-88 “Human dimensions of Chinese adults,” as shown in Figure 8, which provided basic values for the size of Chinese adults according to ergonomic requirements. The standard is applied to technical product upgrades and labor safety protection for industrial products, architectural design, military applications, and in other industries. Based on this standard, the inner diameter of the ring where the positioning block is placed was set to 120 mm, the external diameter was set to 130 mm, and the wall thickness was 10 mm.

(2) *Chin Positioning Module.* The function of the chin positioning module is to fully position the head using the head circumference positioning module. According to ergonomic standards, the shape of the chin rest must be as close as possible to the actual shape of the chin and can be adjusted to enhance the position of the chin.

A 3D model of the chin positioning module was established and is shown in Figure 9. The working principle can be described as follows: a screw-nut slider is installed within long slots in support arms 1 and 2; a cantilever is mounted on the left and right screw-nut sliders, and the front and rear

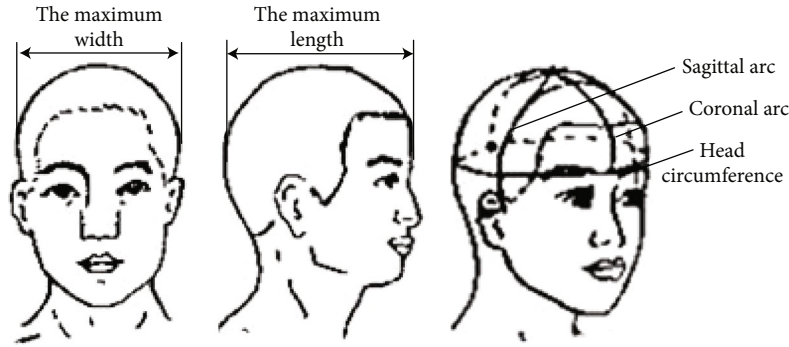


FIGURE 8: Human head parameters.

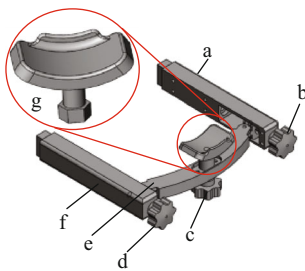


FIGURE 9: Chin positioning adjustment module. (a) The support arm 1. (b) The hand-operated handle screw 1. (c) The hand-operated handle screw 2. (d) The hand-operated handle screw 3. (e) Cantilever. (f) The support arm 2. (g) The chin block.

positions are adjusted by the hand screw handles 1 and 2; the chin rest is installed in the middle of the cantilever, and to move the chin support up and down, the screw nut is adjusted using hand screw handle 3.

Based on the configuration analysis, the chin positioning block can only be used for front and rear and up and down adjustments; therefore, it is only necessary to calculate the up and down and front and rear adjustment lengths. Consulting GB10000-88, the maximum length of the head is 161~200 mm, the length of the back of the measuring head to the back of the plate is 35 mm, such that the chin block before and after back position adjustment is 196~235 mm.

(3) *Backboard*. The backboard supports the installation of the head circumference positioning module and the chin rest positioning module and must meet the installation, positioning, and adjustment requirements of the two modules. Consulting GB10000-88, the height range from the shoulders to the top of the head is 283~446 mm and the shoulder width range is 304~417 mm. The height of the backboard must be adjusted according to the height of the patient while in a seated position, and the lower edge is always the same height as the shoulders of the human body to position the head. A backboard size of 500 × 600 mm was selected.

The head circumference positioning module, chin positioning module, and backboard were assembled, and the 3D structure of the proton heavy ion radiotherapy chair

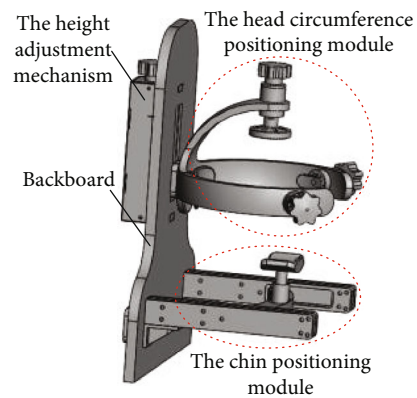


FIGURE 10: The head and neck positioning device of proton heavy ion radiotherapy chair.

head and neck positioning device was determined, as shown in Figure 10.

2.2. Analysis of Kinematic Performance of Treatment Chair

2.2.1. *Positive Kinematic Analysis of Posture Adjustment Mechanism*. A schematic drawing of the 3D model of the proposed posture adjustment mechanism is presented in Figure 11. Posture adjustment can be divided into two parts: position adjustment and angle adjustment. In the whole posture adjustment mechanism, movement of the lower-mobility parallel mechanism is more complicated with X and Y angle adjustment functions. For this reason, a kinematic analysis was only performed on the X and Y angle adjustment parallel platforms.

As shown in Figure 11, the X and Y angle adjustment parallel platform has four branches including two pairs of symmetrical branches, one pair for the x -axis angle adjustment and the other pair for the y -axis angle adjustment. The x -axis angle adjustment was separately analyzed first. The structure is shown in Figure 12.

The base coordinate system $O_1-x_1y_1z_1$ was established on the bottom plane, and the upper moving plane was used to establish the moving coordinate system $O_2-x_2y_2z_2$; R is the length from the center of the bottom platform to the electric push rod; r is the length from the center of the upper moving

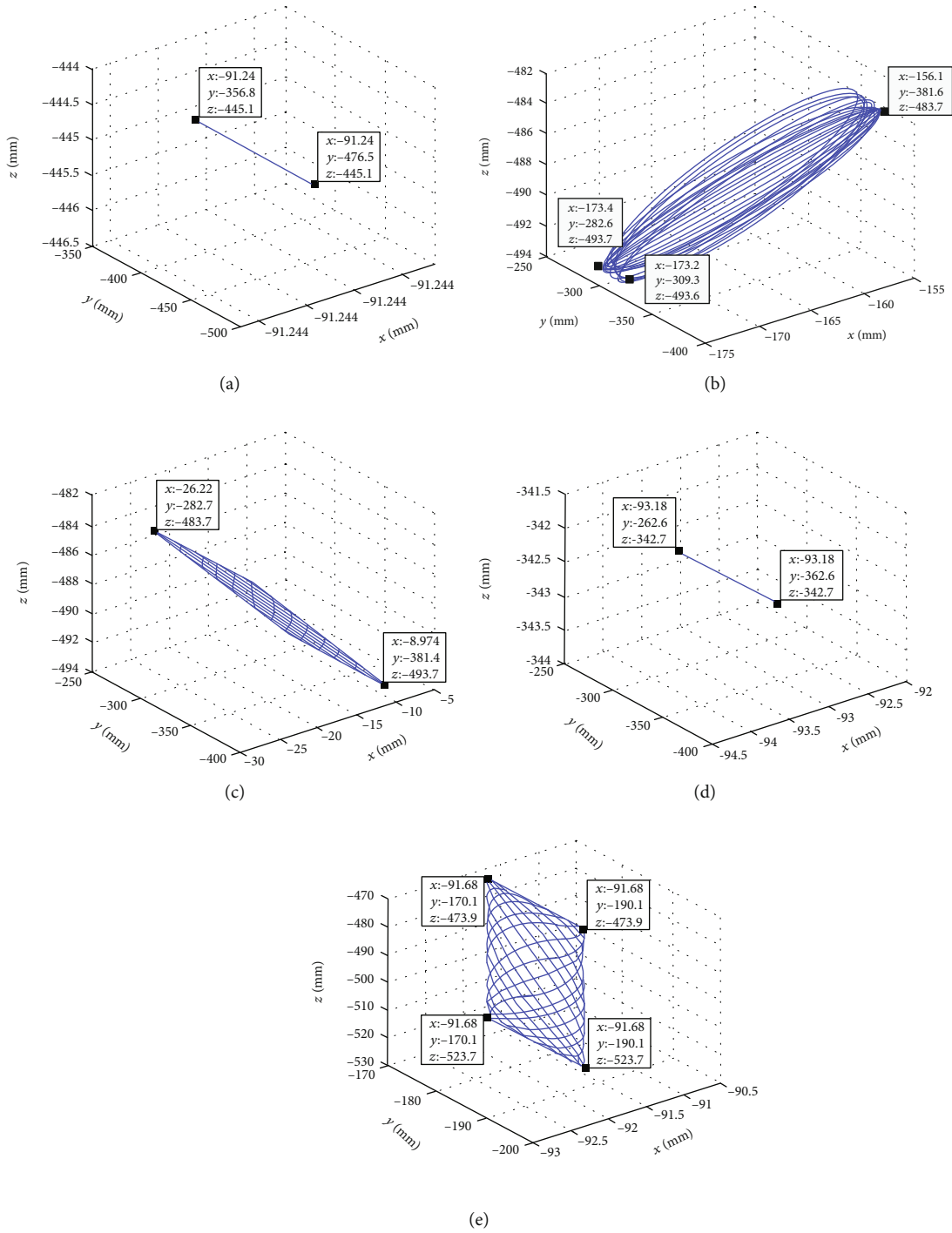


FIGURE 14: Angle adjustment relationship between x -axis and y -axis. (a) The workspace of head top positioning block. (b) The workspace of head circumference positioning block 1. (c) The workspace of head circumference positioning block 2. (d) The workspace of fixed head circumference positioning block. (e) The workspace of chin positioning block.

From equations (6) and (7), the relationship between the x -axis and y -axis adjustment angle x_1 ($x = \alpha, \beta$) and the length of the branch can be obtained. The effective adjustment range of the x -axis and y -axis adjustment angle is $-15^\circ \sim 15^\circ$, the variable x_1 ($x = \alpha, \beta$) ranges from -15° to 15° . The relationship between the three x -axis variables and y -axis adjustment angle x_1 ($x = \alpha, \beta$), electric push rod elongation l_0 , and electric push rod elongation l_i ($i = 1, 2$) is shown in Figure 13.

The four extreme position coordinates indicate that the x -axis and y -axis adjustment angle x_1 ($x = \alpha, \beta$) is between -15° and 15° , the length of the electric push rod l_0 is adjustable from 360 mm to 480 mm, the length of the electric push rod l_i ($i = 1, 2$) is adjustable from 381 mm to 480 mm, and the length of the electric push rods l_3 and l_4 can also be adjusted according to the elongation or shortening of l_1 and l_2 .



FIGURE 15: The universal prototype of the head and neck positioning.

2.2.2. Workspace Analysis of Head and Neck Positioning Device. In robotics, the workspace or reachable workspace is defined as the set of all the target points that can be reached by the end effector when different joints of the robot are in motion. The work ability of the robot is an important kinematic index [16, 17].

For the proton heavy ion radiotherapy process, whether the universal head and neck positioning device of the treatment chair workspace can meet the head and neck positioning requirements of different body types is important and is the basis for measuring the positioning function of the head and neck.

In the present study, the second-generation MATLAB/SimMechanics library was used for the modeling analysis, and the position of the head top positioning block, head circumference positioning block, fixed head circumference positioning block, and chin positioning block was recorded in the base coordinate system.

The simulated workspace of each positioning submodule of the head and neck positioning device is illustrated in Figure 14. The workspace simulation of the above positioning module shows that each module can meet the head and neck positioning requirements of patients.

3. Results and Discussion

The head and neck positioning device is made of PMMA and plastic to avoid radiation damage to the patient and operators. A prototype of the head and neck positioning device shown in Figure 15 was assembled using an acrylic plate and resin material.

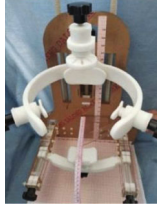
3.1. Positioning Error Test of Each Module of Positioning Device. As shown in Table 3, the chin positioning block has four adjustment limits: proximal low point, proximal high point, distal low point, and distal high point. The center position of the bottom of the backboard was taken as the coordi-

nate origin (0, 0, 0), and a rectangular spatial coordinate system was established. The positive Z direction was set as vertically upwards, the positive direction of the y-axis was set as the outward-facing direction of the vertical backboard, and the x-axis coincides with the lower edge of the backboard and the positive X direction was set to the right. The spatial coordinate position of the center of the concave chin block was measured and compared with the corresponding data calculated during the design stage.

It can be seen from Table 3 that the maximum deviation of the y-axis is 2.5 mm in the process of assembling and adjusting the chin positioning block, which differs quite considerably from results of the finite element analysis. There are two reasons such as large deviation: errors in processing and assembling the parts and the two lead screws are not synchronized when the chin block is adjusted. Owing to this, the chin positioning block cannot be fully adjusted at the distal and proximal ends; however, the maximum deviation along the x-axis and z-axis was still less than 2.5 mm. This meets the positioning requirements, and the chin positioning module of the prototype can be further optimized using the same analysis.

The equipotential method was adopted to measure the block parameters for the head circumference positioning using adjustable head circumference positioning block. First, a point at the end of the head circumference positioning block was marked and the head circumference was adjusted to the position limit; the flexible manipulator was adjusted so that the end coincides with the end of the head circumference positioning bracket; then, the end point center of the head circumference positioning block was replaced with the end of the manipulator, which is easier to measure, as shown in Figure 16(a). The head circumference positioning block was adjusted to other positions, and the end point of the manipulator is measured, as shown in Figure 16(b). The manipulator data includes the position of the center point of the head circumference

TABLE 3: The adjustment parameter of chin positioning block.

Position	Proximal low point	Proximal high point	Distal low point	Distal high point	
Calculating coordinates	(0, 165.0, 145.0)	(0, 165.0, 162.0)	(0, 235.0, 145.0)	(0, 235.0, 162.0)	
Location description	Chin positioning block at the proximal low point	Chin positioning block at the proximal high point	Chin positioning block at the distal low point	Chin positioning block at the distal high point	
Measurement diagram					
Measuring coordinates	(1.5, 167.0, 143.5)	(-1.5, 167.5, 161.0)	(1.0, 234.5, 143.0)	(0.5, 235.0, 160.5)	
Error (mm)	Δx	1.5	-1.5	1.0	0.5
	Δy	2.0	2.5	-0.5	0
	Δz	1.5	-1.0	-2.0	-1.5

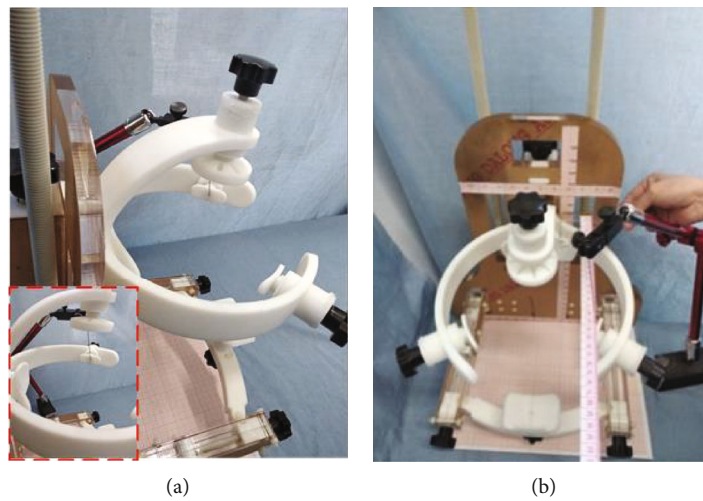


FIGURE 16: The universal prototype of the head and neck positioning. (a) The equipotential point mark of head circumference positioning block. (b) The equipotential point measurement.

positioning block. The head top positioning parameter was also measured using this method.

Based on the above method, coordinates and errors of the end center position of the head circumference positioning block and the head top positioning block are shown in Table 4.

From Table 4, the error of the head circumference positioning block along the y -axis and z -axis is large, and the error along the z -axis is a maximum of 3 mm. The head top positioning block also exhibited large errors along the y -axis and z -axis, and the maximum error was 2 mm.

When the head of the patient is positioned, the top of the head generates an upward supporting force that acts on the head circumference positioning bracket frame and reduces

the error. The experimental results provide reference values for further design improvements and balance the error caused by the self-weight of the head circumference positioning bracket frame.

3.2. Ergonomic Evaluation Experiment. The universal head and neck positioning device was designed from an ergonomic perspective; therefore, the design can be evaluated using human-machine system evaluation methods, which are generally divided into three categories: experimental methods, simulations, and actual operational measurements [18–21]. The present study selected the experimental approach to evaluate the general purpose of the head

TABLE 4: The coordinates and errors of the head circumference positioning block and the head top positioning block.

Module	State	Calculating coordinates	Measuring coordinates	Error (mm)		
				Δx	Δy	Δz
Head circumference positioning block 1	High position and extension	(-64.7, 173.8, 360.0)	(-63.5, 174.5, 357.0)	1.2	0.7	-3.0
	High position and shorten	(-82.0, 183.8, 360.0)	(-84.0, 182.0, 358.0)	-2.0	-1.8	-2
	Low position and extension	(-64.7, 173.8, 260.0)	(-64.0, 173.5, 258.5)	0.7	-0.3	-1.5
	Low position and shorten	(-82.0, 183.8, 260.0)	(-81.0, 183.0, 261.0)	1.0	-0.8	1.0
Head circumference positioning block 2	High position and extension	(64.7, 173.8, 360.0)	(65.0, 171.0, 358.0)	0.3	-2.8	-2.0
	High position and shorten	(82.0, 183.8, 360.0)	(83.5, 183.0, 358.0)	1.5	-0.8	-2.0
	Low position and extension	(64.7, 173.8, 260.0)	(65.5, 174.5, 260.0)	0.8	0.7	0
	Low position and shorten	(82.0, 183.8, 260.0)	(80.0, 182.5, 259.0)	-2.0	-1.3	-1.0
Fixed head circumference positioning block 3	High position	(0, 34.5, 360.0)	(0, 35.0, 358.5)	0	0.5	-1.5
	Low position	(0, 34.5, 260.0)	(0, 33.5, 261.0)	0	-1.0	1.0
Head top positioning block	High position and extension	(0, 135.0, 430.0)	(1.0, 133.5, 428.5)	1.0	-1.5	-1.5
	High position and shorten	(0, 135.0, 450.0)	(0.5, 133.5, 449.0)	0.5	-1.5	-1.0
	Low position and extension	(0, 135.0, 330.0)	(0, 134.0, 328.0)	0	-1.0	-2.0
	Low position and shorten	(0, 135.0, 350.0)	(-0.5, 133.5, 348.5)	-0.5	-1.5	-1.5

and neck positioning device. The following experimental procedure was carried out:

- (1) An evaluation form was prepared from the perspective of “human, machine, and environment” and evaluated and compiled using ergonomic principles and details of the universal head and neck positioning device, as shown in Table 5. Collected data included the size of a user’s head and 22 additional measurements from the three submodules. The evaluation data was then divided into five grades according to user experience, thereby providing feedback on the rationality of the modular design
- (2) An evaluation sample was defined based on the selection criteria. The main factor affecting positioning in this experiment was the head circumference, which was selected according to the normal distribution. A total of 12 human volunteers were selected for the evaluation. The head size distribution is presented in Table 6
- (3) Head and neck positioning experiments were performed. Briefly, the head and neck of volunteers participating in the experiment were positioned, as shown in Figure 17, and the evaluation form was filled out based on their experiences
- (4) The evaluation results were statistically analyzed. Evaluation scores were counted for all items according to the head circumference, average scores were calculated, and evaluation score curves were plotted, as shown in Figure 18

From the curves in Figure 18(a), it can be observed that the expansion of the adjustable positioning block meets the needs of users with moderate head dimensions but can also meet the needs of larger and smaller users. Smaller users gave

higher evaluation scores for the comfort of each positioning block, but the scores of larger users were poor.

Overall, the adjustment efficiency of the adjustable positioning block was low, and since the larger user is taller than the small user, only small length adjustments are needed for the large user. From Figure 18(b), it can be seen that the size of the chin positioning block is more suitable for larger users and small users gave slightly lower evaluation scores.

In general, adjustment efficiency scores of the chin positioning block were fairly low, with scores of large users only slightly higher because the length must only be adjusted small amount. Moreover, larger users found the device more comfortable than small users. It can be seen from Figure 18(c) that the positioning block mounting efficiency is higher for large head circumferences. The backplane was more difficult for smaller users to adjust, whereas the size of the head space was more suitable for small- and medium-sized users; therefore, comfort for large users was poor.

In summary, the universal head and neck positioning device can better meet the needs of users of medium head sizes and must be further optimized to better meet the needs of small and large users.

4. Conclusions

This paper presented the design of a proton heavy ion radiotherapy chair with a head and neck localization function. The design of the posture adjustment module and head and neck positioning module was based on U-TRIZ theory and ergonomics, respectively. A positive kinematic analysis of the posture adjustment mechanism of the treatment chair and workspace analysis of the head and neck positioning device were carried out, as well as a stiffness and strength analysis under several limit states. Finally, a positioning error experiment and ergonomics evaluation were performed using a prototype of the universal head

TABLE 5: The evaluation form.

The evaluation form of the head and neck positioning device						
Through the subjective feelings of the volunteers during the experiment, the performance of the head circumference positioning module, the chin positioning module, and the backboard module was evaluated from the perspective of ergonomics.						
Name	Scoring standard: very suitable: 5, suitable: 3, general: 1, inappropriate: -3,					
Gender	very inappropriate: -5					
Head size parameter	Head circumference	Head full height	Eye height	Maximum width of the head	Maximum length of the head	
Unit (mm)						
The universal head and neck positioning device evaluation	Submodule	Evaluation project			Score	Comment
	The head circumference positioning module evaluation	(01) Whether the adjustable head circumference positioning block 1 and 2 is suitable				
		(02) Whether the fixed head circumference positioning block 3 is suitable				
		(03) Whether the adjustable head top positioning block 4 is suitable				
		(04) Whether the expansion amount of adjustable head circumference positioning blocks 1 and 2 is suitable				
		(05) Whether the expansion amount of adjustable head top positioning block 4 is suitable				
		(06) Whether the adjustment efficiency of head circumference adjustable positioning blocks 1 and 2 is efficient				
		(07) Whether the adjustment efficiency of head top positioning block 4 is efficient				
		(08) Whether the adjustable head circumference positioning block 1, 2 is comfortable				
		(09) Whether the fixed head circumference positioning block 3 is comfortable				
		(10) Whether the adjustable head top positioning block 4 is comfortable				
	The chin positioning module evaluation	(11) Whether the head circumference positioning is stable				
		(12) Whether the chin positioning block is suitable				
		(13) Whether the adjustment amount of the chin positioning block is sufficient				
		(14) Whether the adjustment efficiency of the chin positioning block is efficient				
		(15) Whether the chin positioning block is comfortable				
		(16) Whether the support arms 1 and 2 press the shoulder				
		(17) Whether the head circumference positioning block frame is efficient				
	The backboard module evaluation	(18) Whether the height of the backboard is easy to adjust				
		(19) Whether the height adjustment of the backboard is stable				
		(20) Is the device safe?				
		(21) Is it easy to grasp the hand-held handle?				
(22) Is the head space the right size?						
Suggest:						

TABLE 6: Volunteer head circumference size distribution table.

Head circumference size	510-519	520-529	530-539	540-549	550-559	560-569	570-579	580-589
Number	1	1	1	2	3	2	1	1

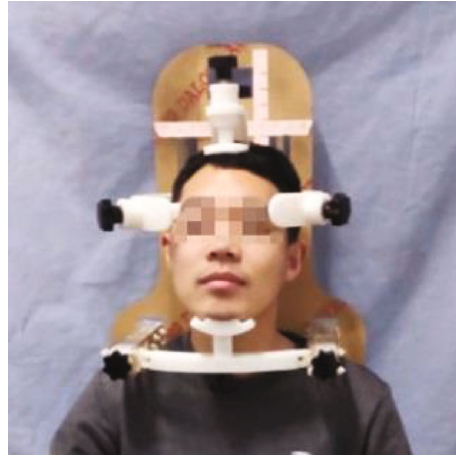


FIGURE 17: The experiment of head and neck positioning.

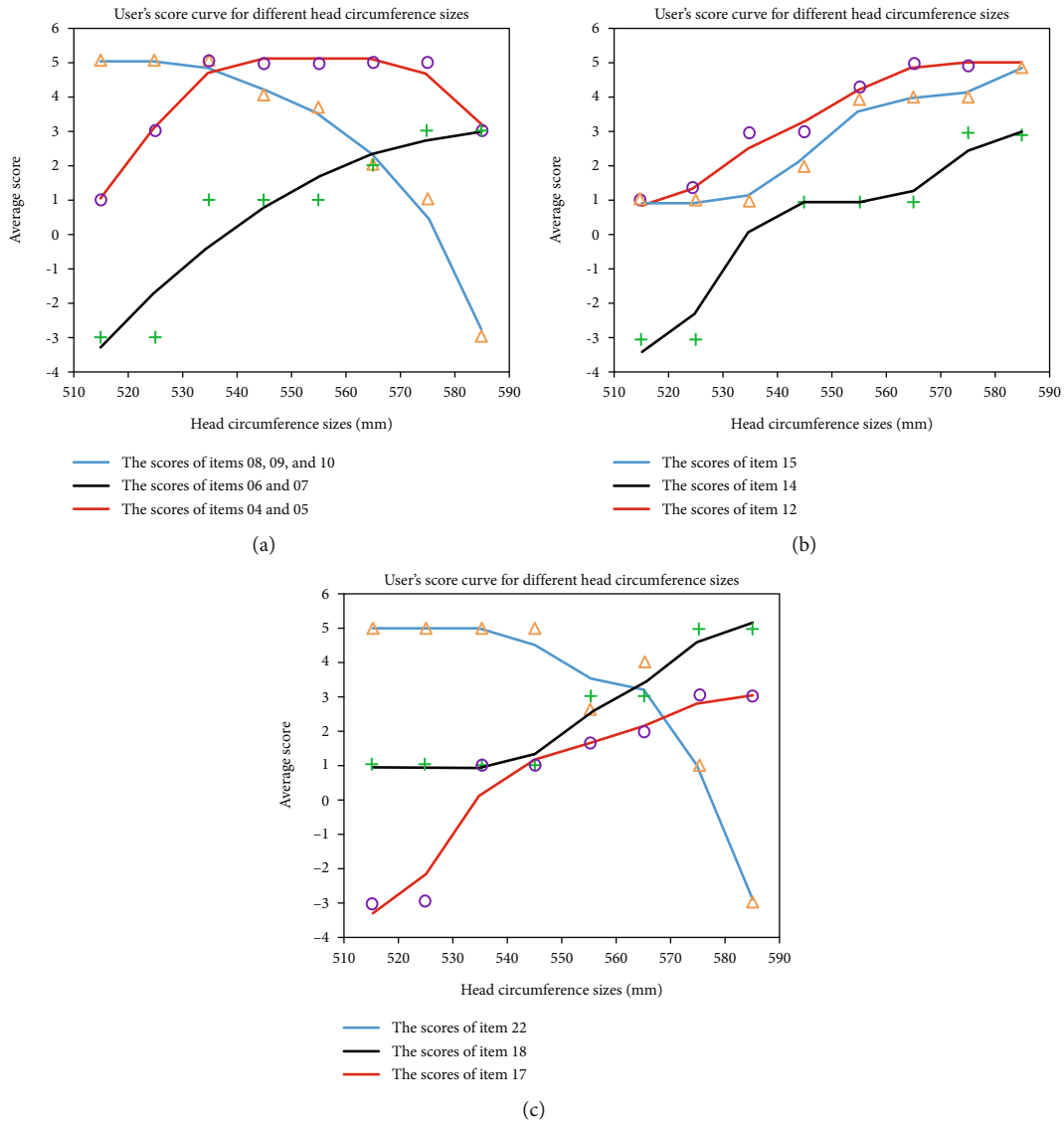


FIGURE 18: The evaluation scoring curve of universal head and neck positioning device. (a) The evaluation scoring curve of head circumference positioning module. (b) The evaluation scoring curve of chin positioning module. (c) The evaluation scoring curve of backboard module.

and neck positioning device. The results show that the head and neck positioning device can meet the head and neck positioning requirements of medium-sized users much better than existing chairs; however, further optimization is still needed to meet the needs of all users.

Data Availability

The data used to support the findings of this study are available from the corresponding author upon request.

Conflicts of Interest

The authors declare that they have no conflicts of interest.

Acknowledgments

This research was supported by the Natural Science Foundation of China (Grant No. 51675142) and by the Key Projects of Natural Science Foundation of Heilongjiang Province of China (Grant No. ZD2018013) and by the Reserve Leader Funding Project of Leading Talent Echelon of Heilongjiang Province of China (Grant No. 2501050628).

References

- [1] J. Li, "The project management practice of Shanghai Proton Heavy Ion Hospital," *China Engineering Consulting*, vol. 22, no. 2, pp. 52–55, 2015.
- [2] S. F. Li, M. Z. Shankou, and Z. J. Wang, "Research status of heavy ion radiation therapy for malignant tumors," *Chinese Journal of Clinicians (Electronic Edition)*, vol. 5, no. 10, pp. 2975–2981, 2011.
- [3] S. Mizutani, Y. Takada, R. Kohno, K. Hotta, R. Tansho, and T. Akimoto, "Application of dose kernel calculation using a simplified Monte Carlo method to treatment plan for scanned proton beams," *Journal of Applied Clinical Medical Physics*, vol. 17, no. 2, pp. 315–327, 2016.
- [4] L. Wang and X. Y. Dai, "Current status and prospects of global proton heavy ion hospitals," *Chinese Hospital Architecture & Equipment*, vol. 2, no. 1, pp. 26–31, 2016.
- [5] J. X. Xie and L. Zhang, "Proton/heavy ion radiotherapy technology and application," *China Medical Device Information*, vol. 1, no. 1, pp. 1–4, 2016.
- [6] National Taiwan University of Pathology, "Dyspnea and orthopnea," *Contemporary Medicine*, vol. 11, no. 369, pp. 594–598, 2004.
- [7] D. Schardt and P. Heeg, "Device for positioning a tumour patient with a tumour in the head or neck region in a heavy ion therapy chamber," 2003, U.S. Patent 20030164459A1.
- [8] L. V. Behr, "Patient positioning device," U.S. Patent 4446587, 2012.
- [9] Z. H. Wang and M. Wang, "An automatic chair for treating head and neck cancer with protons and heavy ions," C.N. Patent 107007946A, 2017.
- [10] W. Q. Qiu, Y. S. Wu, W. Lu, Z. J. Zhang, P. Q. Lan, and A. C. Luis, "Sitting position fixing device for particle radiotherapy," C.N. Patent 106512238A, 2017.
- [11] Y. D. Zhang, Z. K. Yang, and S. J. Guo, "Design and kinematic analysis of positioning chair for proton heavy ion radiotherapy," in *International Conference on Biological Information and Biomedical Engineering, IEEE*, Shanghai, China, June 2018.
- [12] F. F. Zhu and F. Zhao, "Research on development and design of family emergency products based on U-TRIZ theory," *Packaging Engineering*, vol. 6, no. 14, pp. 29–33, 2018.
- [13] W. C. Zhang, M. Zhao, and J. Chen, "U-TRIZ based SAFC analysis model," *Technology Economics*, vol. 33, no. 12, pp. 7–13, 2014.
- [14] C. J. Vincent, Y. Li, and A. Blandford, "Integration of human factors and ergonomics during medical device design and development: it's all about communication," *Applied Ergonomics*, vol. 45, no. 3, pp. 413–419, 2014.
- [15] J. H. Shentu, "Medical device design and example application based on ergonomics," *Business: Financial Research*, vol. 2, no. 2, pp. 172–172, 2008.
- [16] Y. J. Zhao, Y. D. Zhang, and J. G. Jin, "Method for solving robot workspace based on MATLAB," *Mechanical Science and Technology for Aerospace Engineering*, vol. 28, no. 12, pp. 1657–1661, 2009.
- [17] Y. D. Zhang, X. S. Dai, and S. J. Guo, "Preliminary study of the robotic couch for prostate cancer in proton/heavy radiotherapy," in *International Conference on Biological Information and Biomedical Engineering, IEEE*, Shanghai, 2018.
- [18] S.-w. Hsiao, F.-y. Chiu, and C. S. Chen, "Applying aesthetics measurement to product design," *International Journal of Industrial Ergonomics*, vol. 38, no. 11–12, pp. 910–920, 2008.
- [19] A. Sonderegger and J. Sauer, "The influence of design aesthetics in usability testing: effects on user performance and perceived usability," *Applied Ergonomics*, vol. 41, no. 3, pp. 403–410, 2010.
- [20] D. B. Chaffin, "Improving digital human modelling for proactive ergonomics in design," *Ergonomics*, vol. 48, no. 5, pp. 478–491, 2005.
- [21] V. S. Conn, A. R. Hafdahl, P. S. Cooper, L. M. Brown, and S. L. Lusk, "Meta-analysis of workplace physical activity interventions," *American Journal of Preventive Medicine*, vol. 37, no. 4, pp. 330–339, 2009.

Research Article

Human Gait Analysis Metric for Gait Retraining

Tyagi Ramakrishnan, Seok Hun Kim, and Kyle B. Reed 

University of South Florida, USA

Correspondence should be addressed to Kyle B. Reed; kylereed@usf.edu

Received 19 April 2019; Revised 25 July 2019; Accepted 10 September 2019; Published 11 November 2019

Guest Editor: Michelle Johnson

Copyright © 2019 Tyagi Ramakrishnan et al. This is an open access article distributed under the Creative Commons Attribution License, which permits unrestricted use, distribution, and reproduction in any medium, provided the original work is properly cited.

The combined gait asymmetry metric (CGAM) provides a method to synthesize human gait motion. The metric is weighted to balance each parameter's effect by normalizing the data so all parameters are more equally weighted. It is designed to combine spatial, temporal, kinematic, and kinetic gait parameter asymmetries. It can also combine subsets of the different gait parameters to provide a more thorough analysis. The single number quantifying gait could assist robotic rehabilitation methods to optimize the resulting gait patterns. CGAM will help define quantitative thresholds for achievable balanced overall gait asymmetry. The study presented here compares the combined gait parameters with clinical measures such as timed up and go (TUG), six-minute walk test (6MWT), and gait velocity. The comparisons are made on gait data collected on individuals with stroke before and after twelve sessions of rehabilitation. Step length, step time, and swing time showed a strong correlation to CGAM, but the double limb support asymmetry has nearly no correlation with CGAM and ground reaction force asymmetry has a weak correlation. The CGAM scores were moderately correlated with TUG and strongly correlated to 6MWT and gait velocity.

1. Introduction

Researchers traditionally analyze a small set of gait parameters in order to evaluate the outcomes of their techniques. This often leads to an overreliance on a few parameters and a focus on improving one gait parameter. Few studies in the gait literature aim to correct many gait parameters at the same time. This traditional narrow approach lacks broader understanding of the interaction between various gait parameters and limits potential approaches that can lead to whole-some rehabilitation techniques. In this research study, we examine our combined gait asymmetry metric (CGAM) to give a representation of the overall gait pattern. We use stroke for examining this combined metric because it affects several different aspects of an individual's gait, and many of these aspects are asymmetric. Although we focus on measures of asymmetry, this combined method is not limited by the type or number of parameters evaluated. Our hypothesis is that the outcomes of the combined metric will partially correlate to functional clinical outcome measures. We also use this combined metric to determine if there have been

changes to the individual's gait pattern from baseline to after the clinical intervention.

Figure 1 shows an example of how a combined metric would be useful in analyzing an asymmetric gait pattern. Many existing rehabilitation therapies can change different sets of gait parameters, but some make one parameter worse while correcting others. Even in unimpaired walking, perfect symmetry is not expected [1], so there is space for some parameters to be asymmetric while the overall gait is within a reasonable bound. The CGAM distance (shown in orange in Figure 1) generates a single representation of the measured gait parameters that generally scales with the global deviation from symmetry. The deviation of each measure is scaled based on the variance within that measure, so measures that generally have larger magnitudes of asymmetry (e.g., forces) will be scaled so that each gait parameter has a similar influence on the overall metric. If a therapy reduces the CGAM distance, the overall gait has improved even though some of the individual parameters might have gotten worse. Without a combined metric, it is difficult to determine whether the gait is improving when looking at individual gait parameters.

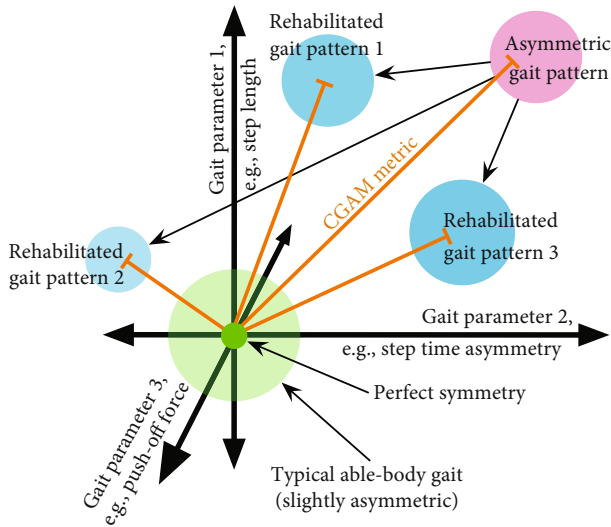


FIGURE 1: Representation of the multidimensional gait parameter space. The orange lines represent the distance each gait is from a symmetric gait (CGAM distance), which helps determine how far away a gait is from ideal. CGAM can also aid in ascertaining whether the overall gait pattern is improving (even if some of the parameters are getting worse). CGAM can incorporate more dimensions than the three shown, but that is hard to visualize.

1.1. Gait Measurements. Gait data is typically collected using motion capture, force plates, and/or wearable sensors. Many variables portray various facets of human gait. There are spatial parameters such as step length defined by the distance covered from the heel strike of one foot to the heel strike of the opposite foot. There are temporal parameters such as step time defined as the time taken between opposite heel strikes. Then, there is swing time, which is the time taken from toe-off to heel strike of the same foot. Double limb support is the time spent when both legs are on the ground. The terminal double limb support is used for this research study. There are kinematic parameters associated with joint angles of the ankle, knee, and hip joints. Hip joints in the case of individuals with stroke and amputees also show abduction and adduction. The kinetic parameters include vertical ground reaction forces, propulsive or push-off forces during toe-off, braking forces during initial contact or heel strike, and ankle, knee, and hip joint moments. Further, some of these parameters are more easily identified by sight alone (e.g., step length, cadence, and gait velocity) while others are nearly impossible to quantify without a sensor (e.g., forces and joint moments) [2].

1.2. Gait Metrics. Several gait metrics combining multiple gait parameters have been used clinically to evaluate different gait impairments. These metrics can also be used to classify gait based on different types of information. There are two types: qualitative [3, 4] and quantitative [5–7] metrics. Many metrics rely on either kinetic or kinematic data to categorize different gait motions and behaviors. Some metrics have the ability to jointly analyze kinetic and kinematic parameters [8, 9]. Machine learning has been used to classify and differentiate gait patterns [10]. Most gait metrics use statistical

analysis like principle component analysis (PCA) and singular variable decomposition (SVD) to reduce dimensionality to make the data computation easier [11]. The processed data is then classified using the Euclidean or similar distances [11]. These distances become the scores which form the central part of the gait metric. Another study by Hoerzer et al. [9] proposed the comprehensive asymmetry index (CAI) which combined gait asymmetry using PCA and Euclidean distances. CAI was effective in identifying that running with shoes reduces gait asymmetry compared to barefoot running. A prior study used a combination of Mahalanobis distances with data reduction techniques on a preprocessed dataset to analyze kinematic and kinetic gait parameters [8]. They developed several metrics to classify the data and showed that they can successfully classify the abnormal data from a standard normal dataset. The precursor to CGAM used a symmetry index processed using PCA measured using Mahalanobis distances. Without the restrictions of dimensionality reduction, CGAM served as a versatile gait asymmetry metric [12–14].

1.3. Effects of Stroke on Gait and Rehabilitation. The analysis in this paper uses an existing dataset from an experimental stroke therapy to examine the effects of combining and jointly assessing gait as opposed to individually assessing a single parameter. We focus on individuals with stroke because they inherently have different capabilities on each side and are asymmetric; as such, it is unlikely that they can ever regain complete symmetry in all parameters. However, it may be possible to achieve a balanced gait where some parameters are slightly asymmetric, but none of them are excessively large. Our proposed joint metric helps to balance all of the parameters. We examine before and after the therapy to help understand what changes have occurred.

Gait after stroke becomes asymmetric (or hemiparetic) as a consequence of altered neuromuscular signals affecting leg motor areas, typically hyperextension at the knee and reduced flexion at the hip, knee, and ankle [15–17]. Hemiparetic gait is characterized by significant asymmetry in temporal (e.g., time spent in double limb support) and spatial (e.g., step length) measures of interlimb coordination [15, 18, 19]. Propulsive force of the paretic limb is reduced compared to the nonparetic limb, as are work and power of the paretic plantar flexors [19, 20]. The significant decrease in propulsive force results in smaller overall step lengths, which in turn affects the patient’s gait velocity. Finally, vertical ground reaction forces (GRFs) are decreased on the paretic limb relative to the nonparetic limb [21], reflecting diminished weight bearing and balancing capabilities by the paretic limb.

Some of the rehabilitation techniques used to restore gait impaired by stroke involve some form of asymmetric perturbations that try to restore the symmetry between the paretic and nonparetic sides [22]. Split-belt treadmills are one method to apply this rehabilitation technique. The split-belt treadmill has two treads that can move at different velocities, which are used to exaggerate the asymmetry of the individual. When the tread speeds are made the same after training, the subject typically has some after-effects that are more

symmetric than when they started [23]. The after-effects are usually improved spatial and temporal symmetry. Unfortunately, these after-effects only partially transfer to walking on the ground. There are other rehabilitation techniques such as body-weight support [24], robotic [25], functional electrical stimulation [26], transcranial magnetic stimulation [27], and full-body gait exoskeletons [28]. Each of the techniques have their merits and train the individual in a specialized manner, which means a combination of these methods may provide additional benefits to the person.

2. CGAM Derivation

The metric presented here has the potential to help categorize and differentiate between multiple asymmetric gaits [29]. CGAM is based on Mahalanobis distances, and it utilizes the asymmetries of gait parameters obtained from data recorded during human walking. The gait parameters that were used in this analysis represent spatial, temporal, and kinetic parameters. This form of a consolidated metric will help researchers identify overall gait asymmetry and improve rehabilitation techniques to provide a well-rounded gait post training. The CGAM metric successfully served as a measure for overall symmetry with 11 different gait parameters and successfully showed differences among gait with multiple physical asymmetries [14]. The mass at the distal end had a larger magnitude on overall gait asymmetry compared to leg length discrepancy. Combined effects are varied based on the cancellation effect between gait parameters [13]. The metric was successful in delineating the differences of prosthetic gait and able-bodied gait at three different walking velocities [14].

Symmetry is calculated using equation (1) where M is the step length, step time, swing time, double limb support (DLS), and ground reaction forces (GRFs). A value of 0 indicates symmetry. The measures include gait evaluations conducted before training and after the completion of training.

$$\text{Symmetry} = 100 * \frac{\text{abs}(M_{\text{paretic}} - M_{\text{nonparetic}})}{0.5 * (M_{\text{paretic}} + M_{\text{nonparetic}})}, \quad (1)$$

$$\text{Modified CGAM} = \sqrt{\frac{\text{Data} * \text{inv}(\Sigma) * \text{Data}'}{\sum(\text{inv}(\Sigma))}}, \quad (2)$$

where

- (i) Modified CGAM distance: weighted distance from ideal symmetry
- (ii) CGAM distance: Mahalanobis distance from ideal symmetry
- (iii) Data: matrix with n columns (11) and m rows (number of steps)
- (iv) Σ : covariance of the data

The modified CGAM [30] works similar to weighted means, but, in this case, the weights are inverse covariances

that are multiplied across the dataset in the numerator. To balance the influence of the inverse of covariance, it is divided by the sum of the inverse covariance matrix, equation (2). This change to the formulation makes the modified CGAM represent the scores closer to the percent asymmetry while still serving as a combined measure of all the gait parameter asymmetries.

3. Methods

The analysis performed in this paper used data collected as part of a separate clinical study. The novel shoe tested was designed to improve the overall gait symmetry and gait function of an individual poststroke. The efficacy of the device is discussed in another paper [31]. That study data is used here so we can evaluate the modified CGAM in the context of a rehabilitation therapy. This study aims to understand how the modified CGAM metric can be used to evaluate the gait of individuals with stroke. The study data consists of six subjects who trained on the device for four weeks. Gait parameters and functional clinical measures were collected throughout the training and used in the modified CGAM analysis presented here.

3.1. Subjects. All subjects agreed to participate in this study and signed a consent form that was approved by the Western Institutional Review Board. Six subjects (4 males and 2 females), aged 57–74 years old with unilateral stroke, completed the training, and the length of time since stroke ranged from 1.2 to 12.5 years. Subject 3 was an outlier and excluded in some of the analyses. At baseline, his double limb support asymmetry was 34 standard deviations above the other subjects' mean and timed up and go (TUG) score was 36 standard deviations above the other subjects' mean.

3.2. Device Used for Gait Training. The device, shown in Figure 2, is designed to change interlimb coordination and strengthen the paretic leg of individuals with asymmetric walking patterns caused by stroke. The concept of this device is similar to that of a split-belt treadmill [32] but allows the individual to walk over ground, which is hypothesized to help with long-term retention of the altered gait pattern [33]. The device is completely passive and uses spiral-like (nonconstant radius) wheels [34], which redirect the downward force generated during walking into a backward force that generates a consistent motion. By not utilizing actuators and fabricating the shoe using rapid manufactured glass-filled nylon, the version used in this study weighs approximately 900 g. Small unidirectional dampers on the front and back axles prevent uncontrolled motions. After the shoe stops moving backward, the user pushes off, and springs attached to the axles reset the position of the wheels for the next step. The front of the device is able to pivot to more naturally conform to the user's toe-off.

3.3. Experiment Procedure. Before training, the subject's gait patterns were evaluated using a ProtoKinetics Zeno Walkway (ProtoKinetics, Havertown, PA). They then completed four weeks of training three times a week under the guidance of a physical therapist. Each of the twelve sessions included six

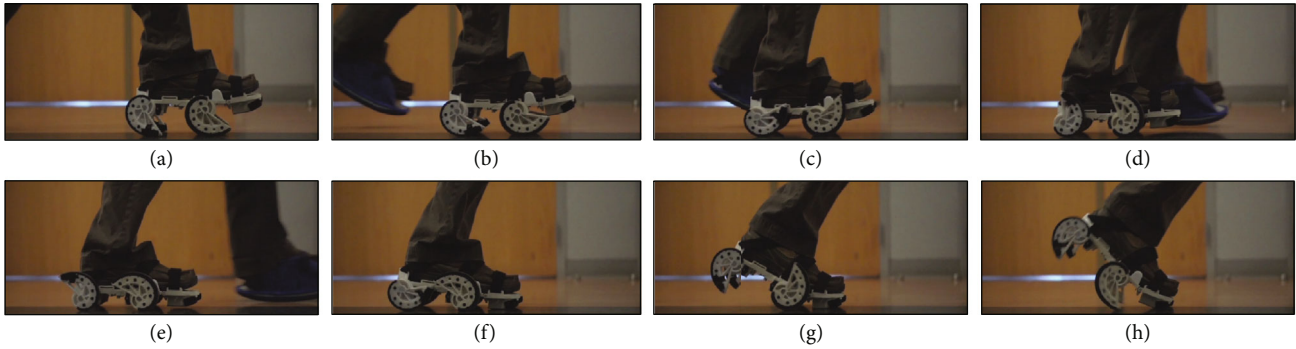


FIGURE 2: As the wearer takes a step, the device pushes the foot backward during stance. This exaggeration of the asymmetry results in a more symmetric gait pattern once the shoe is removed. In addition, the shoe works to strengthen the paretic leg by slightly destabilizing the nonparetic leg, which encourages the wearer to use their paretic leg more. A flexible height- and weight-matched platform worn on the opposite foot equalizes the added height and weight of the device.

bouts of walking for five minutes on the device with about a two-minute break between bouts. The device was attached to the subject's nonparetic foot during training. The subject's gait without the device was measured on the ProtoKinetics Zenon Walkway before the training began [35]; this data will be referred to henceforth as pretest. Gait data was also collected on the walkway prior to the second, third, and fourth week of training sessions; this data will be referred to as midtest. Their gait was tested again within five days after the completion of the training protocol on the walkway; this data will be referred to as post test. Clinical measures included TUG [36], six-minute walk test (6MWT) [37], and gait velocity.

3.4. Data Analysis. The modified CGAM scores for all the trials were calculated using spatial, temporal, and kinetic parameter asymmetries. The R -squared (r^2) was used to assess the correlations between the modified CGAM scores and clinical measures. The correlations between the clinical measures and individual gait parameters were also analyzed using r^2 . The strength of correlation was evaluated based on the absolute value of r as reported by Swinscow et al. [38] where $r = 0.4$ and above is moderate or strong correlation.

4. Results

The individual gait parameter asymmetries are shown in Figure 3 for reference. Details related to the results from the clinical trial are presented in another paper [31]. The below results focus on the modified CGAM.

Table 1 shows the correlation values between the pre- and post test data of each gait parameter for all subjects correlated with the corresponding modified CGAM scores. The pre- and post test performance is important clinically; however it is also important to analyze the correlation for all the midtest data points for the gait parameters, so both time frames are shown. It is interesting to note that step length, step time, and swing time show consistently very strong correlation to the modified CGAM while double limb support asymmetry shows a very weak correlation. The correlations between step length, step time, swing time, and double limb support remain consistent between the pre-/post comparison

and data from all weeks. The ground reaction force has a stronger correlation for all midtests compared to just the pre- and post tests.

Table 2 shows the complete list of r^2 values comparing the gait parameters and modified CGAM to the functional gait measures. Modified CGAM scores show a moderate correlation to TUG and strong correlations with 6MWT and gait velocity. Step time and swing time asymmetries show a similar pattern of correlation as the modified CGAM does. TUG shows a moderate correlation to step time, swing time, and ground reaction force asymmetries, but weak and very weak correlations to step length and double limb support asymmetries, respectively. The 6MWT and gait velocity show moderate correlations to step length asymmetry and strong correlations to step time and swing time asymmetries, but weak correlations to double limb support and ground reaction force asymmetries.

5. Discussion

Comparing the behavior of the gait parameters helps understand the relationship between the gait asymmetries and also evaluates the hypothesis that there exists a balance of asymmetry between gait parameters. For example, most subjects in midtest 1 show a decrease in spatial and temporal asymmetry but have increases in ground reaction force asymmetry. The reverse is observed in midtest 2 where most subjects have decreased ground reaction force but increased spatial and temporal asymmetry. Not all subjects display the same changes, but this highlights the difficulty of determining if the overall gait improved or not since improving one gait parameter may come partially at the expense of making another gait parameter worse. People with hemiparesis due to stroke have different force and motion capabilities on each leg. The paretic leg is weaker and has a more limited range of motion than the nonparetic leg. Rehabilitation science has not advanced to the point where these problems can be fully corrected. Therefore, when we are retraining walking poststroke, we are working with an inherently asymmetric system. From a biomechanical view, two physically different systems (e.g., legs) can only have the same motion if the forces controlling them or the forces resulting from the

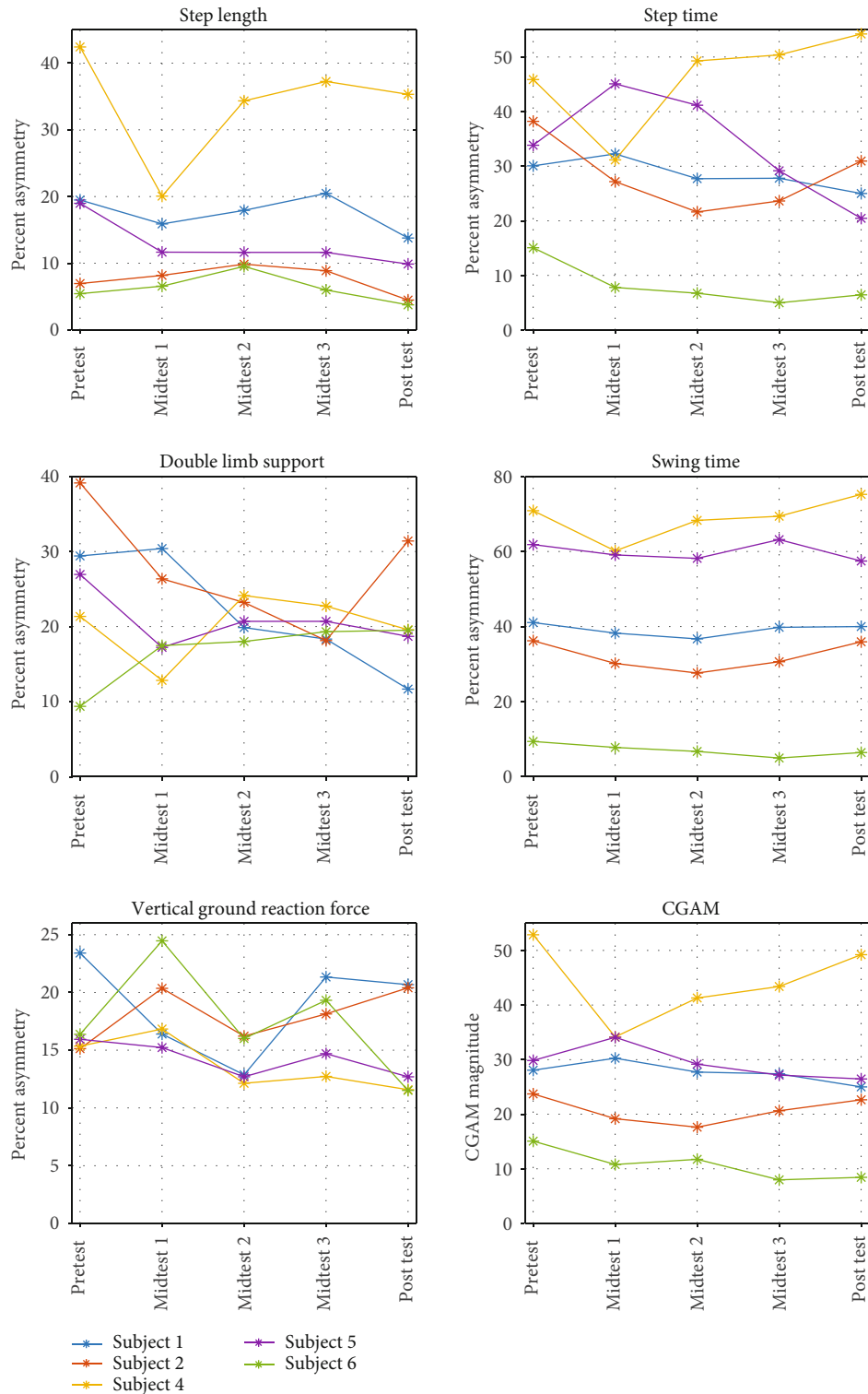


FIGURE 3: Gait parameter asymmetry.

movement are different. When an individual with an asymmetric impairment walks with symmetric step lengths, other aspects of gait become asymmetric, such as the forces in the joints [39, 40], the amount of time standing on each leg [21], and other temporal variables [41, 42], all of which can be detrimental to efficiency and long-term viability.

All subjects decreased the modified CGAM score, which indicates that their overall gait improved. This does not mean that every gait parameter improved. For example, subject 2 had slightly worse swing time and vertical ground reaction force asymmetries and subject 4 had slightly worse step time and swing time asymmetries during the post test compared

TABLE 1: Correlation (r^2) between modified CGAM and gait parameters.

Gait parameter (asymmetry)	Modified CGAM (pre & post)	Modified CGAM (all midtests)
Step length	0.93	0.81
Step time	0.95	0.88
Swing time	0.98	0.89
Double limb support	0.01	0.01
Ground reaction force	0.03	0.18

Bold implies correlation that is moderate or above.

TABLE 2: Correlation (r^2) between clinical measures and gait parameters.

Gait parameter	TUG	6MWT	Gait velocity
Step length asymmetry	0.14	0.21	0.31
Step time asymmetry	0.23	0.53	0.63
Swing time asymmetry	0.29	0.43	0.57
Double limb support asymmetry	0.03	0.14	0.10
Ground reaction force asymmetry	0.26	0.14	0.13
Modified CGAM	0.22	0.41	0.51

Bold implies correlation that is moderate or above.

to the pretest. But, the other gait parameters improved such that the end result was an overall better gait pattern. This suggests that there can be a functional balance between all the gait parameters. Although the resulting gait will have some degree of asymmetry in all measures, it will more likely meet the functional walking goals of individuals with asymmetric impairments.

The modified CGAM can be calculated using any number of input gait parameters. Including more should give a better indication of the overall gait, but care should be given to including a range of different types of parameters like forces, spatial, and temporal parameters. Also of note is that the specific score of modified CGAM with one set of parameters is not directly comparable to modified CGAM computed with a different set of parameters. So, modified CGAM can be very helpful for looking at changes within a study but may not always provide a comparison between studies if the measured parameters are different.

Modified CGAM shows a strong correlation with step length, step time, and swing time. This was consistent when only the pre- and post test data were considered or when all test data including pre- and post tests were analyzed. This means that these three parameters have similar behaviors to their modified CGAM scores while double limb support and ground reaction force asymmetry have more variation in the data.

The modified CGAM scores calculated using the spatial, temporal, and kinetic parameters showed behaviors similar to some of the underlying gait parameter asymmetries (see Figure 3) and also some of the functional measures. Although it would be expected to have some correlation

to the underlying parameters, having moderate to strong correlation with the functional measures shows evidence that a measure of overall symmetry which is used as factor for gait quality is related to gait function signified by gait velocity and 6MWT. These findings also offer some evidence to validate the modified CGAM metric.

6. Conclusions

To summarize, the research suggests that rehabilitating gait asymmetries should be a holistic approach. Targeting certain types of asymmetry may not be the correct approach as it may adversely affect other gait parameters that may lead to pervasive long-term effects. The modified CGAM metric showed potential for being used as a quantitative metric for impairments that cause gait asymmetries. Further, the research suggests that it is important to consider quantitative metrics such as modified CGAM and subjective metrics such as pain and quality of life data to evaluate overall improvement of an individual's gait. The simple asymmetric perturbations applied on the gait patterns showed that it is possible to combat the negative effects of asymmetric impairment with asymmetry. To tackle these problems, this research has shown that quantitative metrics along with clinical evaluation offer a good direction in evaluating and rehabilitating asymmetric gait patterns.

Data Availability

The data used to support the findings of this study are available from the corresponding author upon request.

Conflicts of Interest

K. B. Reed has a licensed patent (US 9,295,302) related to the rehabilitation device used in this work. A management plan has been implemented and followed to reduce any effects of this conflict of interest.

Acknowledgments

Portions of this work have been published in Ramakrishnan's PhD dissertation [29]. Funding for this research has been provided by the Florida High Tech Corridor. This material is based upon work supported by the USA National Science Foundation under Grant Number IIS-1910434.

References

- [1] J. B. Dingwell and B. L. Davis, "A rehabilitation treadmill with software for providing real-time gait analysis and visual feedback," *Journal of Biomechanical Engineering*, vol. 118, no. 2, pp. 253–255, 1996.
- [2] I. Handžić and K. B. Reed, "Perception of gait patterns that deviate from normal and symmetric biped locomotion," *Frontiers in Psychology*, vol. 6, p. 199, 2015.
- [3] D. M. Wrisley, G. F. Marchetti, D. K. Kuharsky, and S. L. Whitney, "Reliability, internal consistency, and validity of data obtained with the functional gait assessment," *Physical Therapy*, vol. 82, no. 10, pp. 906–918, 2004.

- [4] J. McConvey and S. E. Bennett, "Reliability of the dynamic gait index in individuals with multiple sclerosis," *Archives of Physical Medicine and Rehabilitation*, vol. 86, no. 1, pp. 130–133, 2005.
- [5] L. M. Schutte, U. Narayanan, J. L. Stout, P. Selber, J. R. Gage, and M. H. Schwartz, "An index for quantifying deviations from normal gait," *Gait & Posture*, vol. 11, no. 1, pp. 25–31, 2000.
- [6] M. H. Schwartz and A. Rozumalski, "The gait deviation index: a new comprehensive index of gait pathology," *Gait & Posture*, vol. 28, no. 3, pp. 351–357, 2008.
- [7] A. Rozumalski and M. H. Schwartz, "The GDI-kinetic: a new index for quantifying kinetic deviations from normal gait," *Gait & Posture*, vol. 33, no. 4, pp. 730–732, 2011.
- [8] V. L. Chester, M. Tingley, and E. N. Biden, "An extended index to quantify normality of gait in children," *Gait & Posture*, vol. 25, no. 4, pp. 549–554, 2007.
- [9] S. Hoerzer, P. A. Federolf, C. Maurer, J. Baltich, and B. M. Nigg, "Footwear decreases gait asymmetry during running," *PLoS One*, vol. 10, no. 10, article e0138631, 2015.
- [10] M. Schlafly, Y. Yilmaz, and K. B. Reed, "Feature selection in gait classification of leg length and distal mass," *Informatics in Medicine Unlocked*, vol. 15, p. 100163, 2019.
- [11] A. M. S. Muniz and J. Nadal, "Application of principal component analysis in vertical ground reaction force to discriminate normal and abnormal gait," *Gait & Posture*, vol. 29, no. 1, pp. 31–35, 2009.
- [12] T. Ramakrishnan, M. Schlafly, and K. B. Reed, "Effect of asymmetric knee height on gait asymmetry for unilateral transfemoral amputees," *International Journal of Current Advanced Research*, vol. 6, no. 10, p. 6896, 2017.
- [13] H. Muratagic, T. Ramakrishnan, and K. B. Reed, "Combined effects of leg length discrepancy and the addition of distal mass on gait asymmetry," *Gait & Posture*, vol. 58, article S0966636217309086, pp. 487–492, 2017.
- [14] T. Ramakrishnan, C.-A. Lahiff, and K. B. Reed, "Comparing gait with multiple physical asymmetries using consolidated metrics," *Frontiers in Neurorobotics*, vol. 12, p. 2, 2018.
- [15] M. Brandstater, H. de Bruin, C. Gowland, and B. Clark, "Hemiplegic gait: analysis of temporal variables," *Archives of Physical Medicine and Rehabilitation*, vol. 64, no. 12, pp. 583–587, 1983.
- [16] M. Kelly-Hayes, A. Beiser, C. S. Kase, A. Scaramucci, R. B. D'Agostino, and P. A. Wolf, "The influence of gender and age on disability following ischemic stroke: the Framingham study," *Journal of Stroke and Cerebrovascular Diseases*, vol. 12, no. 3, pp. 119–126, 2003.
- [17] J. C. Wall and G. I. Turnbull, "Gait asymmetries in residual hemiplegia," *Archives of Physical Medicine and Rehabilitation*, vol. 67, no. 8, pp. 550–553, 1986.
- [18] E. B. Titianova and I. M. Tarkka, "Asymmetry in walking performance and postural sway in patients with chronic unilateral cerebral infarction," *Journal of Rehabilitation Research and Development*, vol. 32, pp. 236–244, 1995.
- [19] C. K. Balasubramanian, M. G. Bowden, R. R. Neptune, and S. A. Kautz, "Relationship between step length asymmetry and walking performance in subjects with chronic hemiparesis," *Archives of Physical Medicine and Rehabilitation*, vol. 88, no. 1, pp. 43–49, 2007.
- [20] M. G. Bowden, C. K. Balasubramanian, R. R. Neptune, and S. A. Kautz, "Anterior-posterior ground reaction forces as a measure of paretic leg contribution in hemiparetic walking," *Stroke*, vol. 37, no. 3, pp. 872–876, 2006.
- [21] C. M. Kim and J. J. Eng, "Symmetry in vertical ground reaction force is accompanied by symmetry in temporal but not distance variables of gait in persons with stroke," *Gait & Posture*, vol. 18, no. 1, pp. 23–28, 2003.
- [22] D. S. Reisman, H. McLean, and A. J. Bastian, "Split-belt treadmill training post-stroke: a case study," *Journal of Neurologic Physical Therapy*, vol. 34, no. 4, pp. 202–207, 2010.
- [23] D. S. Reisman, R. Wityk, K. Silver, and A. J. Bastian, "Split-belt treadmill adaptation transfers to overground walking in persons poststroke," *Neurorehabilitation and Neural Repair*, vol. 23, no. 7, pp. 735–744, 2009.
- [24] J. Mehrholz, S. Thomas, and B. Elsner, "Treadmill training and body weight support for walking after stroke," *Cochrane Database of Systematic Reviews*, vol. 2017, no. 8, article CD002840, 2017.
- [25] P.-C. Kao, S. Srivastava, S. K. Agrawal, and J. P. Scholz, "Effect of robotic performance-based error-augmentation versus error-reduction training on the gait of healthy individuals," *Gait & Posture*, vol. 37, no. 1, pp. 113–120, 2013.
- [26] J. J. Daly, J. Zimbelman, K. L. Roenigk et al., "Recovery of coordinated gait: randomized controlled stroke trial of functional electrical stimulation (fes) versus no fes, with weight-supported treadmill and over-ground training," *Neurorehabilitation and Neural Repair*, vol. 25, no. 7, pp. 588–596, 2011.
- [27] R.-Y. Wang, F.-Y. Wang, S.-F. Huang, and Y.-R. Yang, "High-frequency repetitive transcranial magnetic stimulation enhanced treadmill training effects on gait performance in individuals with chronic stroke: a double-blinded randomized controlled pilot trial," *Gait & Posture*, vol. 68, pp. 382–387, 2019.
- [28] P. Cheng and P. Lai, "Comparison of exoskeleton robots and end-effector robots on training methods and gait biomechanics," in *International Conference on Intelligent Robotics and Applications*, pp. 258–266, Springer, 2013.
- [29] T. Ramakrishnan, *Rehabilitating asymmetric gait using asymmetry*, [Ph.D. thesis], University of South Florida library, Tampa, FL, USA, 2017.
- [30] T. Ramakrishnan, H. Muratagic, and K. B. Reed, "Combined gait asymmetry metric," in *2016 38th Annual International Conference of the IEEE Engineering in Medicine and Biology Society (EMBC)*, Orlando, FL, USA, August 2016.
- [31] S. H. Kim, D. E. Huizenga, I. Handzic et al., "Relearning functional and symmetric walking after stroke using a wearable device: a feasibility study," *Journal of Neuroengineering and Rehabilitation*, vol. 16, no. 1, pp. 1–8, 2019.
- [32] D. S. Reisman and A. J. Bastian, "Split-belt treadmill adaptation and GAIT SYMMETRY post-stroke," *Journal of Neurologic Physical Therapy*, vol. 29, no. 4, p. 196, 2005.
- [33] I. Handzic, E. Vasudevan, and K. B. Reed, "Developing a gait enhancing mobile shoe to alter over-ground walking coordination," in *2012 IEEE International Conference on Robotics and Automation*, pp. 4129–4142, Saint Paul, MN, USA, May 2012.
- [34] I. Handzic and K. B. Reed, "Kinetic shapes: analysis, verification, and applications," *Journal of Mechanical Design*, vol. 136, no. 6, article 061005, pp. 0610051–0610058, 2014.
- [35] R. C. Lynall, L. A. Zukowski, P. Plummer, and J. P. Mihalik, "Reliability and validity of the protokinetics movement

- analysis software in measuring center of pressure during walking,” *Gait & Posture*, vol. 52, article S0966636216307111, pp. 308–311, 2017.
- [36] S. S. Ng and C. W. Hui-Chan, “The timed up & go test: its reliability and association with lower-limb impairments and locomotor capacities in people with chronic stroke,” *Archives of Physical Medicine and Rehabilitation*, vol. 86, no. 8, pp. 1641–1647, 2005.
- [37] P. S. Pohl, P. W. Duncan, S. Perera et al., “Influence of stroke-related impairments on performance in 6-minute walk test,” *Journal of Rehabilitation Research and Development*, vol. 39, no. 4, pp. 439–444, 2002.
- [38] T. D. V. Swinscow and M. J. Campbell, *Statistics at square one*, BMJ, London, 2002.
- [39] F. P. Carpes, C. B. Mota, and I. E. Faria, “On the bilateral asymmetry during running and cycling - A review considering leg preference,” *Physical Therapy in Sport*, vol. 11, no. 4, pp. 136–142, 2010.
- [40] I. Handzic, H. Muratagic, and K. Reed, “Passive kinematic synchronization of dissimilar and uncoupled rotating systems,” *Nonlinear Dynamics and Systems Theory*, vol. 15, pp. 383–399, 2015.
- [41] H. Sadeghi, P. Allard, F. Prince, and H. Labelle, “Symmetry and limb dominance in able-bodied gait: a review,” *Gait & Posture*, vol. 12, no. 1, pp. 34–45, 2000.
- [42] M. J. Highsmith, J. T. Kahle, S. L. Carey et al., “Kinetic asymmetry in transfemoral amputees while performing sit to stand and stand to sit movements,” *Gait & Posture*, vol. 34, no. 1, pp. 86–91, 2011.

Research Article

Kinematic Parameters for Tracking Patient Progress during Upper Limb Robot-Assisted Rehabilitation: An Observational Study on Subacute Stroke Subjects

Michela Goffredo ¹, Stefano Mazzoleni ^{2,3}, Annalisa Gison, ¹ Francesco Infarinato ¹, Sanaz Pournajaf, ¹ Daniele Galafate, ¹ Maurizio Agosti, ⁴ Federico Posteraro ⁵, and Marco Franceschini^{1,6}

¹Department of Neurorehabilitation, IRCCS San Raffaele Pisana, Rome, Italy

²The BioRobotics Institute, Scuola Superiore Sant'Anna, Pisa, Italy

³Rehabilitation Bioengineering Laboratory, Volterra, Italy

⁴Rehabilitation Medicine Service, NHS-University Hospital of Parma, Parma, Italy

⁵Rehabilitation Department, Versilia Hospital, AUSL Tuscany North West, Camaiore, Italy

⁶San Raffaele University, Rome, Italy

Correspondence should be addressed to Michela Goffredo; michela.goffredo@sanraffaele.it

Received 3 April 2019; Revised 2 August 2019; Accepted 14 August 2019; Published 21 October 2019

Guest Editor: Francesca Cordella

Copyright © 2019 Michela Goffredo et al. This is an open access article distributed under the Creative Commons Attribution License, which permits unrestricted use, distribution, and reproduction in any medium, provided the original work is properly cited.

Background. Upper limb robot-assisted therapy (RT) provides intensive, repetitive, and task-specific treatment, and its efficacy for stroke survivors is well established in literature. Biomechanical data from robotic devices has been widely employed for patient's assessment, but rarely it has been analysed for tracking patient progress during RT. The goal of this retrospective study is to analyse built-in kinematic data registered by a planar end-effector robot for assessing the time course of motor recovery and patient's workspace exploration skills. A comparison of subjects having mild and severe motor impairment has been also conducted. For that purpose, kinematic data recorded by a planar end-effector robot have been processed for investigating how motor performance in executing point-to-point trajectories with different directions changes during RT. **Methods.** Observational retrospective study of 68 subacute stroke patients who conducted 20 daily sessions of upper limb RT with the InMotion 2.0 (Bionik Laboratories, USA): planar point-to-point reaching tasks with an "assist as needed" strategy. The following kinematic parameters (KPs) were computed for each subject and for each point-to-point trajectory executed during RT: movement accuracy, movement speed, number of peak speed, and task completion time. The Wilcoxon signed-rank tests were used with clinical outcomes. the Friedman test and post hoc Conover's test (Bonferroni's correction) were applied to KPs. A secondary data analysis has been conducted by comparing patients having different severities of motor impairment. The level of significance was set at p value < 0.05 . **Results.** At the RT onset, the movements were less accurate and smoothed, and showed higher times of execution than those executed at the end of treatment. The analysis of the time course of KPs highlighted that RT seems to improve the motor function mainly in the first sessions of treatment: most KPs show significant intersession differences during the first 5/10 sessions. Afterwards, no further significant variations occurred. The ability to perform movements away from the body and from the hemiparetic side remains more challenging. The results obtained from the data stratification show significant differences between subjects with mild and severe motor impairment. **Conclusion.** Significant improvements in motor performance were registered during the time course of upper limb RT in subacute stroke patients. The outcomes depend on movement direction and motor impairment and pave the way to optimize healthcare resources and to design patient-tailored rehabilitative protocols.

1. Introduction

The recovery of upper limb motor impairment after stroke requires prolonged periods of rehabilitation treatment, even if started at an early stage, and the prognosis for functional recovery is often worse than that of lower extremities. The functional recovery process requires a complex integration of muscle activities involving proximal and distal regions of the upper limb, and the execution of movements away from the body and from the hemiparetic side is usually rather challenging [1]. Published studies suggest that there is a highly predictable poor outcome for the return of isolated arm or hand movements 6 months after stroke on the basis of the Fugl-Meyer motor scores [2, 3]. Furthermore, upper limb functional impairment occurs in up to 85% of stroke survivors with a significant long-term impact on activities of daily living (ADLs) and quality of life [4]. Since stroke rehabilitation is often described as a process of active motor relearning, motor task repetition and intensity of the treatment can play an important role in rehabilitation, since they promote neuroplasticity and improve the functional outcome [5, 6].

Robot-assisted therapy (RT) is able to provide high-intensive, repetitive, task-specific, and interactive treatment of the impaired upper limb. In addition, RT is a safe, reproducible, and customizable rehabilitation treatment for promoting the motor learning [7–9]. The efficacy of poststroke RT in improving motor and functional outcomes, and the acceptability are well established in literature [10–13].

Clinical studies on RT usually assess patient's motor ability with a traditional approach based on ordinal measurement scales, which are administered to patients at the beginning and at the end of the period of treatment [11]. However, robotic devices not only provide an assisted upper limb mobilisation but also include sensors that gather biomechanical data during the therapy with a high level of resolution and accuracy [14, 15]. Therefore, robots for rehabilitation provide objective built-in data that can be used to derive measures related to subject's motor impairment. Such movement-related measures allow to quantitatively and ecologically track patient progress over a period of time, providing clinicians greater insight into how components of motor control and coordination change day-by-day with recovery [16–18].

In poststroke upper limb RT, built-in measures have been widely employed for a quantitative patient's assessment [19–38], and they have been classified into kinematic parameters, kinetic parameters, and neuromechanical parameters [16]. A recent review by Tran et al. [39] associated the kinematic parameters (KPs) to the International Classification of Functioning, Disability and Health (ICF) domains. The KPs have been moderately correlated to clinical outcome measures [15, 20, 24] and their validity and reliability have been established [40–42]. However, the majority of published studies employed KPs for assessing patient's status only at the beginning and at the end of the period of treatment [19–24, 26, 35–37]. However, robots for rehabilitation register data during each session of RT and thus allow day-to-day tracking of motor performance [16–18]. Some studies proposed mathematical approaches for modelling the temporal

evolution of KPs during RT [25, 28–30, 32–34, 38], which the aim of deeper understanding of the functional and physiological mechanisms underlying the time course of recovery. These models are generally based on the analysis of the overall end-effector trajectory, although it was composed by as set of point-to-point movements having different directions in the workplace. To our knowledge, only Panarese et al. [30] analysed the submovements, each in a different direction, finding that motor recovery was direction-dependent. Other published studies are aimed at understanding whether built-in movement measures could be employed in clinical practice for optimizing the length of poststroke RT [27, 31]. To this extent, Mazzoleni et al. [27] analysed KPs registered by 25 subacute stroke subjects during RT with a planar end-effector robot and found that kinematics significantly improved in the first sessions of treatment, and that a plateau occurred after 10th session. These results were confirmed in a subsequent study by the same group on 12 subacute and 12 chronic stroke patients [31]. These outcomes were encouraging although a restricted number of patients was recruited, and the analysis of KPs did not investigate whether the recovery was dependent from the direction of the movement. Thus, additional research with a higher number of stroke patients is needed in order to understand how kinematic data from robotics devices can be exploited in clinical practice for optimizing and personalizing the RT.

The goal of this retrospective study is to analyse built-in kinematic data registered by a planar end-effector robot for assessing the time course of motor recovery and patient's workspace exploration skills. For that purpose, kinematic data recorded by a planar end-effector robot have been processed for investigating how motor performance in executing point-to-point trajectories with different directions changes during RT. A comparison of subjects having mild and severe motor impairment has been also conducted. The results of this study could help the clinicians to optimise poststroke upper limb RT in terms of length of the therapy and direction of point-to-point movements that need a more intensive training.

2. Materials and Methods

2.1. Subjects and Clinical Assessment. An observational retrospective study was conducted on a database of 271 inpatients who underwent upper limb RT with the InMotion 2.0 robot (Bionik Laboratories, Watertown, MA, USA) at the IRCCS San Raffaele Pisana of Rome between January 2011 and December 2017.

Inclusion criteria for the patient selection were age between 18 and 80 years, first event of unilateral hemiparetic stroke, subacute phase (RT started within 30 ± 7 days post-stroke), upper limb Chedoke-McMaster scores between 2 and 5, and RT for 20 sessions.

Exclusion criteria were bilateral impairment, chronic phase, RT for less than 20 sessions, RT interruption for more than 3 consecutive days, presence of other severe medical conditions, and incomplete data in the database.

The following demographic data have been extracted from the electronic medical records: age, sex, aetiology, stroke location, and distance from the acute event.

The following clinical assessments were registered at the beginning (T1) and at the end (T2) of the period of treatment: modified Barthel Index (BI), which is a measure of ADLs and depicts the degree of independence of a patient from any assistance; Motricity Index of the impaired upper limb (MIul), which assesses the arm motor impairment and ranges from 0 to 100 [43]. These clinical outcome measures are usually delivered as routine clinical assessments. Patient's privacy was preserved by identifying each record in the database by means of a unique alphanumeric code.

2.2. Ethical Considerations. Since March 2012, the Italian Data Protection Authority (Garante per la protezione dei dati personali) declared that IRCCS (Istituto di Ricovero e Cura a Carattere Scientifico—Institute for Scientific Research and Health Care) can perform retrospective studies without the approval of the local Ethical Committee [44] since only a formal communication is needed. Such communication has been registered by the Ethical Committee of the IRCCS San Raffaele Pisana of Rome (date: 22/02/2017; code number: 06/17) that waived the need of participants' consent.

2.3. Robot-Assisted Therapy. All subjects conducted 20 daily sessions of upper limb RT by using the InMotion2 system (Bionik Laboratories, Watertown, MA, USA), which is a two-DOF robotic device designed for neurological applications. The subject's arm was placed in a support attached to the robot end-effector and performed eight-direction planar point-to-point reaching task with an "assist as needed" strategy. We followed the methods of Franceschini et al. 2018 [45].

Each task involved the training of different muscle synergies, moving the end-effector from a central target to 8 peripheral targets, equally spaced on a 0.14 m radius circumference and vice versa (Figure 1). A visual biofeedback was delivered from a monitor placed in front of the subject. The duration of each session was fixed to 45 minutes, as in published clinical studies on poststroke upper limb RT with the same device [12, 20, 35, 45]. The number of repetitions of each session was planned as follows: (i) a series of 16 assisted clockwise repetitions to each target (training), (ii) a series of 16 unassisted clockwise repetitions to each target (record 1), (iii) 3 series of 320 assisted clockwise repetitions (adaptive), and (iv) a series of 16 unassisted clockwise repetitions to each target (record 2). However, since the number of repetitions in the record 1 and record 2 series depended on the patient's residual upper limb abilities, not all patients were able to execute all planned unassisted repetitions.

Every missed session was retrieved and subjects who were not able to retrieve sessions, or interrupted the treatment for more than 3 consecutive days, were excluded from the study.

In addition, all patients underwent conventional physiotherapy sessions according to the standardised rehabilitation protocol for subacute stroke patients of IRCCS San Raffaele Pisana in Rome. The following treatments were provided by



FIGURE 1: Upper limb RT based on the InMotion 2.0 robotic system.

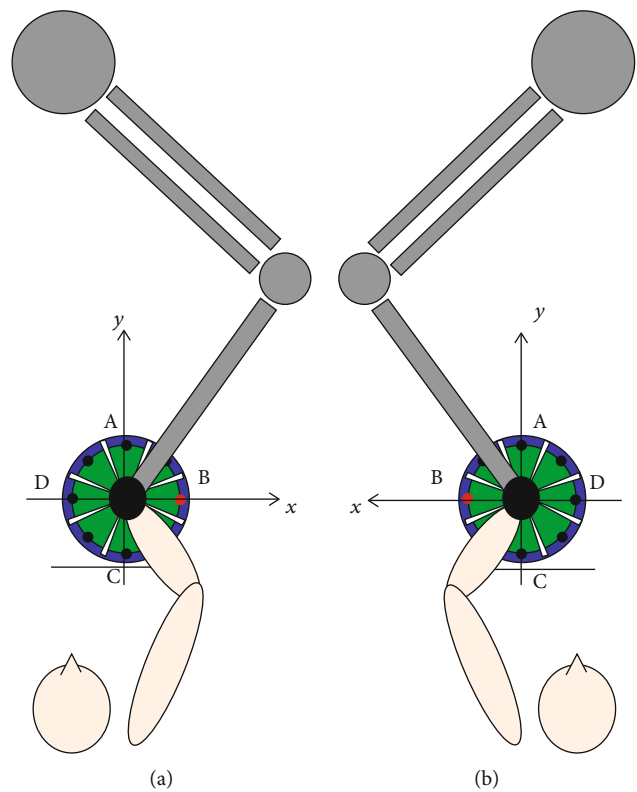


FIGURE 2: Experimental setup and reference system in case of left (a) or right (b) affected limb.

senior physical therapists: assisted stretching, shoulder and arm exercises, and functional reaching tasks.

2.4. Kinematic Parameters. Kinematic data were recorded at the end-effector robot during the record 1 and record 2 series at a sampling frequency of 200 Hz. As subjects used the robot with the hemiparetic upper limb, the position of the end-effector over time has been expressed with respect to a reference system consistent with the lesion side (Figure 2).

We processed the data of the second unassisted clockwise repetition of the record 2 series, with a customised MATLAB® routine. Then, we downsampled the data, considering the 1st, 5th, 10th, 15th, and 20th sessions of RT and we calculated the following KPs for each trajectory

TABLE 1: Correspondence between the target position and the joint movements.

Target label	Target coordinates (m)	Elbow movement	Shoulder movement
A	(0.00, 0.14)	Extension	Internal rotation and flexion
B	(0.14, 0.00)	Flexion	Abduction
C	(0.00, -0.14)	Flexion	External rotation and extension
D	(-0.14, 0.00)	Extension	Adduction

Target coordinates are expressed as (x, y) , taking into account the reference system shown in Figure 2.

from the central target to the peripheral ones: movement accuracy (MovAc), movement speed (MS), number of peak speed (nPS), and task completion time (TCT). These KPs described functional abilities [27, 29] and are representative of two different ICF domains [39]: MovAc, MS, and nPS are in the “body function and structure” domain, while TCT belongs to the “activities” one. The KPs computed in this study are considered as “performance metrics” for assessing the quality of the movement by assuming that normal reaching movements are straight, accurate, smoothed, and fairly quick [17, 18].

The MovAc is a measure of accuracy: the value is 0 if the trajectory lies exactly on a straight line connecting the targets. It is computed as the mean absolute value of the minimum distance of each point of the actual path travelled by the subject from the ideal one (i.e., the straight line connecting the targets).

The MS has been computed from the discrete-time velocity signals $v_x[k]$ and $v_y[k]$ along the x and y axes, respectively (the reference coordinate system is shown in Figure 2), as the mean value of the resultant velocities in the xy plane:

$$MS = \frac{1}{N} \sum_{k=1}^N \sqrt{(v_x[k])^2 + (v_y[k])^2}, \quad (1)$$

where N is the number of samples for each trajectory.

The nPS is a metric used for assessing the smoothness of the movement in stroke patients [24]: low nPS values derive from few accelerations and decelerations, i.e., smooth movement. The nPS is defined as the number of peaks of the resultant velocity:

$$v_{xy}[k] = \sqrt{(v_x[k])^2 + (v_y[k])^2}. \quad (2)$$

The TCT is the time required to carry out each single point-to-point trajectory from the central target to the peripheral one.

Therefore, the KP values have been calculated for each subject and for each point-to-point trajectory executed at the 1st, 5th, 10th, 15th, and 20th sessions of RT.

The time course of motor recovery was studied by considering the point-to-point trajectories from the central target to the four principal targets depicted in Figure 2. Since the reference system is consistent with the lesion side, each target corresponded to specific anatomical joint movements (Table 1). Therefore, the considered point-to-

point trajectories described different muscle synergies involved for the execution of the reaching tasks [46, 47].

Patient’s workspace exploration skills, i.e., the capacity to execute movements towards all peripheral targets, were described at T1 (1st session) and T2 (20th session): the KPs were averaged, normalised between the minimum (0 value) and the maximum (1 value), and depicted in a polar diagram.

A secondary data analysis has been conducted by stratifying patients with respect to the severity of motor impairment at baseline, assessed with the MIul. A recent study on outcome predictors after upper limb RT with the same robot [45] found that subacute stroke patients whose MIul score was higher than 48 at T1 have higher probability to increase their independence in ADLs at T2. For this reason, patients were divided into two groups: subjects with mild motor impairment (MIul > 48) and those with severe motor impairment (MIul ≤ 48) at T1. The intergroup comparison has been conducted for each point-to-point trajectory executed at the 1st, 5th, 10th, 15th, and 20th sessions of RT.

2.5. Statistics. Descriptive statistics were computed in order to appropriately explain the characteristics of the sample. Data are represented as frequency (with the relative percentage), mean value with standard deviation (SD), and median value with interquartile range (IQR) for the categorical, continuous, and ordinal variables, respectively.

Wilcoxon signed-rank tests were used to find significant differences in ordinal clinical variables. To detect intrasubject differences of the KPs during the time course of the rehabilitation period, a nonparametric repetitive-dependent measure test was applied (Friedman test). Conover’s test was used for the post hoc analysis to locate significant differences between sessions. Bonferroni’s correction was applied for multiple comparisons. The Mann-Whitney U tests were used to compare the KPs (for each movement direction and RT session) of subjects with mild motor impairment (MIul > 48 at T1) with the ones obtained from subjects with severe impairment (MIul ≤ 48 at T1).

For all statistical analyses, the α value was set at p value < 0.05 and the software was SPSS, version 20.0 (SPSS Inc., Chicago, IL, USA, 2004).

3. Results

Starting from the 271 patients, 68 hemiparetic ischemic and haemorrhagic stroke subjects satisfied the inclusion criteria and were recruited in the study (Figure 3). The mean age was 65.28 years (SD 12.71 years), 23 (33.82%) patients were female, and 21 (30.88%) subjects were affected by stroke on

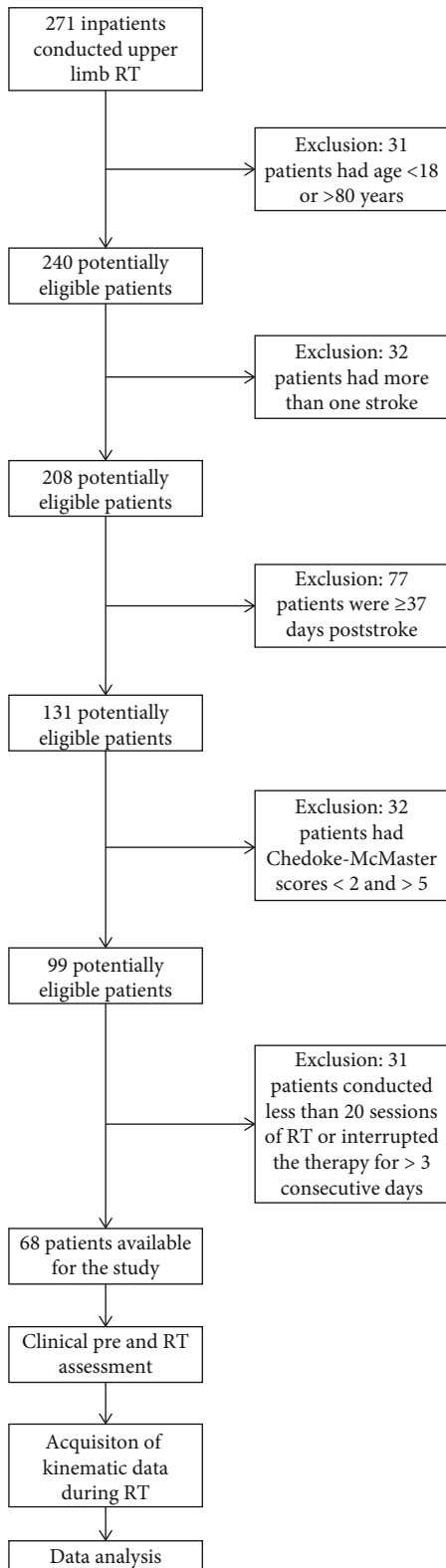


FIGURE 3: Consort diagram.

the right side. Table 2 shows the demographic characteristics of the sample at baseline and the clinical scores (BI and MIul) at T1 and T2. At the end of RT, the clinical outcomes show an increase in ADLs and in motor function of the paretic upper

limb: the Wilcoxon signed-rank tests evidenced statistically significant improvements in both BI (p value < 0.001) and MIul (p value < 0.001) scores, in accordance with studies on the efficacy of RT in stroke survivors [11, 12].

The nonparametric repetitive-dependent measure tests (Friedman tests) were applied to each point-to-point trajectory and for each KP. The analysis did not reveal a significant difference for the overall MovAc changes in all movement directions. Conversely, significant temporal differences were found in MS in the movements towards the targets A ($\chi^2 = 22.04$; p value < 0.001), B ($\chi^2 = 33.96$; p value < 0.001), C ($\chi^2 = 44.84$; p value < 0.001), and D ($\chi^2 = 34.44$; p value < 0.001). An analogous result was obtained on nPS: targets A ($\chi^2 = 53.83$; p value < 0.001), B ($\chi^2 = 33.27$; p value < 0.001), C ($\chi^2 = 31.49$; p value < 0.001), and D ($\chi^2 = 39.18$; p value < 0.001). Similarly, the overall temporal decrease of TCT was significant in all movement directions: targets A ($\chi^2 = 59.98$; p value < 0.001), B ($\chi^2 = 44.08$; p value < 0.001), C ($\chi^2 = 42.80$; p value < 0.001), and D ($\chi^2 = 45.83$; p value < 0.001).

The Figures 4–7 show each KP (mean values and SDs) obtained from the point-to-point trajectories (A, B, C, D) executed by the 68 subjects at the 1st, 5th, 10th, 15th, and 20th sessions of RT. The statistical analysis of intersession difference is shown with a representation of the corresponding p values, obtained with the post hoc Conover's tests (Bonferroni correction). At the RT onset (1st session), all point-to-point movements are characterised by curved trajectories (mean MovAc at T1 = 0.019 m) with distinct sub movements (mean nPS at T1 = 4.47) executed at low mean speed (mean MS at T1 = 0.064 m/s) and with a high time of execution (mean TCT at T1 = 5.69 s). At the end of treatment, the data are significantly different: mean MovAc at T2 = 0.017 m, mean nPS at T2 = 2.81, mean MS at T2 = 0.10 m/s, and mean TCT at T2 = 0.10 s.

The MovAc (Figure 4) represents the accuracy (low values represent straighter movements) of the trajectory, and it decreases during the course of the treatment. Such behaviour is noticeable in all movement directions, with a significant trend in the tasks towards the target C. The tasks that involve the elbow extension and shoulder internal rotation movements (i.e., reaching the target A) are characterised by higher MovAc values both at the 1st (mean MovAc = 0.03 m) and at the 20th sessions (mean MovAc = 0.018 m). The trajectories towards target C have a significant decrease of MovAc after the 10th session, and the values are sustained afterwards. The mean MovAc obtained from the movement direction A were 0.03 m at the 1st session, of 0.023 m at the 10th session, and of 0.018 m at the 20th session. Reaching the target C registered a mean value of MovAc of 0.026 m at the 1st session, of 0.019 m at the 10th session, and of 0.017 m at the 20th session. Data from trajectories towards target D were characterised by a mean MovAc of 0.026 m at the 1st session, of 0.017 m at the 10th session, and of 0.016 m at the 20th session. Movements towards the targets A, B, and D do not have significant intersession changes of MovAc.

The MS (Figure 5) increases in all movement directions during RT. The mean speed significantly changed after the 5th session, and the values are maintained in the subsequent

TABLE 2: Characteristics of the sample and clinical outcomes.

Variables	<i>n</i> (%)	T1 median (IQR)	T2 median (IQR)	<i>p</i> value
Gender, male/female	45 (66.18)/23 (33.82)			
Aetiology, ischemic/haemorrhagic	49 (72.05)/19 (27.95)			
Lesion side, left/right	29 (42.62)/39 (57.35)			
BI		26.50 (9.90-49.00)	79.50 (39.90-97.10)	<0.001
MIul		43.00 (1.00-78.15)	77.00 (14.30-100.00)	<0.001

IQR: interquartile range; BI: modified Barthel Index; MIul: Motricity Index paretic upper limb.

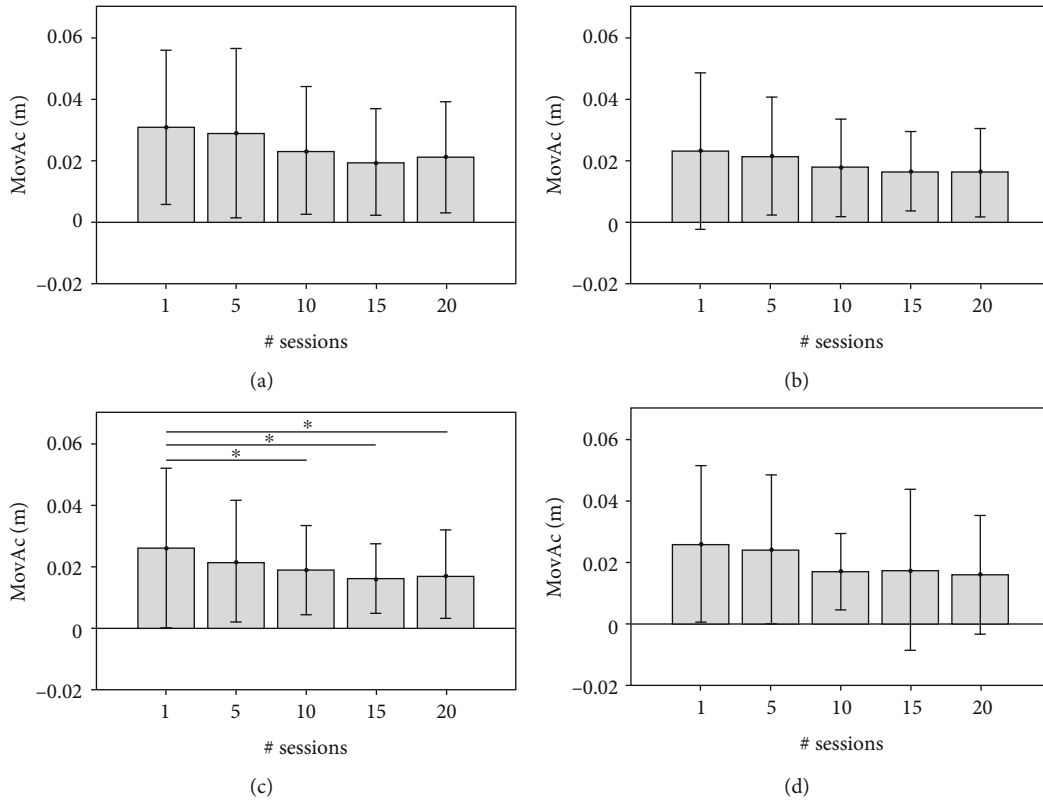


FIGURE 4: MovAc values (mean and standard deviation) at 1st, 5th, 10th, 15th, and 20th sessions of RT and significant post hoc comparisons between sessions (Conover's test): **p* value < 0.05; ***p* value < 0.001; ****p* value < 0.0001. The data obtained by analysing the end-effector trajectories towards the four targets (A, B, C, D) are showed separately.

ones. Analogous to MovAc, the MS highlights lower performances of the tasks that involve the elbow extension and shoulder internal rotation (i.e., reaching target A) that show the lowest velocities (mean MS of 0.06 m/s, 0.084 m/s, 0.084 m/s at the 1st, 10th, and 20th sessions, respectively). The remaining tasks almost doubled their movement speed after the 5th session and such value persists over time. For example, the mean MS of target B was 0.073 m/s, 0.010 m/s, 0.011 m/s at the 1st, 10th, and 20th sessions, respectively. Significant intersession variations were registered between the 1st session and the following ones in all movement directions.

The nPs (Figure 6) represents the smoothness (low values represent high smoothness) of the trajectory which decreases in all the movement directions. Thus, the patients tended to have less distinct submovements during the course of RT. For instance, the mean numbers of peaks in movements

toward the target A were 6.23 at the 1st session, 4.00 at the 10th session, and 3.25 at the 20th session of RT. A plateau trend after the 5th session is found in tasks towards targets A, B, and C.

Movements towards target C showed a significant variation of smoothness after the 10th session.

A similar decreasing temporal evolution is found in TCT values, where trajectories towards the target A were characterised by higher times of execution at every session. Specifically, the mean TCT obtained from the movement direction A were 6.93 s at the 1st session, of 4.55 s at the 10th session, and of 3.58 s at the 20th session. In all movement directions, the post hoc intersession analysis revealed significant differences between the 1st session and the following ones.

Figure 8 describes patient's workspace exploration skills at T1 (red line) and T2 (black line). Each point of the polar

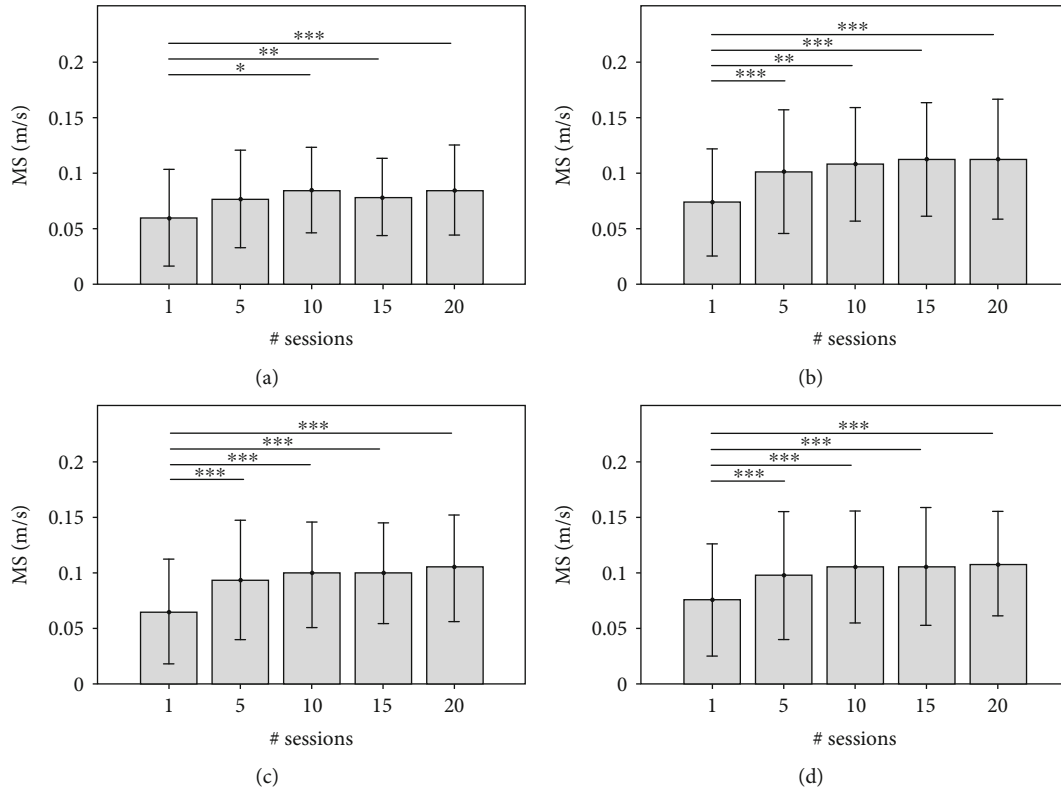


FIGURE 5: MS values (mean and standard deviation) at 1st, 5th, 10th, 15th, and 20th sessions of RT and significant post hoc comparisons between sessions (Conover’s test): **p* value < 0.05; ***p* value < 0.001; ****p* value < 0.0001. The data obtained by analysing the end-effector trajectories towards the four targets (A, B, C, D) are showed separately.

plots represents the mean values of the normalised KP with respect to the 8 movement directions. At T1, the trajectories towards target A showed the highest values on MovAc, nPs, and TCT, and the lowest value of MS. The figures show a motor improvement after RT in the trajectories towards all targets. At T2, the MovAc is still high towards target A (0.25), while in the other directions is about 0.08. MS increased to the maximum value in all trajectories, except to the one towards target A, where the speed at the end of RT is half of the others. The nPS and TCT decrease in all point-to-point trajectories, although the movements towards targets A and C have keep higher values also at T2.

The secondary data analysis divided the sample into 2 groups with a criteria based on the motor impairment at T1: specifically 37 patients had MIul ≤ 48, and 31 patients had MIul > 48.

Patients with severe upper limb motor impairment (MIul ≤ 48) showed higher values of MovAc in all point-to-point trajectories and RT sessions (mean MovAc of 0.022 m at the 1st session, of 0.023 m at the 10th session, and of 0.020 m at the 20th session) than patients with MIul > 48 (mean MovAc of 0.020 m at the 1st session, of 0.015 m at the 10th session, and of 0.011 m at the 20th session). Significant intergroup MovAc differences were registered in movements towards target A (*W* = 813.00; *p* value = 0.003) and target B (*W* = 745.00; *p* value = 0.003) at the 15th session, towards target C at the 20th session (*W* = 734.50; *p* value = 0.005), and towards target

D and the 1st (*W* = 776.00; *p* value = 0.013), 10th (*W* = 822.50; *p* value = 0.002), 15th (*W* = 804.00; *p* value = 0.005), and 20th (*W* = 867.50; *p* value < 0.001) sessions.

Subjects with MIul > 48 executed faster trajectories (higher MS values) than their peers with MIul ≤ 48. Significant intergroup differences were found in all sessions for movements towards target A (*W* = 0.00; *p* value < 0.001), in the 1st session for directions B (*W* = 385.00; *p* value = 0.02) and C (*W* = 400.50; *p* value = 0.03), and the 10th session for directions B (*W* = 392.50; *p* value = 0.03) and D (*W* = 395.00; *p* value = 0.03).

The number of peaks of the resultant velocity was always higher in the group with more severe impairment. In subjects with MIul ≤ 48, the mean numbers of peaks of trajectories toward the target A were 6.45 at the 1st session, 2.84 at the 10th session, and 3.59 at the 20th session of RT. In subjects with MIul > 48, the nPs toward the target A were 4.29 at the 1st session, 2.47 at the 10th session, and 2.31 at the 20th session of RT. The Mann-Whitney *U* test revealed significant differences in movements towards target A (1st session: *W* = 784.00, *p* value = 0.01; 5th session: *W* = 754.50, *p* value = 0.02; 15th session: *W* = 842.00, *p* value < 0.001), B (1st session: *W* = 757.00, *p* value = 0.02; 5th session: *W* = 728.00, *p* value = 0.04; 10th session: *W* = 732.50, *p* value = 0.04), C (5th session: *W* = 784.00, *p* value = 0.01; 10th session: *W* = 859.00, *p* value < 0.001; 15th session: *W* = 773.00, *p* value = 0.01), and D (1st session: *W* = 814.50, *p* value = 0.0003).

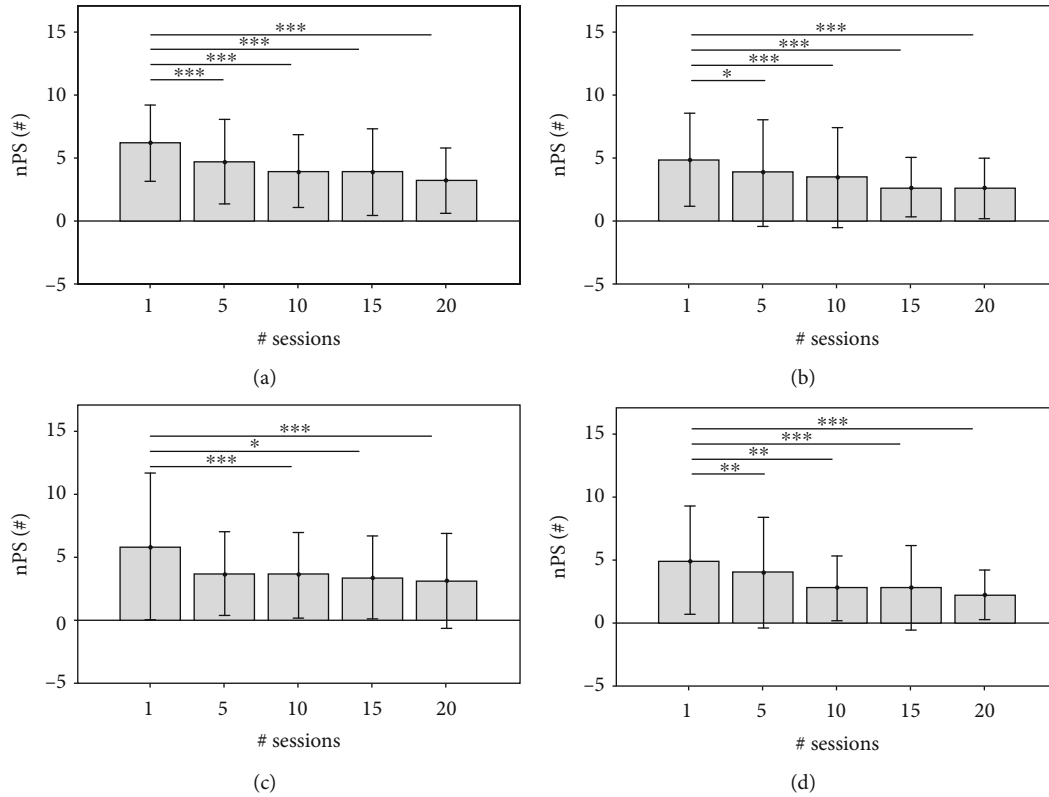


FIGURE 6: nPS values (mean and standard deviation) at 1st, 5th, 10th, 15th, and 20th sessions of RT and significant post hoc comparisons between sessions (Conover's test): * p value < 0.05; ** p value < 0.001; *** p value < 0.0001. The data obtained by analysing the end-effector trajectories towards the four targets (A, B, C, D) are showed separately.

The TCT values confirmed the trend of other KPs: subjects having severe upper limb impairment had significant higher time of execution than subjects with mild impairment did. The intergroup analysis showed significant differences in movements towards target A (1st session: $W = 734.50$, p value = 0.04; 15th session: $W = 843.50$, p value < 0.001), B (5th session: $W = 761.50$, p value = 0.02; 10th session: $W = 754.50$, p value = 0.03; 15th session: $W = 740.00$, p value = 0.04), C (1st session: $W = 758.50$, p value = 0.02; 5th session: $W = 750.00$, p value = 0.03; 10th session: $W = 835.50$, p value = 0.001; 15th session: $W = 779.00$, p value = 0.01; 20th session: $W = 744.50$, p value = 0.04), and D (1st session: $W = 813.50$, p value = 0.0003; 10th session: $W = 779.00$, p value = 0.01; 15th session: $W = 792.50$, p value = 0.007; 20th session: $W = 818.00$, p value = 0.0027).

4. Discussion

Kinematic data recorded by a planar end-effector robot during the RT of 68 subacute stroke patients was processed for assessing the time course of motor recovery and patient's workspace exploration skills. A set of KPs, which are representative of motor performance, were calculated, and their changes with respect to time and movement direction were analysed.

The data analysis showed that RT leads to significant improvements in kinematic components of upper motor per-

formance. Changes of movement kinematics have been described in terms of accuracy, velocity, smoothness, and time of execution of the motor tasks.

At the RT onset, the point-to-point trajectories were less accurate and smoothed, and showed higher times of execution than those executed at the end of treatment. These findings are in agreement with studies [25, 27, 29, 31] that associated the variations of KPs to motor recovery, registering an improvement of KPs during the period of treatment.

The analysis of the time course of KPs highlighted that RT seems to improve the motor function mainly in the first sessions of treatment: most KPs showed significant intersession differences during the first 5/10 sessions. Afterwards, no further significant variations occurred. Similar results have been found in studies on a limited number of stroke patients [27, 31].

The descriptive analysis of different movement directions showed that the ability to perform movements away from the body (target A) and from the hemiparetic side (target B) was initially limited: these movements had low accuracy, speed, smoothness, and higher execution times compared with movements toward the body (target C) and toward the hemiparetic side (target D). At the end of the treatment, the workspace was successfully restored, although the movements that involved elbow extensions and shoulder internal rotation (target A) remained rather

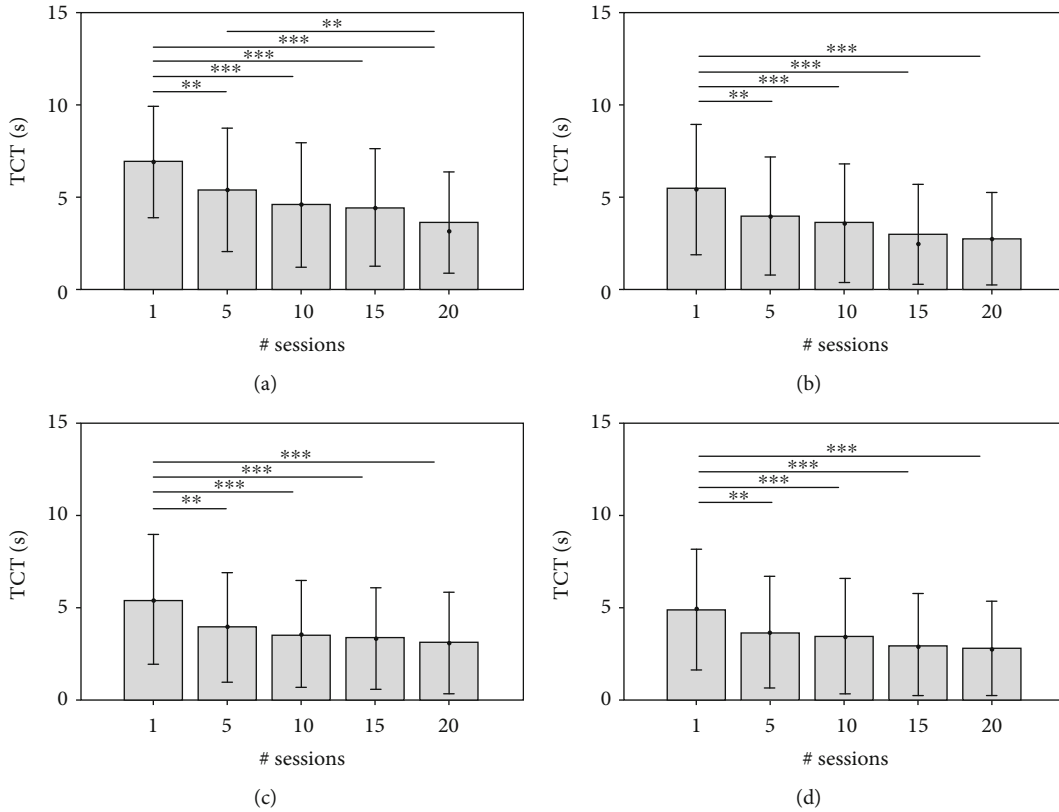


FIGURE 7: TCT values (mean and standard deviation) at 1st, 5th, 10th, 15th, and 20th sessions of RT and significant post hoc comparisons between sessions (Conover’s test): **p* value < 0.05; ***p* value < 0.001; ****p* value < 0.0001. The data obtained by analysing the end-effector trajectories towards the four targets (A, B, C, D) are showed separately.

challenging to be performed. The results are in accordance with similar studies on motor recovery of stroke patients [1, 46] and RT [7, 11, 30] and suggest that different mechanisms are responsible for recovering movements toward different target positions, in agreement with studies on motor synergies in stroke survivors [30, 47].

The results obtained from data stratification evidenced that at T1, the majority of KPs were significantly different (MovAc, target D; MS, targets A, B, C; nPs, targets A, B, D; TCT, targets A, C, D). During the time course of RT, such differences persisted only in trajectories towards target A (MS, nPs), C (TCT), and D (MovAc, TCT). The two groups of patients did not register any significant difference in the other KPs over time.

This study presented several limitations that deserve to be discussed. Firstly, normative reference values of KPs are not available for both healthy subjects and stroke patients who performed conventional upper limb therapy. Secondly, the study employed a planar end-effector robot, while 3D exoskeleton devices for upper limb RT are commercially available. Thirdly, the MovAc values could be influenced by the number of samples of the trajectory and by the systematically curved behaviour of normal reaching movements [48]: it could justify the differences, in terms of statistical outcomes, between MovAc and the other KPs. Finally, the study is retrospective; therefore, it did not assess clinical and kinematic effects of prolonged RT (>20 sessions) and did not include

a follow-up assessment. However, since a recent study on the long-term clinical effects (after 6 months) of upper limb RT in subacute stroke patients found that the clinical improvements observed at the end of treatment persisted over time [13], we are confident that such trend could be noticed in KPs too.

The research agenda should include the gathering of normative reference values, the implementation of advanced algorithms for the analysis of movement during RT, and the investigation of recently released devices for 3D upper limb rehabilitation.

5. Conclusions

Robotic systems for stroke rehabilitation may be considered as a tool with a twofold aim: (i) training the patient with an assist-as-needed approach and (ii) assisting the clinicians to plan and personalise the rehabilitation treatments. The results obtained by analysing kinematic data from 68 subacute stroke patients showed significant improvements in motor performance in the first 5-10 sessions of RT. Moreover, the recovery was different for each movement direction. Such outcomes are in accordance with literature on the topic [27, 31, 34].

Future studies on a larger sample of subjects may highlight the clinical characteristics of patients who may benefit upper limb RT. Moreover, a more detailed analysis of KPs

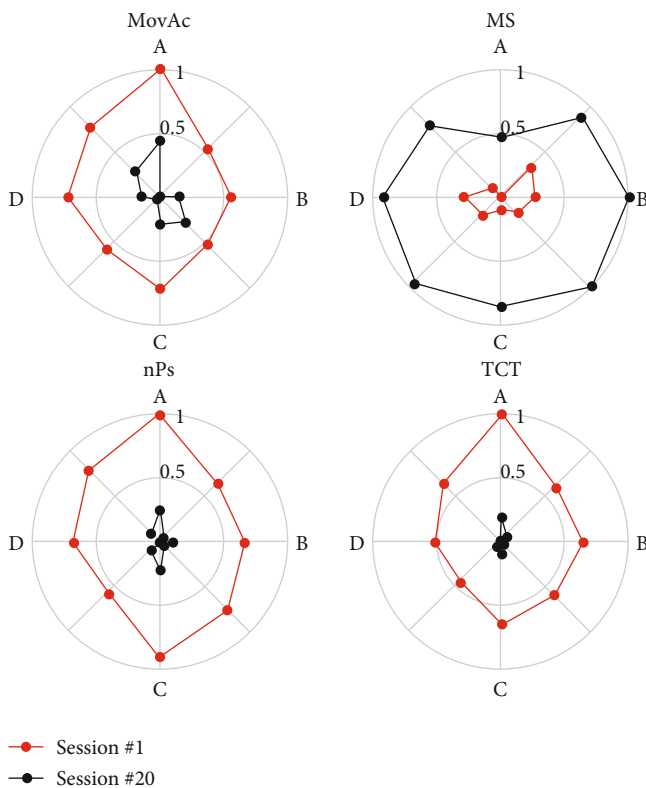


FIGURE 8: Polar plots of KP changes. Each figure represents the mean values of each KP at the start (red line) and at the end (black line) of RT. The changes of each KP are normalised between the minimum (0 is the circle centre) and the maximum (1 is the circle border) values.

calculated in the first session of RT may contribute to optimize healthcare resources and to design patient-tailored rehabilitative protocols with an ecological approach.

Data Availability

The authors are available to send data to those who request it.

Additional Points

Consent for Publication. All authors gave their consent for the manuscript publication.

Ethical Approval

Since March 2012, the Italian Data Protection Authority (Garante per la protezione dei dati personali) declared that IRCCS (Istituto di Ricovero e Cura a Carattere Scientifico—Institute for Scientific Research and Health Care) can perform retrospective studies without the approval of the local Ethical Committee since only a formal communication is needed. Such communication has been registered by the Ethical Committee of the IRCCS San Raffaele Pisana of Rome (date: 22/02/2017; code number: 06/17) that waived the need of participants' consent.

Conflicts of Interest

The authors have declared that no competing interests exist.

Authors' Contributions

MG, SM, FP, and MF conceived the design of the work. MG and FI acquired the data. MG, SM, and MA conceived the algorithm and analysed the data. All authors contributed in interpreting data for the work. MG, SP, SM, and MF drafted the manuscript. FP, AG, and DG revised it critically for important intellectual content. All authors read and approved the final version of the manuscript.

Acknowledgments

This project was partially funded by the Ministry of Health (ricerca corrente).

References

- [1] B. Rohrer, S. Fasoli, H. I. Krebs et al., "Submovements grow larger, fewer, and more blended during stroke recovery," *Motor Control*, vol. 8, no. 4, pp. 472–483, 2004.
- [2] S. M. Lai, S. Studenski, P. W. Duncan, and S. Perera, "Persisting consequences of stroke measured by the Stroke Impact Scale," *Stroke*, vol. 33, no. 7, pp. 1840–1844, 2002.
- [3] G. Kwakkel, B. J. Kollen, J. van der Grond, and A. J. Prevo, "Probability of regaining dexterity in the flaccid upper limb: impact of severity of paresis and time since onset in acute stroke," *Stroke*, vol. 34, no. 9, pp. 2181–2186, 2003.
- [4] D. S. Nichols-Larsen, P. C. Clark, A. Zeringue, A. Greenspan, and S. Blanton, "Factors influencing stroke survivors' quality of life during subacute recovery," *Stroke*, vol. 36, no. 7, 2005.
- [5] A. C. Lo, P. D. Guarino, L. G. Richards et al., "Robot-assisted therapy for long-term upper-limb impairment after stroke," *New England Journal of Medicine*, vol. 362, no. 19, pp. 1772–1783, 2010.
- [6] European Stroke Organisation (ESO) Executive Committee; ESO Writing Committee, "Guidelines for management of ischaemic stroke and transient ischaemic attack 2008," *Cerebrovascular Diseases*, vol. 25, pp. 457–507, 2008.
- [7] B. R. Brewer, S. K. McDowell, and L. C. Worthen-Chaudhari, "Poststroke upper extremity rehabilitation: a review of robotic systems and clinical results," *Topics in Stroke Rehabilitation*, vol. 14, no. 6, pp. 22–44, 2007.
- [8] J. Mehrholz, M. Pohl, T. Platz, J. Kugler, and B. Elsner, "Electromechanical and robot-assisted arm training for improving activities of daily living, arm function, and arm muscle strength after stroke," *Cochrane Database of Systematic Reviews*, vol. 6, 2018.
- [9] M. Babaiasl, S. H. Mahdioun, P. Jaryani, and M. Yazdani, "A review of technological and clinical aspects of robot-aided rehabilitation of upper-extremity after stroke," *Disability and Rehabilitation: Assistive Technology*, vol. 11, no. 4, pp. 263–280, 2016.
- [10] S. Masiero, M. Armani, and G. Rosati, "Upper-limb robot-assisted therapy in rehabilitation of acute stroke patients: focused review and results of new randomized controlled trial," *The Journal of Rehabilitation Research and Development*, vol. 48, no. 4, p. 355, 2011.

- [11] J. M. Veerbeek, A. C. Langbroek-Amersfoort, E. E. van Wegen, C. G. Meskers, and G. Kwakkel, "Effects of robot-assisted therapy for the upper limb after stroke: a systematic review and meta-analysis," *Neurorehabilitation and Neural Repair*, vol. 31, no. 2, pp. 107–121, 2017.
- [12] P. Sale, M. Franceschini, S. Mazzoleni, E. Palma, M. Agosti, and F. Posteraro, "Effects of upper limb robot-assisted therapy on motor recovery in subacute stroke patients," *Journal of NeuroEngineering and Rehabilitation*, vol. 11, no. 1, p. 104, 2014.
- [13] M. Franceschini, S. Mazzoleni, M. Goffredo et al., "Upper limb robot-assisted rehabilitation versus physical therapy on subacute stroke patients: a follow-up study," *Journal of Bodywork and Movement Therapies*, 2019.
- [14] S. H. Scott and S. P. Dukelow, "Potential of robots as next-generation technology for clinical assessment of neurological disorders and upper-limb therapy," *The Journal of Rehabilitation Research and Development*, vol. 48, no. 4, 2011.
- [15] C. Bosecker, L. Dipietro, B. Volpe, and H. Igo Krebs, "Kinematic robot-based evaluation scales and clinical counterparts to measure upper limb motor performance in patients with chronic stroke," *Neurorehabilitation and Neural Repair*, vol. 24, no. 1, pp. 62–69, 2010.
- [16] S. Balasubramanian, R. Colombo, I. Sterpi, V. Sanguineti, and E. Burdet, "Robotic assessment of upper limb motor function after stroke," *American Journal of Physical Medicine & Rehabilitation*, vol. 91, no. 11, pp. S255–S269, 2012.
- [17] H. I. Krebs, M. Krams, D. K. Agrafiotis et al., "Robotic measurement of arm movements after stroke establishes biomarkers of motor recovery," *Stroke*, vol. 45, no. 1, pp. 200–204, 2014.
- [18] N. Nordin, S. Q. Xie, and B. Wünsche, "Assessment of movement quality in robot-assisted upper limb rehabilitation after stroke: a review," *Journal of Neuroengineering and Rehabilitation*, vol. 11, no. 1, p. 137, 2014.
- [19] L. Dipietro, H. I. Krebs, B. T. Volpe et al., "Learning, not adaptation, characterizes stroke motor recovery: evidence from kinematic changes induced by robot-assisted therapy in trained and untrained task in the same workspace," *IEEE Transactions on Neural Systems and Rehabilitation Engineering*, vol. 20, no. 1, pp. 48–57, 2011.
- [20] C. Duret, O. Courtial, and A. G. Grosmaire, "Kinematic measures for upper limb motor assessment during robot-mediated training in patients with severe sub-acute stroke," *Restorative Neurology and Neuroscience*, vol. 34, no. 2, pp. 237–245, 2016.
- [21] S. Mazzoleni, L. Puzzolante, L. Zollo, P. Dario, and F. Posteraro, "Mechanisms of motor recovery in chronic and subacute stroke patients following a robot-aided training," *IEEE Transactions on Haptics*, vol. 7, no. 2, pp. 175–180, 2014.
- [22] L. Zollo, L. Rossini, M. Bravi, G. Magrone, S. Sterzi, and E. Guglielmelli, "Quantitative evaluation of upper-limb motor control in robot-aided rehabilitation," *Medical & Biological Engineering & Computing*, vol. 49, no. 10, p. 1131, 2011.
- [23] R. Colombo, F. Pisano, C. Delconte et al., "Comparison of exercise training effect with different robotic devices for upper limb rehabilitation: a retrospective study," *European Journal of Physical and Rehabilitation Medicine*, vol. 53, no. 2, pp. 240–248, 2016.
- [24] S. Mazzoleni, F. Posteraro, F. Forte, S. Micera, P. Dario, and M. C. Carrozza, "Biomechanical assessment of reaching movements in post-stroke patients during a robot-aided rehabilitation," *Applied Bionics and Biomechanics*, vol. 8, no. 1, 54 pages, 2011.
- [25] R. Colombo, F. Pisano, S. Micera et al., "Robotic techniques for upper limb evaluation and rehabilitation of stroke patients," *IEEE Transactions on Neural Systems and Rehabilitation Engineering*, vol. 13, no. 3, pp. 311–324, 2005.
- [26] S. Mazzoleni, P. Sale, M. Franceschini et al., "Effects of proximal and distal robot-assisted upper limb rehabilitation on chronic stroke recovery," *NeuroRehabilitation*, vol. 33, no. 1, pp. 33–39, 2013.
- [27] S. Mazzoleni, M. C. Carrozza, P. Sale, M. Franceschini, F. Posteraro, and M. Tiboni, "Effects of upper limb robot-assisted therapy on motor recovery of subacute stroke patients: a kinematic approach," in *2013 IEEE 13th International Conference on Rehabilitation Robotics (ICORR)*, pp. 1–5, Seattle, WA, USA., 2013 June.
- [28] R. Colombo, I. Sterpi, A. Mazzone, C. Delconte, G. Minuco, and F. Pisano, "Measuring changes of movement dynamics during robot-aided neurorehabilitation of stroke patients," *IEEE Transactions on Neural Systems and Rehabilitation Engineering*, vol. 18, no. 1, pp. 75–85, 2010.
- [29] R. Colombo, I. Sterpi, C. Delconte, A. Mazzone, and F. Pisano, "Time course of recovery during robotic neurorehabilitation of the upper limb in sub-acute and chronic stroke patients," in *Converging Clinical and Engineering Research on Neurorehabilitation*, pp. 3–8, Springer, Berlin, Heidelberg, 2013.
- [30] A. Panarese, R. Colombo, I. Sterpi, F. Pisano, and S. Micera, "Tracking motor improvement at the subtask level during robot-aided neurorehabilitation of stroke patients," *Neurorehabilitation and Neural Repair*, vol. 26, no. 7, pp. 822–833, 2012.
- [31] S. Mazzoleni, L. Buono, P. Dario, and F. Posteraro, "Upper limb robot-assisted therapy in subacute and chronic stroke patients: preliminary results on initial exposure based on kinematic measures," in *5th IEEE RAS/EMBS International Conference on Biomedical Robotics and Biomechatronics*, pp. 265–269, Sao Paulo, Brazil., 2014 August.
- [32] R. Colombo, F. Pisano, S. Micera et al., "Assessing mechanisms of recovery during robot-aided neurorehabilitation of the upper limb," *Neurorehabilitation and Neural Repair*, vol. 22, no. 1, pp. 50–63, 2008.
- [33] M. Casadio and V. Sanguineti, "Learning, retention, and slackening: a model of the dynamics of recovery in robot therapy," *IEEE Transactions on Neural Systems and Rehabilitation Engineering*, vol. 20, no. 3, pp. 286–296, 2012.
- [34] G. Sedda, S. Summa, and V. Sanguineti, "Computational models of the recovery process in robot-assisted training," in *Rehabilitation Robotics*, pp. 117–135, Academic Press, 2018.
- [35] O. Pila, C. Duret, F.-X. Laborne, J.-M. Gracies, N. Bayle, and E. Hutin, "Pattern of improvement in upper limb pointing task kinematics after a 3-month training program with robotic assistance in stroke," *Journal of Neuroengineering and Rehabilitation*, vol. 14, no. 1, 2017.
- [36] C. Duret, O. Pila, A. G. Grosmaire, and T. Koepfel, "Can robot-based measurements improve prediction of motor performance after robot-assisted upper-limb rehabilitation in patients with moderate-to-severe sub-acute stroke?," *Restorative Neurology and Neuroscience*, vol. 37, no. 2, pp. 119–129, 2019.
- [37] E. Palermo, D. R. Hayes, E. F. Russo, R. S. Calabrò, A. Pacilli, and S. Filoni, "Translational effects of robot-mediated therapy in subacute stroke patients: an experimental evaluation of upper limb motor recovery," *PeerJ*, vol. 6, p. e5544, 2018.

- [38] R. Colombo, I. Sterpi, A. Mazzone, C. Delconte, and F. Pisano, "Taking a lesson from patients' recovery strategies to optimize training during robot-aided rehabilitation," *IEEE Transactions on Neural Systems and Rehabilitation Engineering*, vol. 20, no. 3, pp. 276–285, 2012.
- [39] V. D. Tran, P. Dario, and S. Mazzoleni, "Kinematic measures for upper limb robot-assisted therapy following stroke and correlations with clinical outcome measures: a review," *Medical Engineering and Physics*, vol. 53, pp. 13–31, 2018.
- [40] R. Colombo, I. Cusmano, I. Sterpi, A. Mazzone, C. Delconte, and F. Pisano, "Test–retest reliability of robotic assessment measures for the evaluation of upper limb recovery," *IEEE Transactions on Neural Systems and Rehabilitation Engineering*, vol. 22, no. 5, pp. 1020–1029, 2014.
- [41] A. McKenzie, L. Dodakian, J. See et al., "Validity of robot-based assessments of upper extremity function," *Archives of Physical Medicine and Rehabilitation*, vol. 98, no. 10, pp. 1969–1976, 2017.
- [42] M. Germanotta, A. Cruciani, C. Pecchioli et al., "Reliability, validity and discriminant ability of the instrumental indices provided by a novel planar robotic device for upper limb rehabilitation," *Journal of Neuroengineering and Rehabilitation*, vol. 15, no. 1, 2018.
- [43] D. T. Wade, "Measuring arm impairment and disability after stroke," *International Disability Studies*, vol. 11, no. 2, pp. 89–92, 1989.
- [44] Garante per la protezione dei dati personali, "Autorizzazione generale al trattamento dei dati personali effettuato per scopi di ricerca scientifica - 1° marzo 2012," *Gazzetta Ufficiale della Repubblica Italiana*, vol. 72, pp. 47–52, 2012.
- [45] M. Franceschini, M. Goffredo, S. Pournajaf et al., "Predictors of activities of daily living outcomes after upper limb robot-assisted therapy in subacute stroke patients," *PLoS One*, vol. 13, no. 2, p. e0193235, 2018.
- [46] S. B. O'Sullivan, T. J. Schmitz, and G. Fulk, *Physical Rehabilitation*, 2013, FA Davis.
- [47] P. Raghavan, "Upper limb motor impairment after stroke," *Physical Medicine and Rehabilitation Clinics of North America*, vol. 26, no. 4, pp. 599–610, 2015.
- [48] R. J. Van Beers, P. Haggard, and D. M. Wolpert, "The role of execution noise in movement variability," *Journal of Neurophysiology*, vol. 91, no. 2, pp. 1050–1063, 2004.

Research Article

Measurement and Analysis of Gait Pattern during Stair Walk for Improvement of Robotic Locomotion Rehabilitation System

Sang-Eun Park,¹ Ye-Ji Ho,¹ Min Ho Chun,² Jaesoon Choi ^{1,3} and Youngjin Moon ^{1,4}

¹Biomedical Engineering Research Center, Asan Institute for Life Sciences, Asan Medical Center, Seoul, Republic of Korea

²Department of Rehabilitation Medicine, Asan Medical Center, University of Ulsan College of Medicine, Seoul, Republic of Korea

³Department of Biomedical Engineering, College of Medicine, University of Ulsan, Seoul, Republic of Korea

⁴Department of Convergence Medicine, College of Medicine, University of Ulsan, Seoul, Republic of Korea

Correspondence should be addressed to Youngjin Moon; jacobian@amc.seoul.kr

Received 9 April 2019; Revised 26 June 2019; Accepted 13 August 2019; Published 13 October 2019

Academic Editor: Loredana Zollo

Copyright © 2019 Sang-Eun Park et al. This is an open access article distributed under the Creative Commons Attribution License, which permits unrestricted use, distribution, and reproduction in any medium, provided the original work is properly cited.

Background. Robotic locomotion rehabilitation systems have been used for gait training in patients who have had a stroke. Most commercialized systems allow patients to perform simple exercises such as balancing or level walking, but an additional function such as stair-walk training is required to provide a wide range of recovery cycle rehabilitation. In this study, we analyzed stair-gait patterns and applied the result to a robotic rehabilitation system that can provide a vertical motion of footplates. **Methods.** To obtain applicable data for the robotic system with vertically movable footplates, stair-walk action was measured using an optical marker-based motion capture system. The spatial position data of joints during stair walking was obtained from six healthy adults who participated in the experiment. The measured marker data were converted into joint kinematic data by using an algorithm that included resampling and normalization. The spatial position data are represented as angular trajectories and the relative displacement of each joint on the anatomical sagittal plane and movements of hip joints on the anatomical transverse plane. **Results.** The average range of motion (ROM) of each joint was estimated as $(-6.75^\circ, 48.69^\circ)$ at the hip, $(8.20^\circ, 93.78^\circ)$ at the knee, and $(-17.78^\circ, 11.75^\circ)$ at the ankle during ascent and as $(6.41^\circ, 31.67^\circ)$ at the hip, $(7.38^\circ, 91.93^\circ)$ at the knee, and $(-24.89^\circ, 24.18^\circ)$ at the ankle during descent. Additionally, we attempted to create a more natural stair-gait pattern by analyzing the movement of the hip on the anatomical transverse plane. The hip movements were estimated to within ± 1.57 cm and ± 2.00 cm for hip translation and to within $\pm 2.52^\circ$ and $\pm 2.70^\circ$ for hip rotation during stair ascent and stair descent, respectively. **Conclusions.** Based on the results, standard patterns of stair ascent and stair descent were derived and applied to a lower-limb rehabilitation robot with vertically movable footplates. The relative trajectory from the experiment ascertained that the function of stair walking in the robotic system properly worked within a normal ROM.

1. Background

According to a report by the United Nations, every year, more than 795,000 people in the United States have a stroke. Stroke patients 85 years of age and older make up 17% of all stroke patients. The worldwide percentage of the population 65 years of age or older is projected to grow from 9.1% to 15.9% between 2015 and 2050. Because of rapid aging, over the period from 2010 to 2050, the number of incident strokes is expected to more than double [1, 2]. Strokes are the most representative cause of serious long-term disabilities such as hemiplegia in adults. Therefore, rehabilitation of locomotion

is one of the main goals for people who have had a stroke. Traditional therapies usually focus on treadmill training to restore the functional mobility of the affected limbs [3, 4]. During such rehabilitation training, a patient is made to stand on a treadmill with his/her body supported by a suspension system [5], and several physiotherapists make and/or assist the walking movements of the patients' legs by manual handwork [6, 7]. However, the task is very difficult and laborious for therapists, and the procedure is complex to the extent that their excessive burden can lead to inconsistent quality of the task or reduced duration of net training. For these reasons, various robotic locomotion therapy systems

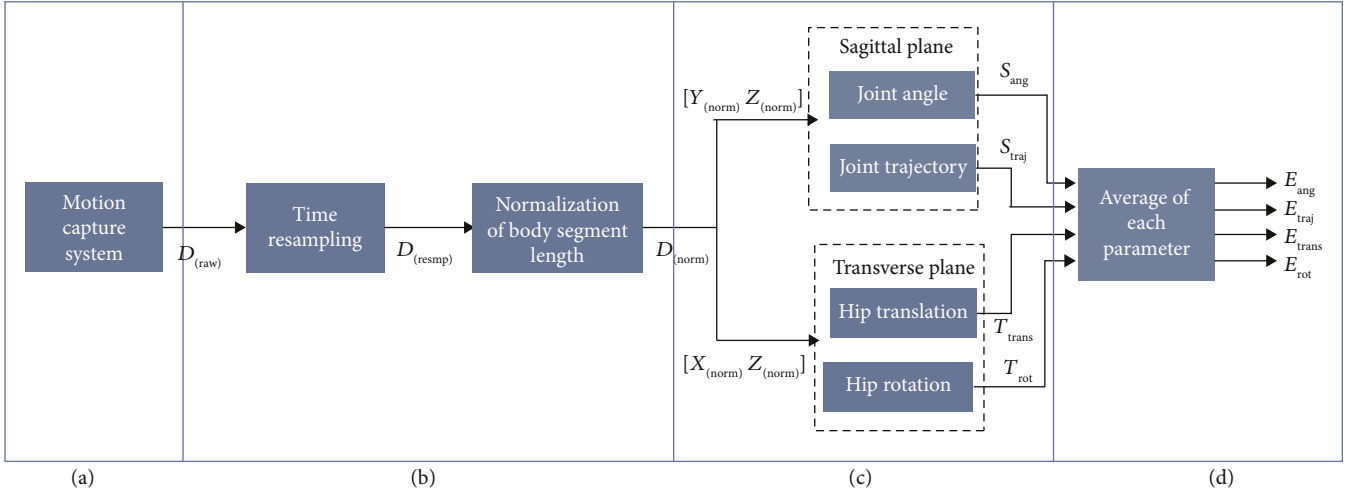


FIGURE 1: Protocol for analyzing a stair-walk pattern: (a) experiment and data acquisition with a motion capture system, (b) normalization of time and body segment length, (c) calculation of each parameter to analyze motion during stair ascent/descent, and (d) averaging every dataset to unify stair-gait pattern.

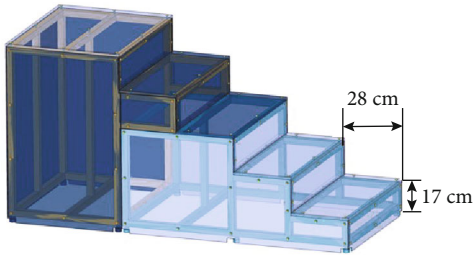


FIGURE 2: The experimental staircase was designed to have five steps. It had a 17 cm riser height and a 28 cm tread length according to the Korean building standards law.

have been developed, and some of them have been used to train patients in the clinical field [8–11].

Usually, these systems are based on treadmill-type trainers in combination with exoskeletons and body weight support (BWS) systems. The Lokomat® (Hocoma AG, Switzerland) uses linear actuators that control the joint angles at the hip and knee. The system is synchronized with the speed of the orthosis and the treadmill [12–14]. Similarly, the ReoAmbulator™ (Motorika, USA) employs powered leg orthosis and robotic arms, which enable patients to contribute during walking on the treadmill. The robotic arms are attached laterally to the thigh and shank of the patient for control of the lower limbs [15, 16]. The LokoHelp (Lokohelp Group, Germany) aids the gait-training program on the treadmill without the use of exoskeletons on a patients' legs. It consists of an ankle orthosis for foot-drop prevention and a harness [17]. Such treadmill-type devices provide training programs exclusively for level walking owing to their mechanical structure.

In traditional rehabilitation, therapists allow patients to perform special gaits such as ascending or descending stairs. This training is more effective in improving the gait ability of patients with low severity impairments than simple

TABLE 1: Information about each subject.

Subject no.	Gender	Length of the thigh (cm)	Length of the lower leg (cm)
Sub 1	Male	36.67	38.09
Sub 2	Female	34.41	33.85
Sub 3	Male	40.04	41.69
Sub 4	Male	36.38	40.79
Sub 5	Female	36.19	35.08
Sub 6	Male	40.81	39.90
Mean value of the length (standard deviation)		37.42 (2.47)	38.23 (3.18)

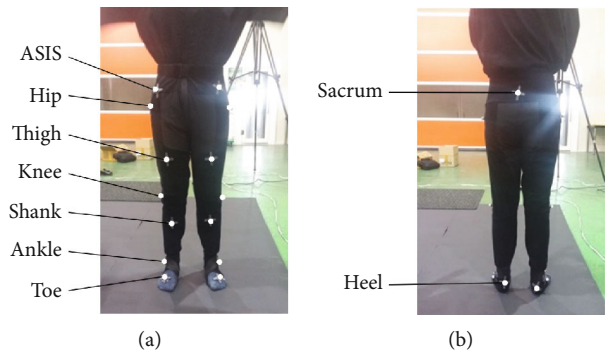


FIGURE 3: Markers were placed on a subject at the hip, thigh, knee, shank, ankle, and toe on both the right and the left sides including ASIS. (a) Front side. (b) Back side.

exercises or level walking because the activities require more muscle strength, balancing abilities, and complex movements [9, 18–20]. However, such an additional function can be aided by just a few robotic systems of the footplate type. The G-EO System™ (Reha Technology AG, Switzerland) is composed of robotic end-effector devices that allow



FIGURE 4: (a) Experimental environment for a camera setup (blue circles). (b) Position of the staircase. Yellow, red, and white arrows on the figures define the axes in coordinate space.

simulation of stair ascent and stair descent with a BWS system [21]. The GaitMaster5 system by the University of Tsukuba in Japan, is a lower-limb orthosis system; the patient straps his/her feet into pads connected to motion platforms. These platforms can move the user's foot forward (simulating walking) or up and down, similar to climbing [22]. The footplates guide the feet, thereby reproducing the gait trajectory of the ankle joint. These technologies tend to focus on movements of the ankle joint; furthermore, the absence of an exoskeleton or other structure that can control the hip and knee does not allow support of the joints. As a result, it may become challenging for patients to train correctly and effectively using systems where those joints are unconstrained [10].

The robotic lower-limb rehabilitation system gait trainer, M181-1, was developed by Cyborg-Lab, Korea [23]. The system facilitates level walking using robotic linkages and separate left and right footplates that track a patient's foot motion on the ground plane. As an improvement in the functionality of the system, the function of stair walking can be considered and a rehabilitation system that includes stair walking is expected to actively train patients. This rehabilitation system is a hybrid of the footplate and treadmill types because the system has footplates but the feet of a user do not always touch the plates. If the footplates of the robot are vertically and independently controlled, the patient can train not only for level walking but also for stair walking. In other words, this robotic system can be designed to provide patients with various gait exercises by combining exoskeletal links with spatially movable footplates.

In this study, a standard gait pattern of stair walking was created and converted into applicable data that implemented the stair-walking function in the M181-1 system. Thus, this study focused on the analysis of joint movement in stair ascent and stair descent for the application to the joint actuators of the robotic locomotion rehabilitation system. The first step of the protocol involved an experiment to acquire motion data using a motion capture system. The second was processing the data and calculating the parameters on

the anatomical sagittal and transverse planes. Finally, the average of each motion parameter was estimated as a standard stair-walk pattern.

2. Methods

To make a patient train with a natural gait pattern, hip motion in the medial-lateral direction and hip rotation, as well as the movement of each joint on the sagittal plane, need to be applied to the robot. Figure 1 indicates the process of analyzing stair-gait motion. The protocol has four steps: (a) position data acquisition, (b) data rescaling on the time and body segment length, (c) calculation of parameters for motion analysis, and (d) creation of a standard gait pattern.

2.1. Experiment for Data Acquisition. For the test, a laboratory staircase composed of five steps and having a riser height and tread length of 17 cm and 28 cm, respectively, was prepared according to the Korean building standards law [24]. The prepared staircase is shown in Figure 2. Six healthy participants, four males and two females, participated in this study. Table 1 summarizes information about the subjects.

To generate a reference standard gait pattern, the experiment was planned with subjects having no disorders in their lower limbs. The subjects were asked to repeatedly ascend and descend stairs at a self-selected velocity (normal pace) five times. The mean stride speeds were approximately 0.88 m/s in stair ascent and 0.96 m/s in stair descent. The method of stair walking was step-to-step, and a stride cycle was defined as the motion from the contact of the right foot of the first (third) step to the foot contact of the third (fifth) step, as described in [25]. Briefly, two cycles of stair-gaits were measured from the six subjects.

The highly complicated structure of the human skeleton enables movement with high degrees of freedom. Each body part moves in an unpredictable and complex motion trajectory. There are many types of systems for measuring body movements, such as optical marker-based tracking systems, markerless visual systems, and inertial measurement unit-

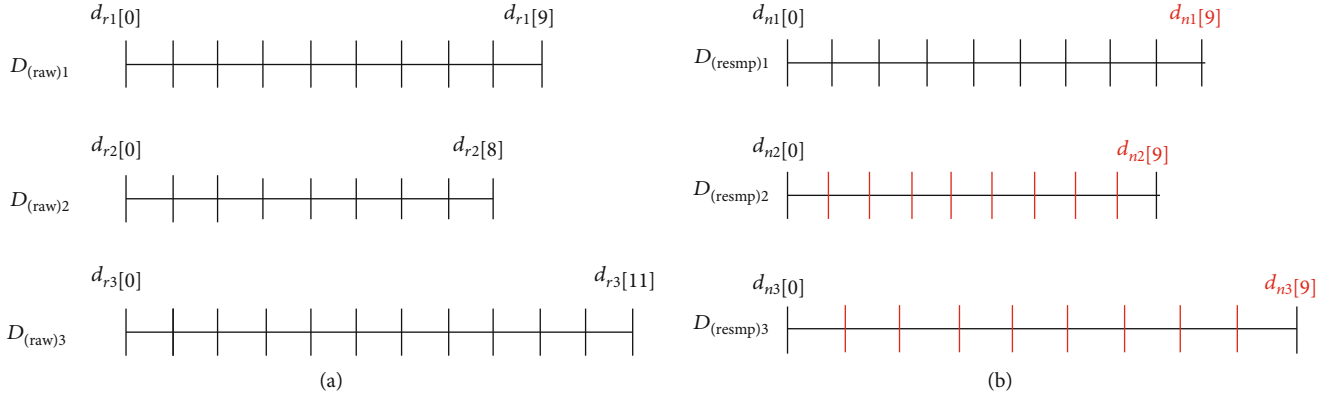


FIGURE 5: (a) Example of resampling datasets that have different lengths. (b) The vertical red lines are replaced using points by the cubic spline algorithm.

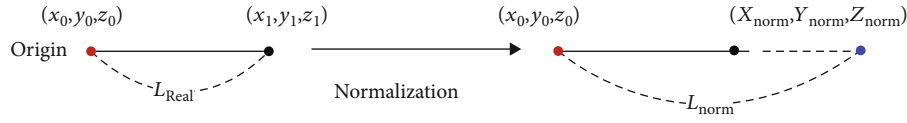


FIGURE 6: Normalization of body segment length.

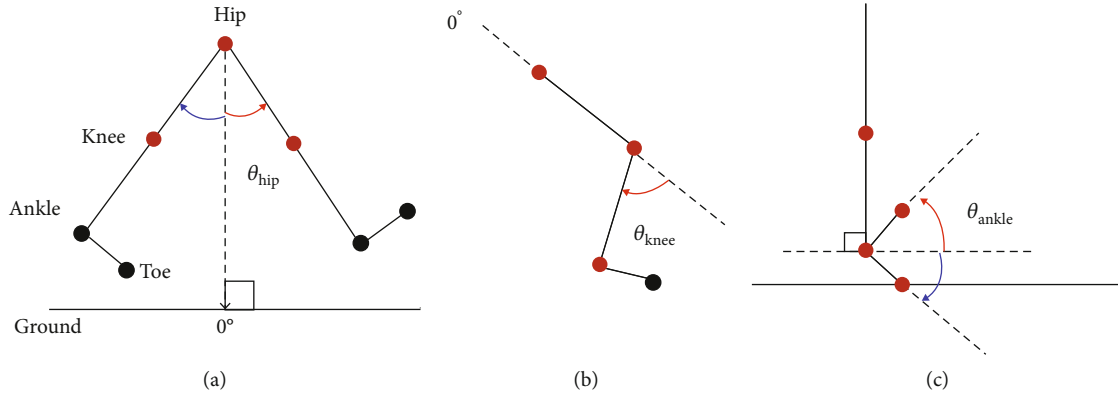


FIGURE 7: Definition of joint angles $S_{(ang)}$: (a) flexion/extension of hip joint θ_{hip} , (b) flexion/extension of the knee joint θ_{knee} , and (c) dorsi-/plantar-flexion of ankle joint θ_{ankle} . The red points indicate joints, and the red/blue arrows denote the positive/negative sign of angular direction.

(IMU-) based systems, which can be used to capture irregular human motion [26]. Because the optical marker-based system is frequently used in medicine [27–29] owing to its relatively high accuracy and minimal uncertainty of the subject's movement, the optical marker-based system was used to measure the normal stair-gait pattern in this study.

To acquire the position data of each joint in three-dimensional (3D) space, 17 optical markers were placed, one on the subject's sacrum, and two on the left and right anterior superior iliac spine (ASIS), hip, thigh, knee, shank, ankle, heel, and toe. Figure 3 presents the arrangement of the markers on the front and back sides of a subject. The placements of the reflective markers were determined for accurate tracking of anatomical landmarks related to kinematic variables during gait [31–34].

During the experiment, the positional information of the markers on the subjects was recorded at a rate of 160 Hz

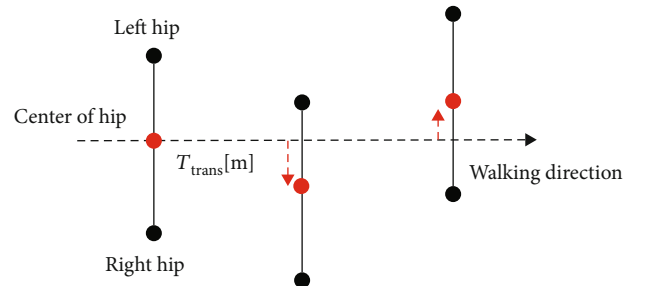


FIGURE 8: Definition of mediolateral movement, T_{trans} .

using a Prime 41 (OptiTrack, NaturalPoint Inc., USA) 3D motion capture system. The accuracy of this equipment is submillimeter, with a latency of 5.5 ms [30]. The calibration was performed with errors less than 2 mm. As shown in Figure 4(a), eight cameras, marked in blue circles, were

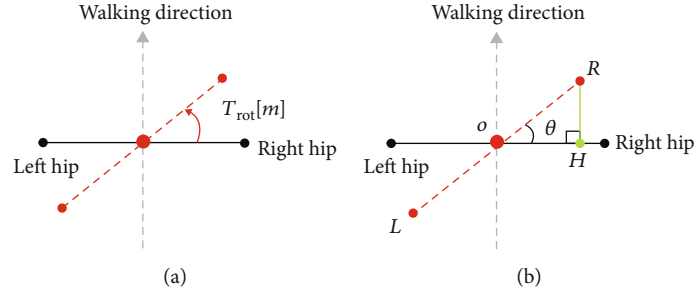


FIGURE 9: Definition of hip rotation angle T_{rot} : T_{rot} in (a) equals the included angle θ of the right triangle ΔROH in (b).

placed in a square with approximate dimensions of $10 \text{ m} \times 10 \text{ m}$. The x -axis was defined as the direction of walking, with the y -axis as the vertical direction. The direction of the right (negative value) and left sides (positive value) was defined as the z -axis. The experimental staircase was installed at the center of the square.

The datasets $D_{(raw)} = [X_{(raw)} Y_{(raw)} Z_{(raw)}]$ measured by the motion capture system consisted of the x , y , and z coordinates for one cycle of stair walking. Each portion of the datasets, $X_{(raw)}$, $Y_{(raw)}$, and $Z_{(raw)}$, denoted by time-series data for the attached 17 markers, was expressed by $X_{(raw)} \in R^{17 \times N}$, $Y_{(raw)} \in R^{17 \times N}$, and $Z_{(raw)} \in R^{17 \times N}$, where N is the number of data points recorded for each marker. The value of N was different among the obtained datasets because of each participant's walking speed. In this study, the datasets were obtained for the six subjects who completed two stride cycles of stair ascent and descent a total of five times. Thus, a total 60 datasets of $D_{(raw)}$ (6 subjects \times 5 times \times 2 cycles = 60 sets) were used for motion analysis of stair ascent and stair descent.

2.2. Data Preprocessing for Normalization. Because of the participants' own habits in walking, the walking velocity varied per person or trial. The lengths of body segments and the gap between the joints were also different among the participants. Therefore, it was necessary to normalize the data for time and space to simplify various conditions.

To unify the stride time condition, every $D_{(raw)}$ was resampled to dataset $D_{(resmp)} = [X_{(resmp)} Y_{(resmp)} Z_{(resmp)}]$ with the same number (M) of components by applying the interpolation method of a cubic spline. The cubic spline is a function constructed of piecewise third-order polynomials that are smoother and have smaller errors than some other interpolating polynomials [35, 36]. Figure 5 shows an example of resampling the data $D_{(raw)k}[m]$ ($k = 1, 2$, and 3 and $m = 0, 1, \dots, M_k - 1$, where k and M_k are constants), which is measured with the same sampling frequency but with a different length M_k . $D_{(resmp)k}$ is a modified dataset with the same number of samples ($M = 10$ in the example). To analyze the gait motion, the duration of a stride was divided into several sequences by physical and functional properties, such as period, i.e., stance and swing. The temporal unit was Stride cycle (%) for the analysis [20, 33, 37]. Therefore, the components of $D_{(resmp)}[m]$ ($m = 0, \dots, M - 1$, where M is a

constant) are considered as the identical functional sequence of gait cycle when m is an equal value for all cycles. Accordingly, if m is the same in every dataset, the parameters associated with the sagittal and transverse planes, S and T , respectively, in Figure 1 are averaged in the final step of the analysis protocol to generate a standard gait pattern.

The dataset also needed to be normalized in space to standardize the trajectories of the joints because the length of each body segment is different from the other. Hence, the positional trajectories of the joints were reconstructed by obtaining the equivalent lengths of each body segment. Figure 6 expresses the method for normalization of the body segment length.

A real segment length, L_{Real} , from reference point $P_0 = (x_0, y_0, z_0)$ to the other point $P_1 = (x_1, y_1, z_1)$ was rearranged to a new point $P_{(norm)} = (x_{norm}, y_{norm}, z_{norm})$ with the desired length $L_{(norm)}$. We decided $L_{(norm)}$ to be the average value of the length of the lower leg and thigh in Table 1. The relation between normalized point $P_{(norm)}$, the reference point P_0 , and the new point P_1 is shown in (1) and the normalized dataset $D_{(norm)}$ was computed through the equation given in [38].

$$P_{(norm)} = P_0 - \frac{L_{norm}}{L_{Real}} (P_0 - P_1). \quad (1)$$

2.3. Parameters for Motion Analysis. The hip, knee, and ankle joints were mainly characterized by large ranges of motion (ROMs) in the sagittal plane rather than in the coronal or transverse mobility [9, 18–20]. Despite the small actions on the transverse plane, it is important that hip movement can contribute to the advancement of muscle strength and effective balance training [39]. Thus, the parameters for analysis of motion on the transverse plane, in particular the hip joint, as well as that on the sagittal plane were examined. Four parameters were considered in this study: joint flexion/extension angle and positional trajectory (on the sagittal plane), tendency of hip translation, and hip rotation (on the transverse plane). These were determined by the relevant positions either to the sagittal plane $[Y_{(norm)} Z_{(norm)}]$ or to the transverse plane $[X_{(norm)} Z_{(norm)}]$.

The first parameter was angular trajectory $S_{ang} = [\theta_{hip}, \theta_{knee}, \theta_{ankle}]$, which signifies the trend of the hip, knee, and ankle during a stride on the stair. The angular trajectory was obtained from the first law of cosines. The directions

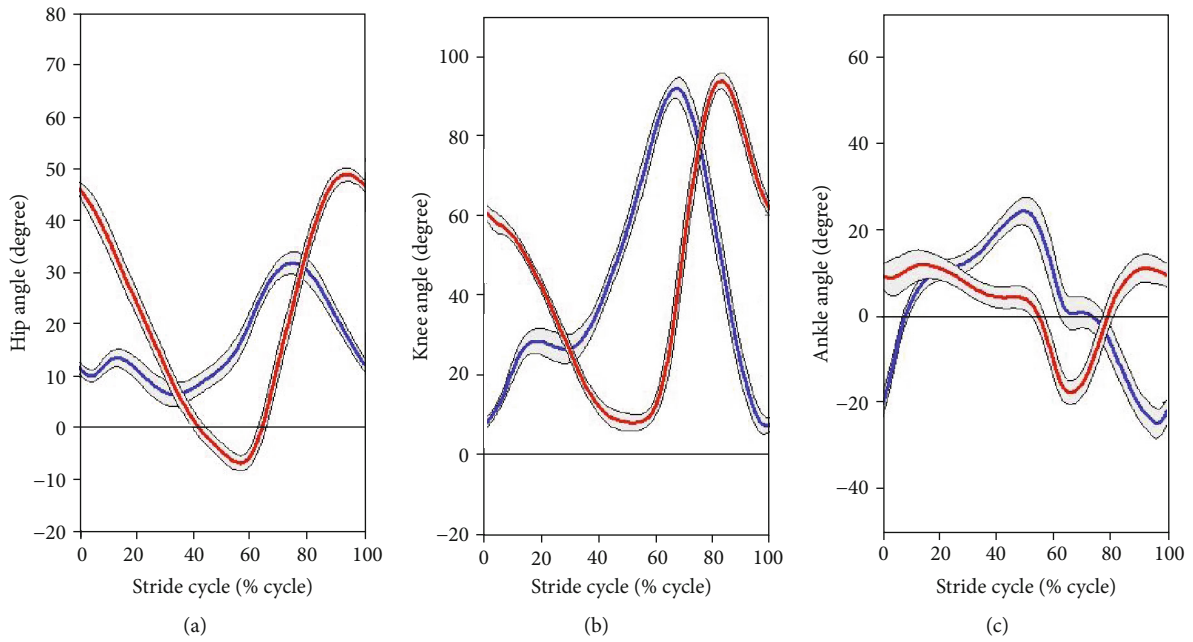


FIGURE 10: Mean angles of the (a) hip, (b) knee, and (c) ankle joint: the blue lines indicate the variation of the joint angle during stair ascent, and the red lines indicate the variation of the joint angle during stair descent.

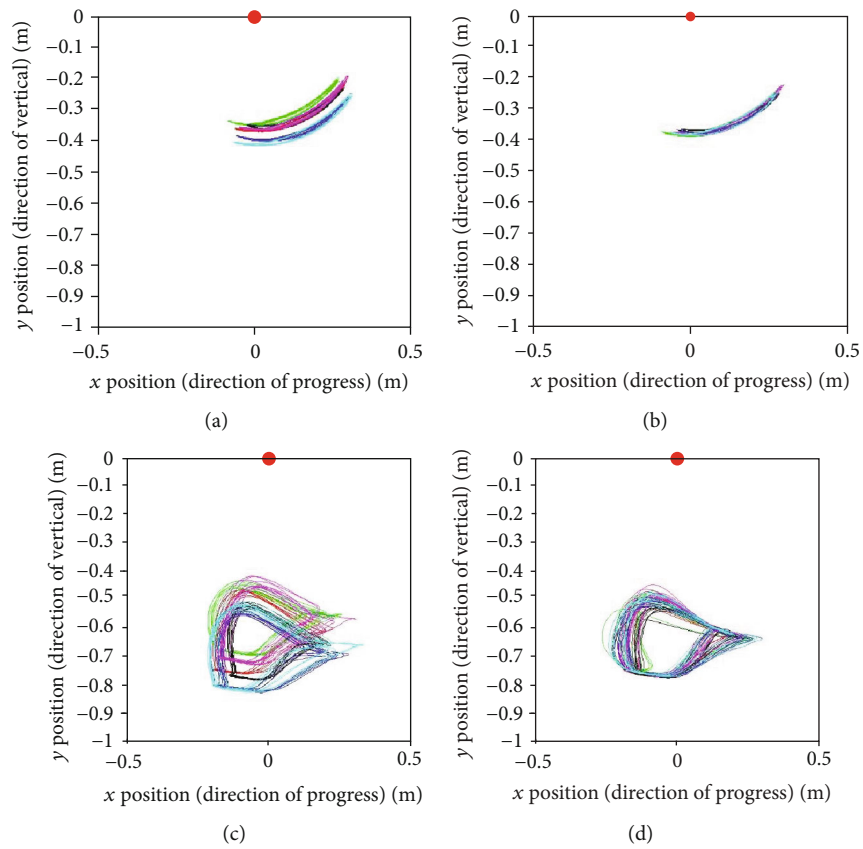


FIGURE 11: Relative trajectories from the hip joint during stair ascent: (a) knee trajectories and (c) ankle trajectories of each subject. (b and d) Knee and ankle trajectories are shown as a result of normalization for the lengths of the body segments.

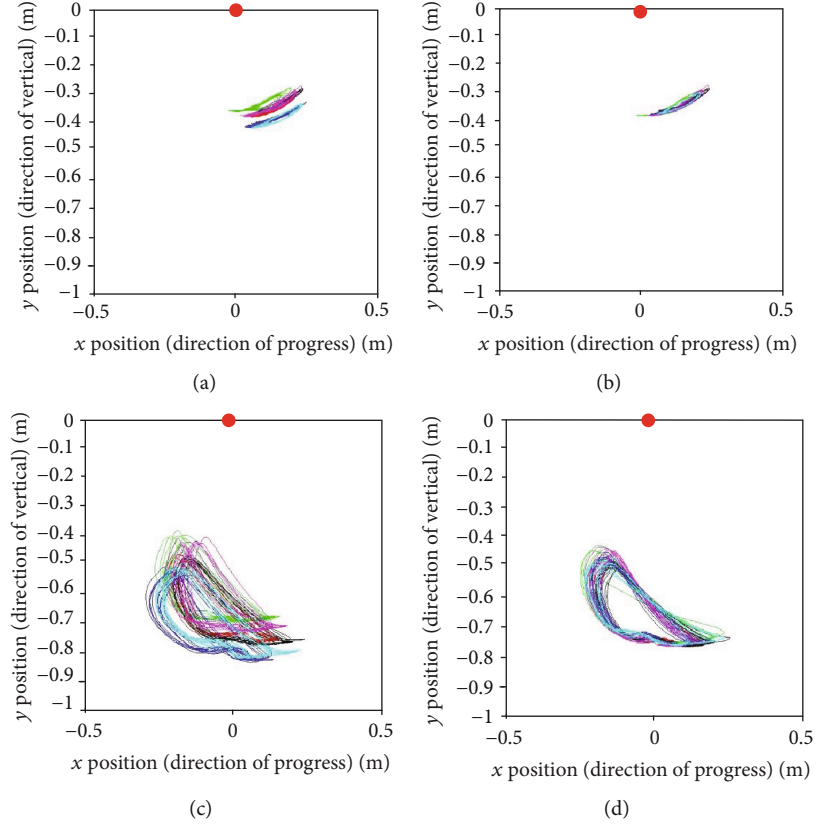


FIGURE 12: Relative trajectories from the hip joint during stair descent: (a) knee trajectories and (c) ankle trajectories of each subject. (b and d) Knee and ankle trajectories are shown as a result of normalization for the lengths of the body segments.

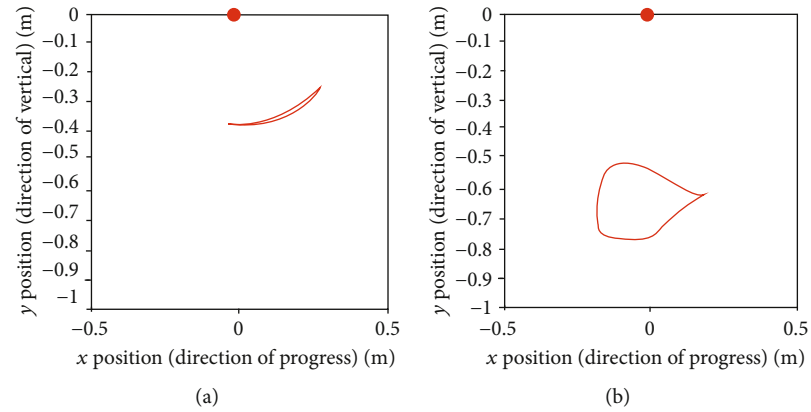


FIGURE 13: Standard trajectories of the (a) knee and (b) ankle during stair ascent.

indicated in Figure 7 and the following conditions defined these angles and their signs (positive/negative):

- (i) If the hip joint poses on hip flexion, $\theta_{\text{hip}} > 0$
- (ii) If the knee joint poses on knee flexion, $\theta_{\text{knee}} > 0$
- (iii) If the ankle joint poses on dorsiflexion, $\theta_{\text{ankle}} > 0$

The joints of the robot should be designed to move in a closed-loop pattern to generate a repetitive gait motion in the fixed system even if the resulting data from the experiment

is an open curve. For this reason, the trajectories of the joints, as secondary parameters, were replaced with relative positions from a point for stair-gait patterns during a circular walk. The reference point was set as the hip marker position. In other words, the position of the hip is considered as (0, 0) and the positions of the knee and ankle, which were secondary parameters, moved relatively to the reference point.

In general, most existing robotic locomotion rehabilitation systems address the kinematics on the sagittal plane because the lower limb is akin to working predominantly for flexion/extension during locomotion. Such a movement

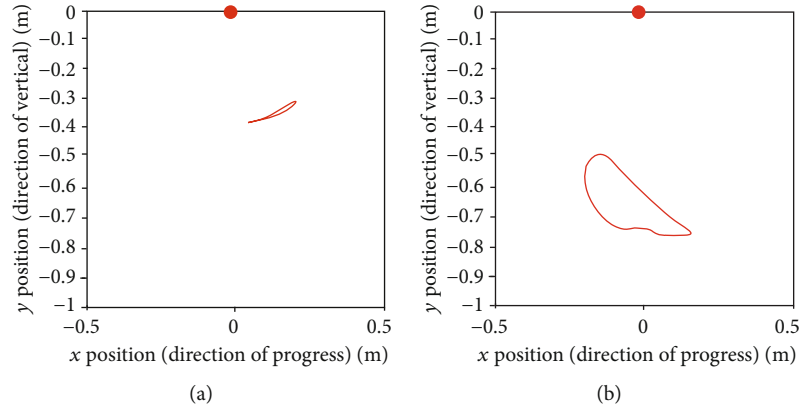


FIGURE 14: Standard trajectories of the (a) knee and (b) ankle during stair descent.

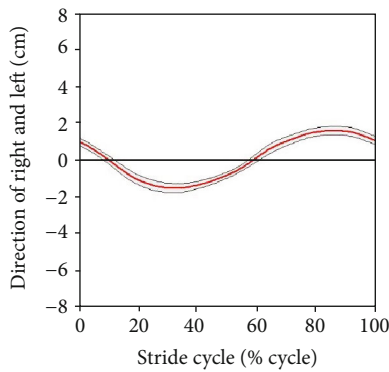


FIGURE 15: Variation of hip translation during stair ascent.

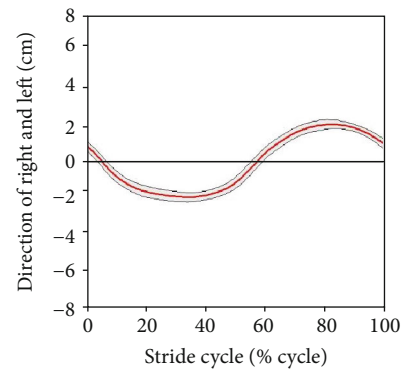


FIGURE 17: Variation of hip translation during stair descent.

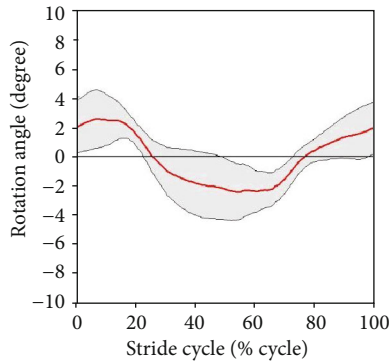


FIGURE 16: Variation of hip rotation during stair ascent.

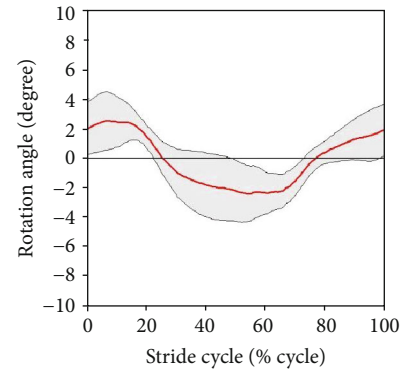


FIGURE 18: Variation of hip rotation during stair descent.

constrained to only one anatomical plane can prevent meaningful training for more effective therapeutic impact. The hip joint, especially, has distinct movement on the transverse plane owing to weight bearing or weight shifting during walking. Among the features of relevance to the robotic gait-training system [39], the hip translational movement, T_{trans} , in the mediolateral direction is considered as the third parameter. Figure 8 shows the method used to calculate the variation of hip movement on the transverse plane. The length between the left and right hip markers is considered a constant because it is an intrinsic value as the length of a body segment. The variation of mediolateral hip movement can be measured in terms of displacement of the center of the hip segment.

TABLE 2: ROM on all subjects applying to the motion of the robotic system.

	Stair ascent		Stair descent	
	Min.	Max.	Min.	Max.
Hip angle	-14.87°	56.10°	-4.62°	40.18°
Knee angle	0.051°	104.11°	0.0048°	104.14°
Ankle angle	-36.93°	24.13°	-37.87°	35.87°
Hip translation	-2.68 cm	2.68 cm	-3.17 cm	3.17 cm
Hip rotation	-16.71°	16.66°	-10.60°	10.29°

TABLE 3: Principal standard deviation within each subject.

	Sub 1		Sub 2		Sub 3		Sub 4		Sub 5		Sub 6	
	Min.	Max.	Min.	Max.	Min.	Max.	Min.	Max.	Min.	Max.	Min.	Max.
Stair ascent												
Hip angle	1.16	5.02	1.62	8.12	0.64	6.89	1.17	6.89	1.17	6.50	1.04	5.60
Knee angle	1.18	11.83	0.86	16.41	1.12	15.85	0.89	10.16	1.44	7.69	0.79	4.99
Ankle angle	0.51	7.77	1.10	8.66	1.30	8.89	1.35	8.54	0.61	7.54	0.36	4.17
Hip trans.	0.15	0.39	0.10	0.49	0.15	0.46	0.14	0.68	0.21	0.69	0.17	0.32
Hip rotation	1.31	6.52	1.09	4.47	0.14	2.00	0.27	2.70	0.02	2.50	0.32	2.72
Stair descent												
Hip angle	0.63	3.26	0.91	5.29	0.68	4.92	1.19	5.09	1.26	3.45	0.53	2.79
Knee angle	0.81	8.03	1.59	10.42	1.05	15.27	1.51	11.79	0.93	5.84	0.61	6.81
Ankle angle	1.09	6.27	1.15	6.78	1.20	8.69	2.49	11.49	0.44	6.78	0.33	5.57
Hip trans.	0.21	0.28	0.13	0.87	0.29	0.91	0.16	0.90	0.07	0.68	0.14	0.61
Hip rotation	0.17	1.35	0.51	1.77	0.41	1.70	0.73	3.28	0.06	3.00	0.11	1.25

Although the participants performed stair walking in the same coordinates and location, the planes on which their trajectories were described were not exactly coincident. In other words, the walking directions for all the data sets were different. Therefore, the data sets were manipulated so that they were in the same sagittal plane using the rotational displacement formula [40]. Thus, the right and left hip markers made a line, and the center point on the line drew a curve along weight shift. Then, trends of positional variation of the center point between the hip joints in the same walking direction could be determined.

The last parameter for the motion analysis is the angular displacement associated with the hip rotation during gait. Figure 9 indicates the methods for calculating the variation of hip rotation on the transverse plane. The hip rotation, T_{rot} , was defined as the angle between the line perpendicular to the walking direction and the line of hip markers. The rotation angle was determined by making a right triangle and finding the included angle with the inverse tangent function as shown Figure 9(b). The parameter was defined as a positive value where the right hip marker was placed in front of the left hip marker.

The result of the data processing such as normalization and interpolation makes trajectories for a gait cycle, but it might not be appropriate to be applied to a fixed type rehabilitation robot. If values in the beginning and end points of the trajectories are different, they make a discontinuity when the robot is working because the robot needs a cyclic gait pattern. Therefore, the points of the beginning and the end points on all results should match to make a cyclic pattern. To resolve this problem, the obtained datasets were processed by the cubic spline method using the points corresponding to the first 5% (0 to 5%) and the last 5% (96 to 100%) of the stride cycle.

3. Results

3.1. Angular and Positional Trajectories of Joints on the Sagittal Plane. As mentioned in the previous section, we calculated two parameters of joint angles and trajectories on the

TABLE 4: Principal standard deviation of all subjects.

	Stair ascent		Stair descent	
	Min.	Max.	Min.	Max.
Hip angle	2.12	6.28	2.30	4.86
Knee angle	2.96	12.22	2.55	11.18
Ankle angle	4.57	8.70	3.73	11.10
Hip translation	0.32	0.53	0.38	0.69
Hip rotation	1.47	4.42	1.80	3.17

sagittal plane to analyze stair-walk motion. Figure 10 shows variations in the hip, knee, and ankle joint angles during stair ascent (red line) and stair descent (blue line), and their standard deviations are given by the gray areas. In this study, the average ROMs for the subjects' hip joints in extension/flexion during a stair ascent and descent cycle were $(-6.75^\circ, 48.69^\circ)$ and $(6.41^\circ, 31.67^\circ)$, respectively. The average ROM of the knee joints in extension/flexion was $(8.20^\circ, 93.78^\circ)$ during stair ascent and $(7.38^\circ, 91.93^\circ)$ during stair descent. Additionally, the average ROMs of ankle joints in plantar-/dorsiflexion were $(-17.78^\circ, 11.75^\circ)$ and $(-24.89^\circ, 24.18^\circ)$ during stair ascent and descent, respectively.

Figures 11 and 12 present the relative trajectories of the knee and ankle joints for the hip joint on the sagittal plane during stair ascent and descent, respectively. The different colors of trajectories in Figures 11 and 12 present different subjects. To reduce the individual variation in the lengths of the body segments, the data were normalized with the algorithm described in Section 2.2. The red points on these figures represent the hip marker at the reference point (0, 0).

After normalization, we attempted to find the standard trajectories of the knee and ankle. As shown in Figures 13 and 14, the averaged trajectories of the normalized datasets, the red lines, are considered the standard trajectories in this experiment.

3.2. Hip Movement on the Transverse Plane. Figures 15 and 16 present the variation in hip translation and rotation,

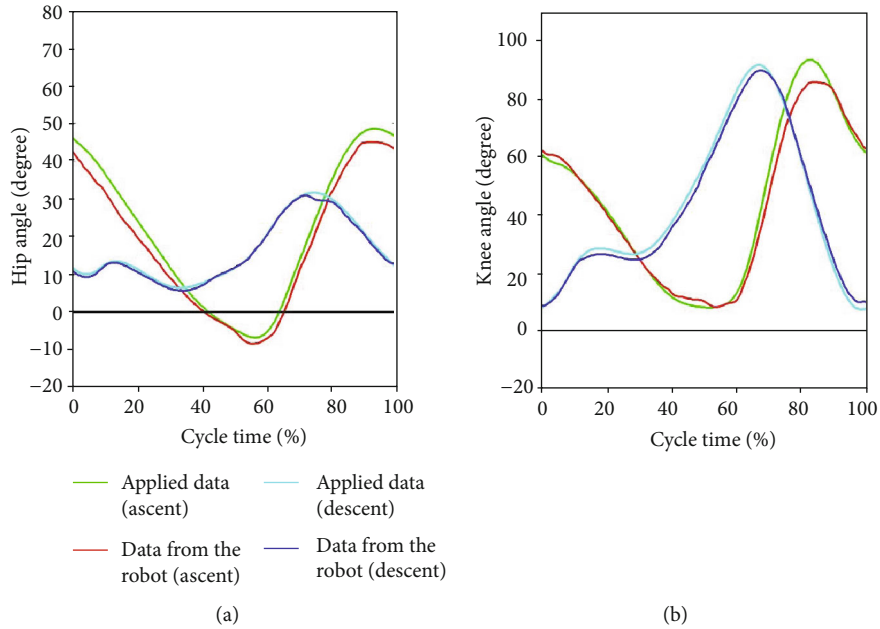


FIGURE 19: Comparison of the angular trajectories on (a) hip joint and (b) knee joint between robot movement and experimental data.

respectively, during a stair-ascent cycle. The translation/rotation is indicated by the red line. The standard deviation is indicated by gray lines. When ascending a stair, the averaged ROMs on the transverse plane were within ± 1.57 cm for translation and $\pm 2.52^\circ$ for rotational movement.

As with Figures 15 and 16, Figures 17 and 18 indicate trends in the hip movement for a stair-gait cycle. The range of translation movement was estimated to be within ± 2.00 cm, and hip rotation was estimated to be within $\pm 2.70^\circ$. Table 2 shows the maximum range in which subjects actually moved in the experiment.

Table 2 shows the minimum and maximum values of data, which consist of the resampled 120 datasets from the experiment. The values in Table 2 cover the range of all subjects' motion.

Because the gait cycle was divided into 200 phases to derive the pattern of stair walking, standard deviation values were different for each point in Figure 10 and Figures 15–18. Thus, the principal estimation of standard deviations for each result for each motion is summarized in Tables 3 and 4. Table 3 shows the maximal and minimal values of standard deviations for each subject. Table 4 presents the principal estimations of standard deviation on each result in Figure 10 and Figures 13–18.

3.3. Application of Derived Pattern to the Robotic System. If the trajectory is compared with the joint displacement data of a robotic training system served by itself, it can ascertain whether the system properly works within a normal ROM, e.g., the height of a leg lift. Actual angular trajectories performed by the robotic system designed for stair walking during stair ascent and descent are displayed in Figure 19. The trajectories generally follow the gait pattern obtained from this study (green and light blue line) even though there is some delay or errors—average errors within $\pm 8\%$ were calculated.

4. Discussion

In this study, we attempted to create patterns of stair walking for application to a robotic lower-limb rehabilitation system. A subject's legs moved in a cyclical pattern during stair negotiation. The movement of the lower limb primarily appears as a flexion/extension of each joint [20]. Therefore, initially, variations in the joint angles of the hips, knees, and ankles were extracted on the anatomical sagittal plane such that the robotic exoskeleton of the gait-training system can work with the most basic gait pattern. The calculated angular variations of the hips, knees, and ankles, as shown in Figure 10, were used to establish the basic pattern in stair ascent and stair descent.

As shown in Table 1, the subjects had different stride lengths and leg lengths in the stair-walk experiment. Therefore, we normalized the lengths of body segments before calculating the knee and ankle trajectories relative to the hip. As shown in Figures 11 and 12, it was easy to find the trend of the normalized knee and ankle joint trajectories. Additionally, the normalization is supposed to establish criteria for the gait pattern to drive a robotic gait trainer after standardization of the relative trajectories. Figures 13 and 14 show the desired tracks of the knee and ankle joints for a robotic system mimicking the experimental pattern in Figure 10.

In addition to the analysis on the sagittal plane, we tried to examine the hip joint on the transverse plane. The medial-lateral movements of the hip during stair walking seemed to be similar among the subjects, as shown in Figures 15 and 17. However, the variation in hip rotation angles had large standard deviations, as shown in Figures 16 and 18. This is due to differences in the gait patterns of each individual, such as step length, body segment length, gender, and other anatomical factors. Its effectiveness should be investigated by a clinical test, which, however, is beyond the scope of this work.

The exoskeleton of the robotic system was designed based on the results shown in Table 2, and it could move within a range that covered all subjects. As shown in Tables 3 and 4, standard deviations on the sagittal plane in Table 3 are larger than those in Table 4, and the results on the transverse plane in Table 4 are larger than those in Table 3. It means that the standard patterns on the sagittal plane reflected the general trend of stair walk, and the variation within an individual on the transverse plane is larger than among subjects. Therefore, each joint of the exoskeleton was controlled by a standard pattern in Figure 10 for reflecting general patterns on the robotic system. On the other hand, hip movements on the transverse plane were controlled within ranges of standard deviations depending on the individual difference as shown in Figures 15–18.

As compared to the motion of a robot with the derived standard pattern shown in Figure 19, the trend of the motion between the applied data and that measured from the robot is almost similar, but some inevitable errors occurred. These errors are considered to be due to variations in the measuring or control method in the robot.

5. Conclusions

The present study has shown the process of analysis and the method for acquiring the motion patterns of lower limbs during stair walking. The ROMs determined through this study covered the clinically known ROMs in accordance with each gait phase [20, 25, 41, 42]. Consequently, we concluded that our experimental results indicate normal stair-gait patterns for the hip, knee, and ankle on the sagittal plane. However, there are several features that should be considered when analyzing hip rotation because it tends to be more influenced by diverse individual walking habits or body type. Therefore, we need to experiment further with algorithms that consider various factors when determining the normal gait pattern of a rotated hip during stair walking. Moreover, further research is required on the application of the obtained data to a robot to ascertain whether natural stair-walk training is possible after an additional study has been conducted on hip rotation.

Data Availability

The kinematic data used to support the findings of this study are available from the corresponding author upon request.

Disclosure

This paper is an extended version of a paper presented at the 39th annual International Conference of the IEEE Engineering in Medicine and Biological Society (EMBC), held in Jeju, Korea, on 11–15 July 2017 [23].

Conflicts of Interest

The authors declare that there is no conflict of interest regarding the publication of this paper.

Acknowledgments

This study was jointly supported by the Technology Innovation Program (grant number: 20000843) funded by the Ministry of Trade, Industry, and Energy (MOTIE, South Korea), a grant of the Asan Institute for Life Sciences intramural research project funded by Asan Medical Center (grant number: 2019-692), and a grant of the Korea Health Technology R&D Project through the Korea Health Industry Development Institute (KHIDI) funded by the Ministry of Health & Welfare, Republic of Korea (grant number: HI17C2410).

References

- [1] E. J. Benjamin, P. Muntner, A. Alonso et al., “Heart disease and stroke statistics—2019 update: a report from the American Heart Association,” *Circulation*, vol. 139, no. 10, pp. e56–e528, 2019.
- [2] United Nations, “Department of Economic and Social Affairs,” in *World Population Prospects: The 2019 Revision: Highlights*, United Nations, New York, NY, USA, 2019.
- [3] A. Wernig, S. Müller, A. Nanassy, and E. Cagol, “Laufband therapy based on “rules of spinal locomotion” is effective in spinal cord injured persons,” *European Journal of Neuroscience*, vol. 7, no. 4, pp. 823–829, 1995.
- [4] S. Hesse, C. Bertelt, M. T. Jahnke et al., “Treadmill training with partial body weight support compared with physiotherapy in nonambulatory hemiparetic patients,” *Stroke*, vol. 26, no. 6, pp. 976–981, 1995.
- [5] M. Visintin, H. Barbeau, N. Korner-Bitensky, and N. E. Mayo, “A new approach to retrain gait in stroke patients through body weight support and treadmill stimulation,” *Stroke*, vol. 29, no. 6, pp. 1122–1128, 1998.
- [6] J. Galvez and D. Reinkensmeyer, “Robotics for gait training after spinal cord injury,” *Topics in Spinal Cord Injury Rehabilitation*, vol. 11, no. 2, pp. 18–33, 2005.
- [7] S. B. Brozman and R. C. Manske, *Clinical Orthopaedic Rehabilitation: An Evidence-Based Approach*, Elsevier Health Sciences, USA, 3rd ed. edition, 2011.
- [8] S. P. Sayers and J. Krug, “Robotic gait-assisted therapy in patients with neurological injury,” *Missouri Medicine*, vol. 105, no. 2, pp. 153–158, 2008.
- [9] I. Diaz, J. J. Gil, and E. Sanchez, “Lower-limb robotic rehabilitation: literature review and challenges,” *Journal of Robotics*, vol. 2011, Article ID 759764, 11 pages, 2011.
- [10] A. Pennycott, D. Wyss, H. Vallery, V. Klamroth-Marganska, and R. Riener, “Towards more effective robotic gait training for stroke rehabilitation: a review,” *Journal of Neuroengineering and Rehabilitation*, vol. 9, no. 1, p. 65, 2012.
- [11] M. Dzahir and S.-i. Yamamoto, “Recent trends in lower-limb robotic rehabilitation orthosis: control scheme and strategy for pneumatic muscle actuated gait trainers,” *Robotics*, vol. 3, no. 2, pp. 120–148, 2014.
- [12] S. Jezernik, G. Colombo, T. Keller, H. Frueh, and M. Morari, “Robotic orthosis Lokomat: a rehabilitation and research tool,” *Neuromodulation: Technology at the Neural Interface*, vol. 6, no. 2, pp. 108–115, 2003.
- [13] G. Colombo, M. Joerg, R. Schreier, and V. Dietz, “Treadmill training of paraplegic patients using a robotic orthosis,” *Journal of Rehabilitation Research and Development*, vol. 37, no. 6, pp. 693–700, 2000.

- [14] S. Jezernik, G. Colombo, and M. Morari, "Automatic gait-pattern adaptation algorithms for rehabilitation with a 4-DOF robotic orthosis," *IEEE Transactions on Robotics and Automation*, vol. 20, no. 3, pp. 574–582, 2004.
- [15] G. R. West, *Powered gait orthosis and method of utilizing same*, U.S. Patent 6 689 075, 2004.
- [16] S. Fisher, L. Lucas, and T. Adam Thrasher, "Robot-assisted gait training for patients with hemiparesis due to stroke," *Topics in Stroke Rehabilitation*, vol. 18, no. 3, pp. 269–276, 2011.
- [17] S. Freivogel, J. Mehrholz, T. Husak-Sotomayor, and D. Schmalohr, "Gait training with the newly developed "LokoHelp"-system is feasible for non-ambulatory patients after stroke, spinal cord and brain injury. A feasibility study," *Brain Injury*, vol. 22, no. 7-8, pp. 625–632, 2008.
- [18] J. J. Eng and P. F. Tang, "Gait training strategies to optimize walking ability in people with stroke: a synthesis of the evidence," *Expert Review of Neurotherapeutics*, vol. 7, no. 10, pp. 1417–1436, 2007.
- [19] Y. K. Choi, K. Kim, and J. U. Choi, "Effects of stair task training on walking ability in stroke patients," *Journal of Physical Therapy Science*, vol. 29, no. 2, pp. 235–237, 2017.
- [20] J. Perry and J. M. Burnfield, "Stair negotiation," in *Gait Analysis: Normal and Pathological Function*, pp. 365–384, Slack Incorporated, NJ, USA, 2nd ed. edition, 2010.
- [21] S. Hesse, A. Waldner, and C. Tomelleri, "Innovative gait robot for the repetitive practice of floor walking and stair climbing up and down in stroke patients," *Journal of NeuroEngineering and Rehabilitation*, vol. 7, no. 1, 2010.
- [22] H. Yano, S. Tamefusa, N. Tanaka, H. Saitou, and H. Iwata, "Gait rehabilitation system for stair climbing and descending," in *2010 IEEE Haptics Symposium*, pp. 393–400, Waltham, Mass, USA, 2010.
- [23] S. E. Park, Y. J. Ho, Y. Moon, and J. Choi, "Analysis of gait pattern during stair walk for improvement of gait training robot," in *Proceedings of 39th annual International Conference of the IEEE Engineering in Medicine and Biological Society (EMBC)*, Jeju, Korea, July 2017.
- [24] "Enforcement decree of the building act," in *Ministry of Land, Infrastructure and Transport*, Ministry of Land, Infrastructure and Transport, Korea, 2017.
- [25] A. Protopapadaki, W. I. Drechsler, M. C. Cramp, F. J. Coutts, and O. M. Scott, "Hip, knee, ankle kinematics and kinetics during stair ascent and descent in healthy young individuals," *Clinical biomechanics*, vol. 22, no. 2, pp. 203–210, 2007.
- [26] H. Zhou and H. Hu, "Human motion tracking for rehabilitation—a survey," *Biomedical Signal Processing and Control*, vol. 3, no. 1, pp. 1–18, 2008.
- [27] P. Kejonen, K. Kauranen, and H. Vanharanta, "The relationship between anthropometric factors and body-balancing movements in postural balance," *Archives of Physical Medicine and Rehabilitation*, vol. 84, no. 1, pp. 17–22, 2003.
- [28] R. A. Brady, M. J. Pavol, T. M. Owings, and M. D. Grabiner, "Foot displacement but not velocity predicts the outcome of a slip induced in young subjects while walking," *Journal of Biomechanics*, vol. 33, no. 7, pp. 803–808, 2000.
- [29] I. W. Charlton, P. Tate, P. Smyth, and L. Roren, "Repeatability of an optimised lower body model," *Gait & Posture*, vol. 20, no. 2, pp. 213–221, 2004.
- [30] *Prime 41 Data Sheet*, NaturalPoint Inc, Corvallis, OR, USA, 2012.
- [31] D. Tabakin, "A comparison of 3D gait models based on the Helen Hayes marker-set," *phD. Dissertation*, Univ. Cape Town, South Africa, 2000.
- [32] U. Della Croce, A. Cappozzo, and D. C. Kerrigan, "Pelvis and lower limb anatomical landmark calibration precision and its propagation to bone geometry and joint angles," *Medical & Biological Engineering & Computing*, vol. 37, no. 2, pp. 155–161, 1999.
- [33] U. Della Croce, V. Camomilla, A. Leardini, and A. Cappozzo, "Femoral anatomical frame: assessment of various definitions," *Medical Engineering & Physics*, vol. 25, no. 5, pp. 425–431, 2003.
- [34] C. L. Vaughan, B. L. Davis, and C. O. Jeremy, *Dynamics of Human Gait*, Kiboho Publishers, Cape Town, South Africa, 2nd ed. edition, 1999.
- [35] S. C. Chapra and R. P. Canale, "Spline interpolation," in *Numerical Methods for Engineers*, pp. 511–525, McGraw Hill, New York, NY, USA, 7th ed. edition, 2015.
- [36] R. L. Burden and J. D. Faires, "Interpolation and polynomial approximation," in *Numerical Analysis*, Thomson Brooks/Cole, Pacific Grove, CA, USA, 9th ed. edition, 2016.
- [37] C. Kirtley, "Observational gait analysis," in *Clinical Gait Analysis: Theory and Practice*, pp. 267–278, Elsevier Health Sciences, 2006.
- [38] S. Aksoy and R. M. Haralick, "Feature normalization and likelihood-based similarity measures for image retrieval," *Pattern Recognition Letters*, vol. 22, no. 5, pp. 563–582, 2001.
- [39] M. S. Gaston, E. Rutz, T. Dreher, and R. Brunner, "Transverse plane rotation of the foot and transverse hip and pelvic kinematics in diplegic cerebral palsy," *Gait & Posture*, vol. 34, no. 2, pp. 218–221, 2011.
- [40] E. Kreyszig, "Vector differential calculus. Grad, div, curl," in *Advanced Engineering Mathematics*, pp. 354–412, John Wiley & Sons, Hobokrn, USA, 10th ed. edition, 2010.
- [41] S. Nadeau, B. J. McFadyen, and F. Malouin, "Frontal and sagittal plane analyses of the stair climbing task in healthy adults aged over 40 years: what are the challenges compared to level walking?," *Clinical biomechanics*, vol. 18, no. 10, pp. 950–959, 2003.
- [42] R. Riener, M. Rabuffetti, and C. Frigo, "Stair ascent and descent at different inclinations," *Gait & posture*, vol. 15, no. 1, pp. 32–44, 2002.

Research Article

Effect of Common Pavements on Interjoint Coordination of Walking with and without Robotic Exoskeleton

Jinlei Wang,¹ Jing Qiu ,² Lei Hou,² Xiaojuan Zheng,² and Suihuai Yu¹

¹Northwestern Polytechnical University, China

²University of Electronic Science and Technology of China, China

Correspondence should be addressed to Jing Qiu; qiuqing@uestc.edu.cn

Received 22 March 2019; Revised 23 July 2019; Accepted 2 September 2019; Published 1 October 2019

Guest Editor: Michelle Johnson

Copyright © 2019 Jinlei Wang et al. This is an open access article distributed under the Creative Commons Attribution License, which permits unrestricted use, distribution, and reproduction in any medium, provided the original work is properly cited.

Background. The analysis and comprehension of the coordination control of a human gait on common grounds benefit the development of robotic exoskeleton for motor recovery. **Objective.** This study investigated whether the common grounds effect the interjoint coordination of healthy participants with/without exoskeletons in walking. **Methods.** The knee-ankle coordination and hip-knee coordination of 8 healthy participants in a sagittal plane were measured on five kinds of pavements (tiled, carpet, wooden, concrete, and pebbled) with/without exoskeletons, using the continuous relative phase (CRP). The root mean square of CRP (CRP_{RMS}) over each phase of the gait cycle is used to analyze the magnitude of dephasing between joints, and the standard deviation of CRP (CRP_{SD}) in the full gait cycle is used to assess the variability of coordination patterns between joints. **Results.** The $CRP_{Hip-Knee/RMS}$ of the carpet pavement with exoskeleton is different from that of other pavements (except the tiled pavement) in the midstance phase. The $CRP_{Hip-Knee/RMS}$ on the pebble pavement without exoskeleton is less than that on the other pavements in all phases. The $CRP_{Hip-Knee/SD}$ of the pebble pavement without exoskeleton is smaller than that of other pavements. The $CRP_{Knee-Ankle/SD}$ with/without exoskeleton is similar across all pavements. **Conclusion.** The compressive capacity of the pavement and the unevenness of the pavement are important factors that influence interjoint coordination, which can be used as key control elements of gait to adapt different pavements for robotic exoskeleton. **Novelty.** We provide a basis of parameter change of kinematics on different common grounds for the design and optimization of robotic exoskeleton for motor recovery.

1. Introduction

The robotic exoskeleton provides assistance in time and replicates human walking at some extent. The interjoint coordination patterns of human walking are applied to the gait control for robotic exoskeleton. However, the gait of robotic exoskeleton for rehabilitation is usually fixed, and the robotic exoskeleton for rehabilitation cannot perceive ground changes. Although much is known about the intersegmental coordination of walking on the treadmill or uneven ground [1], the effect of common grounds such as the tiled ground on interjoint coordination has not been studied systematically.

The information of walking patterns, such as the coordination pattern between joints, provides basic data to

classification and algorithm of gait control [2] for robotic exoskeleton. The robotic exoskeleton reduces the muscular effort compared to free walking [3, 4]. To increase walking efficiency of humans, it needs to reduce impact on the natural walking gait by minimizing changes in kinematics [5]. In addition, the appropriate assistive strategies constitute the human-robot motion, which benefits the assistive isotropy of the motion, and improves the assistive efficiency of the force [6]. Matching the assistance pattern of exoskeleton with the individual also needs to maximize the advantage of the device and minimize the human energy cost during walking [7].

The interjoint coordination in a sagittal plane was analyzed by the continuous relative phase (CRP) [8], which correlated temporal-spatial parameters [9] in joints and was

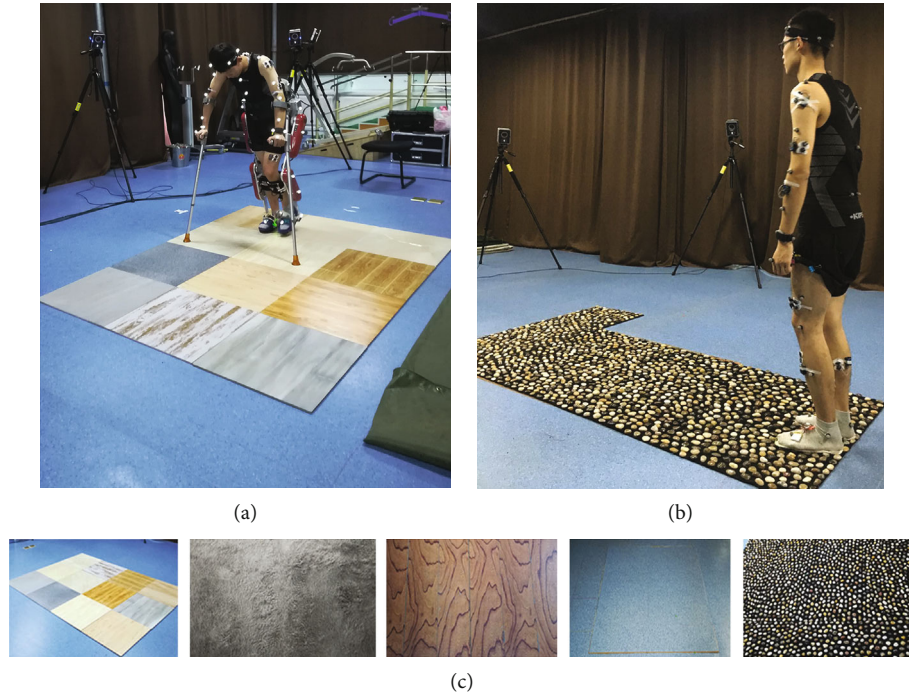


FIGURE 1: Experimental environment: (a) participant with exoskeleton walking on tiled pavement, (b) participant without exoskeleton walking on pebbled pavement, and (c) tiled pavement, carpet pavement, wooden pavement, concrete pavement, and pebbled pavement.

used to evaluate the intersegment coordination [1, 10–12] as well as the interjoint coordination [8, 13, 14]. Human walking on different kinds of grounds seems to adopt different walking patterns through adjusting the joint kinematic. Still, the coordination patterns of a human body with exoskeletons normally imitate the coordination patterns of the human body without exoskeletons. The more similar the interjoint coordination patterns of robotic exoskeleton is to that of a normal person, the better for hemiplegic patients on motor recovery. It will be detrimental to the rehabilitation of hemiplegic patients if the tendency of the joint angle of the human body with/without exoskeleton is so different. Robotic lower limb exoskeletons have significant potential for gait assistance and rehabilitation [15]. However, we partly understand how people walking with robotic devices adapt to the daily living environment. Studying how an individual adapts or responds to different grounds in walking remains an open challenge [16, 17].

What is more, it is hard to find studies focusing on the effect of common grounds on joint kinematics when humans walk on different kinds of grounds with exoskeleton in daily life. Hence, in the current study, five kinds of pavements (tiled pavement, carpet pavement, wooden pavement, concrete pavement, and pebble pavement) were paved with real material in the experimental environment to figure out which joint the humans would adjust to adapt different pavements and to see if they adjust the patterns of joint kinematics to adapt different kinds of grounds. Based on CRP, the consistent proximal-to-distal coordination, such as hip-knee coordination and knee-ankle coordination, was measured with/without exoskeleton on five kinds of pavements across eight healthy participants in this study. We also expect the

study of consistent proximal-to-distal coordination to provide support for the motion planning of robotic exoskeleton during walking on different kinds of grounds. The hypotheses of this study are as follows:

Hypothesis 1: when walking with exoskeletons on the five kinds of pavements, the pattern and variability of interjoint coordination would be similar between different pavements

Hypothesis 2: when walking without exoskeletons on the five kinds of pavements, there would be a significant difference between different pavements in the pattern and variability of interjoint coordination

2. Methods

Eight young and healthy participants (age: 23 ± 1.6 years, sex: male, leg length: 0.89 ± 0.03 m, mass: 76.6 ± 6.4 kg, and height: 172.6 ± 6.5 cm) were recruited to take part in the experiment with written informed consent before the experiment. All procedures were approved by the Sichuan Provincial Rehabilitation Hospital Review Board.

The kinematics data were captured by the VICON System (V5, Oxford, VICON, UK) with 8 infrared cameras at 100 Hz. The human-exoskeleton system marker set (Figure 1(a)) was a modification of a marker set in the VICON system. The human and exoskeleton were regarded as a whole system in the modification of the marker set, so markers placed on the human's pelvis, legs, ankles, and heels are moved to the exoskeleton's pelvis, legs, ankles, and heels. Thirty-nine reflective markers were placed on the human-exoskeleton system, including the seventh cervical vertebrae, sternum, shoulders, elbows, anterior-superior iliac spine,

TABLE 1: Friction coefficients of pavements.

Pavements	Tiled	Carpet	Wooden	Concrete	Pebbled
Coefficient of frictions	0.32	0.15	0.33	0.34	0.20

TABLE 2: Gait parameters with/without exoskeleton at five kinds of pavements.

	With exoskeleton					Without exoskeleton				
	Tiled	Carpet	Wooden	Concrete	Pebbled	Tiled	Carpet	Wooden	Concrete	Pebbled
Peak ankle dorsiflexion in midstance (°)	9 ± 5	9 ± 4	6 ± 5	6 ± 6	8 ± 4	14 ± 3	13 ± 5	14 ± 4	14 ± 2	12 ± 8
Peak ankle plantar flexion in late stance (°)	N	N	N	N	N	9 ± 8	10 ± 7	9 ± 7	7 ± 8	3 ± 7
Peak ankle dorsiflexion in swing (°)	10 ± 5	10 ± 4	10 ± 12	8 ± 6	9 ± 5	6 ± 5	7 ± 6	6 ± 5	6 ± 6	9 ± 8
Peak knee flexion in swing (°)	34 ± 1	34 ± 1	21 ± 18	26 ± 16	34 ± 1	34 ± 11	31 ± 9	31 ± 8	31 ± 8	23 ± 16
Peak hip extension in late stance (°)	4 ± 2	4 ± 2	2 ± 2	3 ± 3	3 ± 2	9 ± 6	10 ± 7	8 ± 6	8 ± 7	6 ± 7
Peak hip flexion in swing (°)	34 ± 1	34 ± 1	21 ± 18	26 ± 16	34 ± 1	34 ± 11	31 ± 9	31 ± 8	31 ± 8	23 ± 16

Peak values as the mean ± standard deviation; N: no data.

exoskeleton thighs, exoskeleton knees, exoskeleton shanks, exoskeleton ankles, 2nd metatarsal heads, and exoskeleton heels. In addition, four markers were stuck on the headband and two markers were stuck on the wristband.

The lower limb exoskeleton called AIDER (Figure 1(a)) is developed by our lab, which can assist walking for T7-T12 SCI patients with a height of 160-185 cm. The main controller and battery are set on the back. Two motors are, respectively, fixed on the unilateral hip joint and the knee joint to provide active drives, and one spring is fixed on the ankle joint to provide passive drives. Two adjustable crutches with two keys interacting with the main controller wirelessly assist the balance of the human-exoskeleton system. The interfaces between AIDER and the participant's body are two foot bindings, two bands tied to the front protection pad to constraint the calf, two bands tied to the back protection pad to constraint the thigh, and two buckled waist belts limiting the upper body in it. AIDER (8 degrees of freedom, 26 kg) allows patients to walk at the speed of 0.03 m/s-0.9 m/s.

Five typical pavements (Figure 1(c)) are made of real materials. The sizes of all simulated surfaces with different friction coefficients (Table 1) are 3 m by 1 m. Pavements were tiled pavement, carpet pavement, wooden pavement, concrete pavement, and pebble pavement. Participants first walked without exoskeleton on the ranked pavements for 2 meters for 4 times at normal speed, and then, they walked with exoskeleton on the pavements at normal speed for 2 meters for 4 times after at least 1-hour training. To ensure the safety of participants, a researcher followed the participants' walking with exoskeleton throughout the whole experiment.

The gait cycle from heel strike to heel strike was determined by the trajectory of heel markers. All variables were normalized from 0 to 1, compared with a stride cycle. Each joint's angle in a sagittal plane was interpolated to the same quantity in one gait cycle. The angular velocity of each joint was derived from the differentiation of angle displacement. The phase angle is equal to the arctangent of the ratio of

the normalized angular velocity to the normalized angular displacement, and CRP is equal to the phase angle of the proximal joint minus the phase angle of the distal joint [9, 11, 14]. The root mean square of CRP (CRP_{RMS}) was selected to analyze the magnitude of dephasing between joints at a specific phase of the gait cycle, and the standard deviation of CRP (CRP_{SD}) was selected to assess the variability of the coordination pattern between joints in the full gait cycle [9]. Peak ankle dorsiflexion in the midstance, peak ankle plantar flexion in the late stance, peak ankle dorsiflexion in swing, peak knee flexion in swing, peak hip extension in the late stance, and peak hip flexion in swing were selected as six key parameters for the kinematic analysis. All data were processed by MATLAB (MathWorks, Natick, MA, USA). To examine the changes in kinematics across one gait cycle for ankle, knee, and hip joints, the paired *t*-test was used to analyze the statistical significance of gait parameters between pavements by SPSS (v25, IBM Corp., Armonk, USA). The value of significance level was set at an alpha value of 0.05.

3. Results

3.1. Joint Kinematics. In a gait cycle, the trends of hip, knee, and ankle angles of the human system are not exactly the same as normal people. The overall angle of the hip, knee, and ankle joints of the human-machine system is much smaller than that of a normal person. Peak ankle dorsiflexion with exoskeleton in the midstance phase is larger than that without exoskeleton on five kinds of pavements (Table 2). With exoskeleton, there is a significant difference in the peak ankle dorsiflexion in the midstance between the carpet pavement and the pebble pavement (paired *t*-tests, $p = 0.009$). Without exoskeleton, the peak ankle plantar flexion (paired *t*-tests, $p = 0.031$) in the late stance phase has a significant difference between the pebble pavement and the carpet pavement. Similarly, without exoskeleton, the peak ankle plantar flexion (paired *t*-tests, $p = 0.043$) in the late stance phase has a significant difference between the pebble pavement

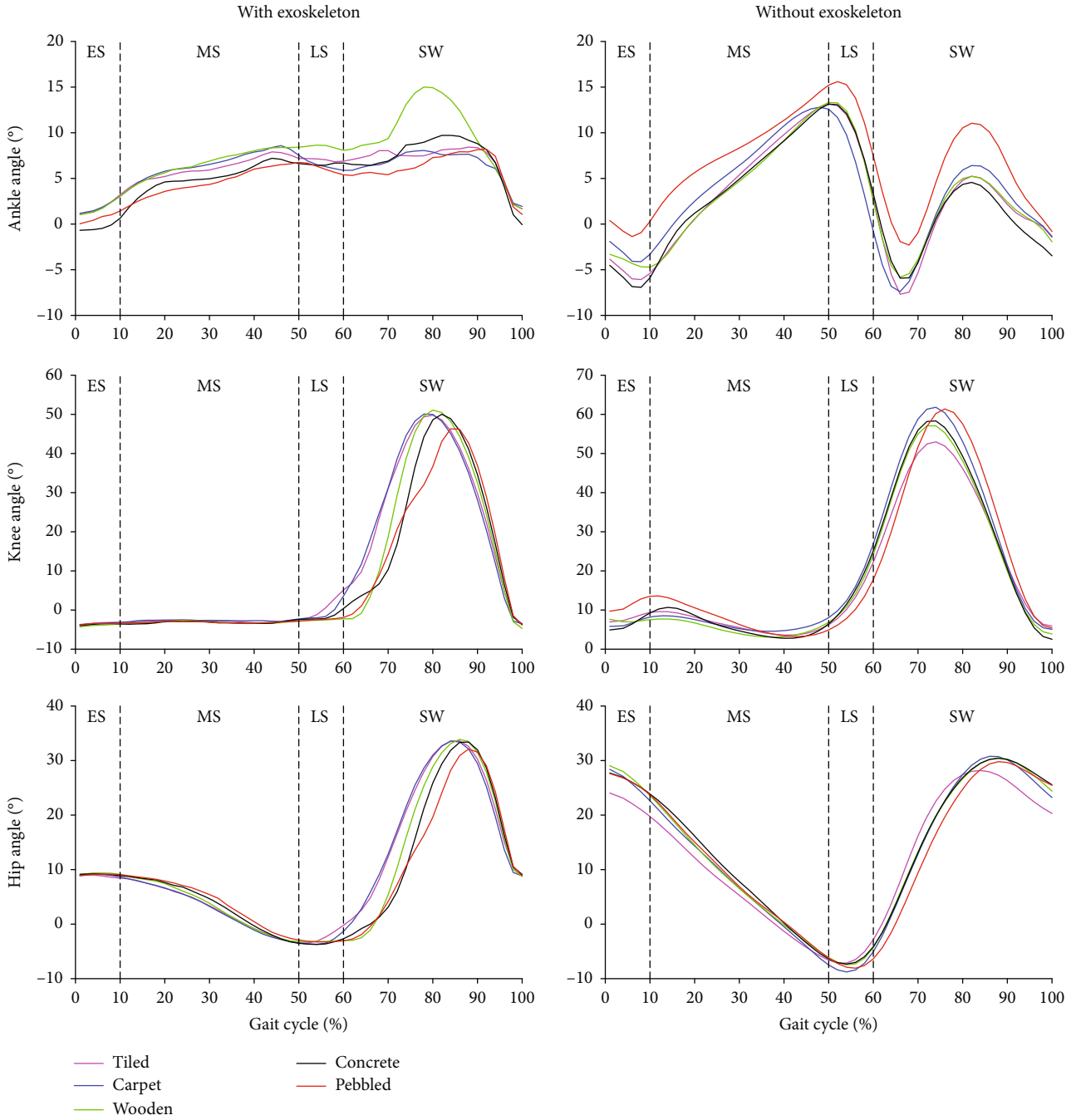


FIGURE 2: Changes in kinematics at the ankle, knee, and hip. Mean angle of the ankle, knee, and hip in a sagittal plane for participants ($n = 8$) with/without exoskeleton over the gait cycle on each kind of pavements. The gait cycle is from the heel to the next heel strike of the left foot. ES = early stance; MS = midstance; LS = late stance; SW = swing phase.

and the wooden pavement. The ungiven results of paired t -test of peak values with/without exoskeleton between pavements indicate no significant difference.

On five types of pavements, the trends (see Figure 2) of the joint angle of the human-exoskeleton system are significantly different from the trends of the joint angle without exoskeleton. The ankle angle with exoskeleton over the gait cycle (except the early stance phase) on the pebbled pavement is the smallest among the five kinds of pavements, but the

ankle angle without exoskeleton over the gait cycle on the pebble pavement is the largest among the five kinds of pavements. With/without exoskeleton, the knee angle in the stance phase tends to be consistent on the five kinds of pavements. On the contrary, the knee angle in the stance phase with/without exoskeleton tends to be different in the five kinds of pavements. Although the hip angle with exoskeleton in the stance phase on the pebbled pavement is almost larger than that on the other pavements, the hip angle with

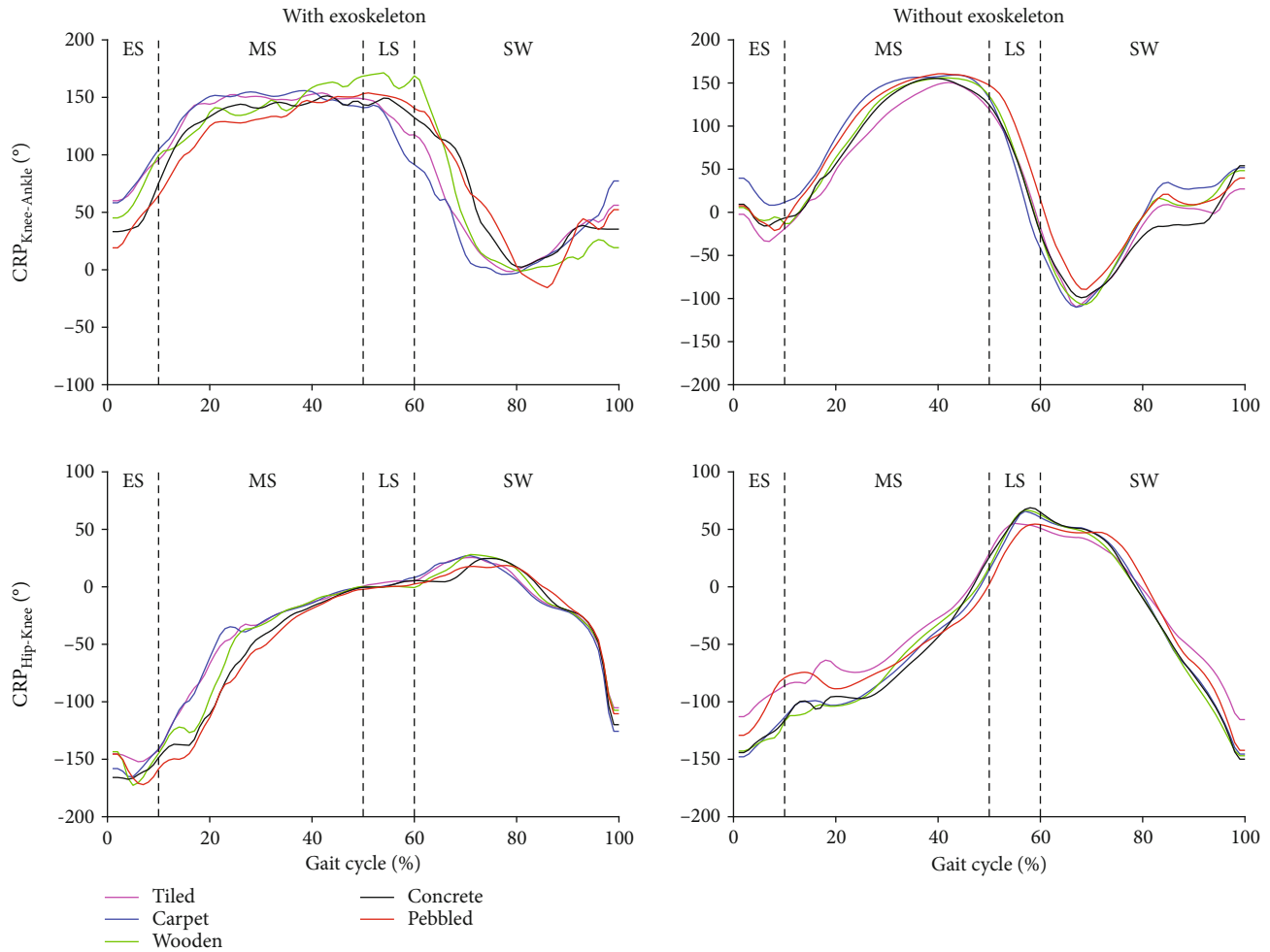


FIGURE 3: Continuous relative phase (CRP) patterns between the knee and ankle and between the hip and knee in the sagittal plane. Mean CRP for participants ($n = 8$) with/without exoskeleton over the gait cycle on each kind of pavements. The gait cycle is from the heel strike to the next heel strike of the left foot. ES = early stance; MS = midstance; LS = late stance; SW = swing phase.

exoskeleton in the first half of the swing phase on the pebble pavement is smaller than the hip angle with exoskeleton on the other pavements. This trend is similar to the hip angle without exoskeleton.

3.2. Measurement of Interjoint Coordination. This study explored the effects of different pavements on coordination patterns, using the root mean square of CRP. RMS values indicate the magnitude of the dephasing between two adjacent joints but not on which joint precedes [12]. However, the CRP curves (Figure 3) provide which joint precedes on the specific pavement with/without exoskeleton: the knee precedes the ankle at all phases of the gait cycle on pavements (except the pebble pavement in the swing phase) with exoskeleton, and the hip precedes the knee in the stance phase on all pavements with exoskeleton. The knee precedes the ankle in the midstance phases on pavements without exoskeleton, and the ankle precedes the knee in the early stance phase on pavements (except the carpet pavement) without exoskeleton. The knee precedes the hip in the early stance phase and in the midstance phase on all pavements without

exoskeleton, while the hip precedes the knee in the late stance phase on all pavements without exoskeleton.

The $CRP_{Hip-Knee/RMS}$ on the pebble pavement with exoskeleton is larger than that on the other pavements in the early stance phase and in the midstance phase. On the contrary, the $CRP_{Hip-Knee/RMS}$ on pebbled pavement without exoskeleton is less than that on the other pavements in all phases, while the $CRP_{Hip-Knee/RMS}$ on the tiled pavement without exoskeleton is less than that on the other pavements in all phases (as seen in Table 3). With exoskeleton, the $CRP_{Hip-Knee/RMS}$ in the midstance phase has a significant difference between the carpet pavement and the wooden pavement (paired t -tests, $p = 0.034$), between the carpet pavement and the concrete pavement (paired t -tests, $p = 0.028$), and between the carpet pavement and the pebble pavement (paired t -tests, $p = 0.044$). Moreover, the $CRP_{Hip-Knee/RMS}$ with exoskeleton in the late stance phase has a significant difference between the wooden pavement and the pebble pavement (paired t -tests, $p = 0.029$) and in the swing phase between the carpet pavement and the wooden pavement (paired t -tests, $p = 0.024$). Without exoskeleton,

TABLE 3: Coordination: CRP root mean square (CRP_{RMS}) and variability (CRP_{SD}) over the full gait cycle for participants ($n = 8$) with/without exoskeleton over the gait cycle on each kind of pavements.

	With exoskeleton					Without exoskeleton				
	Tiled	Carpet	Wooden	Concrete	Pebbled	Tiled	Carpet	Wooden	Concrete	Pebbled
	$CRP_{Hip-Knee/RMS}$									
Early stance	148 ± 33	155 ± 18	158 ± 22	161 ± 27	162 ± 15	139 ± 20	313 ± 20	133 ± 30	130 ± 21	107 ± 37
Midstance	55 ± 27	53 ± 20	67 ± 30	77 ± 31	83 ± 31	82 ± 25	79 ± 22	79 ± 17	80 ± 21	52 ± 35
Late stance	6 ± 8	5 ± 5	1 ± 1	4 ± 6	2 ± 1	62 ± 21	56 ± 14	56 ± 10	58 ± 20	44 ± 20
Swing	34 ± 7	38 ± 6	34 ± 7	35 ± 8	33 ± 7	74 ± 5	71 ± 9	73 ± 11	72 ± 8	71 ± 9
	$CRP_{Knee-Ankle/RMS}$									
Early stance	82 ± 63	86 ± 59	77 ± 61	56 ± 58	50 ± 47	38 ± 47	42 ± 26	40 ± 33	28 ± 13	29 ± 14
Midstance	148 ± 50	149 ± 47	147 ± 39	141 ± 59	136 ± 57	120 ± 14	133 ± 13	125 ± 17	123 ± 15	130 ± 11
Late stance	138 ± 60	129 ± 52	166 ± 13	146 ± 50	151 ± 58	87 ± 41	90 ± 20	93 ± 25	86 ± 27	112 ± 32
Swing	58 ± 30	50 ± 24	70 ± 11	71 ± 26	82 ± 28	75 ± 11	74 ± 12	74 ± 13	72 ± 28	59 ± 20
$CRP_{Hip-Knee/SD}$	55 ± 13	57 ± 9	60 ± 11	63 ± 11	65 ± 10	75 ± 6	71 ± 7	71 ± 8	71 ± 9	63 ± 9
$CRP_{Knee-Ankle/SD}$	64 ± 16	64 ± 16	71 ± 5	63 ± 21	67 ± 13	89 ± 8	90 ± 8	89 ± 9	87 ± 15	84 ± 11

Root mean square (RMS) as the mean ± standard deviation. (0–10%) data points in one gait cycle for each participant, (10–50%) data points in one gait cycle for midstance, (50–60%) data points in one gait cycle for late stance, and (60–100%) data points in one gait cycle for the swing phase.

the $CRP_{Hip-Knee/RMS}$ in the early stance phase has a significant difference between the tiled pavement and the concrete pavement (paired t -tests, $p = 0.02$) and between the wooden pavement and the pebble pavement (paired t -tests, $p = 0.009$). In addition, the $CRP_{Hip-Knee/RMS}$ without exoskeleton in the late stance phase has a significant difference between the carpet pavement and the pebble pavement (paired t -tests, $p = 0.033$) and between the concrete pavement and the pebble pavement (paired t -tests, $p = 0.033$).

The $CRP_{Knee-Ankle/RMS}$ on the tiled pavement with exoskeleton is larger than that on the other pavements in the early stance phase and in the midstance phase, while the $CRP_{Knee-Ankle/RMS}$ on the tiled pavement with exoskeleton is the less than that on the other pavements in the late stance phase and in the swing phase. On the contrary, the $CRP_{Knee-Ankle/RMS}$ on the pebble pavement with exoskeleton is the less than that on the other pavements in the early stance phase and in the midstance phase, while the $CRP_{Knee-Ankle/RMS}$ on the tiled pavement with exoskeleton is larger than that on the other pavements in the late stance phase and in the swing phase. The $CRP_{Knee-Ankle/RMS}$ on the pebble pavement without exoskeleton is less than that on the other pavements in the early stance phase and in the swing phase, while the $CRP_{Knee-Ankle/RMS}$ on the tiled pavement without exoskeleton is larger than that on the other pavements in the midstance phase and late stance phase. The $CRP_{Knee-Ankle/RMS}$ on the carpet pavement without exoskeleton is larger than that on the other pavements in the early stance phase and in the midstance phase (as seen in Table 3). With exoskeleton, there is a significant difference of the $CRP_{Knee-Ankle/RMS}$ between the carpet pavement and the pebble pavement in the late stance phase (paired t -tests, $p = 0.027$) and in the swing phase (paired t -tests, $p = 0.026$). Without exoskeleton, there is a significant difference of the $CRP_{Knee-Ankle/RMS}$ in the midstance phase between the tiled pavement and the carpet pavement (paired t -tests, $p = 0.01$)

and in the late stance phase between the concrete pavement and the pebble pavement (paired t -tests, $p = 0.048$).

With exoskeleton, there is a significant difference of the $CRP_{Hip-Knee/SD}$ between the carpet pavement and the wooden pavement (paired t -tests, $p = 0.024$) in the full gait cycle. Without exoskeleton, there is a significant difference of the $CRP_{Hip-Knee/SD}$ in the full gait cycle between the tiled pavement and the concrete pavement (paired t -tests, $p = 0.029$), between the tiled pavement and the pebble pavement (paired t -tests, $p = 0.033$), between the carpet pavement and the pebble pavement (paired t -tests, $p = 0.015$), and between the wooden pavement and the pebble pavement (paired t -tests, $p = 0.005$). The trends of CRP with exoskeleton oscillate more frequently than the trends of CRP without exoskeleton over the gait cycle on the pavements.

4. Discussion

Our results suggest that the common pavements cause a significant difference of interjoint coordination with/without exoskeleton only in some phases of the gait cycle, so the hypothesis 1 and the hypothesis 2 are only partially proved. The compressive capacity of the carpet pavement is obviously lower than the other pavements, which may cause the difference of $CRP_{Hip-Knee/RMS}$ with exoskeleton between the carpet pavement and other pavements (except the tiled pavement) in the midstance. Moreover, the compressive capacity of the carpet pavement may cause the difference of $CRP_{Knee-Ankle/RMS}$ with exoskeleton between the carpet pavement and the pebble pavement in the late stance phase and in the swing phase. However, the unevenness of pebble pavement as another influencing factor should not be ignored. Because the unevenness of the pebble pavement increases the physical energy consumption [18], the $CRP_{Hip-Knee/RMS}$ of the pebble pavement without exoskeleton is lower than the other pavements and

statistically different from the carpet pavement and the concrete pavement. The unevenness of the pebble pavement may induce the cautious dynamic neuromuscular control [13] of participants and enhance their leg stiffness [1, 10] so that the $CRP_{Hip-Knee/SD}$ of the pebble pavement without exoskeleton is smaller than that of other pavements and statistically different from that of other pavements (except concrete pavement). When walking on pavements with exoskeleton, participants need to adjust the center of gravity to keep the human-exoskeleton system balance with the help of crutches and prepare for the next step in stance, which may cause the difference of interjoint coordination patterns with exoskeleton between pavements.

The exoskeleton was set in a fixed gait and joint moment, so the peak values should be similar between pavements. However, the peak ankle dorsiflexion of walking on the carpet pavement in the midstance is significantly different from that of walking on the pebble pavement, which may due to the active intervention from participants on the ankle. When the participants without exoskeleton walk on the pavements, it is only found that the peak ankle plantar flexion in the late stance phase on the pebble pavement is significantly different from that on the carpet pavement and the wooden pavement. This result indicates that the friction coefficients of pavements do not impose on gait parameters in kinematics, but the unevenness of pavements obviously affects the gait parameters in kinematics [1, 10]. From the peak values without exoskeleton at all pavements, the human mainly adjusts the ankle dorsiflexion in the swing phase to adapt common pavements. Due to the fixed gait and joint moment of exoskeleton, the conditions that the knee precedes the ankle without exoskeleton on all pavements in the early stance and in the swing phase were reversed. Similarly, the conditions that the hip precedes the knee without exoskeleton on all pavements in the late stance phase were also reversed (Figure 3).

5. Conclusions and Limitations

In summary, our work reveals the effect of common pavements on interjoint coordination with/without exoskeleton. The compressive capacity of the pavement and the unevenness of pavement are important factors that influence the interjoint coordination. The compressive capacity of the pavement can modify the magnitude of dephasing between the hip and knee with exoskeleton in the midstance phase and in the swing phase. The unevenness of the pavement can change the magnitude of dephasing between the hip and the knee without exoskeleton in the early stance phase and in the late stance phase and increases the stability of the coordination pattern between the hip and the knee without exoskeleton. The finding suggests that the identification of the compressive capacity and the unevenness of common grounds should be used for the control strategy of exoskeleton to enhance the coordination and benefit the motor rehabilitation.

There are three limitations that need to be considered. First, the effects of physiological characteristics such as age, gender, and weight on the gait parameters of different pave-

ment kinematics have not been included. Second, there are not only random displacements between the human body and the exoskeleton but also individual differences between human bodies, which make it difficult for the human-exoskeleton model to measure the exact gait parameters of human-exoskeleton. Therefore, in exoskeleton experiments, there are uncertain errors in the gait parameters of human-exoskeleton. Third, this study did not explore muscle adaptation and joint kinetics of people who may adapt to different friction coefficients. Future work will focus on the effects of different friction coefficient pavements on muscle adaptation and joint dynamics, which can further explain how people adapt to pavements with different coefficients of friction.

Data Availability

The data that support the findings of this study are available on request from the corresponding author, Jing Qiu.

Conflicts of Interest

The authors declare that they have no conflicts of interest.

Acknowledgments

This research was supported by the Fundamental Research Funds for the Central Universities of China (No. ZYGX2015J148). Furthermore, we are grateful for all experimental participants.

References

- [1] A. S. Voloshina, A. D. Kuo, M. A. Daley, and D. P. Ferris, "Biomechanics and energetics of walking on uneven terrain," *Journal of Experimental Biology*, vol. 216, no. 21, pp. 3963–3970, 2013.
- [2] J.-S. Wang, C.-W. Lin, Y.-T. C. Yang, and Y.-J. Ho, "Walking pattern classification and walking distance estimation algorithms using gait phase information," *IEEE Transactions on Biomedical Engineering*, vol. 59, no. 10, pp. 2884–2892, 2012.
- [3] T. Lenzi, M. C. Carrozza, and S. K. Agrawal, "Powered hip exoskeletons can reduce the user's hip and ankle muscle activations during walking," *IEEE Transactions on Neural Systems and Rehabilitation Engineering*, vol. 21, no. 6, pp. 938–948, 2013.
- [4] H.-J. Lee, S. Lee, W. H. Chang et al., "A wearable hip assist robot can improve gait function and cardiopulmonary metabolic efficiency in elderly adults," *IEEE Transactions on Neural Systems and Rehabilitation Engineering*, vol. 25, no. 9, pp. 1–1557, 2017.
- [5] Y. Ding, I. Galiana, A. T. Asbeck et al., "Biomechanical and physiological evaluation of multi-joint assistance with soft exosuits," *IEEE Transactions on Neural Systems and Rehabilitation Engineering*, vol. 25, no. 2, pp. 119–130, 2017.
- [6] J. Li, B. Shen, L. Zhang, C. Tao, and R. Ji, "Kinematics and performance analysis of a serial hip assistive mechanism," *Advances in Mechanical Engineering*, vol. 10, no. 4, 2018.
- [7] J. Zhang, P. Fiers, K. A. Witte et al., "Human-in-the-loop optimization of exoskeleton assistance during walking," *Science*, vol. 356, no. 6344, pp. 1280–1284, 2017.

- [8] R. Burgess-Limerick, B. Abernethy, and R. J. Neal, "Relative phase quantifies interjoint coordination," *Journal of Biomechanics*, vol. 26, no. 1, pp. 91–94, 1993.
- [9] E. Hutin, D. Pradon, F. Barbier, B. Bussel, J. M. Gracies, and N. Roche, "Walking velocity and lower limb coordination in hemiparesis," *Gait & Posture*, vol. 36, no. 2, pp. 205–211, 2012.
- [10] A. S. Voloshina and D. P. Ferris, "Biomechanics and energetics of running on uneven terrain," *Journal of Experimental Biology*, vol. 218, no. 5, pp. 711–719, 2015.
- [11] J. Hamill, R. E. A. van Emmerik, B. C. Heiderscheit, and L. Li, "A dynamical systems approach to lower extremity running injuries," *Clinical biomechanics*, vol. 14, no. 5, pp. 297–308, 1999.
- [12] E. Hutin, D. Pradon, F. Barbier, J. M. Gracies, B. Bussel, and N. Roche, "Lower limb coordination patterns in hemiparetic gait: factors of knee flexion impairment," *Clinical Biomechanics (Bristol, Avon)*, vol. 26, no. 3, pp. 304–311, 2011.
- [13] S. L. Chiu, C. C. Chang, and L. S. Chou, "Inter-joint coordination of overground versus treadmill walking in young adults," *Gait & Posture*, vol. 41, no. 1, pp. 316–318, 2015.
- [14] S. L. Chiu and L. S. Chou, "Effect of walking speed on inter-joint coordination differs between young and elderly adults," *Journal of Biomechanics*, vol. 45, no. 2, pp. 275–280, 2012.
- [15] D. Ferris, G. Sawicki, and A. Domingo, "Powered lower limb orthoses for gait rehabilitation," *Topics in Spinal Cord Injury Rehabilitation*, vol. 11, no. 2, pp. 34–49, 2005.
- [16] T. K. Uchida, A. Seth, S. Pouya, C. L. Dembia, J. L. Hicks, and S. L. Delp, "Simulating ideal assistive devices to reduce the metabolic cost of running," *PLoS One*, vol. 11, no. 9, article e0163417, 2016.
- [17] L. Wang, E. H. F. van Asseldonk, and H. van der Kooij, "Model predictive control-based gait pattern generation for wearable exoskeletons," in *Rehabilitation Robotics (ICORR), 2011 IEEE International Conference*, IEEE, 2011.
- [18] R. G. Soule and R. F. Goldman, "Terrain coefficients for energy cost prediction," *Journal of Applied Physiology*, vol. 32, no. 5, pp. 706–708, 1972.

Research Article

Bioinspired Implementation and Assessment of a Remote-Controlled Robot

Yves Rybarczyk^{1,2} and Diogo Gil Carvalho³

¹Intelligent & Interactive Systems Lab (SI2 Lab), Universidad de Las Américas, 170125 Quito, Ecuador

²Dalarna University, 791-88 Falun, Sweden

³Department of Electrical Engineering, CTS/UNINOVA, Nova University of Lisbon, 2829-516 Monte de Caparica, Portugal

Correspondence should be addressed to Yves Rybarczyk; y.rybarczyk@fct.unl.pt

Received 26 February 2019; Revised 9 May 2019; Accepted 21 August 2019; Published 11 September 2019

Guest Editor: Francesca Cordella

Copyright © 2019 Yves Rybarczyk and Diogo Gil Carvalho. This is an open access article distributed under the Creative Commons Attribution License, which permits unrestricted use, distribution, and reproduction in any medium, provided the original work is properly cited.

Daily activities are characterized by an increasing interaction with smart machines that present a certain level of autonomy. However, the intelligence of such electronic devices is not always transparent for the end user. This study is aimed at assessing the quality of the remote control of a mobile robot whether the artefact exhibits a human-like behavior or not. The bioinspired behavior implemented in the robot is the well-described two-thirds power law. The performance of participants who teleoperate the semiautonomous vehicle implementing the biological law is compared to a manual and nonbiological mode of control. The results show that the time required to complete the path and the number of collisions with obstacles are significantly lower in the biological condition than in the two other conditions. Also, the highest percentage of occurrences of curvilinear or smooth trajectories are obtained when the steering is assisted by an integration of the power law in the robot's way of working. This advanced analysis of the performance based on the naturalness of the movement kinematics provides a refined evaluation of the quality of the Human-Machine Interaction (HMI). This finding is consistent with the hypothesis of a relationship between the power law and jerk minimization. In addition, the outcome of this study supports the theory of a CNS origin of the power law. The discussion addresses the implications of the anthropocentric approach to enhance the HMI.

1. Introduction

Industries face an increasing demand for collaborative robots that exhibit human-like behaviors. This trend is justified by the fact that it is easier for an operator to predict the actions of a robot that behaves more like a human being than like a machine [1]. A study that uses the experimental paradigm of Motor Interference (MI) shows that the motor performance of an individual can be influenced by the perception of the movements of a robot, if the machine replicates some characteristics of biological motion [2–4]. In particular, it seems that the movement velocity profile is sufficient to create this interference. This result suggests that a movement can be processed as biologic by the human brain, even if it is not produced by a living being, on the condition that the artefact motion simulates (even approximatively) certain biological kinematics [5]. Moreover, the physical aspect of

the robot seems relevant. For instance, the human-robot interaction tends to be improved when the machine has a humanoid appearance [6]. This fact can be explained by an unconscious tendency of the human being to anthropomorphize the artefacts they interact with, in order to predict their behavior and increase their acceptance of the machine [7].

Besides the situation of interaction, the implementation of human-like behaviors in a robot's way of working also seems to benefit an operator that has to control a machine. This statement is particularly true in the context of teleoperation, which implies several limitations for a human operator. For instance, the sensorial information received by the teleoperator can be altered, for example, the field of view is reduced, not all the sensorial modalities are restituted (e.g., audition and proprioception), and the response of the system is delayed. Another aspect is the necessity to build or accommodate new motor schemes to be able to control the user

interface of the device, which augments the mental workload. A promising approach to reduce the gap between the user and the telerobot is to implement human-like behaviors in a robot [8, 9]. For instance, Rybarczyk et al. [10, 11] have studied the effect of the implementation in a mobile robot of the human behavior of visuomotor anticipation over the locomotion, in which the direction of the robot pan-tilt camera is automatically oriented toward the tangent point of the inside curve of the path, as walkers/cyclists/drivers do [12–14]. The results show that the motor performances of the teleoperators are enhanced when they steer the bioinspired robot. A correlation between the replication of biological laws and the level of expertise is also observed in the case of the telemanipulation of robotic arms, such as in telesurgery [15].

Different strategies are used to implement human-like behaviors in a robot. A traditional approach applied in the industry is to create anthropomorphic collaborative robots (or cobots) that are trained to imitate biological motions, through machine learning algorithms [16]. In the case of the teleoperation, it seems that individuals feel also more comfortable to control an anthropomorphic robot arm in which the motion trajectory of the end effector is like a biological movement [17]. Jerk minimization is one of the principal human-like behaviors that has been implemented to model a natural trajectory planning [18, 19]. The minimum jerk is characterized by a bell-shaped velocity profile, in which the movement speed increases progressively, reaches a peak near the midpoint, and then decreases slowly. This absence of abrupt changes seems to support the execution of a smooth motion [20]. Another fundamental motor behavior is the relationship between the velocity and the curvature of the biological movements, which is known as the two-thirds power law [21, 22]. This law states that the angular velocity of the end effector is proportional to the two-third root of its curvature or, equivalently, that the instantaneous tangential velocity (v_t) is proportional to the third root of the radius of curvature (r_t), as described in equation (1). In other words, it means that the velocity of the movement decreases in the highly curved parts of the trajectory and increases when the trajectory becomes straighter. Implementing this model in a mobile robot tends to improve the raw performance when steering the vehicle [23].

$$v_t = k r_t^{-1/3}. \quad (1)$$

Nevertheless, few studies are interested in considering refined features to gauge the quality of the Human-Machine Interaction (HMI). Instead of focusing only on the raw performance (e.g., completion time of the task and percentage occurrence of errors), these studies analyze the kinematics of the robot control [24–26]. To proceed with such an advanced assessment, the human behaviors are now used as criteria to estimate an appropriate interaction. For instance, minimum jerk, smoothness, and 2/3 power law can be applied as a reference to evaluate a suitable interaction between a human operator and an artefact [17, 27]. These three features are compared in a study that

aimed at assessing the motor control of a robot arm to assist surgeons [15]. The results show that both smoothness and minimum jerk are significant measures of expertise levels. The end-effector trajectory evolves from sharp and jerky in novices to smooth in experts. Thus, the authors conclude that these two features are excellent criteria to evaluate motor skill in the conditions of human-robot interaction. Although the power law is also identified as a discriminant measure of expertise, registering such a biological law seems to depend on the characteristics of the artefact. For example, some studies have demonstrated that this law is replicated in situations of teleoperation [11] and use of prostheses [28].

Actually, there is a controversy regarding the origins and the violations of the 2/3 power law during the execution of the biological movements [22, 29–31]. On the one hand, some studies tend to demonstrate that the power law is a signature of the Central Nervous System (CNS) [32–34], because it seems to be independent of the dynamics of the limbs. This law is indeed observed in a wide variety of activities such as drawing [21], walking [35], and smooth pursuit eye [36]. On the other hand, different studies defend a biomechanical [30] or, even, an artefactual explanation [37, 38]. There are also contradictory results regarding the relationship between smoothness, minimum jerk, and power law. Some studies show evidences that these features are related to each other [32, 39], whereas others suggest the contrary [15, 29].

The present work attempts to tackle these different contradictory findings about the 2/3 power law by integrating this bioinspired kinematics in a remote-controlled mobile robot. An experiment is designed to compare the teleoperation of a robot with the 2/3 power law (biological condition) versus two modes of control that do not implement this human-like behavior (manual condition and nonbiological condition). In the biological mode, the engine speed is automatically servo controlled by the vehicle trajectory according to the power law equation. In the manual mode, the user has to control both the velocity and the direction of the mobile device. In the third condition, the vehicle speed is also automatic, but the calculation of the relationship between geometry and kinematics violates the biological motion. This last condition is used as a control to make sure that the potential difference of performance between the two main conditions (biologic vs. manual) is not caused by a dissimilar complexity of the task (i.e., number of parameters that must be controlled by the participants). We posit the hypothesis that semiautonomous driving, in which the velocity is automatically set according to the power law principles (biological mode), should promote a significantly faster, safer, and more natural steering than the nonassisted (manual mode) and nonbiologic (artificial mode) control. The quality of the interaction is assessed from both the raw performance (completion time and number of collisions) and refined parameters based on the smoothness of the trajectories.

The remainder of the manuscript is organized into three main sections. First, the implementation of the teleoperation system is described. The experimental protocol

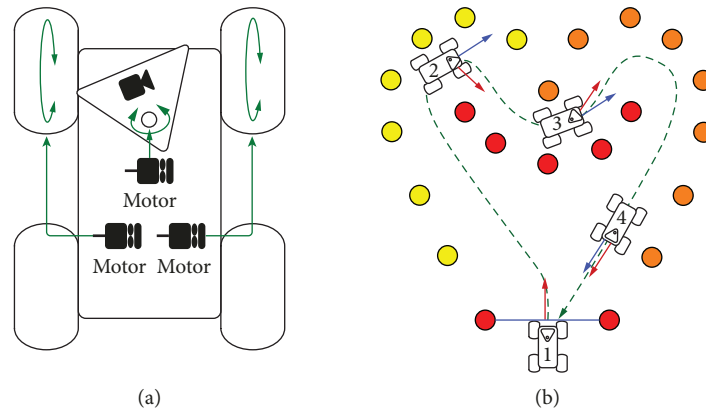


FIGURE 1: (a) Schematic representation of the robot (top view) designed for the study. Two independent motors drive the front wheels, and a third one controls the rotation of the pan camera. This mobile vision is implemented by default to promote a visual anticipation over the change of direction. (b) Illustration of the camera behavior in some specific locations of the path. The blue arrow indicates the instantaneous direction of the vehicle and the red arrow represents the orientation of the pan camera at the same moment. It is notable that the angle between the two arrows is inversely proportional to the radius of curvature of the robot trajectory. The more curved is the shape of the path (e.g., position 2), the larger is the angle between the orientation of the camera and the direction of the vehicle, and vice versa (e.g., position 4).

and conditions (manual vs. nonbiologic vs. biologic) are also explained in detail. Second, the results of the performance for each condition are presented, analyzed, and discussed. Finally, the outcomes are interpreted, in order to draw some conclusions and perspectives regarding the application of the anthropocentric approach in the human-robot interaction, as well as the origins of the power law and its relationship with jerk minimization.

2. Material and Methods

2.1. System Architecture. The three main elements that compose the system are (i) a NXT mobile robot, (ii) an Android device for the remote control, and a pan IP camera. Since the experiment is carried out in a situation of teleoperation (i.e., indirect perception and action on the robot environment), a wireless connection is used to support the communication between the principal components of the architecture. Two different protocols of communication are applied. The Android-based remote control communicates with the NXT through Bluetooth technology. In addition, the connection between the IP camera and the smartphone is supported by Wi-Fi communication. The robot is connected to the IP camera thanks to a support library that permits the system integration between the two entities. Thus, the operators use the Android remote control device to interact with the whole system, which allows them to steer the mobile robot and receive a visual feedback from the pan IP camera. An Android application is developed and implemented on the smartphone to permit such an interaction. The tactile user interface enables the operator to control the trajectories of the vehicle, to choose the steering mode of the robot (manual vs. nonbiologic vs. biologic), to calibrate the pan camera, and to turn the system on or off.

2.2. Robot Behavior. The vehicle is built on four wheels, employing a front-wheel-drive system (Figure 1(a)). The two front wheels are moved by two independent motors. The differential of speed between the right and the left wheel rotation allows the vehicle to turn. The pan camera is set on a mobile structure, which is moved by another motor. The orientation of the camera is determined automatically based on the direction of the robot, that is, the camera points toward the inside of the vehicle trajectory. Since any change of direction is systematically anticipated by a rotation of the camera proportional to the curvature of the vehicle trajectory, a visual prediction over the robot motion is provided to the operator. This mechanism inspired from the human behavior [12, 14] is implemented by default, because it facilitates the teleoperation [8, 10]. Figure 1(b) shows examples of this visuolocomotor coupling between camera and robot for different curves of the path.

3. Experimental Conditions

3.1. Manual Condition. Both speed and direction of the vehicle are manually controlled by the operator in this experimental condition. Concentric semicircles that correspond to different speed levels are displayed on the control panel of the user's interface (Figure 2(a)). The bigger is the radius of the semicircle, the higher is the speed. Thus, the vehicle velocity is calculated based on the distance between the center of all concentric semicircles and the selected semicircle. The direction of the robot is determined by the angle between the vertical of the screen and the location of the user's fingertip. The range of angles goes from 0° to 180° , rotating counter clockwise. If the fingertip of the user is positioned between 0° and 90° , the robot turns right, with a curvature proportional to the angle between the vertical (90°) and the position of the finger (the more

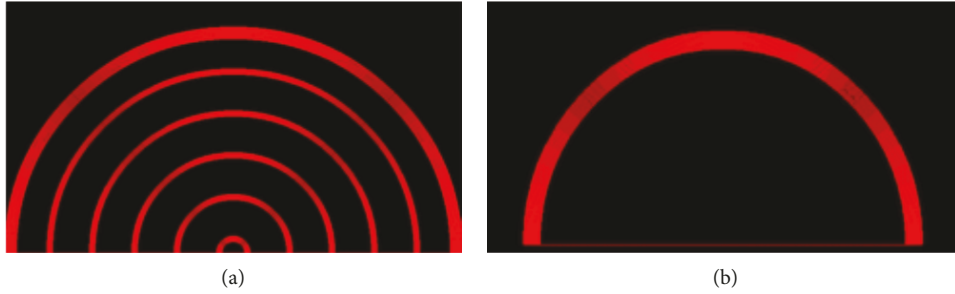


FIGURE 2: (a) Representation of the GUI for the manual mode of driving. Each concentric circle represents a different speed (the larger the radius of the semicircle, the higher the velocity). (b) User interface for the biological and nonbiological conditions. A single semicircle enables the user to directly control the direction of the robot and indirectly set the speed of the vehicle.

the location of the finger tends to 0° , the more the vehicle turns right). On the contrary, if the position of the finger is between 90° and 180° , the vehicle turns left (again, the radius of the curvature of the trajectory depends on the angle from the vertical of the screen). The controller of the robot is constantly waiting for an input sent from the graphic user interface, in order to update the direction and speed of the mobile platform.

3.2. Biological and Nonbiological Conditions. In these driving modes, the user has only to use the touchscreen interface to control the trajectory of the robot. The speed is automatically set according to the direction of the vehicle. In the biological condition, the $2/3$ power law is used to calculate the speed, which is based on the instantaneous radius of the curvature of the robot trajectory. The maximum velocity of the robot is 30 cm/s , if the vehicle goes straight forward. In the case that the radius of curvature decreases (to the right or to the left), the robot's speed diminishes by a rate of one-third (see equation (1)). In the nonbiological condition, the velocity of the vehicle is also automatic, but it is not set according to the biological motion. The relationship between speed and geometry does not follow a power law, but a linear law described in

$$v_t = k r_t. \quad (2)$$

Since it is not necessary to modulate manually the velocity, the graphic user interface is represented only by a single semicircle (Figure 2(b)). The semicircle allows the operator to control the trajectory of the robot. From the user's perspective, the way to steer the vehicle is identical to the manual mode of driving. The user has to interact with the left and right portion of the semicircle to turn left and right, respectively. The more the fingertip is located to the extremities of the semicircle, the more the robot turns sharply. The only difference between these two semiautomatic modes and the manual one is the fact that the velocity is indirectly and automatically set when the user chooses a determined direction. Precisely, the robot speed is proportional to the selected steering angle. Thus, if the power law is adapted to the remote control of an artefact, the matching between speed and steering

angle should perfectly fit to the human's skills. On the contrary, because of its unnatural behavior, the nonbiological semiautonomous control should be more challenging for the teleoperator. Figure 3 summarizes, through a block diagram, the differences between the manual and semiautomatic modes of control.

4. Experimental Protocol

Thirty people (15 males and 15 females; 23.5 ± 3.5 years) took part in the experiment. All the participants had a normal or corrected-to-normal vision. The procedure conformed to the Declaration of Helsinki and was approved by the Ethical Review Board of the Nova University of Lisbon. The experiment was carried out in a classroom, where the subjects had to teleoperate the NXT vehicle through the Android-based mobile device. The instructions provided to the participants were to steer the robot as safe (the least collisions) and fast (the minimum completion time) as possible through a path delimited by plastic blocks. The entire distance of the route was approximately seven meters and consisted of numerous bends and changes in direction (curves and countercurves). The sequence of the course was as follows: (i) a straight line, (ii) an approximately 150° bend, (iii) a 90° reverse curve, (iv) another 150° bend, and (v) a final straight line (Figure 4). A blue adhesive strip marked the starting and finishing line. The symmetric shape of the setup was especially designed to carry out the route in both directions, clockwise and anticlockwise.

After a training session, all the subjects had to execute the trial twelve times: four repetitions in the manual mode, four repetitions in the biological mode, and four repetitions in the nonbiological mode. The order of the experimental conditions was counterbalanced from one subject to another so that ten individuals started with the manual control, ten others started with the biological control, and the last ten started with the nonbiological control. This counterbalancing was implemented to prevent a possible learning effect, which would bias the outcome of the study. For each of the principal conditions (manual vs. biologic vs. nonbiologic), the trial was performed twice clockwise and twice anticlockwise. The

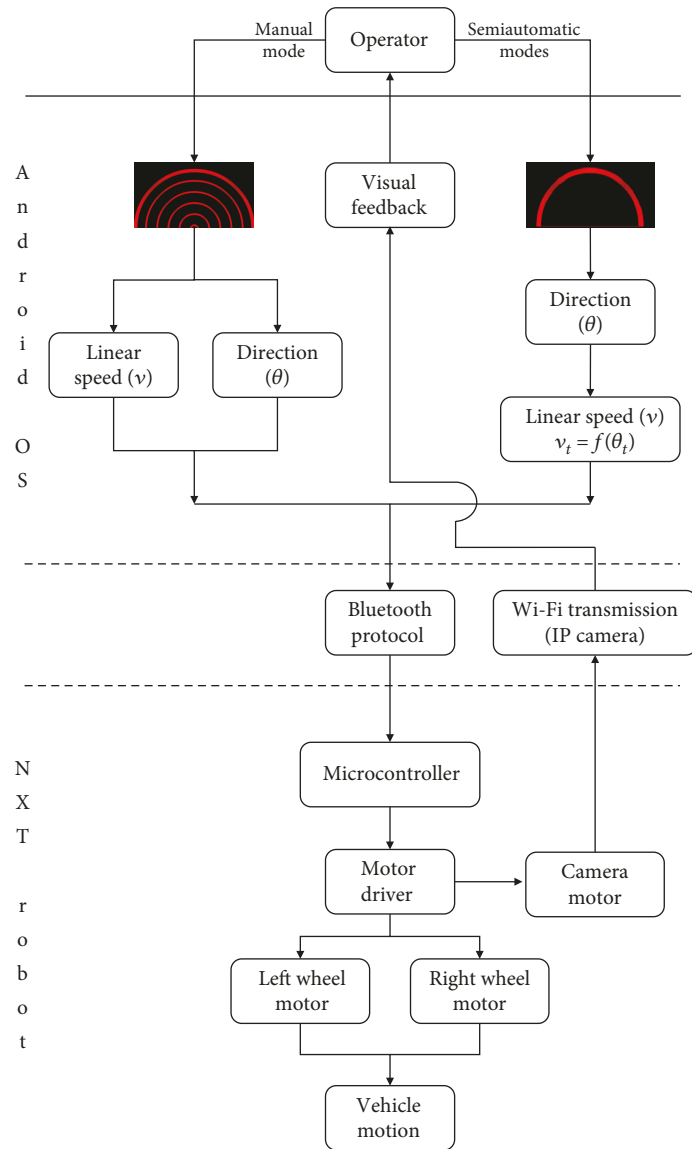


FIGURE 3: Block diagram of the two modes of remote control. If the operator picks the manual mode (left side), the speed and direction are controlled independently. On the contrary, if a semiautomatic mode is selected (right side), the robot speed is automatically calculated from the power law (biological condition) or linear law (nonbiological condition) function of the direction defined by the user.

completion time, the number of collisions, and the robot trajectory were recorded at the end of each trial.

5. Results

The experimental data are statistically analyzed through ANOVA tests for multivariable comparisons and *t*-tests for the pairwise comparisons.

5.1. Completion Time. We first analyzed the time performance of the participants to complete the task. Results indicate that the completion time is significantly affected by the experimental sessions ($p < .05$). A pairwise analysis shows a significant difference between session 1 and session 4 ($p < .03$). This outcome indicates that the required time to guide the vehicle from the starting line to the fin-

ishing line diminishes significantly from session 1 to session 4. No interaction effects are detected between the sessions (1, 2, 3, and 4) and the main conditions (manual, biologic, and nonbiologic).

In addition, the comparison of the completion time between the three conditions indicates a significant difference ($p < .005$). As shown in Figure 5, the participants complete the task faster in the biological mode than in the manual ($p < .01$) and nonbiological ($p < .005$) steering modes. The pairwise analyses confirm the significant difference in session 1 ($p < .01$), session 2 ($p < .05$), and session 3 ($p < .04$). Nevertheless, this statistical difference vanishes in session 4, although the manual and nonbiological modes tend to remain slower than the biological. The reduction of the completion time over the sessions can be explained by a learning effect that occurs in all the conditions.

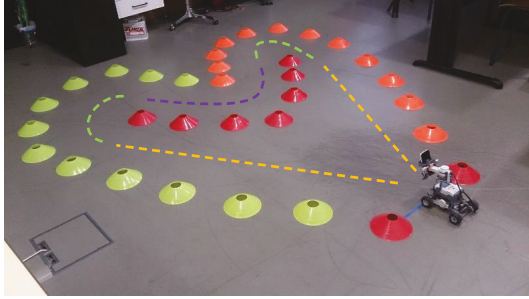


FIGURE 4: Picture of the experimental setting. The symmetric form of the path was chosen to easily alternate the course direction of the robot from one trial to the next: once clockwise and once counter clockwise. This alternation was designed to minimize the environment learning and a consequent machine-like driving of the vehicle. The two straight lines, two 150° bends, and one 90° bend are identified by broken yellow, green, and magenta lines, respectively. Note that these colors are added for a better understanding of the setup but were not visible during the experiment.

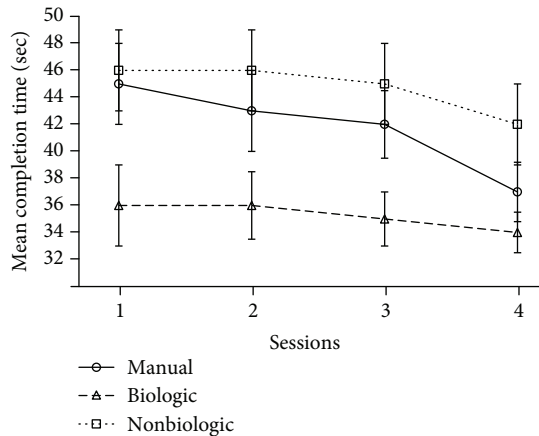


FIGURE 5: Representation of the mean completion time (in seconds) for each of the main conditions (manual vs. biologic vs. nonbiologic) against the four experimental sessions.

5.2. Number of Collisions. The assessment of the rate of collisions was also performed to complement the analysis. The statistical results indicate that the mean number of collisions is significantly different over the sessions ($p < .03$). The pairwise analysis shows a significant diminution of the collisions from session 1 to session 4 ($p < .02$). These outcomes point out that the subjects have improved the quality of their driving skills over the experiment. There is no effect of interaction between the four sessions and the main experimental conditions (manual, biologic, and nonbiologic).

The principal comparison between three conditions shows a significant difference over the whole sessions ($p < .02$). As plotted in Figure 6, more collisions occur in the manual and nonbiological conditions than in the biological condition. The statistical analysis session by session indicates a significant difference in session 1 ($p < .01$) and session 4 ($p < .03$). This last fact suggests that the learning effect does not enable the users in the manual and nonbi-

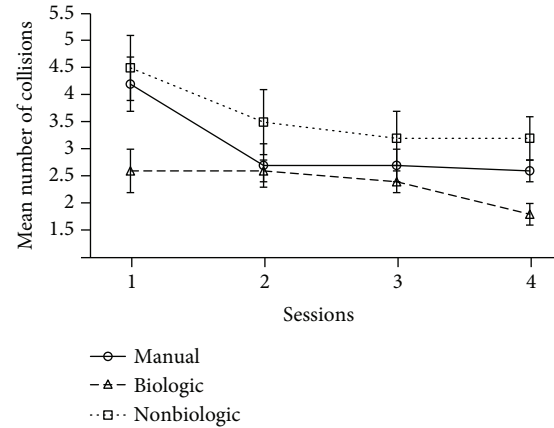


FIGURE 6: Representation of the average number of collisions for each of the main conditions (manual vs. biologic vs. nonbiologic) against the four experimental sessions.

ological modes to get steering skills as good as in the biological condition.

5.3. Trajectory Smoothness. The last results address the question of the movement kinematics through the analysis of the jerk in the control of the robot trajectory. One way to quantify the path smoothness is to calculate the instantaneous radius of curvature of each trajectory, then to evaluate the distribution frequency of the radius for all trials [40]. More specifically, the curve radius (r) is computed from the instantaneous linear velocity (v) divided by the instantaneous rotation speed (w), as described in

$$r_{(m)} = \frac{v_{(m/s)}}{w_{(radians/s)}}. \quad (3)$$

Subsequently, the radius of curvature is converted into a decimal logarithm. Therefore, if the vehicle has a low linear speed and a high velocity of rotation, the curve radius is very small (< 2), and gets smaller as the velocity of rotation increases. The result is a logarithmic value of r that is around zero. Conversely, if the vehicle combines a translation and a rotation (curvilinear trajectory), the curve radius is high (≥ 2) and its logarithm becomes superior to zero. A steering control in which the subject stops and turns in place provides a bimodal distribution of the curve radii, with one peak centered on null values of the logarithm and another peak centered on positive values. On the contrary, a curvilinear (or smooth) trajectory is characterized by a unimodal pattern of distribution centered on a value of the logarithm of the radius of curvature higher than zero. For each trajectory, the distribution of the logarithm of the curve radii is computed and distributed in three categories (small radii, curvilinear trajectories, and straight lines), according to a continuous scale of ranges that permits performing a statistical analysis of the results. To finish, we normalized the distributions, in which the occurrences of radii of curvature in each category are represented by a percentage of all the occurrences for each trajectory.

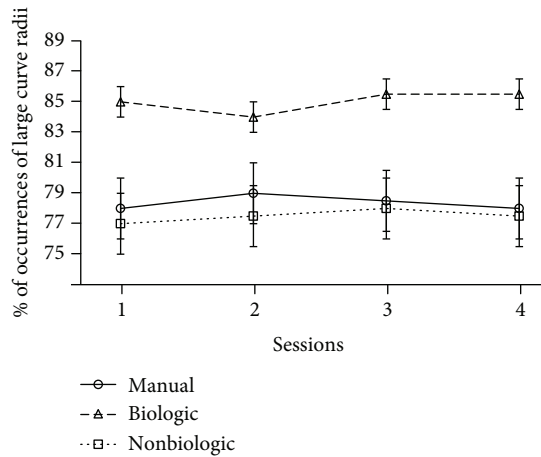


FIGURE 7: Representation of the average rate of large curve radii for each of the main conditions (manual vs. biologic vs. nonbiologic) against the four experimental sessions.

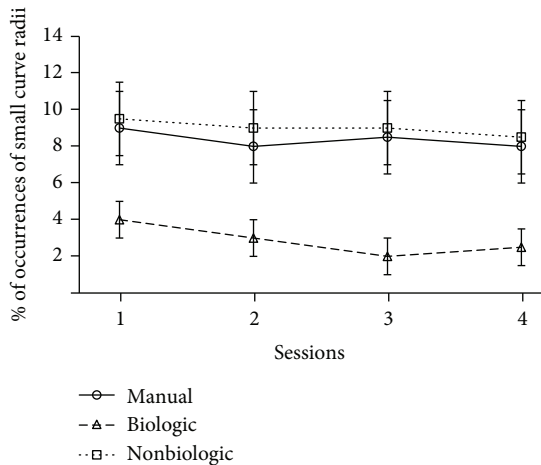


FIGURE 8: Representation of the average rate of small curve radii for each of the main conditions (manual vs. biologic vs. nonbiologic) against the four experimental sessions.

The distribution of large (Figure 7) and small (Figure 8) radii of curvatures is not the same whether the subjects interact with a robot that implements the human-like behavior or a robot that implements the two other modes of control. Thus, the percentage of occurrences of curvilinear trajectories is significantly higher in the biologic than in the manual and nonbiologic conditions ($p < .01$). Similarly, small radii and turn in place are statistically more frequent in the manual and nonbiological than in the biological condition ($p < .01$). In addition, these significant differences are maintained stable over the whole duration of the experiment. It means that four sessions are not enough to provide the teleoperator with a learning effect that could counterbalance the benefit of the bioinspired semiautonomous mode, in terms of the rate of both jerky trajectories ($p < .01$, at session 4) and smooth movements ($p < .01$, at session 4). The difference of steering control can be confirmed by the visualization of the typical paths recorded for each experi-

mental condition (Figure 9). This advanced analysis of the motor performance shows that the operator tends to maximize the smoothness of the robot trajectories, when the vehicle replicates the natural human scheme described by the power law.

6. Discussion

This study consisted in analyzing the effect of the implementation of the $2/3$ power law on the steering control of a vehicle. Three experimental conditions were compared. In the first condition, the participant had to manually control both the speed and the direction of the robot. In the second condition, the velocity of the vehicle was automatically set according to the bioinspired model. Lastly, in the third condition, which was used as a control, the robot speed was automatically calculated through an equation that violated the biological motion. The task of the subjects was to remote control the robot, in order to complete the course as safe and fast as possible. The performance of the participants was recorded on four sessions. The statistical analyses indicate that the number of collisions and the completion time diminish significantly over the sessions. This overall improvement of the performance seems to be related to a learning effect. The main comparison of the study shows that the precision and velocity to accomplish the task are significantly better in the biological condition than in the manual and nonbiological conditions. Since the speed control is automatic in the biological condition, less sensorimotor resources and mental workload of the teleoperators are required to complete the task. This aspect brings an advantage for the individuals, who can focus their attention on the guidance of the vehicle. Nevertheless, the fact that the nonbiological condition is significantly worse than the biological condition means that the automatic setting of the speed must replicate certain characteristics of the natural movement to be effective.

The comparison of the raw performances (speeds and collisions) was complemented by a more advanced assessment based on the analysis of the robot's kinematics. The radii of curvature of the vehicle trajectory were analyzed, in order to evaluate the smoothness of the movements. Like the raw performance, this parameter shows the benefit of implementing a human-like behavior in the robot's way of working. The trajectories are significantly smoother when the power law is integrated into the robot than when this bioinspired model is absent. Remarkably, the study shows that the advantage of the biological law lasts until the end of the experiment, which supposes a stronger impact of the implementation than the learning effect. This result suggests that the power law and minimum jerk are indeed related to each other. Such an outcome is supported by studies that tend to demonstrate that the $2/3$ power law is an optimal solution to smooth the trajectory, because it sets the normal component of the jerk to zero [32, 39, 41]. In addition, it seems that this law satisfies the principle of least action, which states that the amount of work required to complete a trajectory is minimal if the movement obeys the $2/3$ power law [42]. This observation is consistent with an experiment of telemanipulation showing that the motor

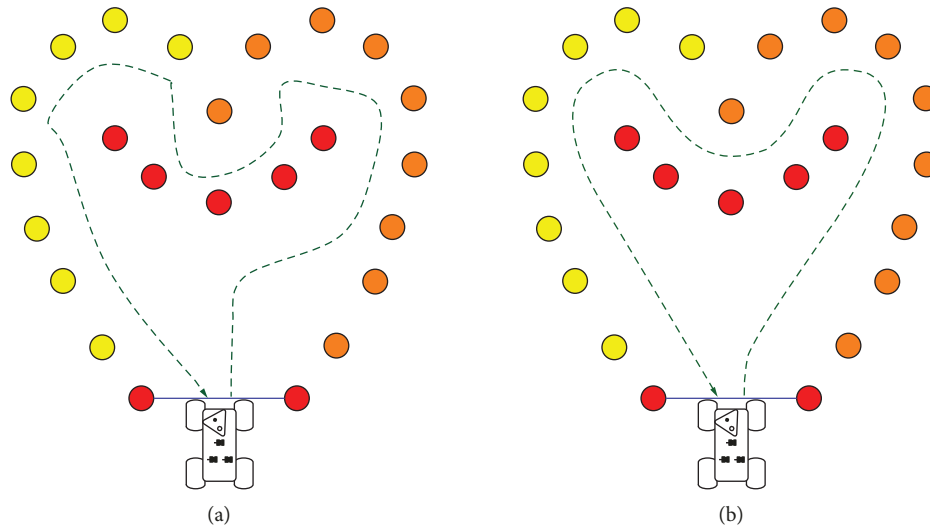


FIGURE 9: Typical example of a path (green dotted line) performed by a robot controlled in the manual or nonbiological mode (a). Notable is the sharp pattern that occurs before the main changes of direction. Sample of a path performed by a robot controlled in the biological mode (b). This condition is characterized by uniformly smoothed trajectories of the vehicle.

skill and performance is negatively correlated with the mental workload of the surgeon during robot-assisted surgery [43]. This finding suggests that the smoothness of the robot movements controlled by an operator could be used as an indirect measurement of the workload.

Furthermore, the fact that the control of a nonanthropomorphic robot is significantly improved when the artefact behaves according to the $2/3$ power law supports the hypothesis of the CNS (Central Nervous System) origin of this law [21, 44]. Viviani and Flash [32] described a correlation between the power law and movement prediction, in order to plan and choose the best trajectory. More precisely, these authors underline that the estimation of the trajectory geometry must be accessible to the motor control system as a part of the internal representation of the predicted movement intention. This is a fundamental feature of the locomotion that requires to program changes in direction one step ahead, in order to overcome the delays due to biomechanical inertia [45]. This motor coordination seems also to occur during the execution of a movement mediated by an artefact, which suggests that this control rule is characteristic of a general scheme of the organization of the action. This observation is supported by the replication of the two-thirds power law in a mobile robot with quite different (bio)mechanics than the human being, which would confirm the hypothesis that this law is not dependent on peripheral biomechanic factors [30, 46], but as issued from an internal model of the movement planning [21, 47].

Moreover, the fact that the operator observes a mobile device that has human-like kinematics can also explain the advantage of the biological mode over the nonbiological. Several experiments show that the observation of a biologically plausible movement facilitates the simultaneous execution, by the observer, of a congruent action [2, 48]. Mirror neurons, and more specifically the Action Observation Network (AON), seem to be involved in this process [49]. In fact, several neuroimaging studies have shown that the activation of

the mirror neuron system areas is modulated by the observer's motor experience [50, 51]. According to predictive coding, the optimal state is a minimal prediction error at all levels of the AON, which is achieved when the observed actions match predicted actions (based on prior visuomotor experience) as closely as possible [52, 53].

To conclude, it is important to mention that it is not always an advantage to automate some parameters of the artefact in a situation of human-machine interaction. Our study suggests that the characteristics of the human being must be taken into account to create appropriate usability rules. Here, the proposed method is to implement a bio-inspired behavior to automate the velocity of a robot. In the case study of the teleoperation of a mobile device or robotic arms, the anthropocentric approach seems to be efficient. A current trend in the automobile industry is to produce more and more autonomic vehicles [54], which is in a certain sense in contradiction with the will of the drivers, who want to keep the control on the technology. Our results suggest that modeling and implementing human-like behaviors in the machine, such as the two-thirds power law [23] or Fitts' law [55], is a promising alternative approach for the automatization of key processes in the artefact's way of working. The advantage of such a method comes from the fact that a car behaving as a living being can be easily understood and appropriated by the end user [36]. Future work will consist in exploring other approaches based on machine learning or reinforcement learning to train the robot to acquire human-like behaviors and, also, improving the transparency of the remote control by providing the operator with natural user interfaces, such as the Kinect, to interact with the machine [17].

Data Availability

The data used to support the findings of this study are available from the corresponding author upon request.

Conflicts of Interest

The authors declare that there is no conflict of interest regarding the publication of this paper.

Acknowledgments

This research was funded by the Universidad de Las Américas, Dirección General de Investigación.

References

- [1] R. C. Arkin and L. Moshkina, *Affect in Human-Robot Interaction*, Georgia Institute of Technology, 2014.
- [2] A. Kupferberg, S. Glasauer, M. Huber, M. Rickert, A. Knoll, and T. Brandt, "Biological movement increases acceptance of humanoid robots as human partners in motor interaction," *Experimental Brain Research*, vol. 26, no. 4, pp. 339–345, 2011.
- [3] T. Chaminade, D. Franklin, E. Oztop, and G. Cheng, "Motor interference between humans and humanoid robots: effect of biological and artificial motion," in *Proceedings of the 4th International Conference on Development and Learning*, pp. 96–101, Osaka, Japan, 2005.
- [4] E. Oztop, D. Franklin, T. Chaminade, and G. Cheng, "Human-humanoid interaction: is a humanoid robot perceived as a human?," in *Proceedings of the 4th IEEE International Conference on Humanoid Robots*, pp. 537–559, Santa Monica, CA, USA, 2004.
- [5] J. Kilner, A. F. C. Hamilton, and S. J. Blakemore, "Interference effect of observed human movement on action is due to velocity profile of biological motion," *Social Neuroscience*, vol. 2, no. 3–4, pp. 158–166, 2007.
- [6] S. Coradeschi, H. Ishiguro, M. Asada et al., "Human-inspired robots," *IEEE Intelligent Systems*, vol. 21, no. 4, pp. 74–85, 2006.
- [7] B. R. Duffy, "Anthropomorphism and the social robot," *Robotics and Autonomous Systems*, vol. 42, no. 3–4, pp. 177–190, 2003.
- [8] Y. Rybarczyk, S. Galerne, P. Hoppenot, E. Colle, and D. Mestre, "The development of robot human-like behaviour for an efficient human-machine co-operation," in *Proceedings of the 6th International Conference of the Association for the Advancement of Assistive Technology in Europe*, Ljubljana, Slovenia, 2001.
- [9] Y. Rybarczyk, O. Ait Aider, P. Hoppenot, and E. Colle, "Remote control of a biomimetics robot assistance system for disabled persons," *AMSE Modelling, Measurement and Control*, vol. 63, no. 4, pp. 47–56, 2002.
- [10] Y. Rybarczyk, D. Mestre, P. Hoppenot, and E. Colle, "Implémentation de mécanismes d'anticipation visuo-motrice en téléopération," *Le Travail Humain*, vol. 67, no. 3, pp. 209–233, 2004.
- [11] Y. P. Rybarczyk and D. Mestre, "Effect of temporal organization of the visuo-locomotor coupling on the predictive steering," *Frontiers in Psychology*, vol. 3, 2012.
- [12] R. Grasso, S. Glasauer, Y. Takei, and A. Berthoz, "The predictive brain: anticipatory control of head direction for the steering of locomotion," *NeuroReport*, vol. 7, no. 6, pp. 1170–1174, 1996.
- [13] J. P. Wann and R. M. Wilkie, "The role of gaze fixation in locomotor control," *Journal of Vision*, vol. 3, no. 9, 2003.
- [14] M. F. Land and D. N. Lee, "Where we look when we steer?," *Nature*, vol. 369, no. 6483, pp. 742–744, 1994.
- [15] S. B. Shafiei, L. Cavuoto, and K. A. Guru, "Motor skill evaluation during robot-assisted surgery," in *Proceedings of the 41st Mechanisms and Robotics Conference*, Cleveland, Ohio, USA, 2017.
- [16] E. De Momi, L. Kranendonk, M. Valenti, N. Enayati, and G. Ferrigno, "A neural network-based approach for trajectory planning in robot-human handover tasks," *Frontiers in Robotics and AI*, vol. 3, 2016.
- [17] H. Su, N. Enayati, L. Vantadori, A. Spinoglio, G. Ferrigno, and E. De Momi, "Online human-like redundancy optimization for teleoperated anthropomorphic manipulators," *International Journal of Advanced Robotic Systems*, vol. 15, no. 6, 2018.
- [18] W. Kim, J. Lee, L. Peternel, N. Tsagarakis, and A. Ajoudani, "Anticipatory robot assistance for the prevention of human static joint overloading in human-robot collaboration," *IEEE Robotics and Automation Letters*, vol. 3, no. 1, pp. 68–75, 2018.
- [19] L. Peternel, N. Tsagarakis, and A. Ajoudani, "A human-robot co-manipulation approach based on human sensorimotor information," *IEEE Transactions on Neural Systems and Rehabilitation Engineering*, vol. 25, no. 7, pp. 811–822, 2017.
- [20] M. Huber, M. Rickert, A. Knoll, T. Brandt, and S. Glasauer, "Human-robot interaction in handing-over tasks," in *Proceedings of the 17th IEEE International Symposium on Robot and Human Interactive Communication*, pp. 107–112, Munich, Germany, 2008.
- [21] F. Lacquaniti, C. Terzuolo, and P. Viviani, "The law relating the kinematic and figural aspects of drawing movements," *Acta Psychologica*, vol. 54, no. 1–3, pp. 115–130, 1983.
- [22] P. Viviani and R. Schneider, "A developmental study of the relationship between geometry and kinematics in drawing movements," *Journal of Experimental Psychology: Human Perception and Performance*, vol. 17, no. 1, pp. 198–218, 1991.
- [23] D. Carvalho, *Controlo remoto de um robô com recurso ao sistema Android [M.S. thesis]*, Nova University of Lisbon, Lisbon, Portugal, 2015, <http://hdl.handle.net/10362/16548>.
- [24] A. M. Jarc and I. Nisky, "Robot-assisted surgery: an emerging platform for human neuroscience research," *Frontiers in Human Neuroscience*, vol. 9, 2015.
- [25] F. Despinoy, D. Bouget, G. Forestier et al., "Unsupervised trajectory segmentation for surgical gesture recognition in robotic training," *IEEE Transactions on Biomedical Engineering*, vol. 63, no. 6, pp. 1280–1291, 2016.
- [26] Y. Rybarczyk, P. Hoppenot, E. Colle, and D. Mestre, "Sensorimotor appropriation of an artefact: a neuroscientific approach," in *Human Machine Interaction—Getting Closer*, pp. 187–212, InTechOpen, London, UK, 2012.
- [27] Y. Rybarczyk, D. Mestre, P. Hoppenot, and E. Colle, "A biological model for the evaluation of human-machine adaptation," *AMSE Modelling, Measurement and Control*, vol. 65, no. 78, pp. 23–33, 2004.
- [28] E. T. Levy, K. E. Gordon, and N. P. Fey, "Residual limb revision surgery alters velocity-curvature coupling during stepping and turning of a transfemoral amputee," in *Proceedings of the 40th Annual International Conference of the IEEE Engineering in Medicine and Biology Society*, Honolulu, HI, USA, 2018.
- [29] S. Schaal and D. Sternad, "Origins and violations of the 2/3 power law in rhythmic three-dimensional arm movements," *Experimental Brain Research*, vol. 136, no. 1, pp. 60–72, 2001.

- [30] P. L. Gribble and D. J. Ostry, "Origins of the power law relation between movement velocity and curvature: modeling the effects of muscle mechanics and limb dynamics," *Journal of Neurophysiology*, vol. 76, no. 5, pp. 2853–2860, 1996.
- [31] M. Zago, A. Matic, T. Flash, A. Gomez-Marin, and F. Lacquaniti, "The speed-curvature power law of movements: a reappraisal," *Experimental Brain Research*, vol. 236, no. 1, pp. 69–82, 2018.
- [32] P. Viviani and T. Flash, "Minimum-jerk, two-thirds power law, and isochrony: converging approaches to movement planning," *Journal of Experimental Psychology: Human Perception and Performance*, vol. 21, no. 1, pp. 32–53, 1995.
- [33] D. Huh and T. J. Sejnowski, "Spectrum of power laws for curved hand movements," *Proceedings of the National Academy of Sciences of the United States of America*, vol. 112, no. 29, pp. E3950–E3958, 2015.
- [34] M. Zago, F. Lacquaniti, and A. Gomez-Marin, "The speed-curvature power law in *Drosophila* larval locomotion," *Biology Letters*, vol. 12, no. 10, 2016.
- [35] S. Vieilledent, Y. Kerlirzin, S. Dalbera, and A. Berthoz, "Relationship between velocity and curvature of a human locomotor trajectory," *Neuroscience Letters*, vol. 305, no. 1, pp. 65–69, 2001.
- [36] C. de'Sperati and P. Viviani, "The relationship between curvature and velocity in two-dimensional smooth pursuit eye movements," *Journal of Neuroscience*, vol. 17, no. 10, pp. 3932–3945, 1997.
- [37] R. S. Marken and D. M. Shaffer, "The power law of movement: an example of a behavioral illusion," *Experimental Brain Research*, vol. 235, no. 6, pp. 1835–1842, 2017.
- [38] R. S. Marken and D. M. Shaffer, "The power law as behavioral illusion: reappraising the reappraisals," *Experimental Brain Research*, vol. 236, no. 5, pp. 1537–1544, 2018.
- [39] S. B. Shafiei, "Intrinsic constraint applied by central nervous system during motor command creation of smooth hand movements," *Archives of Physical Medicine and Rehabilitation*, vol. 97, no. 10, article e49, 2016.
- [40] P. Péruch and D. Mestre, "Between desktop and head immersion: functional visual field during vehicle control and navigation in virtual environments," *Presence: Teleoperators and Virtual Environments*, vol. 8, no. 1, pp. 54–64, 1999.
- [41] E. Todorov and M. I. Jordan, "Smoothness maximization along a predefined path accurately predicts the speed profiles of complex arm movements," *Journal of Neurophysiology*, vol. 80, no. 2, pp. 696–714, 1998.
- [42] S. Lebedev, W. H. Tsui, and P. Van Gelder, "Drawing movements as an outcome of the principle of least action," *Journal of Mathematical Psychology*, vol. 45, no. 1, pp. 43–52, 2001.
- [43] K. A. Guru, S. B. Shafiei, A. Khan, A. A. Hussein, M. Sharif, and E. T. Esfahani, "Understanding cognitive performance during robot-assisted surgery," *Urology*, vol. 86, no. 4, pp. 751–757, 2015.
- [44] P. Viviani and N. Stucchi, "Biological movements look uniform: evidence of motor-perceptual interactions," *Journal of Experimental Psychology: Human Perception and Performance*, vol. 18, no. 3, pp. 603–623, 1992.
- [45] A. E. Patla, S. D. Prentice, C. Robinson, and J. Neufeld, "Visual control of locomotion: strategies for changing direction and for going over obstacles," *Journal of Experimental Psychology: Human Perception and Performance*, vol. 17, no. 3, pp. 603–634, 1991.
- [46] J. Wann, I. Nimmo-Smith, and A. M. Wing, "Relation between velocity and curvature in movement: equivalence and divergence between a power law and a minimum-jerk model," *Journal of Experimental Psychology: Human Perception and Performance*, vol. 14, no. 4, pp. 622–637, 1988.
- [47] J. T. Massey, J. T. Lurito, G. Pellizzer, and A. P. Georgopoulos, "Three-dimensional drawings in isometric conditions: relation between geometry and kinematics," *Experimental Brain Research*, vol. 88, no. 3, pp. 685–690, 1992.
- [48] M. Jeannerod, "Neural simulation of action: a unifying mechanism for motor cognition," *NeuroImage*, vol. 14, no. 1, pp. S103–S109, 2001.
- [49] G. Rizzolatti and C. Sinigaglia, "The functional role of the parieto-frontal mirror circuit: interpretations and misinterpretations," *Nature Reviews Neuroscience*, vol. 11, no. 4, pp. 264–274, 2010.
- [50] B. Calvo-Merino, J. Grèzes, D. E. Glaser, R. E. Passingham, and P. Haggard, "Seeing or doing? Influence of visual and motor familiarity in action observation," *Current Biology*, vol. 16, no. 19, pp. 1905–1910, 2006.
- [51] E. S. Cross, D. J. M. Kraemer, A. F. C. Hamilton, W. M. Kelley, and S. T. Grafton, "Sensitivity of the action observation network to physical and observational learning," *Cerebral Cortex*, vol. 19, no. 2, pp. 315–326, 2009.
- [52] A. Neal and J. M. Kilner, "What is simulated in the action observation network when we observe actions?," *The European Journal of Neuroscience*, vol. 32, no. 10, pp. 1765–1770, 2010.
- [53] M. B. Schippers and C. Keysers, "Mapping the flow of information within the putative mirror neuron system during gesture observation," *NeuroImage*, vol. 57, no. 1, pp. 37–44, 2011.
- [54] K. Curran and J. Lee, "Autonomic vehicles," *Computer and Information Science*, vol. 1, no. 1, 2008.
- [55] J. V. Drapers, B. C. Jared, and M. W. Noakes, "Manipulator performance evaluation using Fitts' tapping task," in *Proceedings of the 8th Topical Meeting on Robotics and Remote Systems*, Pittsburgh, PA, USA, 1999.

Research Article

Prediction Algorithm of Parameters of Toe Clearance in the Swing Phase

Tamon Miyake ¹, Masakatsu G. Fujie,² and Shigeki Sugano²

¹Graduate School of Creative Science and Engineering, Waseda University, Tokyo, Japan

²Faculty of Science and Engineering, Waseda University, Tokyo, Japan

Correspondence should be addressed to Tamon Miyake; tamon-tamonc3@ruri.waseda.jp

Received 22 March 2019; Revised 30 June 2019; Accepted 23 July 2019; Published 14 August 2019

Academic Editor: Loredana Zollo

Copyright © 2019 Tamon Miyake et al. This is an open access article distributed under the Creative Commons Attribution License, which permits unrestricted use, distribution, and reproduction in any medium, provided the original work is properly cited.

The adaptive control of gait training robots is aimed at improving the gait performance by assisting motion. In conventional robotics, it has not been possible to adjust the robotic parameters by predicting the toe motion, which is considered a tripping risk indicator. The prediction of toe clearance during walking can decrease the risk of tripping. In this paper, we propose a novel method of predicting toe clearance that uses a radial basis function network. The input data were the angles, angular velocities, and angular accelerations of the hip, knee, and ankle joints in the sagittal plane at the beginning of the swing phase. In the experiments, seven subjects walked on a treadmill for 360 s. The radial basis function network was trained with gait data ranging from 20 to 200 data points and tested with 100 data points. The root mean square error between the true and predicted values was 3.28 mm for the maximum toe clearance in the earlier swing phase and 2.30 mm for the minimum toe clearance in the later swing phase. Moreover, using gait data of other five subjects, the root mean square error between the true and predicted values was 4.04 mm for the maximum toe clearance and 2.88 mm for the minimum toe clearance when the walking velocity changed. This provided higher prediction accuracy compared with existing methods. The proposed algorithm used the information of joint movements at the start of the swing phase and could predict both the future maximum and minimum toe clearances within the same swing phase.

1. Introduction

Robotic technology for physical human-robot interaction has the potential to improve human locomotion. Moreover, robotic assistance can guide gait motion and provide direct somatosensory information. Robotic guidance is effective because the effects of training last longer when people instinctively modify their motion, compared with when they consciously modify their motion [1]. Assistance should be provided only when it is required because the human movement ability decreases when it is not actively used [2]. Hence, there is a need for developing adaptive robotic assistance technology that encourages maximum active patient participation.

The human-centered control of robotics for gait training is being investigated in an attempt to make robotic systems more human-friendly [3]. Gait training robots, such as ALEX and Lokomat, have an interaction force field controller,

which allows patients to walk in a manner that is different from the desired trajectory determined for a healthy person [4–6]. LOPES II, which is an end-effector type robot, is able to switch between low and high mechanical impedance modes using admittance control [7]. These robots adapt to individual differences and adjust their reference trajectory to recover motor functioning for gait trajectory generation. Conventional algorithms are adaptive after human action, and assistance methods for determining the robotic parameters by previously predicting the gait motion have not yet been established.

Falling is one of the most serious problems with locomotion. The risk of falling encourages people to stay indoors, which leads to the weakening of their bodies. Moreover, tripping accounts for 53% of falling incidents [8]. Older individuals are in more risk of tripping while taking small steps because it is difficult for them to assess the height difference at the edges of rugs or carpets [9]. Toe clearance

must be ensured to avoid falling and controlled to reduce the dispersion. The possibility of tripping occurs if the toe approaches the ground at an arbitrary point in the gait cycle. The prediction of toe clearance can reduce the risk of tripping. For robotic assistance to increase the toe clearance when it decreases in the gait cycle, a method of predicting toe clearance is required.

Calculation techniques with wearable sensors deriving the toe clearance have been developed mainly for ambulatory estimation and monitoring of the toe clearance without a camera system [10–14]. The integration of the inertial parameters of the inertial measurement unit (IMU), which consists of triaxial accelerometers and gyroscopes, was carried out to estimate the toe parameters [10–12]. The dedrifted integration of two wireless IMUs attached to the feet can estimate the foot clearance with an error of approximately 20 mm [12]. Owing to this large error, the integration method has a large limitation with regard to calculating the position. A machine learning method has been developed to estimate the gait parameters after the learning phase in each person [13–15]. Using machine learning with Gaussian functions and a hill-climbing feature-selection method, the root mean square error (RMSE) of 6.6 mm was estimated for young individuals [14]. In previous research, the parameters of toe clearance were predicted by a regression model [15]. To the best of our knowledge, Gaussian functions that were applied using acceleration features through the double differentiation of the toe position captured with a motion capture system could predict the minimum toe clearance most accurately (an RMSE of 3.7 mm) for one gait cycle ahead.

The existing prediction method has a limitation with regard to establishing robotic assistance that increases the toe clearance when it decreases, because the system does not use wearable sensors that can communicate with a robot controller. The estimation accuracy is lower when the wearable inertial sensor is used, compared with when the motion capture system is used to extract the input data. Moreover, the existing method is not sufficiently accurate for handling the toe clearance variability between the gait cycles. Additionally, it has been reported that the interquartile range of the minimum toe clearance is approximately 4.3 mm for young individuals and approximately 5.3 mm for older individuals [16]. Detecting a lower value for the minimum toe clearance with a probability of more than 50% may be difficult using this method. Hence, a more accurate toe clearance prediction method that uses wearable sensors to obtain the input data is required for robotic assistance.

We developed a prediction algorithm of minimum toe clearance using the angular information of the lower limb joints [17]. Our hypothesis is that the articular motion information at the lower limb joints at the time when people start to swing their leg is related to the future toe clearance because the toe motion is generated by the swing motion of the lower limb. People control their leg motion based on interjoint coordination, and the angular coordination maintains low dispersion at the limb end points [18]. Therefore, we assumed that the difference between the angular information in a certain phase is related to the difference of toe clearance

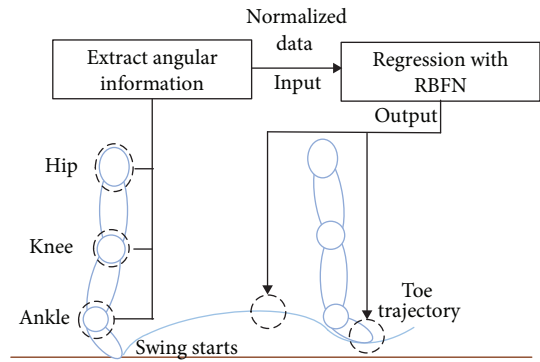


FIGURE 1: Overview of the dataflow of the proposed algorithm.

among the gait cycles. Moreover, we assumed that adding the angular velocity and acceleration of the lower limb joint would be beneficial because these parameters contain information regarding the movement over time. Previous studies have investigated computational technology, such as accelerometers [19, 20], gyroscopes [21, 22], and IMUs [23], for the detection of foot-contact state using wearable sensors and machine learning strategies implementing support vector machines (SVM) [24], linear discriminant analysis (LDA) [25], Gaussian mixture model (GMM) [26], and hidden Markov model (HMM) [27, 28]. Notably, none of these methods can detect the characteristic points of phase change in the angular trajectory. In a previous work, we extracted the characteristic angular point with consideration to the change of synergy between the hip, knee, and ankle joints and only predicted the minimum toe clearance with higher accuracy [17]. However, the wearable sensor tends to deviate while people walk, and the sensed values always contain noises. Compensation is required for the deviation of the sensed values.

In this study, we established an algorithm to predict the characteristic toe clearance parameters in the swing phase using the angles, angular velocities, and angular accelerations of the lower limb joints. We applied machine learning-based regression with Gaussian functions to probabilistically predict the toe clearance with consideration to the noise of the input data. Additionally, we investigated the relationship between the number of training data and the prediction accuracy, and we evaluated the prediction algorithm to investigate whether our method could more accurately predict the toe clearance and detect the lower value of toe clearance.

2. Materials and Methods

The proposed method consisted of extraction of input data and a regression algorithm using the radial basis function network (RBFN) to predict the characteristic parameters of the toe clearance as shown in Figure 1. The algorithm was designed to automatically extract the input data points in an earlier swing phase and normalize these input values to reduce the effect of the deviation of the sensor.

The characteristic phase of input data was extracted with consideration to the synergy between the hip, knee, and ankle joints. The angular trajectory in the angular space is on the

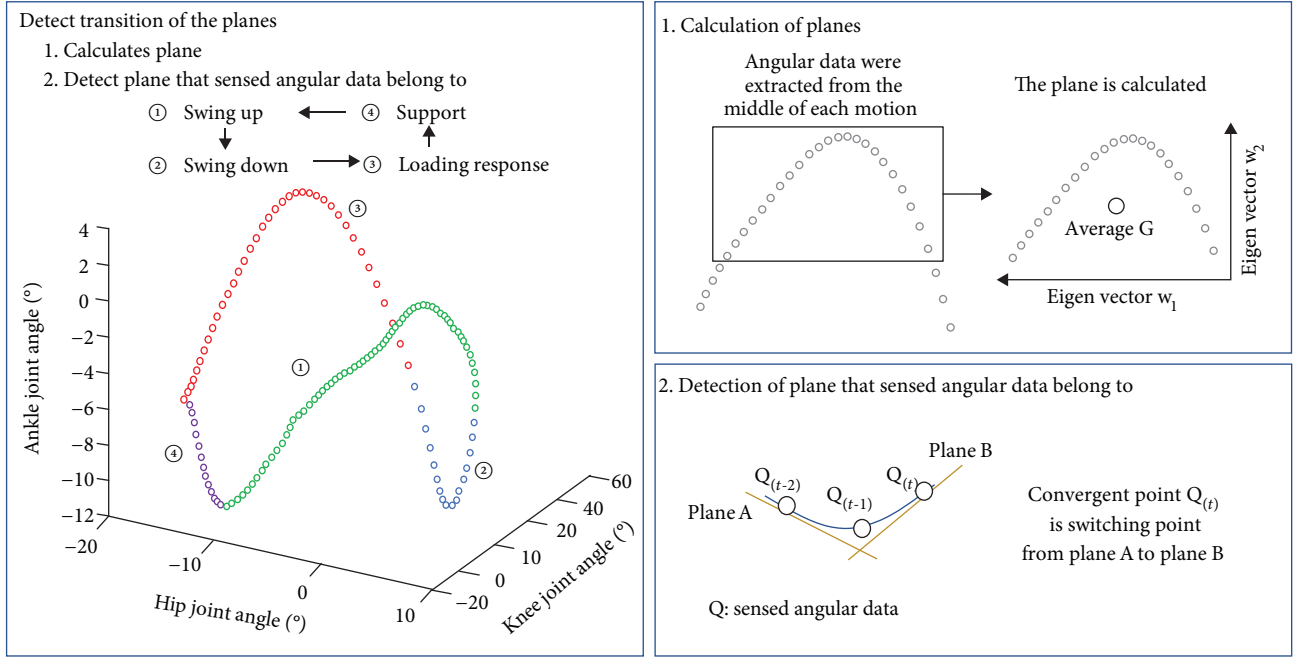


FIGURE 2: Overview of the algorithm for deriving the four planes in the angular space of the hip, knee, and ankle joints and for detecting the transitions of the planes.

planes during walking [29], and the planes of these angles are different in the phases [30]. Detecting the change from the stance phase to the swing plane can be done more clearly in the planes, whereas detecting changes with the angle readings is difficult owing to the presence of noise and fluctuations in the angle range. As shown in Figure 2, the controller explores four planes in one gait cycle because the gait motion of the lower limb consists of the swing of the leg to lift the foot (swing up), the swing of the leg to prepare foot-ground contact (swing down), the loading response to absorb the shock of foot contact (loading response), and support for the body (support). First, the controller derives basis vectors of the planes by extracting parts of the angular data in each phase (block 1 of Figure 1). Second, the controller detects the switching points from the support phase to the swing up phase in an angular space so as to detect the time points when the swing phase starts (block 2 of Figure 1).

Parts of the angular data were extracted based on the hip angle to derive the planes for deriving the basis vectors of the planes (block 1 of the Figure 1). The maximum angle was defined as 100%, and the minimum angle was defined as 0%. First, the angular data were categorized as belonging to the motion of the swing up and were extracted when the hip motion was in more than 10% flexion and the knee joint was in flexion. Next, the angular data corresponding to the motion of the swing down were extracted when the knee joint extended and the hip flexion angle was within 30% after the swinging motion. Additionally, angular data corresponding to the loading response (i.e., dual-support phase) were extracted when the hip joint was in extension, the knee joint was in flexion, and the dorsiflexion angle of the ankle joint was less than 10% from the second minimum value. Finally,

the parts of the angular data corresponding to the motion of supporting the body were extracted when the hip joint was in extension and the ankle joint was in dorsiflexion. The robot extracted the angular data in the middle of the swing or stance phase based on the hip angle readings.

Two basis vectors constituting the plane can be derived using principal component analysis (PCA) and the extracted parts of the angular data. The controller calculates the eigenvectors of the first and second components, which are the basis vectors of the plane, using PCA. The vector from the preprojection coordinates to the postprojection coordinates is orthogonal to the basis vectors of the plane. Moreover, the two eigenvectors w_1 and w_2 are perpendicular to each other. Using this relationship, the coordinates \mathbf{P} on the plane are defined as follows:

$$\mathbf{P} = a_1 \mathbf{w}_1 + a_2 \mathbf{w}_2 + \mathbf{G},$$

$$a_1 = \mathbf{Q} \cdot \mathbf{w}_1 - \mathbf{G} \cdot \mathbf{w}_1, \quad (1)$$

$$a_2 = \mathbf{Q} \cdot \mathbf{w}_2 - \mathbf{G} \cdot \mathbf{w}_2,$$

where a_1 and a_2 are the coefficients of the eigenvectors, \mathbf{G} denotes the coordinates of the mean angle data, and \mathbf{Q} denotes the sensed coordinates of the lower limb articular angular space before projection. a_1 and a_2 are calculated using the inner product of the eigenvectors and orthogonal vectors.

The algorithm calculates the distance from the preprojection coordinates to the postprojection coordinates on each plane to derive the switching points of the planes (block 2 of Figure 1). Additionally, the algorithm calculates the inner

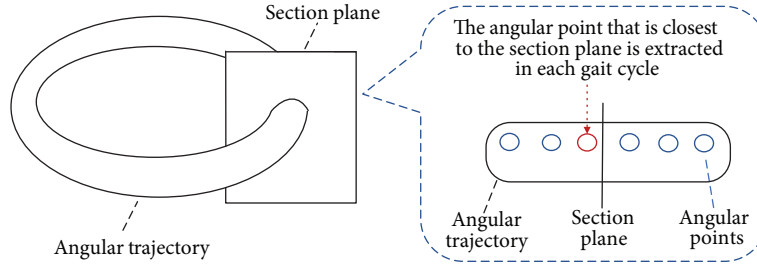


FIGURE 3: Extraction method of input values by finding the angular point that is the closest to the section plane when the gait state changes from the stance phase to the swing phase.

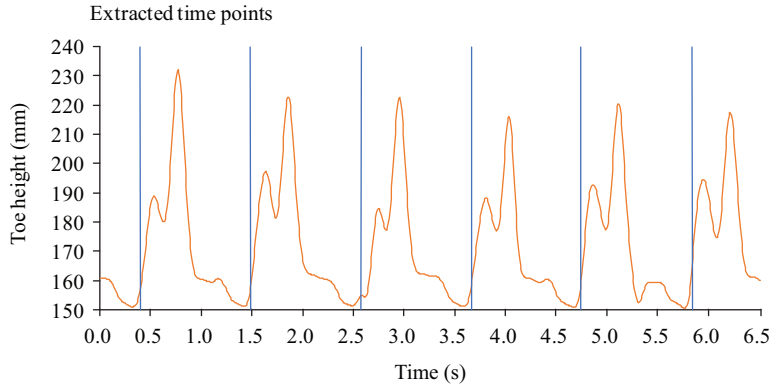


FIGURE 4: Gait phase detection result of extracting time points for use as input to the prediction algorithm.

product between the unit vector from a previously sensed angular point to the currently sensed angular point and the unit vector from a previous projected point to the current projected point. The sensed angular data are recognized as a phase whose plane is closer to the data, compared with the other planes, when the distance is the local minimum and the inner product is more than 0.9.

The phase when the swing starts can be derived by observing whether the angular trajectory passes through the section plane that was previously calculated using the plane structure as shown in Figure 3. The section plane is calculated because it is difficult to detect the switching points of the planes in real time owing to the shifting of the plane during walking. First, the switching points from the plane of support to the plane of swing up were derived using the data obtained from the 20 gait cycles. Next, the section plane of the angular trajectory is calculated when the swing phase starts. The average switching point is estimated, and the normal vector of the section plane is calculated by deriving the vector from the detected switching points to the next sensed angular point. The orthogonal vector \mathbf{v} of the normal vector can be calculated as follows:

$$\mathbf{v} = [2bc, -ac, -ab], \quad (2)$$

where a , b , and c denote the hip, knee, and ankle joint angles that constitute the normal vector, respectively. The basis vectors of the section plane are two orthogonal vectors of the normal vector, which is calculated by deriving the cross product between the first orthogonal vector and the normal

vector. Finally, as shown in Figure 4, the angular points for the input data are extracted by finding the time point where the distance from the sensed angular point to the point projected onto the section plane is minimum.

The parameters of toe clearance were calculated using the RBFN with Gaussian functions, as shown in Figure 5. The RBFN is the linear sum of the radial basis functions, such as the Gaussian functions, for nonlinear curve fitting. The RBFN consists of an input layer, a hidden layer with radial basis functions, and an output layer. This network calculates the distance between the vector of the input data and the centroids of each Gaussian, which are derived using the K -means clustering algorithm to partition the dataset into a predetermined number of groups according to the Euclidean distance. The RBFN structure is expressed as follows:

$$\mathbf{y} = \sum_{k=1}^N \mathbf{w}_k \exp\left(-\frac{\|\mathbf{x} - \mathbf{c}_k\|^2}{\sigma}\right) + \alpha, \quad (3)$$

where \mathbf{y} denotes the output vector, \mathbf{w}_k is the weight vector, \mathbf{x} is the input vector, \mathbf{c}_k is the centroid vector, N is the number of RBF units, α is a variable coefficient, and σ is a variable related to the standard deviation of the Gaussian function. σ is derived as follows [31]:

$$\sigma = \frac{d_{\max}}{\sqrt[m]{Nm}}, \quad (4)$$

where d_{\max} denotes the maximum distance among the data and m is the dimension of the data.

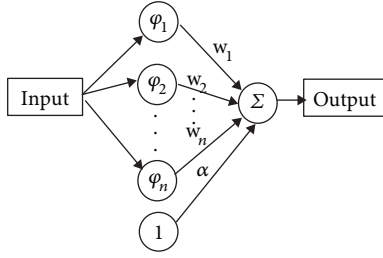


FIGURE 5: Structure of the radial basis function network (RBFN).

The angles of the hip, knee, and ankle joints in the sagittal plane were sensed with wearable angle sensors. The angular velocity and angular acceleration of these joints were derived by differentiating the angles with a pseudo differential. The angles were smoothed using a low-pass filter (with a cutoff frequency of 6 Hz). The equation of the pseudo differential based on an s-plane to z-plane transformation is expressed as follows:

$$Y_n = \frac{X_n - X_{n-1} + T_d Y_{n-1}}{\Delta T}, \quad (5)$$

where T_d denotes the time constant, ΔT denotes the sampling time, which was 8.33 ms, and Y_n and X_n denote the n^{th} differential value and n^{th} input value, respectively. In this study, T_d was considered 167 ms to differentiate the data whose frequency was lower than 6 Hz.

All input values were normalized to reduce the effect of attachment position deviation of the wearable angle sensors. The minimum values in the previous gait cycle were subtracted from the input values. Moreover, all input values were divided by their range of values in the first gait cycle in the training phase for RBFN so as to decrease the effect of the range of values.

3. Human Walking Experiment

Four healthy younger adults (three men and one woman; aged 27 ± 5 years, body weight 57 ± 13 kg, height 1.64 ± 0.13 cm) and two healthy older adults (two men; aged 65 ± 2 years, body weight 62 ± 1 kg, height 1.68 ± 0.03 cm) were recruited in the first experiment. Five healthy young adults (four men and one woman; aged 25 ± 3 years, body weight 58 ± 9 kg, height 1.63 ± 0.7 cm) were recruited in the second experiment. All of them did not have neurological injuries or gait disorders. Before the experiment, the subjects were provided with a detailed account of our experimental objectives and were informed that they could withdraw from the experiment whenever they desired, and we obtained their consent. This experiment was also approved by the institutional review board at Waseda University (No. 2017-085).

Because the maximum values are an indicator of how high people raise their foot and the minimum values are an indicator of how high people can keep their foot above the ground, the maximum toe clearance in the earlier swing phase and the minimum toe clearance in the later swing

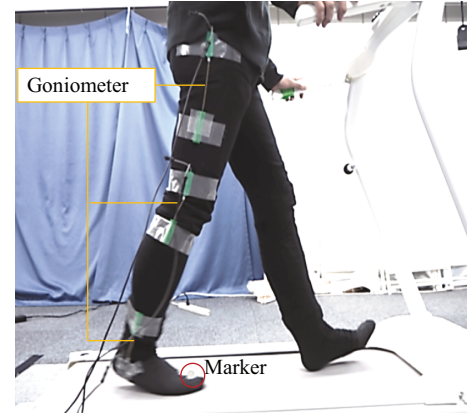


FIGURE 6: Experimental image of subjects walking on a treadmill.

phase were measured to give characteristic toe clearance data. The toe coordinates of the right foot were measured with a motion capture system (Raptor-E; Motion Analysis, Santa Rosa, CA, USA). The marker for the measurement was attached to the first metatarsophalangeal joint of the foot. The angles of the right hip, knee, and ankle joints were measured with goniometers (SG110 and SG150, Biometrics Ltd., Newport, UK), which are wearable angle sensors. The subjects walked on a treadmill as shown in Figure 6.

The 6 subjects were instructed to continue walking for 360 s at a preferred constant speed ranging from 2.1 km/h to 3.0 km/h in the first experiment. We investigated the number of training data points required for the RBFN to improve the prediction accuracy. We used 20 to 200 gait cycle data points for the training and 100 gait cycle data points for the RBFN test. The number of RBF units was set from two to twenty.

The 5 subjects walked for 600 s at 2.0 km/h, 2.5 km/h, and 3.0 km/h in the second experiment. The duration of walking at 2.5 km/h was 360 s, and the duration of walking at 2.0 km/h and 3.0 km/h was 120 s. We investigated whether the RBFN could predict the toe clearance if the walking speed changed. Approximately 160 cycle data of 2.5 km/h walking were used as the training data based on the result of the first experiment, and the 100 gait cycle data points of 2.0 km/h and 3.0 km/h were used as the test data. The number of RBF units was set from two to twenty. Moreover, we added the goniometers for a left leg in this experiment.

We derived the time from the time point where the system extracted the input data to the time points for the maximum and minimum toe clearances. We calculated the average time of all training data and the standard deviation to evaluate whether the system could have previously predicted both the maximum and minimum clearances.

We normalized the maximum and minimum toe clearance values by defining the average of the training data as zero as shown in Figure 7. The toe clearance values that were lower than the average were negative (minus sign), while the values that were higher than the average were positive (plus sign). We calculated the RMSE between the true value and

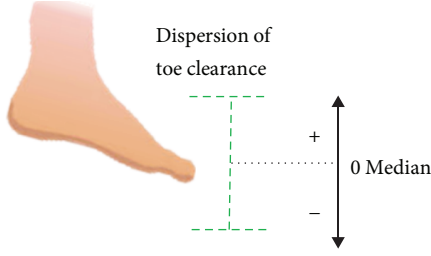


FIGURE 7: Normalization of toe clearance data.

the predicted value of the maximum and minimum toe clearances, as follows:

$$\text{RMSE} = \sqrt{\frac{\sum_{k=1}^n (y_k - \tilde{y}_k)^2}{n}}, \quad (6)$$

where y_k denotes the true value, \tilde{y}_k denotes the predicted value, and n is the number of data points.

Additionally, we estimated the accuracy percentage of the predicted data according to the accuracy of the plus or minus signs and counted the number of predicted values with the same sign as the true value, which was then divided by the total number of data points.

4. Results and Discussion

Figure 8 shows the time from the time points where the system extracted the input data to the time points of the maximum or minimum toe clearances. The input data were extracted 0.1 s before the toe clearance reached the maximum value in the earlier swing phase.

Figures 9 and 10 show the RMSE between the true and predicted data for the maximum and minimum toe clearances corresponding to the number of training data points. The RMSE tended to decrease as the number of training data points increased. Particularly, the RMSE was minimum when the number of training data points was 200 for subjects 1, 3, and 6. The other subjects had a minimum RMSE when the number of training data points was between 80 and 180. For the maximum toe clearance, the average minimum RMSE was 2.99 mm, and the lowest RMSE was 2.31 mm. For the minimum toe clearance, the average minimum RMSE was 2.34 mm, and the lowest RMSE was 1.79 mm. The number of RBF units that minimized the RMSE was approximately five.

Figures 11 and 12 show the accuracy rate of the predicted data for the maximum and minimum toe clearances corresponding to the number of training data points. The average accuracy rate was 71% for the maximum toe clearance and 68% for the minimum toe clearance.

Figure 8 shows the average time from the time points where the system extracted the input data to the time points where the maximum or minimum toe clearances were positive. This means that the proposed algorithm was able to extract the input data before the toe clearance reached its maximum value in the earlier swing phase. However, time was not always constant. The standard deviation was large compared with the time of the gait cycle, which was approx-

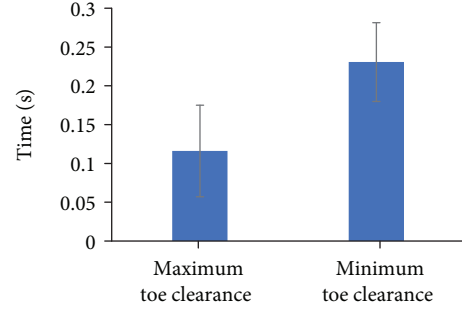


FIGURE 8: Time from points where the system extracted the input data to the points of the maximum and minimum toe clearances. The error bar indicates the standard deviation.

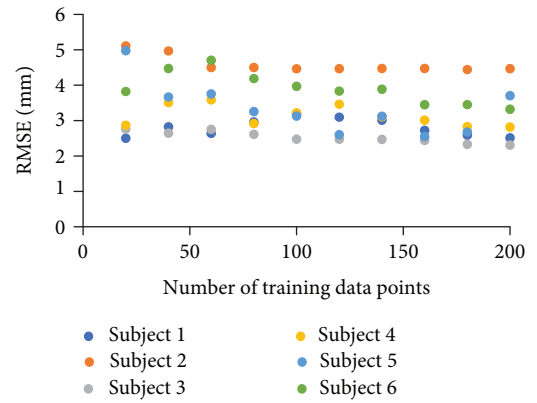


FIGURE 9: Prediction result for maximum toe clearance using 100 test gait data (RMSE).

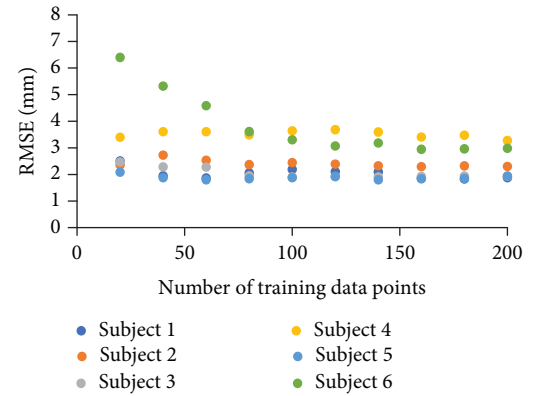


FIGURE 10: Prediction result for minimum toe clearance using 100 test gait data (RMSE).

imately 1.4 s in this experiment. The variance in the detection time plays a role in reducing the time. By improving the accuracy of phase detection, the prediction can be made earlier.

As shown in Figures 9 and 10, the RMSE between the real toe clearance measured by the motion capture system and the predicted toe clearance was the lowest between 80 and 200 training data points. Moreover, the accuracy rate tended to

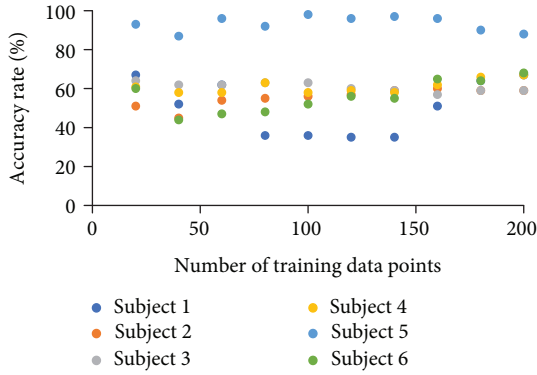


FIGURE 11: Prediction result for maximum toe clearance using 100 test gait data (accuracy rate).

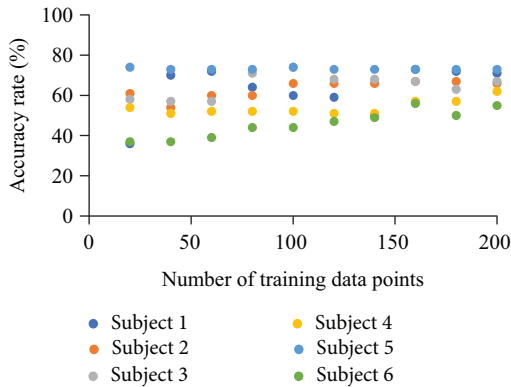


FIGURE 12: Prediction result for minimum toe clearance using 100 test gait data (accuracy rate).

increase when the number of training data points increased. Therefore, a higher number of training data points tended to improve the prediction accuracy, presumably because it became easier to extract the characteristics of the input data space when more training data were provided. The RBFN clusters the input data and calculates the median values of each cluster in the training phase. The output values are determined according to the distance of the input data values from the median values of each cluster. If the number of training data points decreases, it becomes difficult to precisely determine the RBFN parameters because the effect of the input data noise increases. In this experiment, the clustering of training data points and the derivation of the median required approximately 100 to 200 training data points to reduce the variance and the effect of the noise that is always present in data.

As shown in Figures 9 and 10, the RMSE was 2.99 mm for the maximum toe clearance and 2.34 mm for the minimum toe clearance, which is a more accurate prediction compared with previous methods. The RMSE of the maximum toe clearance was higher than the RMSE of the minimum toe clearance, because the variance of the maximum toe clearance was higher than the variance of the minimum toe clearance. The individual difference between the RMSE tended to be higher as the variance of the toe clearance

between cycles increased. The probability of detecting a value lower than that of the median toe clearance was higher than 68%; that is, the probability was higher than the probability of random detection.

Figures 13 and 14 show the RMSE and the accuracy rate of the predicted data for the maximum and minimum toe clearances of 100 test data by training the RBFN using approximately 160 training data in the case of the walking velocity. The prediction error of the minimum toe clearance was lower compared with the previous researches even when the walking speed changed after the RBFN was learned with a constant walking speed. Moreover, the proposed algorithm could detect the value lower than that of the median toe clearance with the probability that was higher than the probability of random detection if walking velocity changed. We assumed that the RBFN parameters reflected the difference of foot kinematics related to the change of the walking velocity because the input data were related to the kinematics of the lower limb. However, the RMSE of the minimum toe clearance and the maximum toe clearance increased when the walking velocity changed. It will be beneficial to train the RMSE with the input data in several conditions for generalized regression. Besides, the standard deviation of the RMSE of all subjects decreased when the left leg joints' information was included as the input values. We assumed that it indicated that more numbers of input parameters related to foot kinematics improved the prediction accuracy. As a future work, we will focus on both the feet and increase of the input parameters of joints of both lower limbs.

The proposed algorithm has an advantage of deriving the toe clearance preliminarily in real time while most previous calculation methods were developed for the estimation of toe clearance [10–14]. Moreover, the prediction accuracy of the proposed algorithm was higher than that of the previous method [15]. Although we normalized the data of the toe clearance for evaluating whether the algorithm could detect the value lower than that of the median toe clearance, the toe height from the ground could be derived because the subtracted value is clear. The proposed system has a limitation because learning is needed in each person, which is similar to previous MTC estimation methods using wearable sensors. Therefore, it requires a learning phase with a camera system before using the algorithm.

The accuracy was lower for subjects whose gait motion and planes in an angular space tended to vary. The angular information always changes with time within one gait cycle. One point on the periodic trajectory in an angular space was extracted in each gait cycle. If phase detection errors occur, it is difficult to compare the articular angle, angular velocity, and angular acceleration differences between the gait cycles. We used the planes of the articular space for the hip, knee, and ankle joints to detect the phase of the angular periodic trajectory. Because the trajectory varied between gait cycles, the planar vectors varied throughout the experiment. The proposed algorithm considered the change of planes by calculating the section plane of the trajectory around the switching points, which was detected by calculating the planes in each gait cycle. However, the phase when the input data were extracted might vary. This study demonstrated that

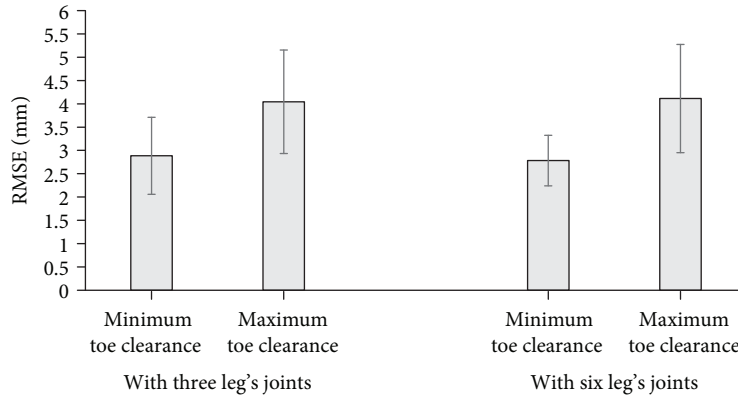


FIGURE 13: The prediction result using 100 test gait data when the walking velocity changes (RMSE). The values are the mean, and the error var means the standard deviation among the five subjects.

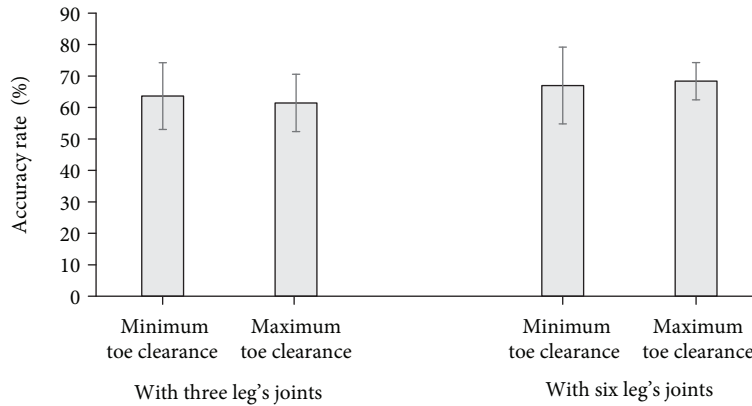


FIGURE 14: The prediction result using 100 test gait data when the walking velocity changes (accuracy rate). The values are the mean, and the error var means the standard deviation among the five subjects.

the toe clearance parameters can be predicted using only angular information in the sagittal plane. The accuracy of gait phase detection and the prediction of toe clearance may improve by increasing the input parameters, such as the angles in the coronal plane or the foot contact information.

5. Conclusions

This paper proposes a novel toe clearance prediction algorithm with an RBFN using the angles, angular velocities, and angular accelerations of the hip, knee, and ankle joints in the sagittal plane. The proposed algorithm can predict both the maximum toe clearance in the earlier swing phase and the minimum toe clearance in the later swing phase at the same time. The error was 2.99 mm for the maximum toe clearance and 2.34 mm for the minimum toe clearance. Moreover, the root mean square error between the true and predicted values was 4.04 mm for the maximum toe clearance, and 2.88 mm for the minimum toe clearance when the walking velocity changed. The errors of the minimum toe clearance are smaller compared with previous methods. The probability of detecting a value lower than the median toe clearance was higher than 68%; that is, the probability was higher than the probability of random detection. Therefore,

a robot using this algorithm may be able to influence the variance of human toe clearance.

In a future work, we will improve the gait phase detection method. Moreover, we will conduct experiments to investigate the effect of robotic assistance with the proposed toe clearance prediction algorithm on older people.

Data Availability

The data used to support the findings of this study are available from the corresponding author upon request.

Conflicts of Interest

The authors declare that there is no conflict of interest regarding the publication of this paper.

Acknowledgments

This work was supported in part by the Program for Leading Graduate Schools, "Graduate Program for Embodiment Informatics" of the Ministry of Education, Culture, Sports, Science and Technology (MEXT) of Japan and Tateisi Science and Technology Foundation and supported by the

Research Institute for Science and Engineering, Waseda University. We thank Edanz Group (<https://www.edanzediting.com/ac>) for editing the draft of this manuscript.

References

- [1] L. A. Malone and A. J. Bastian, "Thinking about walking: effects of conscious correction versus distraction on locomotor adaptation," *Journal of Neurophysiology*, vol. 103, no. 4, pp. 1954–1962, 2010.
- [2] W. M. Bortz 2nd, "The disuse syndrome," *The Western Journal of Medicine*, vol. 141, no. 5, pp. 691–694, 1984.
- [3] R. L. Lëünenburger and G. Colombo, "Human-centered robotics applied to gait training and assessment," *Journal of Rehabilitation Research and Development*, vol. 43, no. 5, pp. 679–694, 2006.
- [4] S. K. Banala, S. H. Kim, S. K. Agrawal, and J. P. Scholz, "Robot assisted gait training with active leg exoskeleton (ALEX)," *IEEE Transactions on Neural Systems and Rehabilitation Engineering*, vol. 17, no. 1, pp. 2–8, 2009.
- [5] R. Rienner, L. Lëünenburger, S. Jezernik, M. Anderschitz, G. Colombo, and V. Dietz, "Patient-cooperative strategies for robot-aided treadmill training: first experimental results," *IEEE Transactions on Neural Systems and Rehabilitation Engineering*, vol. 13, no. 3, pp. 380–394, 2005.
- [6] S. Hussain, S. Q. Xie, and P. K. Jamwal, "Adaptive impedance control of a robotic orthosis for gait rehabilitation," *IEEE Transactions on Cybernetics*, vol. 43, no. 3, pp. 1025–1034, 2013.
- [7] J. Meuleman, E. van Asseldonk, G. van Oort, H. Rietman, and H. van der Kooij, "LOPES II—design and evaluation of an admittance controlled gait training robot with shadow-leg approach," *IEEE Transactions on Neural Systems and Rehabilitation Engineering*, vol. 24, no. 3, pp. 352–363, 2016.
- [8] K. Morgan, M. J. Bendall, H. Dallosso et al., "Falls by elderly people at home: prevalence and associated factors," *Age and Ageing*, vol. 17, no. 6, pp. 365–372, 1988.
- [9] T. Rosen, K. A. Mack, and R. K. Noonan, "Slipping and tripping: fall injuries in adults associated with rugs and carpets," *Journal of Injury and Violence Research*, vol. 5, no. 1, pp. 61–65, 2013.
- [10] N. Kitagawa and N. Ogihara, "Estimation of foot trajectory during human walking by a wearable inertial measurement unit mounted to the foot," *Gait & Posture*, vol. 45, pp. 110–114, 2016.
- [11] B. Mariani, C. Hoskovec, S. Rochat, C. Büla, J. Penders, and K. Aminian, "3D gait assessment in young and elderly subjects using foot-worn inertial sensors," *Journal of Biomechanics*, vol. 43, no. 15, pp. 2999–3006, 2010.
- [12] B. Mariani, S. Rochat, C. J. Büla, and K. Aminian, "Heel and toe clearance estimation for gait analysis using wireless inertial sensors," *IEEE Transactions on Biomedical Engineering*, vol. 59, no. 11, pp. 3162–3168, 2012.
- [13] D. McGrath, B. R. Greene, C. Walsh, and B. Caulfield, "Estimation of minimum ground clearance (MGC) using body-worn inertial sensors," *Journal of Biomechanics*, vol. 44, no. 6, pp. 1083–1088, 2011.
- [14] B. K. Santhiranayagam, D. T. Lai, W. A. Sparrow, and R. K. Begg, "A machine learning approach to estimate minimum toe clearance using inertial measurement units," *Journal of Biomechanics*, vol. 48, no. 16, pp. 4309–4316, 2015.
- [15] D. T. Lai, S. B. Taylor, and R. K. Begg, "Prediction of foot clearance parameters as a precursor to forecasting the risk of tripping and falling," *Human Movement Science*, vol. 31, no. 2, pp. 271–283, 2012.
- [16] P. M. Mills, R. S. Barrett, and S. Morrison, "Toe clearance variability during walking in young and elderly men," *Gait & Posture*, vol. 28, no. 1, pp. 101–107, 2008.
- [17] T. Miyake, M. G. Fujie, and S. Sugano, "Prediction of minimum toe clearance with a radial basis function network at the start of the swing phase," in *2018 40th Annual International Conference of the IEEE Engineering in Medicine and Biology Society (EMBC)*, pp. 1664–1667, Honolulu, HI, USA, July 2018.
- [18] J. P. Scholz and G. Schöner, "The uncontrolled manifold concept: identifying control variables for a functional task," *Experimental Brain Research*, vol. 126, no. 3, pp. 289–306, 1999.
- [19] A. Mansfield and G. M. Lyons, "The use of accelerometry to detect heel contact events for use as a sensor in FES assisted walking," *Medical Engineering & Physics*, vol. 25, no. 10, pp. 879–885, 2003.
- [20] N. Mijailovi, M. Gavrilovi, S. Rafajlovi, and D. B. Popovi, "Gait phases recognition from accelerations and ground reaction forces: application of neural networks," *Signal Processing*, vol. 1, pp. 34–36, 2009.
- [21] I. P. I. Pappas, M. R. Popovic, T. Keller, V. Dietz, and M. Morari, "A reliable gait phase detection system," *IEEE Transactions on Neural Systems and Rehabilitation Engineering*, vol. 9, no. 2, pp. 113–125, 2001.
- [22] A. Mannini and A. M. Sabatini, "Gait phase detection and discrimination between walking-jogging activities using hidden Markov models applied to foot motion data from a gyroscope," *Gait & Posture*, vol. 36, no. 4, pp. 657–661, 2012.
- [23] M. Gori, R. Kamnik, L. Ambrožič et al., "Online phase detection using wearable sensors for walking with a robotic prosthesis," *Sensors*, vol. 14, no. 2, pp. 2776–2794, 2014.
- [24] W. C. Cheng and D. M. Jhan, "Triaxial accelerometer-based fall detection method using a self-constructing cascade-AdaBoost-SVM classifier," *IEEE Journal of Biomedical and Health Informatics*, vol. 17, no. 2, pp. 411–419, 2013.
- [25] S. Li, J. Wang, and X. Wang, "A novel gait recognition analysis system based on body sensor networks for patients with Parkinson's disease," in *2010 IEEE Globecom Workshops*, pp. 256–260, Miami, FL, USA, December 2010.
- [26] J. U. Chu, K. I. Song, S. Han et al., "Gait phase detection from sciatic nerve recordings in functional electrical stimulation systems for foot drop correction," *Physiological Measurement*, vol. 34, no. 5, pp. 541–565, 2013.
- [27] A. Kolawole and A. Tavakkoli, "A novel gait recognition system based on hidden Markov models," in *Advances in Visual Computing. ISVC 2012*, G. Bebis, R. Boyle, B. Parvin, D. Koracin, C. Fowlkes, S. Wang, M.-H. Choi, S. Mantler, J. Schulze, D. Acevedo, K. Mueller, and M. Papka, Eds., vol. 7432 of Lecture Notes in Computer Science, pp. 125–134, Springer, Berlin, Heidelberg, 2012.
- [28] J. Taborri, S. Rossi, E. Palermo, F. Patanè, and P. Cappa, "A novel HMM distributed classifier for the detection of gait phases by means of a wearable inertial sensor network," *Sensors*, vol. 14, no. 9, pp. 16212–16234, 2014.

- [29] Y. P. Ivanenko, G. Cappellini, N. Dominici, R. E. Poppele, and F. Lacquaniti, "Modular control of limb movements during human locomotion," *The Journal of Neuroscience*, vol. 27, no. 41, pp. 11149–11161, 2007.
- [30] T. Funato, S. Aoi, H. Oshima, and K. Tsuchiya, "Variant and invariant patterns embedded in human locomotion through whole body kinematic coordination," *Experimental Brain Research*, vol. 205, no. 4, pp. 497–511, 2010.
- [31] H. Nakayama, M. Arakawa, and R. Sasaki, "Simulation-based optimization using computational intelligence," *Optimization and Engineering*, vol. 3, no. 2, pp. 201–214, 2002.

Research Article

Anthropomorphism Index of Mobility for Artificial Hands

Immaculada Llop-Harillo , Antonio Pérez-González , and Verónica Gracia-Ibáñez 

Grupo de Biomecánica y Ergonomía, Departamento de Ingeniería Mecánica y Construcción, Universitat Jaume I (UJI), 12071, Spain

Correspondence should be addressed to Immaculada Llop-Harillo; illop@uji.es

Received 21 March 2019; Accepted 17 June 2019; Published 28 July 2019

Guest Editor: Francesca Cordella

Copyright © 2019 Immaculada Llop-Harillo et al. This is an open access article distributed under the Creative Commons Attribution License, which permits unrestricted use, distribution, and reproduction in any medium, provided the original work is properly cited.

The increasing development of anthropomorphic artificial hands makes necessary quick metrics that analyze their anthropomorphism. In this study, a human grasp experiment on the most important grasp types was undertaken in order to obtain an Anthropomorphism Index of Mobility (AIM) for artificial hands. The AIM evaluates the topology of the whole hand, joints and degrees of freedom (DoFs), and the possibility to control these DoFs independently. It uses a set of weighting factors, obtained from analysis of human grasping, depending on the relevance of the different groups of DoFs of the hand. The computation of the index is straightforward, making it a useful tool for analyzing new artificial hands in early stages of the design process and for grading human-likeness of existing artificial hands. Thirteen artificial hands, both prosthetic and robotic, were evaluated and compared using the AIM, highlighting the reasons behind their differences. The AIM was also compared with other indexes in the literature with more cumbersome computation, ranking equally different artificial hands. As the index was primarily proposed for prosthetic hands, normally used as nondominant hands in unilateral amputees, the grasp types selected for the human grasp experiment were the most relevant for the human nondominant hand to reinforce bimanual grasping in activities of daily living. However, it was shown that the effect of using the grasping information from the dominant hand is small, indicating that the index is also valid for evaluating the artificial hand as dominant and so being valid for bilateral amputees or robotic hands.

1. Introduction

In recent years, it has been an increasing development of new affordable and anthropomorphic prosthetic hands [1, 2] as a consequence of the improvements in 3D-printing technologies. The human hand is a complex and marvelous tool whose dexterity has not been achieved by any artificial hand. Evaluating the functional similarity of artificial hands with the human hand is essential for improving current anthropomorphic hand designs. Assessing the capability of the prostheses to perform the main grasp types (GTs) of human grasping could give an insight into the level of functionality restored in patients. Metrics or indexes that quantify numerically the level of anthropomorphism are the way to grade human-likeness and to provide specifications for maximizing the anthropomorphic functionality while designing new artificial hands.

Belter et al. [1] reviewed and compared the mechanical properties of different prosthetic hands, as their degrees of

freedom (DoFs), range of motion, and weight and number of actuators, but an index to compare those properties with the human hand was not defined. Some other previous studies tried to quantify the anthropomorphism of artificial hands with a numerical index. Feix et al. [3] proposed a metric for comparing the anthropomorphic motion capability of robotic and prosthetic hands, the anthropomorphism index (AI), being its computation cumbersome and based only on the position and orientation of the distal phalanges in different GTs. Liarokapis et al. [4] defined an anthropomorphism index to assess the robot's ability to mimic the human hand based on the comparison of the finger phalanx workspaces and also the workspaces of the fingers' base frames. Liu et al. [5] proposed twelve quantified prosthetic hand anthropomorphism evaluation indexes including physical and actuation properties, among which is included a DoF configuration evaluation. This index was based on a matrix of DoF configuration where the element of the matrix is set to 1 if there exist an artificial DoF in the corresponding position,

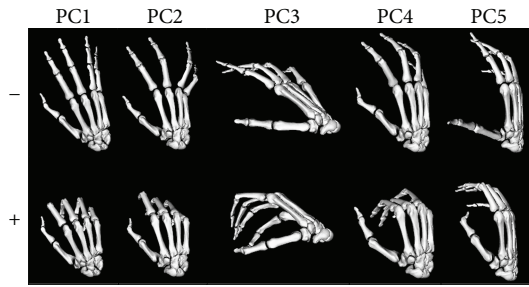


FIGURE 1: Principal components of the degrees of freedom of the human hand performing activities of daily living obtained in [10] (PC1: digit arching, PC2: closure, PC3: palmar arching, PC4: lateral pinch, and PC5: opposition).

otherwise is set to 0. However, this approach does not take into account the relevance of each DoF for grasping during activities of daily living (ADL) nor the underactuation in the joints. Underactuation in artificial hands [6] allows to use less actuators than DoFs while keeping versatility to adapt GTs to different object shapes.

Prostheses design could be different depending on its use for a dominant or nondominant hand; however, in the case of a patient who still has a healthy hand, the most appropriate strategy would be to consider the remaining hand as dominant [7, 8]. Thereby, the design of the prosthesis should be focused for a nondominant hand reinforcing bimanual grasping. The importance of the different GTs for personal autonomy of the patients in ADL has been studied previously by the authors [9], being pulp pinch (PP) (26%), extension grip (EG) (20.8%), tripod pinch (TP) (10.4%), and transverse volar grip (TVG) (8.7%), the most relevant GTs for a nondominant hand to reinforce bimanual grasping, representing together with the nonprehensile one, almost 90% of relevance for autonomy.

In the previous studies by the authors [10], the posture of the right hand from 24 healthy subjects performing 24 representative ADL was recorded with an instrumented glove. ADL were selected from the WHO's International Classification of Functioning, Disability and Health [11]. By applying principal component analysis (PCA), five factors explaining 73.7% of the variance were obtained. As shown in Figure 1, the five main principal components (PCs) of the DoFs of the human hand in ADL were "PC1: digit arching" (flexion of the interphalangeal joints), "PC2: closure" (combination of abduction of the fingers, except for the thumb, with flexion of the metacarpophalangeal joints), "PC3: palmar arching," "PC4: lateral pinch" (represents the lateral opposition of the thumb to the index), and "PC5: opposition" (represents the pad-to-pad opposition of the thumb to the little finger).

The aim of this study is to propose an index to measure the anthropomorphism of prosthetic hands, based on the comparison of the topology of the whole hand (joints and DoFs) and on the possibility to control these DoFs independently. The computation of the index, referred to as Anthropomorphism Index of Mobility (AIM), should weight each DoF depending on its importance for grasping in ADL. To define this importance, we used the information from previous experimental tests performed in the group and specific

tests developed in this study on the main GTs. Furthermore, a preliminary study [12] carried out on four human healthy subjects encouraged us to go deep in the study by increasing the number of subjects, improving the definition of the index, and widening the analysis of its validity to the different types of artificial hands. The AIM is intended to be a quick computation index based on the biomechanics of the human hand and thus providing a way to compare their functional anthropomorphism. Moreover, the relevance of each DoF for functionality, obtained by tests on the human hand in this study, is intended to be useful for other applications in artificial hand design.

2. Materials and Methods

2.1. Human Grasp Experiment. With the purpose of taking into account in the AIM the relevance of each DoF according to its importance for functional grasping, an experiment to measure the kinematics of the human hand in functional grasps was carried out. Twenty subjects, ten males and ten females, all of whom were right-handed and free of hand pathologies or injuries, performed the most relevant GTs for a nondominant hand to reinforce bimanual grasping in ADL (PP, EG, TP, and TVG [9]). Although the grasps were selected for a nondominant hand (most common use of a hand prosthesis for unilateral amputees), subjects were asked to perform grasps with their dominant hand to get the most natural performance of human grasping. The study was approved by the Ethics Committee of the University, and all the subjects gave their written informed consent. The ages of the subjects ranged intentionally between 20 and 51, being the average 35 ± 8 , in order to prevent kinematic alterations due to joint degeneration from ageing. Subjects were selected so that the distribution of hand sizes was representative of the population [13]. The hand width ranged from 70 to 96 mm with an average of 83 mm, and the hand length ranged from 170 to 210 mm with an average of 185 mm.

Twelve objects of different sizes were selected from the Yale-CMU-Berkeley Object and Model Set [14], three for each of the four GTs (PP, EG, TP, and TVG), in order to cover most common requirements in ADL for each one (Figure 2). The subjects were sitting with the hands in the table in a comfortable way: the arms close to the body and parallel to the sagittal plane, the elbows flexed 90° , the wrist on the edge of the table, and the hands laying on the table palms down in a natural posture. This was the starting and ending posture for each grasping action. Subjects were instructed on the different GTs to perform with each object, and objects to be grasped were situated one by one by the researcher at a distance of 30 cm in front of the subjects. Subjects were free to practice the grasps to be sure that it is in the correct posture before starting the recordings. The steps to perform the grasps during the experiment consisted of the following: grasping the object from the table with the correct hand posture/GT, lift it up during two seconds, and finally, release the object again on the table and return the hand to the starting position. The sequence of the twelve objects to grasp during the experiment is shown in Figure 2 in the



FIGURE 2: Grasping tasks of the experiment (a-l). T_g are the tasks ordered (g : indicates the order) followed by the object of the Yale-CMU-Berkeley Object and Model Set [14] to grasp and in brackets the grasp type to be performed in each task (TP: tripod pinch, EG: extension grip, TVG: transverse volar grip, and PP: pulp pinch).

specified order. The experiment was repeated three times per subject.

The kinematics of the hand while performing the grasping postures was recorded (100 Hz) using an instrumented right hand glove with 18 sensors (CyberGlove Systems LLC; San Jose, CA). DoF kinematics corresponding to 16 joint angles (marked with an asterisk in Table 1) was obtained using a previously validated protocol [15]: metacarpophalan-

geal flexion (MCP1 to MCP5, 1 to 5 meaning thumb to little digits), interphalangeal flexion of the thumb (IP1), proximal interphalangeal flexion of the fingers (PIP2 to PIP5), flexion and abduction of the carpometacarpal joint of the thumb (CMC1), relative abduction between finger MCPs (index-middle, middle-ring, and ring-little), and palmar arching. Prior to the tests with objects, the CyberGlove was calibrated for each subject following the calibration

TABLE 1: Joints and degrees of freedom (DoFs) of the human hand corresponding to the four different groups of DoFs defined.

Groups of DoFs	Joints and DoFs of the human hand
Finger flexion-extension (F/E)	MCP2_Flexion*
	PIP2_Flexion*
	DIP2_Flexion
	MCP3_Flexion*
	PIP3_Flexion*
	DIP3_Flexion
	MCP4_Flexion*
	PIP4_Flexion*
	DIP4_Flexion
	MCP5_Flexion*
PIP5_Flexion*	
DIP5_Flexion	
Finger abduction-adduction (AB/AD)	MCP2_Abduction*
	MCP3_Abduction
	MCP4_Abduction*
	MCP5_Abduction*
Palmar arching (P.ARC)	CMC5_Flexion*
	CMC4_Flexion
Thumb opposition (T.OPP)	CMC1_Flexion*
	CMC1_Abduction*
	MCP1_Flexion*
	MCP1_Abduction
	IP1_Flexion*

1: thumb, 2: index finger, 3: middle finger, 4: ring finger, 5: little finger; CMC: carpometacarpal joint, MCP: metacarpophalangeal joint, PIP: proximal interphalangeal joint, DIP: distal interphalangeal joint, IP: interphalangeal joint; * 16 joint angles measured during the experiment with the CyberGlove.

procedure [15]. Starting and final positions while the hand is not moving were trimmed from the recordings. Then, they were filtered with a 2nd-order 2-way low-pass Butterworth filter with cut-off frequency of 5 Hz [16, 17]. The tests were video recorded.

2.2. Index Definition. The Anthropomorphism Index of Mobility (AIM) for an artificial hand was defined based on two main factors: (1) the DoFs present in the hand along with its method of actuation and (2) the relevance of these DoFs for grasping in ADL.

The DoFs of the human hand (HH) [18, 19] were classified into four different functional groups for defining the AIM (Table 1): finger flexion-extension (12 in HH), finger abduction-adduction (4 in HH), palmar arching (2 in HH), and thumb opposition (5 in HH).

The Anthropomorphism Index of Mobility (AIM) was defined with

$$AIM = \sum_i (k_i \cdot w_i), \quad (1)$$

where the summation extends for $i = 1, 2, 3, 4$, corresponding to each one of the four groups of DoFs (Table 1: F/E, AB/AD, P.ARC, and T.OPP), the factor k_i accounts for the type of actuation of the DoFs included in this group, and the factor w_i is a weighting coefficient depending on the relevance of this group of DoF for grasping in ADL. Both the term k_i and the weighting factor w_i were defined to have a range between 0 and 1, and the sum of weighting coefficients w_i for the four groups is unity, so that the AIM reach a maximum value of 1 for the human hand and a very low value for an artificial hand with very poor anthropomorphism.

The factor k_i for each group i was defined to get a high value if the method of actuation for the DoFs in that group allows to control them independently, as in the human hand, and a lower value if the motions of these DoFs are highly coupled during motion. To this end, each DoF in the evaluated hand was classified according to the types included in Table 2.

The independent mobility of a DoF can be ranked qualitatively from better to worse, depending on its class, as $A > B > C > D > E$. Note that B class was considered better than C because it allows mechanical adaptation of the finger to the shape of the object to be grasped and do not suffer from mechanical singular configurations [6]. Pugh's method used in concept design evaluation [20] was employed to convert the ranked list of methods of actuation of the DoFs into a list of numerical coefficients c (last column in Table 2). However, the independent mobility of a DoF is associated not only with the type of actuation in this particular DoF but also with that of the DoFs more proximal in the same serial chain of a digit, i.e., for a finger, the mobility for flexion in the PIP joint is dependent on the mobility for flexion in the MCP joint. Consequently, for that case, the coefficient c_{ij} for the DoF j of the group i was obtained as the multiplication of the coefficient c of this DoF and those located proximally in the same serial kinematic chain. In addition, for assigning the coefficient c to several DoFs underactuated by the same motor or actuator, class A was considered for only one of them and class B or C for others. If a motor actuates several DoFs included in different groups i , the coefficient 1 corresponding to class A was divided among the number of groups and this fraction was assigned to only one of the DoFs in this group, being others classified as either B or C. Finally, the factor k_i for each group i was defined with equation (2), by summing the terms c_{ij} in the group i and dividing by the number of DoFs of the human hand in this group (n_i), which is, according to Table 1, 12 for $i = 1$, 4 for $i = 2$, 2 for $i = 3$, and 5 for $i = 4$.

$$k_i = \frac{\sum_j c_{ij}}{n_i}. \quad (2)$$

The weighting factor w_i in equation (1), accounting for the relative relevance of the DoFs of the group i for grasping in ADL, was defined with

$$w_i = \sum_k (r_{ik} \cdot s_k). \quad (3)$$

TABLE 2: Classification of the DoF depending on the type of actuation and numeric coefficient associated.

Class	Type of actuation of the DoF	c
A	DoF actuated by one independent motor or actuator	1
B	DoF underactuated with other DoFs without a rigid coupling, allowing adaptive grasps (tendons, elastic elements)	0.75
C	DoF underactuated with other DoFs with a rigid coupling, not allowing adaptive grasp (linkages)	0.5
D	No actuation on the DoF, but passive motion allowed	0.25
E	DoF absent in the artificial hand	0

In equation (3), r_{ik} weights the relative contribution of the group of DoFs i ($i = 1,2,3,4$) in human hand functionality represented through PC_k ($k = 1,2,3,4,5$), corresponding to each of the five kinematic functional synergies (see Figure 1) found in a previous study [10]. These PCs account for 73.7% of the variance when performing a wide set of representative ADL. The loading matrix of the PCs obtained in that study, which can be found in Supplementary Materials (available here), was used to calculate r_{ik} as shown in equations (4) and (5). For a PC_k , r_{ik} was computed as the sum of absolute values of the loadings l_{ijk} for the DoFs j included in the group i (according to Table 1) divided by the sum of the absolute value of all the loadings of that PC_k .

$$r_{ik} = \frac{\sum_j |l_{ijk}|}{a_k}, \quad (4)$$

$$a_k = \sum_i \sum_j |l_{ijk}|. \quad (5)$$

On the other hand, s_k in equation (3) contains the information about the importance of the PC_k in the most relevant GTs. To compute this term, first, the human hand kinematics was obtained from the human grasp experiment explained above, but to consider the relation with the functionality of the human hand during ADL, kinematics was transformed to be expressed as scores f_{tk} referred to the five functional PCs (Figure 1) instead of being expressed in the original sixteen variables (joint angles). This information can be found in Supplementary Materials. A greater absolute value of the score of a PC_k in one particular instant t indicates that the position of the hand is better represented by this PC_k . Next, for each of the twelve grasping tasks g (Figure 2), the absolute value of the scores f_{tk} for each PC_k was averaged during the task (equation (6)), and then (equation (7)) these means v_{gbp} were averaged across subjects b and repetitions p . The resulting means v_g were normalized (equation (8)) with respect to their sum across PCs h_g (equation (9)), providing the relative contribution of the five PCs to each grasping task n_g . Finally, these relative contributions were weight-averaged by the relative relevance of the GT for autonomy of each grasping task z_g and divided by 3 because three objects were considered for each GT (equation (10)). The weight z_g for averaging was obtained from the relative use of the four main GT for a nondominant hand in bimanual grasp-

ing [9]: 39.5% for PP, 31.6% for EG, 15.8% for TP, and 13.2% for TVG.

$$(v_{gbp})_k = \frac{\sum_{t=1}^m |f_{tk}|}{m}, \quad (6)$$

$$(v_g)_k = \frac{\sum_b \sum_p (v_{gbp})_k}{b \cdot p}, \quad (7)$$

$$(n_g)_k = \frac{(v_g)_k}{h_g}, \quad (8)$$

$$h_g = \sum_k (v_g)_k, \quad (9)$$

$$s_k = \frac{\sum_g [(n_g)_k \cdot z_g]}{3}. \quad (10)$$

2.3. Artificial Hands. With the objective of exemplifying the use of the AIM and verifying its utility, it was computed for several artificial hands with different topologies and actuation systems. The AIM was obtained for different affordable 3D-printed prosthetic hands, including the IMMA hand designed by the authors [21], some advanced commercial prosthetic hands, and other artificial hands. Some hands of these two later groups have been evaluated with other indexes of anthropomorphism in the literature, such as the anthropomorphism index (AI) [3] and the Total Score of Anthropomorphism (A_R) [4]. The main characteristics of the hands analyzed are described below.

2.3.1. Affordable 3D-Printed Prosthetic Hands

- (i) IMMA hand [21]: 3D-printed five-digit prosthetic hand, with 6 DoFs actuated by tendons: flexion in each finger and flexion and abduction in the thumb. It has three phalanges per finger and its joints are elastic elements. This hand is just a prototype and cannot be used as a prosthesis directly, it needs a socket with motors and a control system, but after a study of the authors [22], it is being considered here to be actuated by two motors following the two actuation synergies obtained from experiments with human actuation
- (ii) Cyborg Beast [23]: five-digit low-cost 3D-printed prosthetic hand for children with upper-limb differences. It is body-powered using the wrist of the amputee as the unique actuator to drive all the finger

tendons. It has two phalanges per finger and 5 DoFs: flexion in each finger and flexion of the thumb. Finger flexion is driven by tendons along the palmar surface of each finger. Elastic cords placed inside the dorsal aspect of the fingers provide passive finger extension. Its joints are Chicago screws and the materials used to print the different parts of the hand are PLA and ABS

- (iii) Flexy-Hand [24]: 3D-printed five-digit prosthetic hand, with 5 DoFs actuated by tendons: flexion in each finger and flexion in the thumb. It has three phalanges per finger and two phalanges in the thumb. The retraction is made through flexible 3D-printed joints. It is body-powered using the wrist of the amputee as the unique actuator to drive all the finger tendons
- (iv) KIT prosthetic hand [25]: five-digit 3D-printed hand prosthesis with underactuated mechanism, sensors, and embedded control system, developed by the Institute for Anthropomatics and Robotics (Karlsruhe Institute of Technology). Two motors (one for the four long fingers and other for the thumb) actuate 10 DoFs (flexion of two joints in each finger) by means of tendons. The four long fingers are simultaneously driven via a force-distributing transmission based on the TUAT/Karlsruhe mechanism providing shape adaptivity (all fingers keep closing until contact regardless of blocked movement in other joints). The passive reopening of the fingers is obtained through custom made springs
- (v) ADA [26]: Ada Hand V1.1 by Open Bionics is a five-digit myoelectric prosthetic hand entirely 3D-printed with flexible material. It is tendon driven and has two phalanges in each finger and one linear actuator for each digit driving their flexion

2.3.2. Commercial Prosthetic Hands

- (i) i-Limb: myoelectronically controlled, externally powered, tendon linking, multiarticulating prosthetic hand of Touch Bionics [27] with eleven joints (two joints in each long finger and three in the thumb). It has five individually powered digits and powered thumb rotation, with manual override
- (ii) Bebionic [28]: multiarticulating myoelectric prosthetic hand developed by RSL Steeper with eleven joints (two joints in each long finger and three in the thumb). It has five actuators, one for each finger, and the thumb has two positions manually placed by the user with an inbuilt sensor detecting the position. Folding links allow the fingers to flex. Among the 14 different grip patterns and hand positions that it can achieve, one of them is the finger adduction grip
- (iii) SensorHand Speed: the Ottobock SensorHand Speed [28] is a myoelectronically controlled hand with three actuated fingers, which are driven by the same motor. It is covered with a cosmetic glove that emulates the ring and little finger using a metal bar within the glove, which couples these fingers to the movements of the middle finger
- (iv) Michelangelo hand: five-digit technologically advanced prosthetic hand of Ottobock [28]. Actively driven elements are the thumb, index finger, and middle finger while the ring finger and little finger passively follow the other fingers. The six joints are controlled by two actuators (one for the flexion/extension of the five digits and the second one allows the thumb to be electronically positioned in an additional axis of movement being abducted/adducted). The fingers are slightly abducted when the MCP joints are extended, and when flexed, the fingertips adduct and touch each other, providing a finger abduction/adduction mode

2.3.3. Other Artificial Hands

- (i) FRH-4 hand: this is a robot hand built for the mobile-assisting robot ARMAR [29]. It has eight independent fluidic actuators: one in the metacarpus that allows the palm to flex in the middle, the index and middle fingers have two each, the ring and little fingers have one for both, and the thumb has two actuators
- (ii) Barrett [30]: three-digit programmable grasper of Robotnik. It has four brushless motors and three multijointed fingers (two phalanges connected by belt transmission), two of them have an extra DoF with 180° of lateral mobility
- (iii) DLR/HIT II [31]: used on Space Justin (humanoid upper body) for telemanipulation is a multisensory robot hand from Harbin Institute of Technology and DLR Institute for Robotics and Mechatronic. It has 15 DoFs, five identical modular fingers with two flat BLDC motors placed in the base. Each finger has three active DoFs (2 DoFs of flexion and one of abduction) and four joints (the motions of distal and medial phalanges are coupled by a linkage). The thumb is fixed in an appropriate orientation of the palm
- (iv) Shadow [32]: the Shadow Dexterous Hand is a humanoid robot hand created by the Shadow Robot Company. The four fingers have 2 one-axis joints (DIP and PIP) and one universal MCP joint; the little finger has an extra one-axis joint on the metacarpal to provide arching. The thumb has a one-axis joint (IP) and two universal joints (MCP and CMC). It contains 20 motors in the forearm (3 DoFs per finger, 5 DoFs in the thumb, 1 DoF in the palm, and 2 DoFs in the wrist)

3. Results and Discussion

Figure 3 shows a representative plot of the mean value and standard deviation across all the subjects (20) and repetitions (3) of the 16 joint angles measured with the CyberGlove

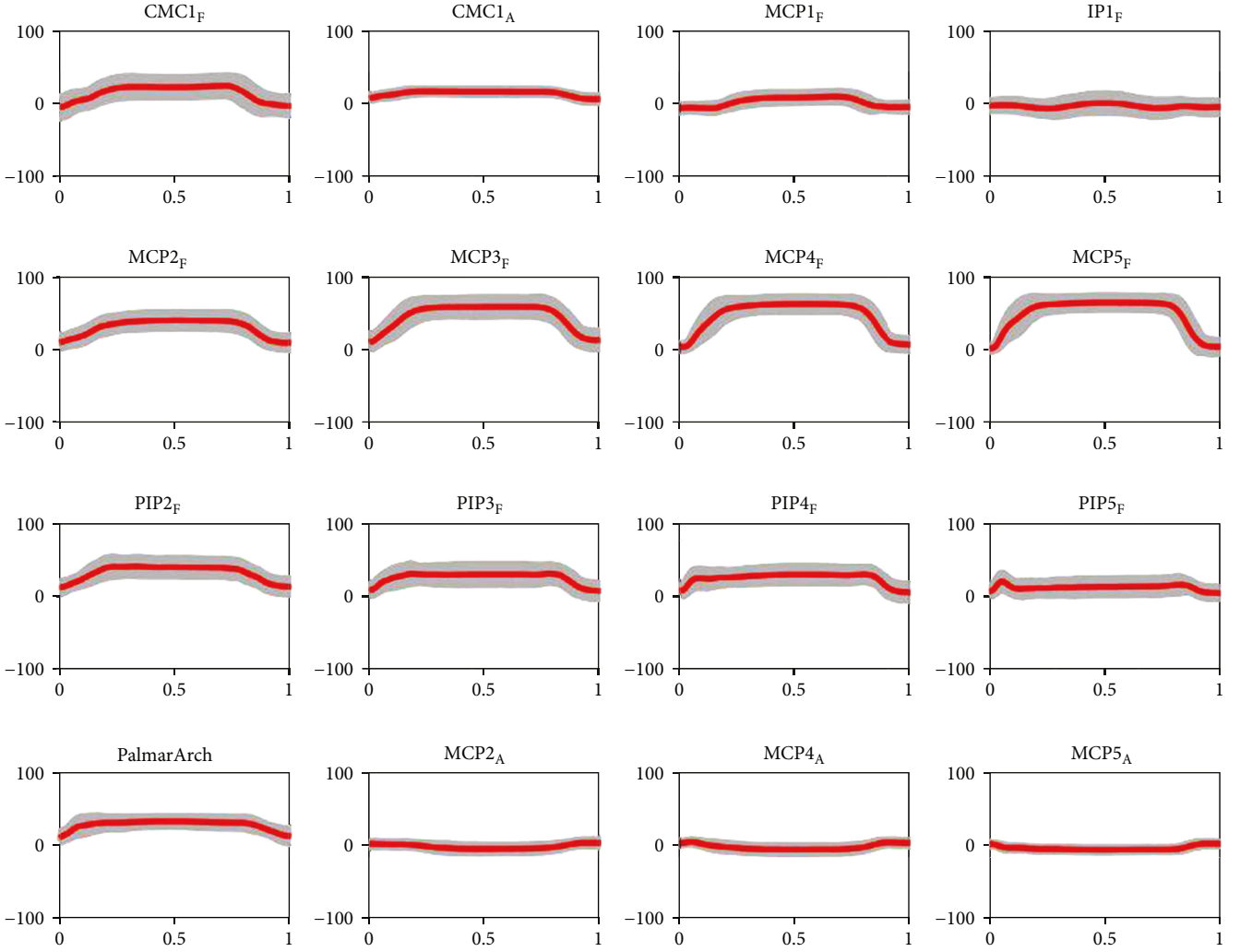


FIGURE 3: Mean and standard deviation of the 16 joint angles (in degrees) measured with the CyberGlove during the extension grip of the plate (T_{02}). The angles are normalized across time (1: thumb, 2: index finger, 3: middle finger, 4: ring finger, and 5: little finger; CMC: carpometacarpal joint, MCP: metacarpophalangeal joint, PIP: proximal interphalangeal joint, DIP: distal interphalangeal joint, IP: interphalangeal joint; F: flexion/extension; and A: abduction/adduction).

while performing a grasp of one object of the human grasp experiment (T_{02} of Figure 2).

Table 3 shows the relative contribution of the five PCs to each grasping task of the human grasp experiment (n_g) _{k} (equation (8)) together with the final value of the parameter s_k for each PC (equation (10)), obtained from these relative contributions weight-averaged by their importance in ADL z_g [9].

The contributions of the different PCs to each grasping task ranged between 9.6% and 39.1%, indicating that all the five PCs have a nonnegligible importance in the twelve grasping tasks analyzed. It can be seen that PC1, corresponding to “digit arching,” is predominant in grasping tasks involving PP ($g = \{4, 8, 12\}$). Moreover, “palmar arching” (PC3) and “lateral pinch” (PC4) synergies are less represented in average in the four main GTs considered in the experiment, leading to lower values of the final parameter s_k for these PCs, although the difference with “opposition” (PC5) is small.

“Digit arching” (PC1) is the most significant synergy, as indicated by the higher value of s_k .

Table 4 shows the matrix r_{ik} (equation (4)) containing the influence of the different groups of DoFs of the human hand on the five kinematic functional synergies (Figure 1) and the resulting parameter w_i after applying equation (3) with this matrix r_{ik} and the vector s_k (Table 3).

The parameter w_i weights the relevance of the different groups of DoFs in the human grasps in ADL. These results indicate that finger flexion-extension is by far the most relevant group of DoFs accounting for more than half of the functionality, followed by thumb opposition and finger abduction-adduction. The palmar arching has a relevance of only 5%. This result by itself is valuable for making decisions during the design of new artificial hand prototypes to maximize their functionality.

Table 5 shows the value of the parameter k_i (equation (2)) for each group of DoFs for the artificial hands analyzed. The

TABLE 3: Mean (SD) of the relative contribution n_g of the five PCs in each grasping task T_g (g : indicates the order of the tasks in Figure 2) and final value of the parameter s_k for each PC.

	PC1 (%)	PC2 (%)	PC3 (%)	PC4 (%)	PC5 (%)
T_{01}	19.2 (6.4)	24.4 (7.6)	18.4 (7.7)	13.0 (7.7)	24.9 (9.7)
T_{02}	22.6 (6.9)	14.2 (6.3)	25.1 (6.1)	22.4 (8.1)	15.7 (8.4)
T_{03}	25.1 (4.7)	23.1 (4.7)	15.6 (4.3)	24.9 (8.9)	11.3 (5.5)
T_{04}	33.5 (6.7)	19.1 (3.8)	12.6 (3.5)	12.1 (4.2)	22.7 (10.6)
T_{05}	22.4 (8.3)	21.4 (8.9)	18.6 (8.5)	17.4 (10.6)	20.1 (13.9)
T_{06}	28.2 (6.0)	21.0 (5.0)	17.9 (5.4)	17.0 (9.5)	16.0 (10.2)
T_{07}	28.3 (5.0)	21.1 (3.8)	12.9 (4.3)	27.0 (9.2)	10.8 (5.8)
T_{08}	39.1 (6.2)	23.6 (4.0)	12.9 (4.6)	11.8 (7.7)	12.5 (7.3)
T_{09}	19.5 (8.2)	24.5 (7.1)	14.3 (7.9)	20.3 (10.1)	21.3 (9.0)
T_{10}	30.9 (6.2)	18.6 (5.2)	20.1 (6.2)	9.6 (5.4)	20.7 (11.7)
T_{11}	19.9 (3.4)	19.8 (7.7)	19.2 (7.9)	18.3 (10.8)	22.8 (13.3)
T_{12}	34.0 (7.4)	20.4 (5.1)	12.8 (4.3)	12.1 (6.5)	20.8 (9.6)
s_k	29.0	20.5	16.5	15.6	18.4

TABLE 4: Matrix r_{ik} and resulting w_i (equation (3)).

Groups of DoFs	Functional synergies					w_i (%)
	PC1 (%)	PC2 (%)	PC3 (%)	PC4 (%)	PC5 (%)	
Finger flexion-extension	79.6	50.7	42.5	51.8	34.9	55
Finger abduction-adduction	8.8	37.8	6.9	20.7	5.4	16
Palmar arching	4.4	3.4	15.3	0.2	1.9	5
Thumb opposition	7.2	8.1	35.3	27.3	57.9	24

TABLE 5: Parameter k_i (equation (2)) for each group of DoFs for the different artificial hands.

Artificial hand	F/E	AB/AD	P.ARC	T.OPP
IMMA	0.48	0.25	0	0.50
Cyborg Beast	0.29	0	0	0.18
Flexy-Hand	0.39	0.25	0	0.23
KIT	0.47	0	0	0.35
ADA	0.58	0.25	0	0.40
i-Limb	0.58	0	0	0.55
Bebionic	0.50	0	0	0.50
SensorHand	0.13	0	0	0.10
Michelangelo	0.13	0	0	0.30
FRH-4	0.46	0	0.50	0.40
Barrett	0.25	0.38	0	0.30
DLR/HIT II	0.83	1	0	0.70
Shadow	0.83	1	0.50	1

F/E: finger flexion-extension, AB/AD: finger abduction-adduction, P.ARC: palmar arching, T.OPP: thumb opposition.

details about the computation for each hand (c_{ij}) are supplied as Supplementary Materials. It can be seen that F/E and T.OPP are the groups of DoFs mainly included and actively driven in the artificial hands, manifested by higher values of k_i . It is worth to note that this fact is coherent with the greater relevance of these groups of DoFs in ADL, as indicated

TABLE 6: Results of the Anthropomorphism Index of Mobility (AIM) for different artificial hands and comparison with other indexes of the literature.

Artificial hand	AIM (%)	AI (%) [3]	A_R (%) [4]
IMMA	42		
Cyborg Beast	20		
Flexy-Hand	31		
KIT	34		
ADA	46		
i-Limb	45		
Bebionic	40		
SensorHand	10	0.25	
Michelangelo	14	2.80	
FRH-4	37	5.20	
Barret	27		10.38
DLR/HIT II	78		26.61
Shadow	88		39.93

by the parameter w_i (Table 4). Notwithstanding, some hands as the SensorHand and Michelangelo showed low scores in F/E because of their rigid fingers without interphalangeal joints. The unique hand with the 5 DoFs in T.OPP actively driven is the Shadow hand. AB/AD is included actively in DLR/HIT II and Shadow hands and passively through the

TABLE 7: Range of motion of the hand joints (in degrees) obtained in the human grasp experiment.

	Thumb (°)			Index (°)			Middle (°)			Ring (°)			Little (°)		
	F CMC	A CMC	F MCP	F IP	F MCP	A MCP	F PIP	F MCP	F PIP	F MCP	A MCP	F PIP	F MCP	A MCP	F PIP
Min	-27	0	-24	-32	-22	-9	0	-16	0	-13	-7	-1	-13	-7	-2
Max	32	28	13	42	51	24	62	65	66	68	16	76	69	12	68
P5	-6	0	-10	-5	-4	-3	1	-1	1	-1	-1	1	-3	-1	0
P95	15	19	2	17	30	9	36	40	42	30	8	49	26	7	40

CMC: carpometacarpal joint, MCP: metacarpophalangeal joint, PIP: proximal interphalangeal joint, DIP: distal interphalangeal joint, IP: interphalangeal joint, F: flexion (+)/extension (-), A: abduction (+)/adduction (-), P: percentile.

use of deformable joints in some 3D-printed hands. Finally, P.ARC is only present in FRH-4 and Shadow hands.

Finally, Table 6 shows the AIM for the different artificial hands, obtained using equation (1) and considering the parameters shown in Tables 4 and 5. Two factors affect the final AIM obtained by a hand (equation (1)): its mobility and type of actuation, represented by the number of DoF, the number of actuators, the number of digits and phalanges per digit, and the type of underactuation, affecting to the final parameters k_i ; and how this mobility and actuation system is distributed among the different groups of DOFs, with regard to the human hand, affecting through the weighting factor w_i (Table 4). The most advanced robotic hands (DLR/HIT II and Shadow) with a significant amount of motors and DoFs, and located in the important groups of DoFs, with higher weight w_i (F/E, T.OPP, and AB/AD), obtained the highest AIM scores, above 75%. The commercial prosthetic hands i-Limb and Bebionic as well as some 3D-printed hands (ADA, IMMA) obtained AIM scores between 40% and 50%. These hands include a reasonable number of motors and DoFs in the important groups (F/E and T.OPP). The rest of the hands obtained scores below 40% with the lowest score being for the SensorHand. The reason behind this lower AIM is an improvable number of DoFs, motors, or type of underactuation in the groups of F/E, T.OPP, or both.

The results shown in Table 6 indicate that the artificial hands analyzed in the literature with other anthropomorphism indexes, such as AI [3] or A_R [4], are ranked equally by the AIM and the other metrics, although the scores are different. The method used to compute the indexes justify these different scores. The AI is obtained from the achievable workspace of positions and orientations of the fingers' distal segments and compares this with information obtained experimentally from human hand grasping. The A_R is based on the computation of the finger phalanx workspace combined with that of the finger base frames, and the comparison with the human hand is made through a simplified model of their joints and geometry. It is worth to note that obtaining AI and A_R involves using complex algorithms and detailed information of the hand design, not easily available, while obtaining the AIM just requires information about the number of DoFs and the possibility to control them independently. Despite these differences in the method used to obtain each index, the fact that they rank equally, the hands as the AIM can be seen as a kind of validation of our index. Two main points can justify the use of

the AIM as a method for evaluating the anthropomorphism of an artificial hand.

- (i) It is really quick to obtain: simply, the parameter k_i has to be calculated, according to the DoFs and actuation methods of the artificial hand and equation (1) has to be applied (w_i is provided above)
- (ii) It analyzes not only the topology but also the functionality of the artificial hand because it takes into account the results obtained in grasping tests and ADL with the human hand

Notwithstanding, some important aspects in the design of an artificial hand are not within the scope of the AIM: the orientation of the joint axes, the range of motion of the different hand joints, the dimension of the phalanges, the friction coefficient of the parts of the hand in contact with the objects, the grasping force exerted by the actuators, the efficiency of the driving linkages, the control system, etc. Some previous studies [33–35] have shown the relevance of these aspects. In this sense, the AIM, involving mainly the topological structure, the number of actuators, and the type of underactuation, can be considered as an index especially useful in the concept design stage. The other design considerations cited above should be taken into account in later design stages: preliminary or detail design. Additional indexes that take into account these aspects could be interesting, and future works can go in this way. The index proposed by Liu et al. [5] considers some of these aspects, but it does not include their relevance for functionality according to human grasping tests. With respect to the phalanx dimensions and the joints' range of motion, the authors developed some studies [13, 16, 36] helping to obtain anthropomorphic designs. However, the evaluation of some of the design aspects cited above is difficult to be performed with indexes, requiring experimentation, after detailed design of the artificial hand and manufacturing a prototype. The authors have proposed methods for this experimental evaluation considering the main GTs in ADL and a special device for actuating the hand prototype [21].

The ranges of motion of the hand joints obtained in the human grasp experiment undertaken in this study are shown in Table 7. A wide range of motion for the different joints was covered with the objects selected in comparison to the functional range of motion of the human hand joints in

ADL [16]. These ranges could be considered as a minimum for prostheses with functional grasping for the main GTs, although general manipulation would recommend using larger ranges if possible.

This study was primarily focused on prosthetic hands, and therefore, the scoring system takes into account the capability of the hand to perform the most important GTs for a nondominant hand to reinforce bimanual grasping (through parameter z_g). For the case of a dominant hand reinforcing bimanual grasping, the parameter z_g for the four GTs considered in this study changes to [9] PP (58.0%), EG (16.6%), TP (9.5%), and TVG (16.0%). The effect of this change on the resulting w_i is negligible and implies a disparity of the AIM obtained for the artificial hands analyzed (Table 6) of a maximum of 1%. Therefore, the AIM is considered useful to evaluate the anthropomorphism of both dominant and nondominant hands. With this result and the result obtained from the comparison of the AIM with other indexes of the literature [3, 4], we can conclude that the index proposed can be valid for artificial both robotic and prosthetic hands, regardless of whether they are dominant or nondominant hands.

4. Conclusion

In this study, we have presented an anthropomorphism index (AIM) that can be used to evaluate and compare the mobility of artificial hands in relation to the human hand functionality, especially in concept design. The AIM evaluates the topology of the whole hand (joints and DoFs) and the possibility to control these DoFs independently according to their functionality. We have shown that the index can be valid for both prosthetic and robotic hands, dominant and nondominant hands. To define the index, the functionality of the different groups of DoFs of the hand (F/E, AB/AD, P.ARC, and T.OPP) was analyzed according to a human grasp experiment on twenty subjects with the four main GTs for personal autonomy in ADL. It was concluded that the relevance of the different groups of DoFs (w_i) was 55% for F/E, 16% for AB/AD, 5% for P.ARC, and 24% for T.OPP. Thirteen artificial hands, including affordable 3D-printed prosthetic hands, advanced commercial prosthetic hands, and robotic hands, were evaluated and compared with the AIM, and the reason for their differences was discussed. The results obtained in this study should be taken into account in the concept design stage of new prototypes in order to obtain new designs that maximize their functionality. Further research will focus on new metrics for later design stages considering other design aspects (range of motion of the joints, relative length of the phalanges, orientation of the joints axes, etc.) and on experimental benchmarks to measure the grasping capability of artificial hands.

Data Availability

The human hand kinematics expressed as joint angles and scores referred to the five PCs, the loading matrix corresponding to these PCs, and the c_{ij} values for the joints of the artificial hands analyzed; the data used to support the

findings of this study are included within the supplementary information files.

Conflicts of Interest

The authors declare that there is no conflict of interest regarding the publication of this paper.

Acknowledgments

This work was supported by the Spanish Ministry of Economy and Competitiveness and ESF (grant number BES-2015-076005); the Spanish Ministry of Economy and Competitiveness, AEI, and ERDF (grant numbers DPI2014-60635-R, DPI2017-89910-R); and Universitat Jaume I (grant numbers UJI-B2017-70, UJI-B2017-51).

Supplementary Materials

The excel file “JointAngles” contains the joint angles for each instant for the twelve tasks repeated three times by twenty subjects during the human grasp experiment. The excel file “Scores” contains the human hand kinematics in the human grasp experiment transformed to scores f_{ik} referred to five functional synergies for the twelve tasks repeated three times by twenty subjects. The excel file “LoadingsMatrix” contains the loadings l_{ijk} of the five functional synergies during ADL. The excel file “ArtificialHands” contains the value c_{ij} according to the method of actuation for each DoF in the artificial hands analyzed and the corresponding k_i of each hand. (*Supplementary Materials*)

References

- [1] J. T. Belter, J. L. Segil, A. M. Dollar, and R. F. Weir, “Mechanical design and performance specifications of anthropomorphic prosthetic hands: a review,” *Journal of Rehabilitation Research and Development*, vol. 50, no. 5, pp. 599–618, 2013.
- [2] J. ten Kate, G. Smit, and P. Breedveld, “3D-printed upper limb prostheses: a review,” *Disability and Rehabilitation. Assistive Technology*, vol. 12, no. 3, pp. 300–314, 2017.
- [3] T. Feix, J. Romero, C. H. Ek, H. B. Schmedmayer, and D. Kragic, “A metric for comparing the anthropomorphic motion capability of artificial hands,” *IEEE Transactions on Robotics*, vol. 29, no. 1, pp. 82–93, 2013.
- [4] M. V. Liarokapis, P. K. Artemiadis, and K. J. Kyriakopoulos, “Quantifying anthropomorphism of robot hands,” in *2013 IEEE International Conference on Robotics and Automation*, pp. 2041–2046, Karlsruhe, Germany, May 2013.
- [5] Y. Liu, D. Yang, L. Jiang, and H. Liu, “A synthetic framework for evaluating the anthropomorphic characteristics of prosthetic hands,” in *2015 IEEE International Conference on Advanced Intelligent Mechatronics (AIM)*, pp. 877–884, Busan, South Korea, July 2015.
- [6] L. Birglen, T. Laliberté, and C. Gosselin, *Underactuated Robotic Hands*, Springer Tracts in Advanced Robotics book series (STAR, volume 40), Springer, 2008.
- [7] M. W. Cornwall, “Prosthetics and patient management: a comprehensive clinical approach,” *Physical Therapy*, vol. 87, no. 4, p. 482, 2007.

- [8] K. E. Yancosek and D. R. Mullineaux, "Stability of handwriting performance following injury-induced hand-dominance transfer in adults: a pilot study," *Journal of Rehabilitation Research and Development*, vol. 48, no. 1, pp. 59–68, 2011.
- [9] V. Gracia-Ibáñez, J. L. Sancho-Bru, and M. Vergara, "Relevance of grasp types to assess functionality for personal autonomy," *Journal of Hand Therapy*, vol. 31, no. 1, pp. 102–110, 2018.
- [10] V. Gracia Ibañez, *Contribution to hand functional assessment based on its kinematics*, Universitat Jaume I, Castelló de la Plana, 2016.
- [11] World Health Organization, *Towards a common language for functioning, disability and health ICF the International Classification of Functioning, Disability and Health*, World Heal. Organ, Geneva, 2002.
- [12] I. Llop-Harillo, A. Pérez-González, and V. Gracia-Ibáñez, *Anthropomorphism index of mobility for hand prostheses*, XXVI Congress of the International Society of Biomechanics, 2017.
- [13] M. Vergara, M. J. Agost, and V. Gracia-Ibáñez, "Dorsal and palmar aspect dimensions of hand anthropometry for designing hand tools and protections," *Human Factors and Ergonomics in Manufacturing & Service Industries*, vol. 28, no. 1, pp. 17–28, 2018.
- [14] B. Calli, A. Walsman, A. Singh, S. Srinivasa, P. Abbeel, and A. M. Dollar, "Benchmarking in manipulation research: using the Yale-CMU-Berkeley object and model set," *IEEE Robotics and Automation Magazine*, vol. 22, no. 3, pp. 36–52, 2015.
- [15] V. Gracia-Ibáñez, M. Vergara, J. H. Buffi, W. M. Murray, and J. L. Sancho-Bru, "Across-subject calibration of an instrumented glove to measure hand movement for clinical purposes," *Computer Methods in Biomechanics and Biomedical Engineering*, vol. 20, no. 6, pp. 587–597, 2017.
- [16] V. Gracia-Ibáñez, M. Vergara, J. L. Sancho-Bru, M. C. Mora, and C. Piqueras, "Functional range of motion of the hand joints in activities of the International Classification of Functioning, Disability and Health," *Journal of Hand Therapy*, vol. 30, no. 3, pp. 337–347, 2017.
- [17] V. Patel, M. Burns, R. Chandramouli, and R. Vinjamuri, "Biometrics based on hand synergies and their neural representations," *IEEE Access*, vol. 5, pp. 13422–13429, 2017.
- [18] I. A. Kapandji, *The Physiology of the Joints: Upper Limb*, Churchill Livingstone, 1982.
- [19] J. L. Sancho-Bru, *Modèl biomecànic de la mà orientat al disseny d'eines manuals*, Universitat Jaume I, 2000.
- [20] D. G. Ullman, *The Mechanical Design Process*, McGraw-Hill, 4th edition, 2010.
- [21] I. Llop-Harillo and A. Pérez-González, "System for the experimental evaluation of anthropomorphic hands. Application to a new 3D-printed prosthetic hand prototype," *International Biomechanics*, vol. 4, no. 2, pp. 50–59, 2017.
- [22] I. Llop-Harillo, A. Pérez-González, and J. Cantero-Ramis, "Analysis of motion synergies in grasping tasks for a 6-DOF tendon-driven prosthetic hand," in *16th International Symposium on Computer Methods in Biomechanics and Biomedical Engineering and 4th Conference on Imaging and Visualization*, New York, 2019.
- [23] J. Zuniga, D. Katsavelis, J. Peck et al., "Cyborg beast: a low-cost 3d-printed prosthetic hand for children with upper-limb differences," *BMC Research Notes*, vol. 8, no. 1, p. 10, 2015.
- [24] Gyrobot, "Flexy-Hand 2," 2014, March 2019, <https://www.thingiverse.com/thing:380665>.
- [25] P. Weiner, J. Starke, F. Hundhausen, J. Beil, and T. Asfour, "The KIT prosthetic hand: design and control," in *2018 IEEE/RSJ International Conference on Intelligent Robots and Systems (IROS)*, Madrid, Spain, October 2018.
- [26] Open Bionics, "Open Bionics hands," 2018, March 2019, <https://openbionicslabs.com/downloads>.
- [27] Touch Bionics, "Touch Bionics products," 2019, March 2019, <http://touchbionics.com/products>.
- [28] Ottobock, "Ottobock myoelectric prosthetics," 2017, March 2019, <https://www.ottobockus.com/prosthetics/upper-limb-prosthetics/solution-overview/myoelectric-prosthetics/>.
- [29] I. Gaiser, S. Schulz, A. Kargov et al., "A new anthropomorphic robotic hand," in *Humanoids 2008 - 8th IEEE-RAS International Conference on Humanoid Robots*, pp. 418–422, Daejeon, South Korea, December 2008.
- [30] Barrett Technology, "BarrettHand," March 2019, <https://www.barrett.com/about-barrethand>.
- [31] H. Liu, K. Wu, P. Meusel et al., "Multisensory five-finger dexterous hand: the DLR/HIT hand II," in *2008 IEEE/RSJ International Conference on Intelligent Robots and Systems*, Nice, France, September 2008.
- [32] Shadow Robot Company, "Shadow dexterous hand," 2019, March 2019, <https://www.shadowrobot.com/products/dexterous-hand/>.
- [33] M. Controzzi, M. D'Alonzo, C. Peccia, C. M. Oddo, M. C. Carrozza, and C. Cipriani, "Bioinspired fingertip for anthropomorphic robotic hands," *Applied Bionics and Biomechanics*, vol. 11, no. 1-2, 38 pages, 2014.
- [34] M. Ceccarelli, N. E. N. Rodríguez, G. Carbone, and C. Lopez-Cajùn, "An optimal design of driving mechanism in a 1 degree of freedom (d.o.f.) anthropomorphic finger," *Applied Bionics and Biomechanics*, vol. 2, no. 2, pp. 103–110, 2005.
- [35] F. J. Andrés, A. Pérez-González, C. Rubert, J. Fuentes, and B. Sospedra, "Comparison of grasping performance of tendon and linkage transmission systems in an electric-powered low-cost hand prosthesis," *Journal of Mechanisms and Robotics*, vol. 11, no. 1, article 011018, 2018.
- [36] I. Llop-Harillo, V. Gracia-Ibáñez, and A. Pérez-González, "Analysis of anthropometric dimensions and joints range of motion of the human hand for application to the design of hand prostheses," in *8th World Congress on Biomechanics*, 2018.